Electrokinetic Transport Phenomena in Nanochannels and Applications of Nanochannel-based Devices in Nanoparticle Detection and Molecule Sensing

by

Ran Peng

A thesis

presented to the University of Waterloo
in fulfilment of the
thesis requirement for the degree of
Doctoral of Philosophy
in
Mechanical and Mechatronics Engineering

Waterloo, Ontario, Canada, 2018

EXAMINING COMMITTEE MEMBERSHIP

The following served on the Examining Committee for this thesis. The decision of the Examining Committee is by majority vote.

External Examiner

NAME	Deyu Li
Title	Professor

Supervisor(s)

NAME	Dongqing Li
Title	Professor

Internal Member

NAME	Mustafa Yavuz
Title	Professor

Internal Member

NAME	Michael Mayer
Title	Associate Professor

Internal-external Member

NAME	Shirley Tang
Title	Associate Professor

AUTHOR'S DECLARATION

I hereby declare that I am the sole author of this thesis. This is a true copy of the thesis, including any required final revisions, as accepted by my examiners.

I understand that my thesis may be made electronically available to the public.

ABSTRACT

Nanofluidics investigates transport phenomena, manipulation, and control of fluids and nano-sized objects in fluidic channels with an at least one-dimensional size smaller than 100 nm. At the nanoscale, fluids and objects exhibit lots of unique physical and mechanical behaviors which cannot be observed in micron-sized or macro-sized structures, especially for electrokinetically driven cases. Electrokinetic transport phenomena in nanochannels offer promising possibilities for new applications of nanofluidic systems, such as drug delivery, DNA sequencing, and biosensing. However, the current widely-used nanofabrication technologies are complicated, time-consuming and expensive. Fundamental research of electrokinetic transport phenomena at the nanoscale has been focused on analytical and numerical models, and very limited experimental studies have been conducted. Resistive pulse sensing (RPS) technology has been integrated with nanofluidics and applied in nanoparticle characterization; however, traditional nano-orifice-based RPS detection systems are not suitable for practical applications due to their bulky size, low sensitivity, and high cost.

This thesis studies electrokinetic transport phenomena in polydimethylsiloxane (PDMS) nanochannels, as well as applications of nanochannel-based nanofluidic devices in nanoparticle detection and molecule sensing. At the beginning of this thesis, a cost-effective, productive and simple method for fabricating disposable PDMS nanofluidic devices by the solvent-induced cracking method and nanoimprint technique is developed. The channel size is controlled by the working parameters of the solvent-induced cracking method while the quantity and locations of these nanocracks are determined by artificial defects. A detailed guideline for making PDMS nanofluidic chips with single nanochannels or multiple nanochannels of controllable channel size and spacing is provided. Nanochannels of 20 nm in depth can be obtained easily by using this method.

Two fundamental research projects are conducted on single-nanochannel-based nanofluidic chips to investigate electrokinetically driven fluids and particles in nanochannels. Electroosmotic flow (EOF) in single nanochannels is measured by the current slope method. Channel size effects, concentration effects and electric field effects upon EOF velocity in nanochannels are investigated systematically. The decrease of EOF velocity due to overlapping of electric double layers (EDLs) is demonstrated by experiments. The experimental results are in good agreement with the numerical simulation results. Electrokinetic (EK) motion of single nanoparticles in single PDMS nanochannels is investigated by particle tracing method systematically. Effects of ionic concentration of the

electrolyte media, applied electric field, and particle-to-channel size ratio on particle velocity are studied. The velocity of nanoparticles inside the single nanochannels is suppressed by the confined nanospace due to interactions between EDLs.

Lastly, by using the nanochannel-based nanofluidic chips, two applications are developed to detect nanoparticles, cations as well as DNA molecules by the RPS technique. A mathematic model for single-gate differential RPS detection systems is developed to evaluate the RPS signals; working parameters involved in particle detection by using the nanochannel-based differential RPS chips are studied experimentally. The signal-to-noise ratio (SNR) of the PDMS nanochannel-based differential RPS systems is also explored by experiments. To enhance the resolution of the nanochannel-based RPS devices, carbon nanotubes (CNTs) are integrated into differential RPS nanofluidic chips to work as the sensing gates. Novel methods to isolate and cut individual CNTs for CNT-based nanofluidic devices are also created. The CNT-channel-based differential RPS chips are used to detect single cations and individual ssDNA molecules. Distinguishing of 15-nt ssDNAs and 30-nt ssDNAs with high resolution has been achieved.

This thesis provides the nanofluidic research community with a comprehensive working procedure for fabricating cost-effective PDMS-based nanofluidic chips. The fundamental studies in this thesis expand our understanding of electrokinetic transport phenomena at the nanoscale, and the differential RPS detection systems developed on the nanochannel-based nanofluidic chips open a new avenue to nanoparticle detection as well as molecule sensing.

ACKNOWLEDGMENTS

First and foremost, I would like to thank my supervisor, Prof. Dongqing Li, for his patient advice, solid support and encouragement. His foresight and confidence in academic research inspired me a lot and changed my life. Without his enthusiasm and advice, I definitely cannot arrive at this stage and finalize this thesis. I also would like to thank the other committee members, Prof. Deyu Li from Vanderbilt University, Prof. Shirley Tang, Prof. Mustafa Yavuz, and Prof. Michael Mayer from the University of Waterloo for their valuable comments.

Hereby, I would like to thank Andy Barber, Mark Griffett from the Department of Mechanical Engineering and Prof. Cui, Prof. Tang, for their technical support. I also would like to appreciate my friends who always backed me during my Ph.D. studies. They are Dr. Biwu Liu, Dr. Li Yu, Dr. Quan Pang, Dr. Xiaoqi Sun, Dr. Zihe Pan and Dr. Yael Ziberman from the Department of Chemistry and the Department of Chemical Engineering. My colleagues at the Microfluidic and Lab-on-a-Chip Lab also helped me a lot and contributed a lot to my productivity. I am grateful to the former group members Fang Zhang, Xiaoling Zhang and the current members Mengqi Li, Kelvin Zhao, Chengfa Wang and Jun Li. It was really enjoyable to work with them.

Many thanks to all of my friends who have been with me, my life in Waterloo would be terrible without you. I would like to thank you guys, Dr. Ning Qin, Dr. Pei Zhao, Hongli Liu and Yuze Huang.

Additionally, I am grateful to my founding sources from Natural Sciences and Engineering Research Council (NSERC) of Canada, and China Scholarship Council (CSC).

Lastly, I would like to thank my parents and my sisters who always support me unconditionally for my entire academic career. I feel truly lucky to have such a supportive family.

TABLE OF CONTENTS

LIST OF FIGURES

LIST OF TABLES

LIST OF ABBREVIATIONS

AFM	Atomic Force Microscopy	**HSP**	Hansen Solubility Parameter
AR	Aspect Ratio	**IL**	Interferometric Lithography
BOE	Buffer Oxide Etching	**IPCVD**	Ionized Physical Vapor Deposition
CCD	Charge-Coupled Device	**MD**	Molecular Dynamics
CNT	Carbon Nanotube	**MHDA**	Mercaptohexadecanoic Acid
CVD	Chemical Vapor Deposition	**MR**	Microchannel Refilling
DC	Direct Current	**MWNT**	Multi-Wall NanoTube
DEP	Dielectrophoresis	**NIL**	Nanoimprint Lithography
DLS	Dynamic Light Scattering	**N-S**	Navier-Strokes
DNA	Deoxyribonucleic Acid	**NSOM**	Near-field Scanning Optical Microscopy
DPN	Dip-pen Nanolithography	**nt**	Nucleotide
DRIE	Deep Reactive Ion Etching	**OPC**	Optical Proximity Correction
DRIE	Deep Reactive Ion Etching	**PC**	Polycarbonate
EBL	Electron Beam Lithography	**PDMS**	Polydimethylsiloxane
EDL	Electric Double Layer	**PMMA**	Poly(methyl methacrylate)
EK	Electrokinetic	**P-N-P**	Poisson-Nernst-Planck
EOF	Electroosmotic Flow	**PS**	Polystyrene
EP	Electrophoresis	**RIE**	Reactive Ion Etching
EPD	Electrophoretic Deposition	**RPS**	Resistive Pulse Sensing
EUV	Extreme Ultraviolet	**SNR**	Signal-to-Noise Ratio
FIB	Focused Ion Beam	**SPL**	Scanning Probe Lithography
FIBCVD	Focused Ion Beam-induced Chemical Vapor Deposition	**STM**	Scanning Tunneling Microscopy
FIBID	Focused Ion Beam Induced Deposition	**TIRF**	Total Internal Reflection Fluorescence
HDT	Hexadecanethiol	**μCP**	Microcontact Printing
H-S	Helmholtz-Smoluchowski		

LIST OF SYMBOLS

Ψ	Electric potential in EDL	d	Diameter of particle or half channel depth
ε_0	Electric permittivity of vacuum	δ_t	Total solubility parameter
ε_r	Dielectric constant of the electrolyte	Ψ_u	Potential at the middle plane of overlapped EDL
e	Unit charge	ρ_e	Net charge density
k_b	Boltzmann constant	F	Faraday constant
$n_{i\infty}$	Number density of ions in bulk solution	c_i	Molar ionic concentration
z_i	Valence of ions	Φ	Externally applied electric potential
T	Temperature	$\boldsymbol{N_i}$	Flux of ion
λ_D	Debye length	D_i	Diffusion coefficient of ion
k_d	Reciprocal of Debye length	μ_i	Ion mobility of ion
M	Molarity of the symmetrical electrolyte	R	Gas constant
$\boldsymbol{V_{EOF}}$	Electroosmotic flow velocity	Re	Reynolds number
ζ_w	Zeta potential of channel surface	ρ_w	Density of fluid
ζ_p	Zeta potential of particle surface	P	Pressure
$\boldsymbol{E_{ex}}$	Externally applied electric field	k_{slope}	Slope of the linear part of current
μ	Viscosity of fluids	ρ_p	Density of particle
a	Radius of spherical particle	NA	Avogadro constant
$\boldsymbol{V_{EK}}$	Electrokinetic velocity of particle	A	Amplification factor of the amplifier
$\boldsymbol{V_{EP}}$	Electrophoretic velocity of particle	R_d	Electrical resistance of detecting channel
V_{av}	Average velocity	R_a	Electrical resistance of amplifier
L	Length of nanochannel or RPS gate	δ	Noise level
σ	Conductivity of the electrolyte solution	γ	Particle-to-sensor volume ratio
D_H	Hydraulic diameter of nanochannel		
ΔR	Electric resistance change of sensing gate		
R_2	Electric resistance of RPS sensing gate		

CHAPTER 1 Introduction

1.1 Problem statement

Nanofluidics investigates transport behaviors, manipulation, and control of fluids and nano-sized objects in nano-sized fluidic paths [1,2]. Electrokinetically driven transport phenomena in nanochannels are unique in comparison with those in microchannels or macro-sized channels, and electrokinetic nanofluidics becomes an increasingly important area in the nanoscience and nanotechnology fields. These unique transport phenomena have been attracting a lot of interest and been investigated extensively. In recent years, nanofluidic devices have emerged as powerful platforms for applications in the fields of bioengineering, analytical chemistry, and disease diagnosis. However, there are still stumbling blocks on this avenue.

Firstly, conventional nanofluidic devices are generally created on solid-state materials such as silicon and glass by focused ion beam (FIB) lithography, electron beam lithography (EBL) and so on. These fabrication technologies (will be reviewed in CHAPTER 2) are complicated, time-consuming and expensive. However, reuse of these devices may trigger large errors during data acquisition due to the change of the surface properties and structural sizes. The main challenge faced by many experiments and applications is the fabrication of reliable nanofluidic devices. Consequently, a productive, cost-effective, reliable and simple technique for nanochannel fabrication is urgently needed in the nanofluidic research community.

Manipulation of fluids and samples in nanochannels is typically achieved by electrokinetically driven technique. However, electrokinetic transport behaviors in nanochannels have not been fully understood yet. A lot of numerical studies have been working on these phenomena, but to date, there are few systematic experimental studies about the nanoscaled electrokinetic transport; for instance, electroosmotic flow (EOF) in nanochannels and electrophoresis of nanoparticles in nanochannels. Most of the related experimental studies are focused mainly on ion transport or conductivity of nanochannels or transport of particle suspensions; little attention has been paid to the fluids and individual nanoparticles. On top of this, PDMS material has been occupying the microfluidic and nanofluidic fields for many years, but a systematic understanding of mass transport in PDMS nanofluidic devices is still lacking. Another main challenge faced by many experiments is the technique involved in the characterization of these dynamic transport behaviors

Lastly, nanofluidic devices are born for the upcoming nanometer era. For example, nanofluidic devices developed based on the resistive pulse sensing (RPS) technique have been applied in detecting and sizing nanoparticles, virus, DNAs and biomolecules and so on. However, the traditionally designed RPS system is the "capillary-in-a-tank" style. Specifically, a capillary with a small nano-orifice (the sensing gate) is immersed in a tank of electrolyte solution, and an electric field is applied between the two ends of the nano-orifice. As objects pass through the sensing gate one by one and partially displace the electrolyte solution in the sensing gate, the electric current inside the sensing gate area changes accordingly, generating electric current "pulse" signals. The nano-orifice-based RPS system has several shortcomings. For example, the detection system is bulky and complicated which is not suitable for real-time detection; the signal-to-noise ratio (SNR) of the nano-orifice-based detecting system is low; loss of translocation events may happen due to the low aspect ratio of the nano-orifice; asymmetric sensing gates would give rise to asymmetric RPS signals and result in errors in the data analysis. Furthermore, fabrication of nano-orifices is also technically challenging for the practical applications as mentioned above. As a consequence, an on-chip detection system is highly desirable.

1.2 Research objectives

The purpose of this thesis is to solve the above-mentioned obstacles and challenges in the nanofluidic field and to provide solutions to the following aspects, i.e., fabrication of cost-effective and productive nanofluidic devices; experimental studies of electrokinetic transport phenomena in nanochannels; and applications of nanochannel-based RPS technique. The objectives of this thesis are listed as follows:

1) Develop a simple method to create nanocracks on polystyrene surfaces with controllable cracking size and locations by the solvent-induced cracking method.

2) Duplicate nanocracks onto SU-8 photoresist and smooth-cast polymer by nanoimprint technique to work as nanochannel molds. The nanochannel molds are used for duplicating disposable PDMS nanofluidic devices.

3) Design and fabricate nanochannel-based nanofluidic devices by connecting nanochannels to microchannel systems.

4) An experimental and numerical investigation of electroosmotic flow in single nanochannels. The current-slope method is applied to characterize EOF velocity in single nanochannels.

5) A systematic study of electrophoresis of single nanoparticles in single nanochannels by both experiments and numerical simulations.

6) Nanochannel-based differential RPS systems developed on PDMS nanofluidic chips and a mathematic model for the single-channel-based differential RPS method.

7) Systematic investigation of working parameters in the nanochannel-based differential RPS technique, including sensitivity, resolution, applied electric field, properties of buffer solution, etc.

8) Fabrication of carbon nanotube (CNT) channel-based differential RPS nanofluidic chips and on-chip detection of single cations, individual ssDNAs and molecules.

1.3 Thesis layout

This thesis is organized into 8 chapters and the structure of this thesis is shown in Figure 1-1, including one section of introduction and one part of literature review, two fundamental research projects, two application projects and one section about conclusions and future work. CHAPTER 1, the current chapter, gives an overview of this thesis, including a general background, a statement of the problems, motivations and objectives of this thesis. CHAPTER 2 reviews nanochannel fabrication techniques, general electrokinetic transport phenomena, and working principle of the RPS detection method. In the nanofabrication section, nanofabrication technologies from conventional to unconventional, from top-down to bottom-up, from metal, silicon to polymers, as well as device bonding strategies are comprehensively reviewed. In the electrokinetic transport phenomena section, classical theories of electric double layer (EDL), electroosmosis flow (EOF), electrophoresis (EP) and dielectrophoresis (DEP) are introduced. Moreover, classical models for RPS detection systems on microfluidic chips are also summarized in CHAPTER 2.

CHAPTER 3 demonstrates an experimental study of fabricating nanofluidic chips on PDMS material. This chapter starts with a systematic study of creating nanocracks on polystyrene surfaces by the solvent-induced cracking method. The effects of working parameters such as solubility of solvents, heating time, heating temperature and concentration of the solvent on the nanocrack size are investigated. A guideline for creating nanocracks of controllable size is outlined. Artificial defects marked on the polystyrene surfaces are introduced to initialize the formation of nanocracks. Single nanocracks or parallel nanocracks with controllable spacing can be created by using these artificial defects. Thereafter, nanocracks are replicated onto polymers through two strategies by nanoimprint

technology to work as nanochannel molds. PDMS nanochannels are replicated from these channel molds and bonded to PDMS microchannel systems to form the final nanofluidic devices. Optimal working parameters to fabricate single-nanochannel-based nanofluidic devices and multi-nanochannel-based nanofluidic devices are summarized.

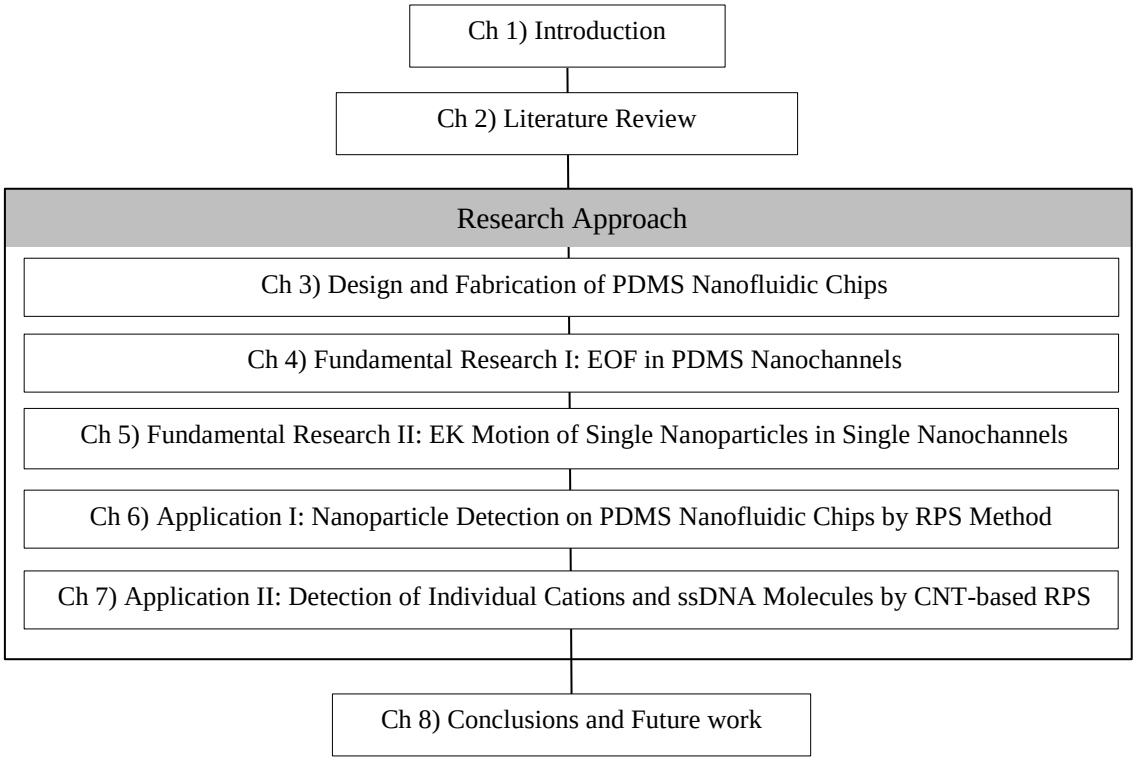

Figure 1-1 Layout and structure of the thesis.

CHAPTER 4 studies EOF in PDMS nanochannels by both experiments and numerical simulations. Electroosmotic flow velocity in single nanochannels is measured by the current slope method. Effects of channel size, ionic concentration of the electrolyte solutions and applied electric field upon the EOF velocity are studied systematically. The experimental results are compared with those of the numerical simulations conducted by COMSOL software, providing a better understanding of EOF in a confined nanospace. CHAPTER 5 investigates electrokinetic (EK) motion of single nanoparticles in single nanochannels. The average velocity of the nanoparticles is measured by particle tracing method. Effects of particle size, ionic concentration, and applied electric field on the velocity of these nanoparticles are studied.

CHAPTER 6 describes an experimental study of detecting and sizing nanoparticles on nanochannel-based differential RPS nanofluidic chips. A mathematic model for the differential RPS method is presented. The resolution, sensitivity, and selective applications of the nanochannel-based

PDMS nanofluidic chips are investigated. Additionally, the working parameters involved in the nanochannel-based RPS detection systems are systematically investigated to optimize the working conditions. In CHAPTER 7, a CNT-channel-based RPS nanofluidic chip is developed to detect single cations and individual ssDNA molecules. A novel method to fabricate CNT-based nanofluidic chips is demonstrated, and a mathematical model for multiple-channel-based RPS systems is also presented in this chapter. Finally, major conclusions, contributions and future directions are summarized and discussed in CHAPTER 8.

CHAPTER 2 Background and Literature Review

This chapter provides an overview of classical theories in electrokinetic transport phenomena, conventional and unconventional technologies in nanofluidic device fabrication and working principle of the RPS detection method. The fundamental knowledge of interfacial electrokinetics includes electric double layer (EDL) theory, electroosmotic flow (EOF), electrophoresis (EP), and dielectrophoresis (DEP). Existing conventional nanofabrication methods include lithography, etching and deposition, and unconventional methods cover nanomaterial-assisted approach, self-assembled method, and deformation of elastomeric materials and so on. Sealing of devices can be achieved by thermal bonding, anodic bonding, and self-enclosed strategy. On top of this, classical mathematical models for detecting particles by using traditional RPS systems are demonstrated. This chapter builds up a fundamental background of this thesis.

2.1 Theory of electrokinetic transport phenomena

2.1.1 Electric double layer (EDL) theory

EDL dominates electrokinetic transport behaviors in both microchannels and nanochannels. The surfaces of most materials spontaneously acquire electrostatic charges when they contact with neutral electrolyte solutions. There are many mechanisms involved in the formation this surface charge, but the most common case is caused by ionization of the surface groups. A charged surface repels co-ions and attracts counterions, which results in a net charge distribution near the solid surface. The charge distribution near the surface can be described by an EDL model (Figure 2-1 (a)). An EDL contains two layers: an immobile layer (also called Stern layer) and a diffuse layer which is mobile. The electric potential at the outer plane of the Stern layer (shear plane) is referred as the ζ potential, as shown in Figure 2-1 (b). Zeta potential is widely used in the chemistry and interfacial science fields. The electric potential distribution and ion distribution in the diffuse layer can be calculated by combining the Poisson equation and the Boltzmann distribution [3]:

$$\nabla^2\Psi = -\frac{\mathrm{e}}{\varepsilon_0\varepsilon_r}\sum z_i\, n_{i\infty} exp\left[-\frac{z_i e\Psi}{k_b T}\right] \qquad (2\text{-}1)$$

Equation (2-1) is also called the Poisson-Boltzmann (P-B) equation, where Ψ is the electric potential, ε_r is the dielectric constant of the electrolyte, ε_0 is the electric permittivity of vacuum, e is the unit charge, k_b is the Boltzmann constant, $n_{i\infty}$ is the number density of ions in the bulk solution,

z_i is the valence, and T is the temperature. For symmetrical electrolyte solutions (1:1, for example), the P-B equation can be rewritten as:

$$\nabla^2\Psi = \frac{2zen_{i\infty}}{\varepsilon_0\varepsilon_r}\sinh\left(\frac{ze\Psi}{k_bT}\right) \qquad (2\text{-}2)$$

The thickness of the Stern layer is very thin, usually several angstroms, and the thickness of the diffuse layer is about three to five times of the Debye length (λ_D) which is a function of the electrolyte concentration.

$$k_d{}^{-1} = \lambda_D = \sqrt{\frac{\varepsilon_0\varepsilon_r k_b\, T}{2n_{i\infty}\,(ze)^2}} \qquad (2\text{-}3)$$

As a result, in a symmetrical electrolyte system (1:1), the Debye length can be simply calculated by [3]

$$\lambda_D = \frac{3.04}{z\sqrt{M}} \times 10^{-10}(m) \qquad (2\text{-}4)$$

where M is the molarity of the symmetrical electrolyte solution.

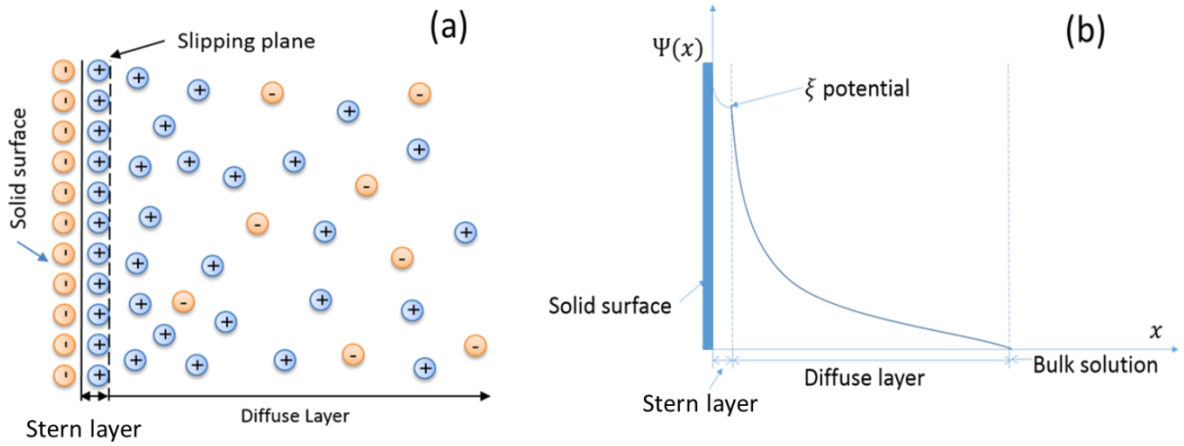

Figure 2-1 Schematic of (a) ion distribution and (b) electric potential distribution in an electric double layer.

2.1.2 Electroosmotic flow (EOF)

Electroosmotic flow describes fluid motion caused by interactions between the EDL adjacent to a channel surface and an externally applied electric field. As a solid channel surface contacts with electrolytes, an EDL will be generated near the channel surface as mentioned above. When an external electric field is applied between the entrance and exit of the channel, the net charges in the

diffuse layer move along the channel surface due to the electrostatic force. The motion of these charged ions, in turn, drives the liquid flow in the channel by viscous force, and the motion of fluids is called electroosmotic flow. In microchannels, the EDL is negligible because in most cases the thickness of the EDL is extremely small compared with the channel size. EOF velocity in microchannels can be evaluated by the Helmholtz-Smoluchowski (H-S) equation:

$$\boldsymbol{V_{EOF}} = -\frac{\varepsilon_0 \varepsilon_r \zeta_w}{\mu} \boldsymbol{E_{ex}} \qquad (2\text{-}5)$$

where $\boldsymbol{E_{ex}}$ is the externally applied electric field, ζ_w is the zeta potential of the channel wall and μ is the viscosity of the electrolyte solution. In a microchannel, the thickness of EDL is negligible and the EOF velocity profile in the microchannel is plug-like, as shown in Figure 2-2 (a).

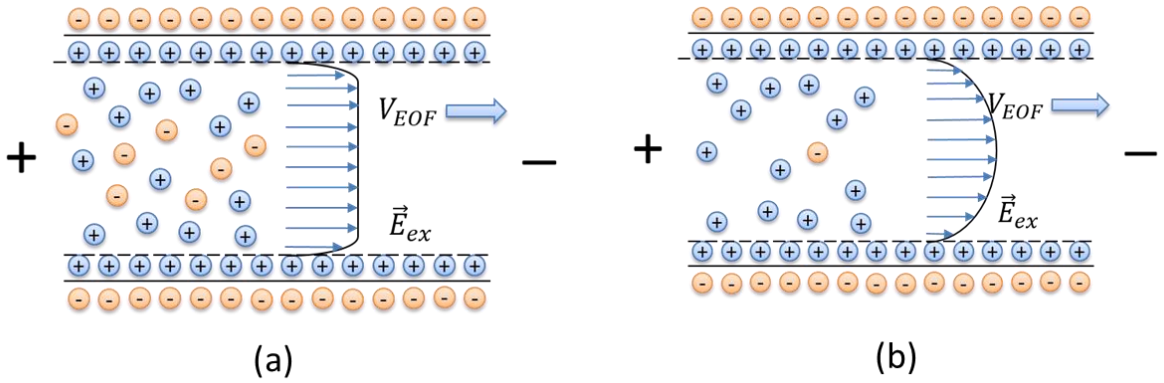

Figure 2-2 Schematic of EOF in a microchannel and in a nanochannel. (a) Plug-like EOF velocity profile in a microchannel without overlap of EDL. (b) Parabolic-shaped velocity profile in a nanochannel with overlapped EDL.

EOF in a nanochannel is different from that in a microchannel sometimes due to the limited channel size. When the channel size scales down and is comparable with the thickness of EDL, EDLs are likely to overlap and interact with each other, therefore, P-B equation (Equation (2-1)) and H-S theorem (Equation (2-5)) used in microchannels are not applicable anymore [4]. The fluid velocity inside the diffuse layers of a nanochannel cannot get fully developed in comparison with those in a microchannel, and the velocity profile is parabolic-shaped, as shown in Figure 2-2 (b). For the extreme case, even the continuum hypothesis cannot survive when the channel size is extremely small and comparable to the free path of the fluid molecules [5]. A comprehensive analytical model of EOF in nanochannels is presented in CHAPTER 4.

2.1.3 Electrophoresis (EP) of spherical particles

Electrophoresis describes the motion of charged particles suspended in fluids under an externally applied electric field. Electrophoresis has been widely used as an analytical technique in the biochemistry field for molecule separation. In theory, a charged particle suspended in a liquid is subjected to a Coulomb force when an external electric field is applied. As a consequence, the particle moves in the liquid. The difference between electrophoresis and electroosmosis is: in electroosmosis, the solid phase is stationary, the fluid moves when an electric field is applied; however, in electrophoresis, the solid phase (the particles) keeps moving when an electric field is applied, while the liquid phase is stationary, as illustrated in Figure 2-3 (a). Generally speaking, for a finite thickness EDL around a charged particle, three factors should be considered in evaluating electrophoretic motion, i.e. electrophoretic retardation effects due to the existence of EDL and EOF around the particle, relaxation effects caused by the polarization of the particle, and surface conductance effects due to the presence of surface charge.

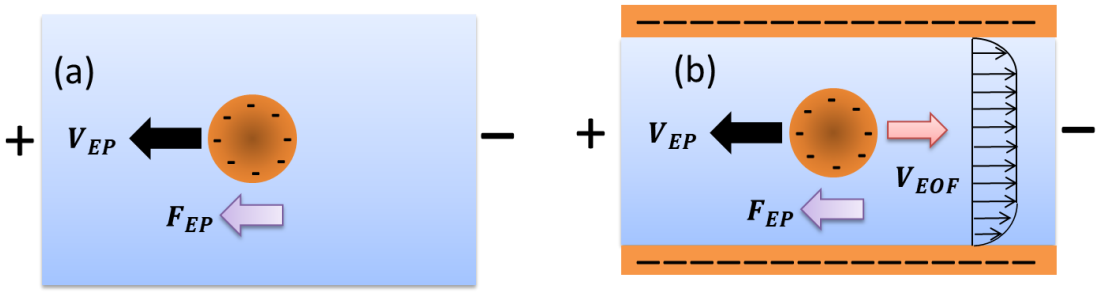

Figure 2-3 Schematic of electrophoretic motion of a spherical particle in (a) a stationary liquid, and (b) in a microchannel.

Electrophoresis in the limit of large Debye length, $k_d a \ll 1$. Electrophoretic velocity of a rigid and electrically non-conducting spherical particle in a stationary pure dielectric liquid (containing no free charged ions) can be calculated by the following equation:

$$\boldsymbol{V_{EP}} = \frac{2}{3}\frac{\varepsilon_0 \varepsilon_r \zeta_p}{\mu}\boldsymbol{E_{ex}} \qquad (2\text{-}6)$$

where $\boldsymbol{V_{EP}}$ is the velocity of the particle and ζ_p is the zeta potential of the particle surface, a is the radius of the spherical particle. Equation (2-6) is also called Huckel's solution, in which the retardation effect is considered but the relaxation effect is not taken into account. Here the velocity is smaller than that of the EOF velocity in Equation (2-5), because EOF generated in the diffuse layer

outside of the particle surface increases the friction of the electrophoresis motion of the particle. This reduction behavior is also called electrophoretic retardation effects.

Electrophoresis in the limit of small Debye length, $k_d a \gg 1$. When a particle is large and the Debye length is small, the thickness of EDL is extremely thin compared with the radius of the particle, and the curvature of the particle can be negligible. Electrophoresis of the particle can be simplified as movement of fluids respect to a planner surface. The electrophoresis velocity of the particle can be calculated by

$$\boldsymbol{V_{EP}} = \frac{\varepsilon_0 \varepsilon_r \zeta_p \boldsymbol{E_{ex}}}{\mu} \qquad (2\text{-}7)$$

Equation (2-7) is also referred to as the H-S equation which is similar to Equation (2-5). This equation is for the extreme case, large particle, and extreme thin EDL but differ by a factor of 2/3 from Equation (2-6). Here, H-S equation has to meet four restrictions and assumptions: (i) usual hydrodynamic equations for the motion of viscous fluids are still applicable in both inside and outside of EDL; (ii) laminar flow with low Re number, the inertia term is negligible; (iii) the electric field in EDL is not affected by the externally applied electric field (This assumption is not valid for large zeta potential cases because the density of counterions in the EDL is so large and the ionic fluxes due to the externally applied electric field would distort the EDL. For large zeta potential, the distortion of EDL should be taken into account.); (iv) the thickness of the EDL is small in comparison with the radius of the curvature at any point of the surface.

Henry bridged these two extreme cases and developed a more general form of the electrophoretic motion velocity which considers the thickness of the EDL

$$\boldsymbol{V_{EP}} = \frac{2}{3}\frac{\varepsilon_0 \varepsilon_r \zeta_p \boldsymbol{E_{ex}}}{\mu} f(k_d a) \qquad (2\text{-}8)$$

Equation (2-8) is also called Henry's equation and $f(k_d a)$ is the Henry's factor. There are two assuptions in Henry's approach: (i) the EDL is not affected by the externally applied electric field, (ii) low surface zeta potential, $\frac{ze\zeta_p}{k_b T} < 1$. Henry's factor approaches 1 for thick EDL ($k_d a \ll 1$) and $3/2$ for thin EDL ($k_d a \gg 1$). A general curve fit equation for Henry's factor is [6]

$$f(ka) = \frac{3}{2} - \frac{1}{2[1 + a_1 (k_d a)^{a_2}]} \qquad (2\text{-}9)$$

where $a_1 = 0.072$ and $a_2 = 1.13$.

Electrophoresis of a particle in a microchannel. However, in a microchannel, the particle also moves with EOF caused by the existence of electrostatic charges on the channel surface (see Figure 2-3 (b)). Therefore, electrokinetic motion of a particle in a microchannel involves both electroosmosis and electrophoresis and can be calculated by

$$\boldsymbol{V_{EK}} = \boldsymbol{V_{EP}} + \boldsymbol{V_{EOF}} = \frac{\varepsilon_0 \varepsilon_r \boldsymbol{E_{ex}}}{\mu}\left[f(k_d a)\zeta_p - \zeta_w\right] \qquad (2\text{-}10)$$

From the above equation, one can conclude that the direction of the EK motion of the particle is dependent on the zeta potentials of both the channel wall ζ_w and the particle ζ_p.

2.1.4 Dielectrophoresis (DEP)

Dielectrophoresis describes the motion of dielectric particles in a non-uniform electric field. The particle can be electrically neutral or initially charged. Electrically polarizable particles are likely to get charged locally and subjected to Coulomb forces when a non-uniform electric field is applied. However, the forces at the two polarized ends cannot be canceled because of the non-uniform applied electric field. As a result, the particles move in the non-uniform electric field. According to the direction of the DEP motion, DEP is categorized into positive DEP (p-DEP) and negative DEP (n-DEP) [3].

For a homogeneous spherical particle of radius *a*, the DEP force can be calculated by

$$\boldsymbol{F_{DEP}} = 2\pi a^3 Re\left\{\frac{\varepsilon_p^* - \varepsilon_m^*}{\varepsilon_p^* + 2\varepsilon_m^*}\right\}\nabla|\boldsymbol{E}_\infty|^2 \qquad (2\text{-}11)$$

where ε_p^* and ε_m^* are the frequency dependent dielectric constants of the spherical particle and the medium, respectively. $\frac{\varepsilon_p^* - \varepsilon_m^*}{\varepsilon_p^* + 2\varepsilon_m^*}$ is the Clausius-Mossotti factor which varies with the frequency of the electric field.

2.2 Nanofluidic device fabrication techniques [*]

2.2.1 Lithography methods

Photolithography. Standard photolithography generally involves the transfer of patterns onto substrates coated with light-sensitive photoresists through photomasks over large areas and removing of the resist layers selectively [7]. A typical photolithography system includes four key parts: (i) a

[*] "Nano" means character size in the range of 1 nm to 100 nm. In this review section, the "nano" is extended to sub-micron level so that we can get a comprehensive review of fabrication techniques.

photomask with patterns; (ii) a light source; (iii) a photoresist and (iv) a developing procedure. For traditional photolithography: firstly, the photoresist is coated onto a substrate followed by a soft bake process to vaporize the solvent; then, the photoresist layer is exposed to the UV light through the photomask followed by a post bake process to enable a fully crosslinking of the photoresist patterns; finally, the developing process is employed to remove the selective parts to create the final designed patterns. 3D microstructures can be obtained by inclined/rotated lithography [8].

The resolution of the photolithography method is limited by the resolution of the photomask and the wavelength of the incident light. For example, for 365 nm ultraviolet (UV) light source, the smallest feature size created by this system can only be about 200 nm. Finer patterns can be obtained by decreasing the wavelength of the light, using smaller feature sized masks or utilizing maskless technologies. The following lithography methods are developed based on these strategies.

Deep-UV lithography. UV light has a wavelength ranging from 400 nm to 10 nm. General light (UVA) has a wavelength of about 365 nm which has been widely used in conventional photolithography on an SU8 photoresist layer, for example. Deep-UV lights can create finer structures than that of UVA light because deep UV has a shorter wavelength (shorter than 300 nm) and a stronger energy than that of UVA light (400 nm-315 nm). Similarly, extreme ultraviolet (EUV) [9] as a special part of deep-UV, is also a powerful candidate for smaller feather size fabrication [10]. In 1975, a sub-micrometer long channel with an aspect ratio (AR) of 15 was created on polymethyl methacrylate-based (PMMA-based) photoresist by deep-UV light [11].

X-ray lithography. X-rays with energy in the range of 100 eV to 100 KeV have wavelengths of 0.01 nm to 10 nm can create smaller feather size than deep-UV. However, the photomasks used in the X-ray lithography are the biggest challenge for this technique because the photomasks should be capable of absorbing X-rays in order to generate shadow patterns on the photoresist substrate [10]. Nano-crystalline diamond film [12], silicon, boron nitride and silicon nitride working as the membrane, and gold or tungsten working as the absorber are the most promising materials for X-ray masks [13]. The X-ray source can be X-ray tubes, plasma sources and storage rings [14]. Many kinds of materials, such as PMMA, Thomson, can be used as the X-ray photoresists [13,14]. The minimum feature size fabricated by X-ray lithography was about 100 nm by 2000 [15,16]. The smallest feature created by X-ray lithography by 2013 was sub-25 nm, which is comparable to the size achieved by EBL [17]. Direct writing of thin film by hard X-ray or focused X-ray [17–21] and 3D structures such as flyover channels and grating can also be achieved by X-ray lithography [22,23].

Electron beam lithography (EBL). Electron beam lithography as a conventional nanofabrication tool has been widely used in both the nanoelectronics field and the semiconductor industry [24,25]. E-beam has a wide range of energy from 1 KeV to 200 KeV, with a spot size down to several nanometers. The resolution of EBL is determined by the electron beam spot size as well as the scattering range of the electrons. In principle, a higher e-beam energy level contributes to a smaller feature size, and no photomask is needed. Materials such as PMMA, calixarene, polystyrene (PS), polycarbonates (PC), polynorbornene and even silk have been used as high-resolution photoresists [24,26–30]. Electron-beam-induced etching and electron-beam-induced oxide deposition techniques have also been utilized to fabricate 3-D nanofeatures [31,32]. The smallest size ever created by EBL was 2 nm [33]. EBL is a time-consuming and expensive technique; therefore, it is impractical for large-area nanostructure fabrication. Additionally, proximity effect [25,34–36] caused by backscattering of electrons limits the resolution to some degree. However, EBL is still an irreplaceable tool for unique nanopores and nanochannels which are widely used as masks in NIL, photolithography, etc.

Focused ion beam lithography (FIB). Focused ion beam (FIB) lithography is different from EBL. FIB has a much stronger energy than electron beam and is able to produce higher quality nanopatterns by directly writing on hard materials without proximity effect. As a direct writing method, FIB is able to write on a variety of materials with various geometries. Both conductive materials such as aluminum [37] and gold [38] and nonconductive materials, such as silicon [39], silicon nitride (SiN) [40], polymer [41] can be used in FIB lithography. Currently, there are four nanofabrication approaches based on FIB: implanting, milling, ion-induced deposition and ion-induced etching. FIB implantation usually forms resistance layers for the etching process, for example, high energy Ga^+ has been used to form Ga_2O_3 protection layer in RIE [42]. Milling is the most popular method to fabricate nanostructures on substrates directly [38,41,43–45]. Nanochannels of 5 nm wide have been milled on an insulating substrate [46]. FIB-induced deposition (FIBID) is used to create nanofeatures by initiating and localizing chemical vapor deposition (CVD) on a specific place, also well known as FIBCVD. Ion-induced etching also referred to chemical-assisted ion etching, is a powerful method to enhance the material removing rate by using chemical reactions between the substrate material and the etching gas [42]. A comparable technique is the EBL, and FIB is more excellent than EBL in nanotechnology, but it is still very expensive, and the scanning speed is extremely low.

Scanning probe lithography (SPL). Scanning probe microscopy techniques, including scanning tunneling microscopy (STM), atomic force microscopy (AFM) and near-field scanning optical

microscopy (NSOM), have resolutions of nanometer scale. These advanced tools have been widely used in material science, biology as well as nanofabrication technologies. In nanofabrication, these techniques can be categorized into two groups: force-assisted SPL and bias-assisted SPL, according to the working principles. Both methods utilize the interactions between the substrate surfaces and the probe tips. The substrates can be made of metals [47,48], semiconductors [49], conductive polymers [50], etc., and the probes can be diamond or silicon with a radius of 20-60 nm. For force-assisted SPL, large forces are applied on the hard tips to pattern structures by scratching, polishing or pulling the molecules or atoms on the surfaces. In the bias-assisted SPL, strong electric fields of 10^8 to 10^{10} V/m are applied between the probes and the substrates. Such huge electric fields can lead to electrostatic attraction, electrochemical deposition, anodic oxidation, dielectric breakdown, field emission and so on, and these phenomena can be utilized to fabricate nanopatterns. Dip-pen nanolithography (DPN) is another approach to fabricating nanochannels by depositing molecules or nanoparticles selectively onto a substrate [51–54]. An AFM probe tip writes nanopatterns on a substrate by transferring the "ink" material absorbed on the probe tip to the substrate, and this technique can provide patterns with features size smaller than 50 nm [55].

SPL is a cost-effective tool for nanochannel fabrication with precisely controlled resolution as small as 20 nm. Photomasks with nanopatterns used in the soft lithography method can also be created by SPL. Moreover, various kinds of substrate materials can be used in the nanofabrication processes, making SPL a popular method. However, SPL is not very productive, and it is also challenging to generate reproducible structures due to the variations of the applied load, the size and the shape of the tips, and the velocity of scanning. This technique is still at an early stage. Possible damage or deformation of the tips during fabrication makes it hard to work efficiently and constantly.

Interferometric lithography. Interferometric lithography (IL), also referred to as interference lithography, is a powerful technique for fabricating simple periodical nanometer-sized structures over a large area. IL requires no masking and can be used to develop nanopatterns on various kinds of substrates [56–60]. For the working principle, generally, two or more coherent laser beams split from one light source and interfere with each other to generate periodical lines on the photoresist layers, just like conventional photolithography. The resolution of the patterns is determined by the light wavelength, the angle of the interference and the developing process. Lines as narrow as 40 nm separated by 57 nm have been generated by IL [61]. This method is simple, fast, and free from masks, however, only parallel channels with fixed spacing can be made.

Nanoimprint lithography (NIL). Nanoimprint lithography is a powerful method for high-resolution nanochannel fabrication with high-throughput and low-cost. Another term for this method is "hot embossing" because in the early years, a heating process was involved generally. NIL was initially developed by Chou et al. in the 1990s [62,63], and this technique has been widely used to fabricate nanochannels in nanofluidic systems. The working principle is quite simple: first, a silicon mold with micro/nanopatterns is fabricated by EBL, FIB or standard photolithography followed by an RIE process (will be discussed later). PMMA substrate is attached to the silicon mold and heated over its glass transition temperature with a pressure applied; as a consequence, the patterns on the silicon mold are transferred onto the PMMA surface after the removal of the silicon master. A sealed chip can be obtained by bonding the first PMMA slab onto another piece of PMMA substrate under the conditions of high temperature and high pressure [64]. Another method developed based on the nanoimprint lithography is called soft nanoimprint lithography. First, a rigid mold with nanopatterns is pressed into a photoresist-coated substrate. In order to replicate the patterns onto the photoresist layer successfully, the substrate is usually heated to enhance the fluidity of the photoresist. After the resist is cooled down or weathered a UV exposure process, the resist layer becomes solid. The nanopatterns can be obtained after removal of the rigid mold.

NIL is able to create nanochannels over a large area with high resolution. Channel size smaller than 10 nm with high AR can be fabricated by NIL. Another advantage of NIL is its compatibility with other microfabrication methods in terms of forming complicated micro/nanofluidic devices. However, the bottleneck of NIL is that the molds with nanopatterns can only be created by other techniques, such as EBL, IL, FIB, followed by corresponding etching and deposition processes which are expensive and time-consuming.

2.2.2 Etching and deposition techniques

Etching and deposition are belonging to totally different categories. Etching is a top-down approach, while deposition is just opposite, bottom-up method [65]. These techniques are often used in micro/nanofluidic device fabrication processes, combining with lithography methods as reviewed above. In most practical applications, both etching and deposition are used.

Etching. Etching is a technique to chemically or physically remove layers from the surface of a substrate. The removed part becomes the channel. During the etching process, masks are needed to protect the undesired part of the wafer from etching. The masks can be photoresist such as SU-8 or some material more durable, for instance, silicon nitride. The depth of the channel can be controlled

by adjusting the etching time and the etching rate. The etching rate depends on the etchant concentration, etchant composition, material of the substrate, temperature, electric field, etc. According to the mechanism, wet etching and dry etching are defined. For the wet etching, wafers are immersed in a bath of etchant, and the "naked" part of the wafer will be removed. Different etchants can be used according to the wafer material, for example, silicon dioxide can be etched by the hydrofluoric acid solution. By contrast, dry etching is also called plasma etching or reactive ion etching (RIE), using plasma or ions to react with wafers. Generally, the etching process for both wet etching and dry etching is isotropic. Deep reactive ion etching (DRIE) is designed for deep channels (high AR) by minimizing the isotropic process [66–73].

Deposition. Deposition is a thermodynamic phenomenon, including a phase transition from gas to solid. In the nanochannel fabrication process, deposition is used to "grow" nanometer size layers on substrates. The layers can be metal, polymer or carbon nanotubes, etc. Several techniques have been developed to deposit high-quality thin films, such as electrophoretic deposition (EPD), chemical vapor deposition (CVD), electronic sputtering, ionized physical vapor deposition (IPVD), plasma deposition, etc [74–78]. The deposition process can be adjusted by the deposition time and the deposition rate accordingly. Plenty of nanochannel networks have been produced by etching and deposition approaches [79–87], and generally, etching and deposition are combined in applications. An example of a combination of etching and deposition in nanofabrication is demonstrated as follows.

Edge lithography (Side-wall lithography). The edge lithography method developed by Love et al. [88] has been used to produce nanogaps with a constant width in thin films by combing etching method and deposition method. The fabrication processes are as follows: (a) A standard photolithography process is conducted on a mental deposited substrate surface; (b) After the developing process, the mental layer is over etched, leaving hollow space under the edge of the photoresist; (c) Another layer of mental is deposited on the surface of the photoresist layer as well as the substrate surface; (d) After removing the photoresist, the substrate space under the resist edge appears and (e) etched by the following dry etching process; (f) Finally, the mental layer is removed, leaving nanochannels on the substrate (see Figure 2-4).

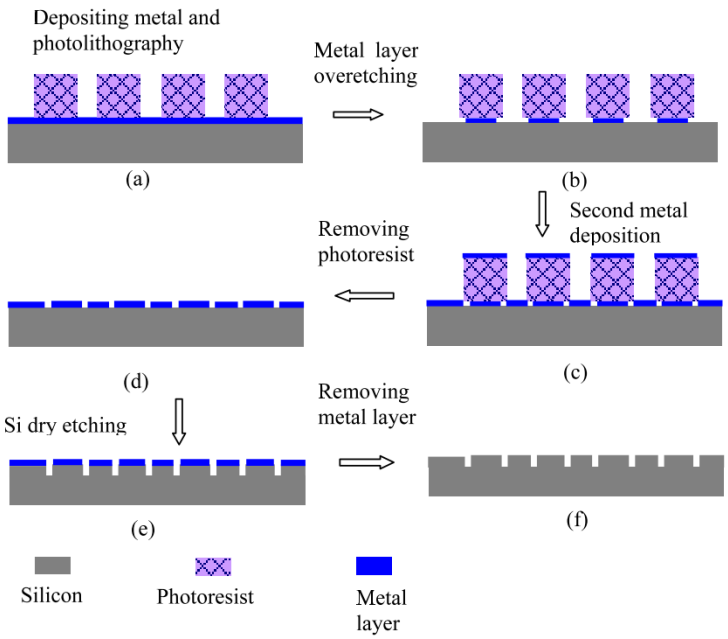

Figure 2-4 Schematic diagram of edge lithography (single-layer over-etching technique).[89]

Based on this approach, several new methods have been developed [89–92]. Chen et al. [89] presented a double thin film over etching method. Continuous patterns with 50 nm feature size to millimeters over large areas have been obtained. Vertical arrays of sealed nanochannels with feature size down to 10 nm have been created by Sordan [90]. Nanogaps of 44 nm wide with a high aspect ratio of 172 on an aluminum film has been produced [91] by deep reactive ion etching (DRIE). Side lithography is also used to fabricate nanochannel mold for hot embossing [92]. Etching and deposition methods are widely used in the nanofabrication, however, the facilities of the deposition and etching systems are complicated and expensive. Long time of training is also needed before one can use them professionally.

2.2.3 Nanomaterial-assisted nanochannel fabrication

A variety of nanomaterials such as nanowires [93–96], nanotubes [97–102], nanomembranes [103,104] and nanofibers [93,105–108] with feature sizes between 1 nm and 100 nm have been used to construct nanofluidic devices. Biomaterials also offer new platforms for nanofabrication, for example, nanopores made of biomolecules were used to detect DNAs [109]. However, fabrication of nanopores will not be reviewed here. We are focusing on the nanochannel fabrication in this thesis.

Nanowires and nanofibers. There are basically two ways to create nanochannels by nanowires or nanofibers, i.e., hot embossing and sacrificial methods. In these methods, nanomaterials are initially deposited onto a substrate surface with a defined location and direction by some method,

such as near-field electrospinning and so on [106,110,111]; then, these nanowires or nanofibers are buried into polymers and selectively removed; as a result, the hollow spaces become the nanochannels; finally, a bonding or sealing process is applied to form the final devices.

In the hot embossing method, nanowires with high hardness function as templates to replicate nanochannels. The first step of this method is to disperse nanowires on a stiff substrate surface. Then, a polymer slab is coved on the substrate with pressure under a certain temperature for a certain period of time. Thereafter, nanowires are embossed into the polymer slab. After separation of the nanowires from the slab, nanopatterns are transferred onto the polymer surface. Finally, another substrate with microchannels is bonded to the slab to form the final nanofluidic device.

For the sacrificial method, nanowires or nanofibers which can be selectively etched are used. These nanowires or nanofibers are bridged on the top of pre-patterned microstructures to function as sacrificial templates. Then, an uncured polymer (PDMS, for example) is poured onto the template to bury these nanowires and nanofibers. After the polymer is cured, sacrificial nanowires are removed from the substrate by an etching process, and nanochannels are created in the polymer stamp.

Nanotubes. The most popular nanotube used in nanochannel fabrication is carbon nanotube (CNT). CNTs are graphitic cylindrical tubes with an inner diameter of several nanometers to hundreds nanometers [65]. Molecularly smooth hydrophobic graphitic walls and high ARs give rise to unique transport phenomena of water and gas [112] inside. CNT membrane provides a promising tool for water filtration, water purification, and gas separation. Nanofluidic devices made of CNTs have also been developed to study transport phenomena of biological molecules and ions [97,99–102]. In these devices, single wall carbon nanotubes (SWCNTs) or multiwall carbon nanotubes (MWCNTs) or other kinds of nanotubes have been directly used as nanochannels by bridging microchannels [100,113] or assembling them in a thin membrane [102].

Nanomaterial-assisted methods are cost-effective and simple; nanomaterials with feature size down to few nanometers can be obtained easily. However, alignment of channels is the biggest challenge during the fabrication process, because the size of the nanomaterials is generally too small to be manipulated by mechanical tools. Several techniques, such as random deposition, dielectrophoresis alignment and electrospinning method, have been used to solve the problem of arrangement, which makes nanomaterial-assisted methods more popular in the nanofluidics field. But uncapping and cutting of nanotubes and controlling of sacrificial of nanowires are still tricky problems.

2.2.4 Deformation of elastomeric materials

Elastomers, such as PDMS, have been widely used to fabricate micro/nanofluidic networks. One problem of the elastomers is that these materials are soft and get collapse easily during the device fabrication processes. Interestingly, the collapse problem has been utilized to create nanochannels or nanoslits recently. In this section, several kinds of nanochannels created by deformable PDMS and other thermoplastic are reviewed [64,110,114–127].

Collapse method. Soft materials with low Young's modulus are likely to trigger unwanted collapse which is a major challenge in nanochannel fabrication. Zhou et al. [119,125] investigated the elastomer collapse mechanism of PDMS stamp, showing that roof collapse is dominated by the adhesion force between the substrate and the PDMS stamp. They also found that electrostatic forces may give rise to the collapse, while the weight of the stamp has little effect on this process. Figure 2-5 shows the principle of nanochannel fabrication by the roof collapse method in detail. The middle part of the suspended channel roof sags to the substrate under an externally applied force, such as adhesion force, electrostatic force, pressure. If the stamp and the substrate were functionalized before the collapse, the middle part of the roof would be bonded to the substrate permanently. The space at the corners of the microchannels becomes nanochannels when the space is narrow enough.

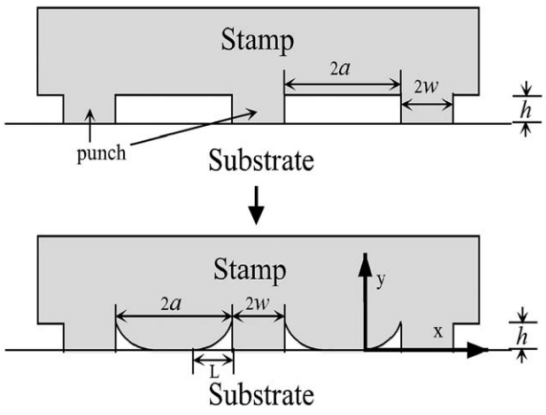

Figure 2-5 Schematic diagram of roof collapse for a soft material stamp on substrate [125].

By using this method, nanochannels as small as 60 nm feature size created by the roof collapse method were reported [123]. The first step is to fabricate a master with microstructure by photolithography or mental layer deposition. The master is used to create PDMS stamps. After bonding PDMS stamps onto the substrate, roof collapse occurs, and nanochannels are obtained at the corners of the microchannels. There are several factors contributing to the final nanochannel size, i.e., the height of the microchannels, Young's modulus of the PDMS (elastomer base/curing agent ratio),

and the applied pressure. Nanochannel molds fabricated by roof collapse have also been reported [122]. This approach consists of three simple steps: firstly, microchannels with submicron height and large in width are prepared by standard soft lithography on a PDMS stamp; secondly, the PDMS stamp is attached to a photoresist coated Si substrate with externally applied force to collapse the channel roof. A UV exposure process is applied to speed up the curing of the photoresist; finally, positive nanochannels are generated at the corners of the microchannels after removal of the PDMS stamp. This technique is simple and cost-effective, only soft lithography, roof collapse, and standard photolithography are needed.

Incomplete bonding method. Kim[128] reported a simple method to fabricate triangular nanochannels by utilizing incomplete bonding between PDMS slabs and substrates. The first step is to create membrane patterns with submicron in height on a substrate surface. The membrane material can be Nafion, oxide layer, etc. The following step is to bond a flat PDMS stamp onto the membrane attached substrate. One can imagine that there would be an incomplete bonding part at the edges of the membrane. The incomplete bonding would result in gaps at the edges of the membrane, and the triangular gaps should have a feature size of nanoscale because the membrane is submicron in height. This method is simple, fast and low-cost; however, it is hard to control the channel size precisely.

Tunable elastomeric nanochannels. Tunable elastomeric nanochannels for separation and manipulation of DNA molecules and nanoparticles are popular recently [120,129–133]. As a typical example, Huh presented the details of fabricating tunable nanochannels in his research [120]. The fabrication process involves several steps. The first step is to create an array of ordered nanocracks by stretching a plasma-oxidized PDMS slab, and these nanocracks are replicated onto UV-curable epoxy to work as channel molds. Then, PDMS stamps with nanochannels are replicated from the nanochannel molds by soft lithography method and bonded onto substrates to form the final nanochannel chips. The size of the nanochannels is adjusted by the force applied on the PDMS chips. Angeli [131] made tunable nanochannels by the same style, but the only difference is that the nanochannel masters were created by FIB.

Mills et al. [130] presented fabrication of fully tunable and reversible nanochannels without using of mask molding. Initially, nanocracks have also created a piece of plasma treated thin PDMS film by stretching. Thereafter, the PDMS film is sandwiched by two thick PDMS stamps and one of them with micrometer size networks which connect to the nanochannels after bonding. The cross-section of the nanochannels can be reversibly opened, closed as well as narrowed and widened by adjusting

the laterally applied tensile strain. Figure 2-6 shows the fabrication processes in detail. However, it is difficult to control the number of cracks on the PDMS films.

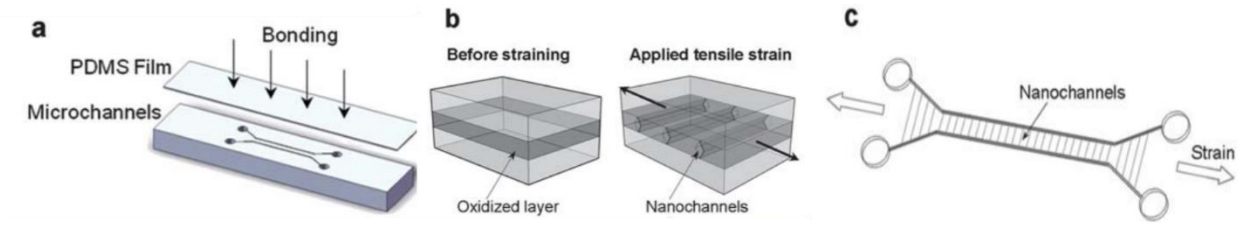

Figure 2-6 Fabrication of tunable nanochannels [130].

Thermal-stretching of microchannel. Thermoplastics are becoming increasingly important in micro/nanofluidic device fabrication because they are durable and cost-effective. For example, PMMA is widely used in nanoimprint lithography as mentioned above. In NIL method, PMMA is heated and pressed onto a master to duplicate nano-sized patterns, and the pressure is applied perpendicular to the PMMA surface. Sivanesan et al. [117] presented a new method to create nanochannels based on thermal deformation of rigid PC substrates. In this work, microchannels with a cross-section of tens of micrometers are built in a polycarbonate (PC) platform first. Nanochannels can be obtained by heating the middle part of the PC platform over its glass transition temperature (150℃) and applying a uniaxial uniform tensile to lengthen the microchannel and reduce the cross-sectional size at the same time. Arrays of nanochannels with 400 nm critical size have been reported.

Other strategies based on elastomeric material deformation. Another method called microchannel refilling (MR) was developed by Li et al. [126] in which only two steps are involved: microchannels are embossed onto a PMMA substrate by hot embossing method, and nanochannels are created by compressing the substrate under a high temperature and a high pressure to shrink the size of the microchannels. Nanochannels of 85 nm in depth and 132 nm in width were created. Microchannel refilling is a quick, easy and cost-effective method to produce nanochannels on polymers or glass substrates.

Femtosecond laser is also used to fabricate nanochannels by laser-induced thermal deformation. Liao et al. [134,135] presented a femtosecond laser direct writing method. Sub-40 nm nanochannels buried on a high-silicate porous glass substrate were achieved. The channels are nanometers in width; however, the depth of the channels is about 1.5 microns. Grimes [116] reported a novel approach to fabricating nanochannels by shrinking thermoplastics under higher temperature. In their work, microchannels were created on a piece of plastic film followed by a heating process in an oven for a

certain period of time, as a result, the channel mold shrunk down by more than 60%, and a new mold with smaller size was obtained. However, nanochannel fabrication by using this method has not been reported.

2.2.5 Other unconventional methods

There are still many unconventional approaches for special types of nanochannels. Some hybrid techniques are also summarized in this section.

Wrinkle film. Wrinkling of thin films on an elastomer surfaces is an effective approach to creating nanochannels on large areas [136–140]. The wrinkles can be developed on PDMS surfaces by treating strain-stretching PDMS films followed by releasing the strain. After plasma treatment, a thin layer of stiff SiOx is generated on the PDMS slab surface, and when the applied strain is released, the stiff skin becomes wrinkle patterns automatically. Wrinkle channels of 950 nm wide and 233 nm deep created by this approach [137] have been reported. The wrinkling method is simple and practical. Applications of the wrinkle method and the properties of the wrinkled thin film have been reviewed by Chung [140].

Self-assembled method. A family of unconventional and stand-alone approaches to fabricate nanostructure is based on self-assembled method [141–157]. The concept of self-assembled behavior is derived from the biology field such as the formation of DNA double helix structure [158]. During a self-assembled process, subunits such as molecules and small particles spontaneously assemble together, forming solid and stable structures. The driven forces of the self-assembled method may come from the natural surface functionalities, electrical field, magnetic field, and local topographies and so on. The subunits are extremely small in the nanometer scale, consequently, the size of the final self-assembled structures can also be down to nanometer scale without defects [55]. Self-assembled technique is a promising method in nanostructure fabrication also due to its outstanding properties of self-repair and self-replication. Nanowires [141], nanotubes [143] and nanopores [145] have also been created by the self-assembled method. However, self-assembled techniques are hard to fabricate nanochannels for microfluidic systems directly. In most cases, some other techniques are still needed. For example, microcontact printing (μCP), reactive ion etching, dip-pen nanolithography (DPN) [54] have been applied on self-assembled monolayers to fabricate nanostructures. Kim et al. [159] developed tunable PDMS nanochannels by using SU-8 sliding-mold method. A SU-8 droplet is dropped on a HDT/MHDA modified surface with a microchannel, and then, the substrate is titled, allowing the droplet to slide downward along the hydrophilicmicrochannel. The SU-8 solution is self-assembled

on the channel surface. After an UV exposure process, a nanochannel mold is obtained. The height of the nanochannel can be adjusted by the tilting angle and the width of the channel can be controlled by the microchannel fabrication process. One problem of this method is that the nanochannels are low in AR, collapse of channel roofs may happen after bonding.

Crack-based nanochannel fabrication. Lithography-free nanochannel array fabrication on a polystyrene (PS) petri dish lid surface has been investigated by Xu [115]. Nanochannels of tens millimeters in length were obtained. To generate a nanochannel array on a PS surface, a certain volume of ethanol is added to a petri dish covered with a petri dish lid. Then, the petri dish is heated by a hot plate to evaporate the ethanol. The ethanol vapor in the petri dish contacts with the lid inner surface directly and interacts with the PS lid free from coffee-ring effect. An array of nanochannels will be created on the inner surface of the petri dish lid eventually. Nanofluidic devices fabricated by this way are transparent, repeatable, and free from complex fabrication processes. Therefore, it is a promising method for developing cost-effective nanofluidic devices.

Crack-based nanochannel fabrication on PDMS surface developed by Zhu et al [120,160,161] has also been used in the nanofluidic field. In this approach, a PDMS slab is exposed to oxygen plasma for a certain time. After exposure, the surface becomes stiff and largely composed of SiOx. A uniform strain is applied to stretch the film; as a result, the stiff skin cracks, forming the interspaced nanochannels. The average crack spacing and crack size can be adjusted by the applied strain, Young's modulus of the PDMS film, the thickness of the film, the oxidation of the PDMS surface, etc. [161] Nanocracks of 120 nm in width and 78 nm in depth have been reported [120,161]. This technique can create nanochannels in a large area without lithography. The procedures and equipment are simple, and the channel size is also tunable and repeatable, as reviewed above. However, the number and locations of these nanocarcks are totally random. A detailed review of the cracking method is presented in CHAPTER 3.

2.2.6 Bonding and sealing of nanofluidic devices

To obtain encapsulated nanochannels, bonding or sealing is a must process. Various methods have been applied in the bonding and sealing process according to the bulk material of the substrates and the cover plates. For example, for silicon-silicon, glass-glass and thermoplastic wafers, thermal fusion method has been widely used; and for some polymers such as PDMS and SU-8 photoresist, plasma [162–164] and UV [165] treatments are often applied. Anodic bonding method is generally applied in silicon-glass bonding, in which both high electric field and high temperature are needed [124,166,167].

Occasionally, adhesive layers such as water glass, spin-on-glass, benzocyclobutene or glue are coated on the wafer surface to enhance the bonding strength [168]. Chemicals such as hydrofluoric acid [162,169], are used to bond glass-glass chip under high pressure at room temperature. The self-enclosed method is another new strategy to fabricate closed nanochannels in which the channels are encapsulated automatically during the fabrication process [170–174].

Thermal bonding. Thermal bonding is commonly used in sealing silicon-based or thermal plastic-based micro/nanofluidic devices by precisely controlling the bonding time, temperature and pressure. During the fusion bonding or sealing process, both the cover plate and the substrate are heated to or over their glass transition temperature; while the externally applied pressure is used to enhance the bonding strength. However, the collapse of the cover plate and the substrate is challenging during the thermal bonding process, especially for nanofluidic devices with low AR channels. In addition, a higher bonding temperature will give rise to a higher possibility of collapse. In order to solve this problem, oxygen plasma treatment [162–164] and adhesive layers are utilized to lower the bonding temperature. For instance, a cover plate coated with SU-8 photoresist can be easily bonded to a substrate with SU-8 nanopatterns. However, adhesive layers may lead to clogging of channels.

Self-enclosed techniques. The self-enclosed technique is used to fabricate nanofluidic devices without sophisticated bonding or sealing process. The nanochannels can be closed or sealed automatically due to the self-closing effects. The working principle of the self-closed technique is based on the microchannel refilling (MR) method. The first step is to fabricate microchannels on a substrate followed by a local deposition, oxidation or melting process to decrease the feature size of the channels [170–174]. In most cases, the speed of deposition, melting or oxidation at the surface of the substrate is higher than that in the inner side of the channel walls, therefore, the top deposition or oxidation pillars will join and result in enclosed channels. Figure 2-7 shows an example of fabricating self-enclosed nanochannels reported by Xia [173], in which channels smaller than 10 nm wide on a silicon wafer over a large area were obtained. Self-sealed circular nanochannels in glass [174], PDMS [172] have also been studied. The self-sealing method is simple and reliable, and there are no leakage problems in the nanofluidic devices. Nonetheless, the channels are usually not transparent, which makes it hard to be used in biological experiments in which optical characterization is needed.

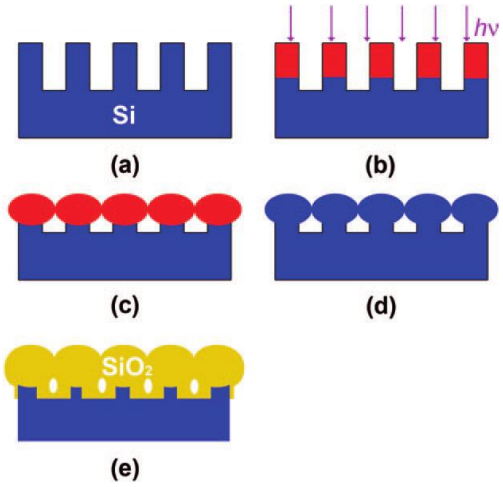

Figure 2-7 Working principle of self-enclosed nanochannels [173]. (a) nanostructure fabrication by NIL; (b) melts the top layer of the structure by laser pulse; (c) molten top layer flows sideward and joins the neighboring pillars; (d) enclosed channel formed; (e) thermal oxidation to shrink the channel size.

Anodic bonding. Anodic bonding, also known as electrostatic bonding or field-assisted bonding, is widely used in assembling and bonding silicon-Pyrex nanofluidic devices. In the bonding process, a silicon wafer and an ionic conductive glass layer are attached together with a tiny force applied. Both the silicon and the glass are placed on a hotplate and heated to the bonding temperature (usually 300-500℃). Under this temperature, ionic glass becomes conductive but without macroscopic deformation. Then, a high voltage is applied to this system with cathode side on the ionic glass side, the mobile cations in the glass move to the cathode side due to the electric field; as a result, a cation depletion layer is generated between the silicon-glass interfaces. The silicon wafer and the glass wafer are forced to intimately contact with each other by the electrostatic field, and a permanently bonded device is obtained [175]. Figure 2-8 is a typical experimental set-up of anodic boning [176]. The process is cheap, easy and reliable; however, the problem of this method is that only the conductor and ionic conductive glass couple can be bonded, for the commonly used polymers, such as PDMS and PMMA, are not applicable.

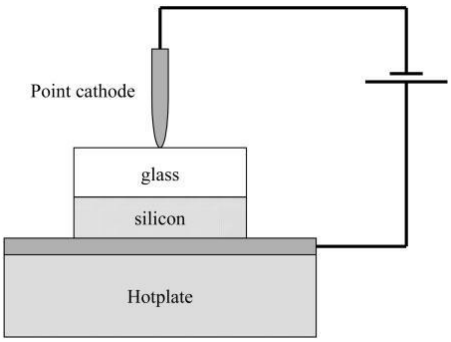

Figure 2-8 Schematic of anodic bonding with a point cathode electrode [176].

2.2.7 Summary

Table 2-1 compares the nanofabrication techniques mentioned in this review section. Characteristics of these methods such as materials, manufacturing facilities and costs, type and size of the nanochannels are summarized. From the table we can easily get the following conclusions:

a. The conventional photolithography method is fast and reliable; however, it is difficult to create channels smaller than 200 nm in width. Conventional photolithography is usually used in microchannel fabrication. In a nanofluidic system, microchannels are sometimes essential, for example for sampling loading and wasting. As a result, conventional photolithography is usually combined with other nanofabrication techniques in nanofluidic device development.

b. Deep UV / x-ray lithography, IL, EBL and FIB are able to fabricate nanochannels with smaller size and higher resolution; however, these methods have the demerits of high-cost, complicated fabrication facilities and time-consuming, etc. On top of these, IL can only create densely arranged arrays which are not applicable in most nanofluidic systems. These methods are generally combined with etching and disposition techniques in fabricating nanochannel molds and photomasks.

c. SPL is able to generate nanopatterns and nanostructures flexible by direct writing with the help of high-tech machines such as AFM and TEM, but it is not realistic for most labs. NIL provide a productive method for nanofabrication, however, it is expensive to fabricate the original masters by EBL, FIB, etching and deposition and so on.

d. By contrast, deposition and etching based methods need less running cost than EBL and FIB, but the fabrication processes are sophisticated and the resolution of channels created by etching and deposition strategies is not as excellent as that fabricated by lithography methods. As mentioned above, etching and deposition are usually used as auxiliary methods in

nanofabrication. Edge lithography is an example of a combination of photolithography, etching, and deposition.

e. Nanomaterials such CNTs have a natural character size in the nanometer scale and can be used to assemble nanofluidic devices with low cost and high productivity. However, it is difficult to manipulate the nano-sized materials. Elastomers and thermal plastics such as PDMS and PMMA are transparent, which enable optical observation of the fluid systems during experiments, especially in nano-transport phenomena studies. Additionally, nanochannels fabricated by deformation of elastomers and thermal plastics are simple and cost-effective. But the quality and repeatability are not very good due to the uncertainty and variability of the elastomers. Wrinkling and cracking methods are relatively simple and cost-effective, but only nanoarrays on large areas can be created by these approaches.

It is impossible to find a one-fits-all strategy for nanofluidic chip fabrication. Nanofabrication techniques with fast processes, low cost, and simple facilities are still in high demand. One of our goals in this thesis is to develop an easy, repeatable, cost-effective and productive method to fabricate single-nanochannel-based nanofluidic devices or multi-channel-based nanofluidic devices on transparent platforms.

Table 2-1 Summary of nanochannel fabrication methods.

	Methods	**Channel type (single/array)**	**Feature size**	**Channel quality**	**Facilities**	**Running cost**	**Time needed**	**Material**	**Mask needed**
Conventional lithography	*Conventional photolithography*	Both	>200 nm	Medium	Photolithography system	Medium	Medium	Photoresist (SU8 series, AZ series) and silicon or glass substrates	Yes
	Deep-UV/X-ray lithography	Both	Sub-25 nm	Good	Light source and Photolithography system	Medium	Medium	PMMA, PCMS,CPMS, Thomson	Yes but special
	IL	Array	> 25 nm	Good	Interferometer and etching system	Medium	Medium	Photoresist and silicon or glass substrate	No
	EBL	Both	>2 nm	Excellent	EBL system and etching system	High	Long	PMMA, calixarene, PS, methyl methacrylate, PC, polynorbornene	No
	FIB	Both	>10 nm	Excellent	FIB system	High	Long	Various, usually silicon based material of polymers	No
	SPL	Both	>20 nm	Excellent	AFM, STM or NSOM systems	High but lower than EBL	Long	Various, such as ITO	No
	NIL	Array	>10 nm	Good	Heating system, pressure system	Low	Medium	Thermal deformation material, Photoresists	Yes
Etching and deposition methods	*Sacrificial layer*	Both	>20 nm	Good	Photolithography, etching and deposition systems	Medium	Long	Various, such as aluminum, chromium, silicon, PTE, nanofibers, AZ1350	Yes, but not nano-sized
	Edge lithography	Array	About 10 nm or	Good	Photolithography, etching	Medium	Long	Various, usually silicon-based	Yes, but not

			larger		and deposition systems			materials	nano-sized
	Oxidation refill	Both	50 nm or larger	Good	Photolithography, etching, deposition and oxidation systems	Medium	Long	Submicron channels, usually made of silicon	Yes, but not nano-size
Nanomaterial	*Nanowires and nanofibers*	Array	20 nm or larger	Low	Electro-spinning system, etching system	Low	Medium	Polymers or mental	No
	Nanotubes	Both	2 nm to hundreds nm	Good	Etching, deposition systems	Medium	Long	CNTs, etc.	No
Elastomeric material deformation	*Collapse method*	Array (triangular)	60 nm or larger	Medium	Photolithography system of EBL system	Medium	Short	PDMS and silicon substrate	Yes but not nanometer size
	Tuneable elastomeric	Array	Tuneable several nm to hundreds nm	Low	Oxidation system or etching and deposition systems	Medium	Medium	PDMS usually	No
	Incomplete bonding	Array (triangular)	Sub-micron	Low	Deposition system or none	Low	Short	PDMS, nano-membrane	No
	Unconventional thermal deformation	Both	Tens nm to submicron	Medium	Various, heating and stretching or compressing tools, NIL system, femtosecond laser, etc.	Various	Short	Various, usually PMMA	Various
Other methods	*Crack-based*	Array	80 nm to hundreds nm	Medium	Plasma oxidation systems or heating tools	Low	Long	PS, PDMS	No
	Wrinkle film	Array	About 230 nm and above	Low	Plasma oxidation systems and heating tools	Low	Short	PDMS	No
	Self-assemble	Various	Nanometer	Various	Various	Various	Various	Various	Various

2.3 Resistive Pulse Sensing (RPS)

RPS technique coined by W. H Coulter in 1953, also well-known as "Coulter Counter", was initially developed for detecting and sizing cells or particles which suspended in electrolyte solutions. Nowadays, RPS has been miniaturized into microfluidic and nanofluidic systems and widely been used in nanoparticle research, bioengineering, and analytical chemistry fields, etc. However, the working principle of the RPS technique is very simple. Figure 2-9 shows an example of an traditional RPS detection system. Generally, an RPS detection system contains a narrow sensing gate and a corresponding current monitoring circuit. The sensing gate bridges two reservoirs filled with an electrolyte solution. When a particle passes through the sensing gate, the electrical resistance of the detecting system changes accordingly, and the current change is recorded by the current monitoring system, as shown in Figure 2-9 (b).

The amplitude of the RPS signals depends on both the particle size and the size of the RPS gate, and there are several classical models related. Here, we assume that the size of the non-conducting spherical particle is d in diameter and the cylindrical sensing channel is D in diameter and L in length. The electrical resistance of the sensing channel filled with the electrolyte solution is assumed to be R_2, and the electrical resistance change of the sensing channel due to passing through of one spherical particle is ΔR. The amplitude of the RPS signal is determined by the relative resistance change $\Delta R/R_2$. The electrical resistance of the sensing gate can be calculated by

$$R_2 = \frac{4}{\sigma}\frac{L}{\pi D^2} \qquad (2\text{-}12)$$

where σ is the conductivity of the electrolyte solution. The relative resistance change $\Delta R/R_2$ can be calculated by several equations under the condition of different particle-to-sensor size ratios:

Infinite Small Particles

For infinite small particles [177], the diameter of the particles is much smaller than the diameter of the sensing channel and the channel is infinitely long, the relative resistance change can be written by Maxwell's equation:

$$\frac{\Delta R}{R_2} = \frac{d^3}{D^2 L} \quad (d \ll D, \mathrm{d} \ll \mathrm{L}) \qquad (2\text{-}13)$$

Small Particles

In Equation (2-13) the relative resistance change is proportional to the volume of the particles. When the particle size becomes larger (d/D<0.5), the relative resistance change can be expressed by Deblois' equation [178]

$$\frac{\Delta R}{R_2} = \frac{d^3}{D^2 L}\left[\frac{D^2}{2L^2} + \frac{1}{\sqrt{1+(D/L)^2}}\right] \mathrm{F}\left(\frac{d^3}{D^3}\right) \qquad (2\text{-}14)$$

where F(x) can be calculated by numerical curve fitting conducted by Saleh [179]

$$F(x) = 1 + 1.264x + 1.347x^2 + 0.648x^3 + 4.167x^4 \qquad (2\text{-}15)$$

Intermediate Particles

For intermediate particles (d/D=0.5~0.8), the relative resistance change can be written as [180,181]:

$$\frac{\Delta R}{R_2} = \frac{d^3}{D^2 L}\,\frac{1}{1-0.8(d/D)^3} \qquad (2\text{-}16)$$

Large Particles

For the large particle cases, the size of the particles is comparable to the diameter of the sensing channel (d/D>0.8), the relative resistance change can be calculated by

$$\frac{\Delta R}{R_2} = \frac{D}{L}\left[\frac{arcsin(d/D)}{\sqrt{1-(d/D)^2}} - \frac{d}{D}\right] \qquad (2\text{-}17)$$

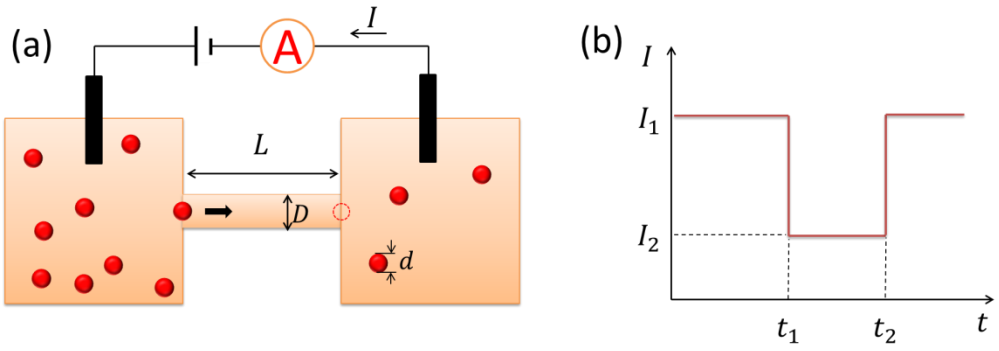

Figure 2-9 Schematic of the traditional resistive pulse sensing method. (a) Components of an RPS detection system. (b) An example of RPS event generated due to translocation of a single particle.

RPS technique has been developed on microfluidic and nanofluidic systems for detecting micron-sized or nano-sized objects, and these classical models are applied in the particle detection. However, it should be noted that the classical theories do not consider off-axis effects, low AR

sensing channel cases, the shape of particles, and surface charge of the particles etc, which are very important in the characterization of nano-sized objects by the RPS method. In this thesis, low-cost, disposable nanochannel-based RPS devices are developed and the above-mentioned factors will be studied and discussed in CHAPTER 6.

2.4 Conclusion

This chapter reviews fundamental theories of electrokinetic transport phenomena, nanofabrication technologies and the resistive pulse sensing technique in general. In the electrokinetic transport phenomena section, classical theories of EDL, EOF, EP, and DEP are introduced, and in the nanofabrication section, conventional and unconventional methods in nanofluidic device fabrication are summarized comprehensively. Classical models of the RPS technique are also reviewed. This chapter provides a solid background for the following chapters, including design and fabrication PDMS nanofluidic devices, fundamental research of electrokinetic transport phenomena in nanochannels and applications of the nanochannel-based RPS detection systems. These theories, models and techniques are for general cases as mentioned above; consquently, an extended review will be presented in the introduction section of each chapter.

CHAPTER 3 Methods: Fabrication of PDMS Nanofluidic Chips [*]

3.1 Introduction

Simple, cost-effective, productive and reliable methods for fabricating nanochannels are highly demanded in the fields of nanotechnology and nanoscience. However, as reviewed in section 2.2, conventional nanofabrication techniques such as EBL and FIB are generally high-cost, time-consuming, while unconventional methods are unreliable and less precise. Nano-crack-assisted fabrication method provides a new strategy for nanofabrication which bridges the gap between the conventional methods and the unconventional methods, allowing easy integration of nanochannels with microchannels on various substrates such as silicon [182,183], PDMS [120,130], SU8 photoresist [184,185]. Crack-assisted nanofabrication techniques take the advantages of failure of the above-mentioned materials and the size of the cracks is comparable to the resolution of conventional technologies [186,187], but there are still a lot of problems by using these crack-based nanochannels in practical applications.

Fabrication of crack-based nanochannels on polymer surfaces for nanofluidic systems was coined by Zhu et al [120,160,161], which opens a new door for low-cost and high-productivity channel fabrication. For instance, Takayama et al. [120,130] created nanocracks on PDMS films by treating the PDMS films with oxygen plasma followed by stretching. The cracks sandwiched between PDMS slabs are tunable in size, however, the size of the nanocracks is too sensitive to the externally applied force, which results in a poor reproducibility. Nanocracking in Si_3N_4 films on Silicon wafers by indentation or self-propagating has been reported by Nam et al [182,183]. These methods can generate high AR nanochannels with smooth channel walls, but the channels are not straight and these methods are not so productive. Kim et al. [188,189] combined the conventional photolithography method with the cracking method and developed a new technique to fabricate nanocracks on UV-exposed SU8 photoresist layers. The locations of the nanocracks are controlled by micronotch structures also fabricated on the SU8 layer. Self-cracking is initialized by post-baking the SU8 layer, and nanocracks are generated due to the gradient of cross-linking density along the direction normal to

[*] A similar version of this chapter was published as:
(a) Peng, R.; Li, D. Fabrication of Nanochannels on Polystyrene Surface. Biomicrofluidics 2015, 9 (2), 24117. http://aip.scitation.org/doi/abs/10.1063/1.4918643.
(b) Peng, R.; Li, D. Fabrication of Polydimethylsiloxane (PDMS) Nanofluidic Chips with Controllable Channel Size and Spacing. Lab Chip 2016, 16, 3767–3776. http://pubs.rsc.org/-/content/articlehtml/2016/lc/c6lc00867d.

the substrate. This technique is productive and is able to create nanochannels in large areas, but the working procedures are still complicated.

Xu [115] developed nanocracks on polystyrene surfaces by utilizing the solvent-induced method. In his work, a certain volume of pure ethanol was placed in a polystyrene petri-dish and covered with a petri-dish lid. During the heating process, the ethanol was vaporized and condensed into liquid form on the petri dish lid inner surface. As a result, the ethanol will swell the lid inner surface, and the following releasing of reagent would initiate cracks on the PS surface due to the natural properties of PS material. Channel arrays of tens millimeters in length were obtained. It is a promising approach for nanochannel fabrication with low cost. However, in their work, the working parameters and mechanism of the solvent-induced method were not sufficiently investigated; furthermore, the nanochannels obtained were in the form of compact arrays and the locations of the nanocracks and the spacing between the cracks are totally random. Consequently, it is difficult to fabricate one single nanochannel and connect such a single nanochannel to microchannels to form a single-nanochannel nanofluidic device. Single-channel nanofluidic devices are the core requirement for the fundamental studies of transport phenomena and manipulation of individual targets in the nanoscale. In addition, in order to obtain accurate, repeatable and durable nanochannel molds, replication of nanocracks from polystyrene surfaces without changing the crack size is still challenging. On top of this, nanostructures duplicated by using regular PDMS are likely to collapse after bonding due to the low Young's modulus of the regular PDMS material.

In order to improve the nanocracking method and to create single nanochannels or nanochannel arrays with controllable size and spacing, a systematic study of nanofluidic device fabrication based on the nanocracking method is conducted in this chapter. Nanocracks are initially created on polystyrene surfaces by the solvent-induced cracking method. The effects of working parameters including solubility of the solvent, concentration of the solvent, heating temperature, heating time on the crack size are examined. Based on the experimental results and the solubility theory, a guideline for fabricating small nanocracks on PS surfaces is provided. In addition, the locations of the nanocracks are well-controlled by artificial defects marked on the PS surfaces. Thereafter, these nanocracks are duplicated onto SU8 photoresist layers or smooth cast layers by nanoimprint technique to work as nanochannel molds. Hard PDMS (h-PDMS) or extra hard PDMS (x-PDMS) are applied during replication of PDMS nanochannels by soft lithography in order to avoid collapse of channel roofs after bonding. Stable nanofluidic chips with high reproducibility and durability are

eventually obtained by bonding plasma-treated PDMS nanochannels with PDMS microchannels by using a homemade alignment system.

3.2 Working procedures and methods

3.2.1 Working procedures for making PDMS nanofluidic chips

Figure 3-1 illustrates the working procedures of fabricating PDMS nanofluidic chips by using the nanocrack-based method. The working procedures can be divided into four stages. (i) Creation of nanocracks on a polystyrene surface by the solvent-induced cracking method (Figure 3-1 (a1)-(a4)) [190]. (ii) Nanochannel molds fabrication by NIL method by using SU8 photoresist (Figure 3-1 (b1)-(d)) and Smooth cast (Figure 3-1 (c1)-(d)). Nanocracks are duplicated onto the polymers, working as nanochannel molds. (iii) Replication of bi-layer PDMS nanochannels from the nanochannel molds by soft lithography method (Figure 3-1 (e)-(g)). (iv) Plasma-assisted PDMS nanofluidic chip bonding (Figure 3-1 (h)-(i)). The experimental details are illustrated as follows.

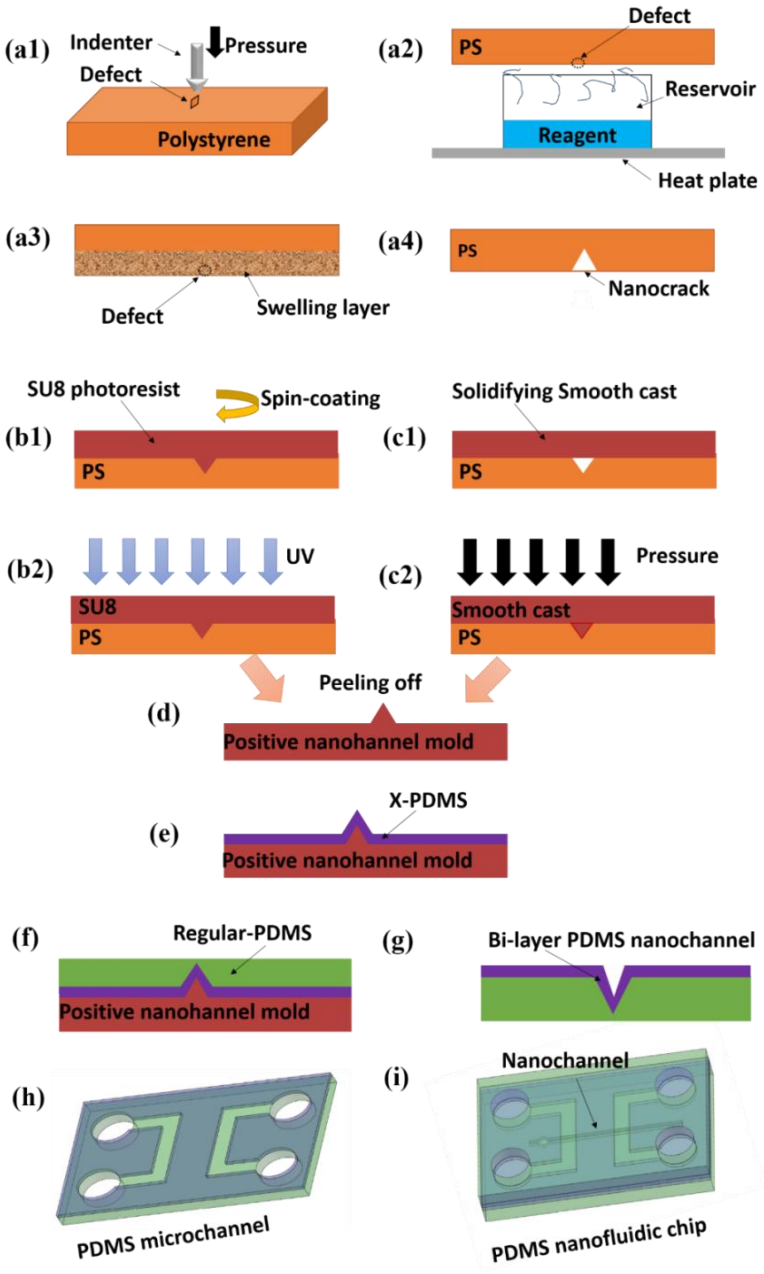

Figure 3-1 Working procedures for fabricating single-channel-based or multi-channel-based nanofluidic chips on PDMS platforms. (a1)–(a4) Working steps for making nanocracks: (a1) making microdefects on a polystyrene slab by using an indenter of a micro-hardness testing system; (a2) absorption of the solvent; (a3) swelling of the polystyrene surface and initialization of nanocracks; (a4) nanocracks on the polystyrene surface. (b1)–(b2) Working procedures for making nanochannel molds by Method A: (b1) spin-coating of SU8 photoresist on the nanocracks; (b2) exposing the SU8 photoresist layer to UV light. (c1) – (c2) Working principle of Method B: (c1) fabrication of

solidifying smooth cast slab; (c2) nanoimprint by using a pressure gauge. (d)–(i) Fabrication of PDMS micro–nanofluidic chips by using the nanochannel mold: (d) nanochannel mold after peeling off; (e) coating of x-PDMS on the nanochannel mold; (f) casting of another layer of regular PDMS on the x-PDMS; (g) bi-layer PDMS nanochannel; (h) fabrication of bi-layer microchannel system; (i) PDMS micro–nanofluidic chip after bonding.

3.2.2 Fabrication of single nanocracks and nanocrack arrays by solvent-induced cracking method

Creation of nanocracks on polystyrene surfaces with controllable size and spacing is conducted in two steps. The first step is to make diamond-shaped artificial defects on polystyrene surfaces (petri dish surfaces (VWR®)) by using a micro-hardness testing indenter (LECO®, MHT series 200) (see Figure 3-1 (a1)). The size and location of these defects are controlled by the micro-hardness testing system, and these defects promise the locations of the nanocracks. Thereafter, nanocracks are initiated from these defects by the solvent-induced cracking method. Briefly, a polystyrene slab with artificial defects is covered onto the opening of a plastic reservoir (17 mm in height and 19 mm in diameter) filled with chemical reagents such as ethanol. The reservoir is placed on a hot plate (Torrey Pines Scientific®) with precisely controlled heating temperature, as shown in Figure 3-1(a2). Consequently, the chemical reagent vaporizes and condenses onto the inner surface of the polystyrene slab. The polystyrene surface absorbs the reagent and swells until the reagent is fully vaporized (Figure 3-1(a3)). Afterwards, the swollen layer shrinks and nanocracks are generates due to the release of the absorbed reagent, as shown in Figure 3-1(a4). The size of the cracks is adjusted by the working parameters used in the solvent-induced cracking method, such as concentration and volume of the reagent, heating temperature, heating time and so on.

To investigate the mechanism of the solvent-induced cracking and the working parameters mentioned above, free cracking on polystyrene surfaces without artificial defects were studied systematically. Chemical reagents such as pure water, acetone (99%), toluene (98.5%) and eight kinds of alcohols, i.e., methanol (99.8%), ethanol (95%), n-propanol (99.5%), isopropanol (99.5%), n-butanol (99%), sec-butanol (99%), tert-butanol (99.5%), n-pentanol (99%) (Fisher Scientific) were tested. The heating temperature was precisely controlled over a large range from 70℃ to 105℃, and the heating time was from 4 hours to 48 hours. Chemical reagent volume from 0.5 mL to 3 mL was also tried. All the experiments were conducted at the ambient temperature about 23 ℃. Under each experimental condition, i.e., one certain temperature, one certain volume, one certain concentration and one certain heating time, the experiments were repeated for at least three times independently,

the number and the width of the cracks as well as the success ratios were recorded. For a given set of condition, if no cracks appeared in the first eight independent experiments, it was believed that the success rate is zero; otherwise, more experiments would be conducted until cracks were observed in three independent experiments. The average crack size was obtained by measuring different cracks for at least five times for each case.

3.2.3 Fabrication of nanochannel molds by nanoimprint lithography

Nanocracks on polystyrene surfaces are not stable, and the crack size changes with time, temperature and chemical environment due to residual stress in the swollen layers. Furthermore, it is also time-consuming to repeat the solvent-induced cracking process. To fix the nanocrack size and to make reliable nanofluidic chips with high reproducibility, the negative nanocracks are replicated onto either SU8 photoresist (Method A) or Smooth cast 305[*] (Method B, Sculpture Supply Canada) by NIL technique. Figure 3-1(b~d) shows the working principles of both method A and method B with details.

In method A, SU8 photoresist is spin-coated onto a polystyrene surface with a single nanocrack or an array of nanocracks at a given speed for a given period of time by a spin-coater (Brewer Science Inc. Cee® 200X) (Figure 3-1(b1)) followed by exposure to UV light for a certain period of time (Figure 3-1(b2)). A stable SU8 photoresist nanochannel mold (Figure 3-1(d)) is obtained by peeling off the SU8 layer from the polystyrene surface after the SU8 layer is crosslinked and strong enough. Finally, the SU8 photoresist layer is attached to a PMMA substrate to work as the nanochannel mold, as shown in Figure 3-2 (Method A).

For method B, Part A and part B of smooth cast 305 are mixed together (10**:**9 by weight) and cast into a petri-dish to form a pre-curing slab. After a pre-curing time, the rubber-like smooth cast slab is peeled off from the petri dish and attached to the polystyrene nanocrack surface (Figure 3-1(c1)). Air bubbles trapped between the two slabs are removed carefully. The two-slab system is sandwiched by a force measurement system (Model TSF, Mark-10®) or a homemade squeezing system[†] with a given pressure applied for a certain period of time (pressurized time), as shown in Figure 3-1(c2). After release of the pressure, the smooth cast slab on the polystyrene surface is left in air for a certain period of time until the smooth cast is solidified and strong enough for peeling off. Finally, a nanochannel mold could be obtained by peeling off the smooth cast layer from the

[*] Details of the smooth cast material can be found: https://www.smooth-on.com/products/smooth-cast-300/.
[†] Details about the home-made squeezing system can be found in Appendix A.

nanocrack surface (Figure 3-1(d)). Figure 3-2 (Method B) illustrates the working procedures in detail. All the nanocracks, nanochannel molds and nanochannels were observed and characterized by the optical microscope and the AFM.

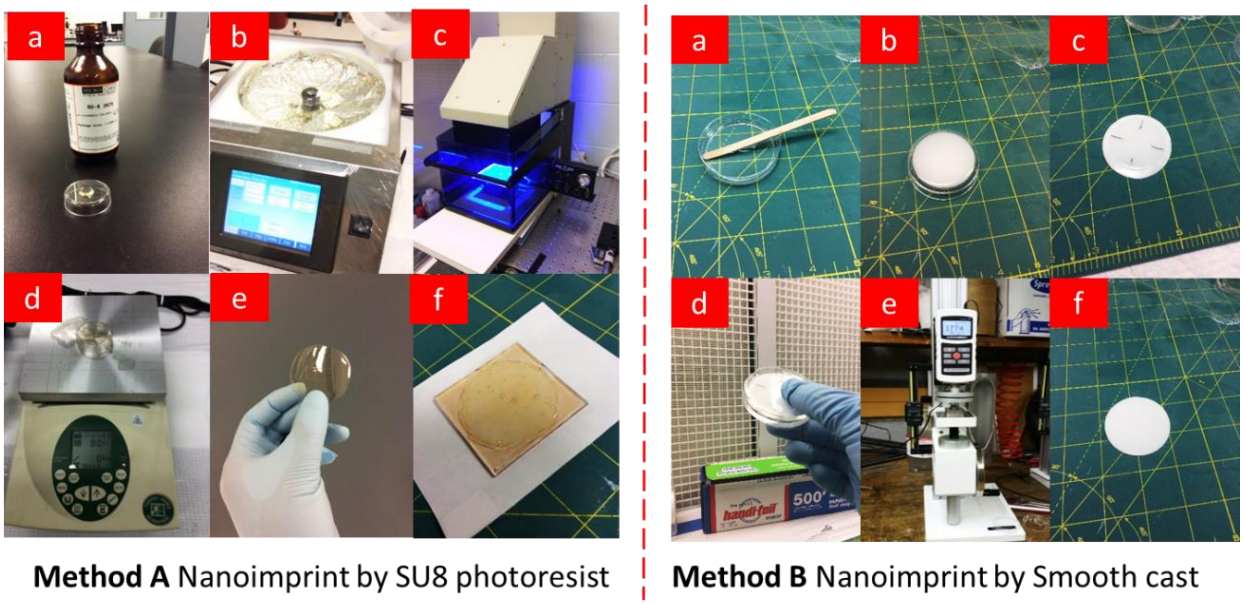

Figure 3-2 Working procedures for making nanochannel molds by using SU8 photoresist (Method A) and Smooth cast (Method B). Method A: (a) a drop of liquid photoresist on the nanocracks, (b) spin-coating of SU8 photoresist, (c) exposure to UV light, (d) heating for a while to solidify the photoresist layer, (e) peeling off the SU8 photoresist layer, (f) attaching the photoresist layer onto a PMMA platform. Method B: (a) pre-curing Smooth cast (liquid form), (b) rubble-like smooth cast, (c) attaching the smooth cast layer onto the nanocracks, (d)Smooth cast-PS system sandwiched by two PDMS slabs, (e) Nanoimprint by applying a pressure, (f) peeling off the Smooth cast from the nanocracks.

3.2.4 Duplication of bi-layer PDMS microchannels and nanochannels by soft lithography

PDMS is an excellent material for making microfluidic chips and can also be used to replicate nanofluidic chips. However, nanopatterns with a feather size smaller than 200 nm on PDMS material can hardly survive after plasma-assisted bonding due to the low Young's modulus (2~3 MPa) of regular PDMS material [191]. To improve the Young's modulus of the regular PDMS and to create stable nanochannels with a size smaller than 50 nm, h-PDMS [192] or x-PDMS [191] with Young's modulus as high as around 10 MPa and 80 MPa are employed.

H-PDMS is prepared by mixing 3.4g VDT 731 with 18μL SIP6831.2 and 0.1g modulator (SIT7900.0) for 5 minutes followed by adding 1g HMS-301 into the mixture. X-PDMS is composed of two parts, part A (vinyl functional part) and part B (crosslinker part). An initial compound of Part A is prepared by mixing 10 g linear vinyl siloxanes (VDT 731) with 16 g Q-siloxanes solution (VQX-221) and heating in an air-purged oven at 50 ℃ for 24 hours to evaporate the solvent. Afterwards, the final Part A is obtained by mixing 25 μL platinum catalyst (SIP 6831.2LC) and 60 μL moderator (SIT 7900.0) into 1.8 g the mixture. The pre-curing x-PDMS solution can be obtained by further mixing 0.6 g part B (linear silicon-hydride siloxane, HMS 501) into part A. All the chemicals used in preparing the h-PDMS and the x-PDMS were purchased from Gelest Inc.

During the experiments, the pre-curing h-PDMS or x-PDMS solution was degassed in a vacuum oven (Isotemp® 280A) for 1~2 min and cast onto the nanochannel mold followed by a 30-minute-heating at 70℃ to solidify the h-PDMS or x-PDMS layer (Figure 3-1(e)). The spin-coated h-PDMS or x-PDMS layer was about 30~50μm thick. Another layer of regular PDMS of about 3 mm thick was cast onto the solidfied h-PDMS of x-PDMS layer followed by a second round of heating process at 80℃ for 2 hours (Figure 3-1(f)). Finally, the bi-layer PDMS nanochannel was peeled off from the channel mold (Figure 3-1(g)). Tips in nanochannel dulplication by using x-PDMS can be found in Appendix FAppendix .

3.2.5 Alignment and bonding of nanofluidic chips

The final nanofluidic chips are obtained by connecting the PDMS nanochannels to microchannel systems. In this chapter, we just demonstrate a simple example of fabricating nanochannel-based nanofluidic devices. The microchannel system contains a pair of “U” shape microchannels designed by AutoCAD® software and fabricated by the standard photolithography method as mentioned in section 2.1.1. Figure 3-1(h) shows an example of the “U” shaped PDMS microchannels. To avoid the collapse of the nanochannel roof during chip bonding, the microchannel system was also replicated by the bi-layer style as described above.

Plasma functionalization has been widely used to seal polymer-based microfluidic or nanofluidic chips. X-PDMS has similar properties of regular PDMS and can be bonded together after plasma treatment. Before bonding, channel reservoirs were punched on the PDMS microchannel slab, and scotch tape was used to clean dust or debris on the microchannel and nanochannel surfaces. Afterwards, the PDMS slabs were treated with plasma for 30 s (Harrick plasma®, PDC-32G) and

bonded together by using a homemade alignment system. For all the processes, no clean room was needed.

Figure 3-3 shows the working principle of the alignment system developed on the stage of an inverted microscope (Nikon, TE-2000). There are two manipulation stages in this system, and both of them can move freely in the horizontal directions. D (see Figure 3-3) is a working stage of the microscope, and A is a manipulation stage with a chip holder created by a 3-D printer (Dimension, Elite). The bonding can be processed in three steps. First, a PDMS slab with nanochannels is placed onto stage D with the nanochannels upwards, and these nanochannels are localized in the middle of the microscope view with the help of a 40× objective lens. The second step is to load the PDMS microchannel slab into the chip holder on stage A with the microchannels surface downwards, and the microchannels are also localized in the middle of the microscope view by using a 10× objective lens which has a longer focal length. In the third step, the PDMS nanochannel slab is lifted by a 100× objective lens manually. For the sake of convenience, here the 100× objective lens just works as a lifting stage for the nanochannel slab. As the upper surface of the nanochannel slab touches the lower surface of the PDMS microchannel slab, the PDMS nanochannels and PDMS microchannels are bonded together automatically due to the properties of the PDMS surfaces after plasma treatment. To minimize deformation of the PDMS slab, a glass slide C is attached to the PDMS slab to work as a temporary substrate. After removing the glass slide, a PDMS-PDMS nanofluidic chip is obtained.

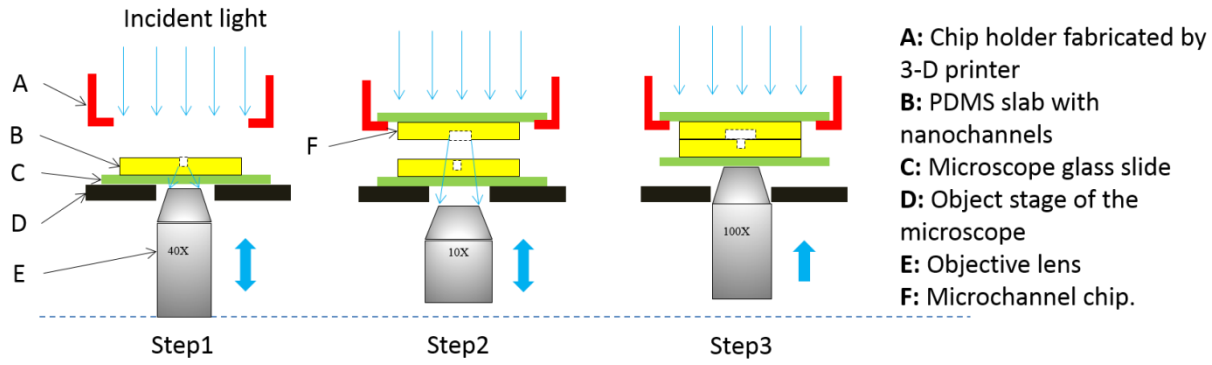

Figure 3-3 Schematic of micro-nanochannel bonding by a home-made alignment system.

3.3 Results and discussion

3.3.1 Nanocrack generation on polystyrene surfaces

3.3.1.1 Mechanism of solvent-induced cracking on PS surfaces

Many studies have been done to investigate solvent-induced cracking on polymer surfaces. [193–197] For instance, Spurr et al. [198] divided the cracking phenomena into three steps: initiation, propagation, and termination. The initiation step determines the locations of the individual cracks, generally, cracks start at surface defects; propagation depicts the initial growth of the cracks, combining with stress releasing; and in the termination step, the cracks stop growing. Moreover, cracking on polymers have to meet three conditions (i) a dilation stress field, (ii) a stress greater than the critical value, (iii) a driving force for cracks to grow [199]. It is widely accepted that the penetration of liquid solvents into polystyrene, causing a reduction of the glass transition temperature T_g, is key to the solvent-induced cracking behavior [194]. The glass transition temperature of polystyrene is about 105℃. However, the glass transition temperature of polystyrene reduces by tens of degree after solvent-induced swelling [200]. Kambour discussed the mechanism of the solvent-induced cracking in detail [200–203]. Xu et al. [115] argued that the surface tension releasing on polystyrene surface due to shrinking process following by the surface swelling is the driving force for the cracks.

In the experiments conducted in this chapter, the formation of nanocracks on polystyrene surface can be divided into the following steps: Firstly, the liquid reagent is heated into vapor which will condense and form a thin liquid film on the surface of the polystyrene lid. Consequently, the solid polystyrene will absorb the liquid and form a swollen layer. Secondly, after a long time of heating, the liquid reagent in the reservoir is fully vaporized. The absorbed reagent will release from the swollen layer and the swollen layer starts shrinking, which will increase the stress in the swollen layer. When the surface stress is larger than a critical value, cracks initiate from defect spots to release the surface stress. The longer the heating time, the more absorbed reagent will release from the swollen layer. As a result, the surface stress becomes larger which will, in turn, contributes to a larger crack size, in both axial and vertical directions. Finally, the swollen layer stops shrinking when the absorbed reagent is completely released, therefore, the cracks stop growing.

The swelling process determines the thickness of the swollen layer, which affects the depth of the cracks. The swollen layer is usually very thin, about 0.1 to $1\mu m$ [204], and the solvent-induced cracking can hardly occur in the bulk layer. The swelling process is controlled by the rate of uptaking of the reagent, which depends on both the solubility of the reagent and the diffusion coefficient. The

diffusion coefficient is dependent on the temperature, concentration gradient, structure and size of the reagent molecules and so forth. For instance, when the reagent molecule is larger or with more bulky molecular structure, the diffusion coefficient will be smaller, which decreases the speed of swelling and results in a thinner swollen layer and a smaller size of cracks.

It is found that a good solvent for a specific kind of solid polymer should have a solubility parameter value close to that of the solid polymer [205]. The solubility parameter "δ", describes the degree of interactions between different materials based on the molecular cohesive energy density, is widely used to predict the critical strains because there are general correlations between the δ difference and the critical strain [194,195,206]. Hansen Solubility Parameter (HSP), is based on the "like dissolves like" principle, and is applied to predict if one polymer material can be dissolved by another solution [206]. And the HSP can be divided into three parts [195]:

$$\delta_t^2 = \delta_d^2 + \delta_p^2 + \delta_h^2 \qquad (3\text{-}1)$$

where δ_t is the total solubility parameter, δ_d refers to the energy from nonpolar dispersion interactions, δ_p stands for energy from dipole interactions, δ_h is the energy from interactions between hydrogen bonds. A larger difference in solubility parameters between the liquid solvent and the solid polymer indicates that a larger critical strains is required to initiate the stress cracking [206]. A larger critical strain means that the cracking process is intense, and large cracks will be created to release the energy if the number of defects is limited.

3.3.1.2 Effect of reagents

Figure 3-4 compares the width of cracks obtained by exposing the polystyrene surfaces to eight kinds of alcohols (1 mL and 2 mL), for 24 hours at 85 ℃ and 90 ℃, respectively. Apparently, from Figure 3-4 (a) and Figure 3-4 (b) one can see that the width of cracks increases with the volume as well as the heating temperature. The effects of heating temperature and volume of reagent will be discussed in the later section. Here, the discussion will concentrate on the dependence of cracks on the different types of alcohols. As shown in Figure 3-4, cracks created by methanol are larger than that made by other alcohols, and the crack size created by tert-butanol is the smallest. Figure 3-5 shows the pictures of the cracks created by heating 2 mL pure alcohols at 90 ℃ for 12 hours. For (a) methanol, (b) ethanol, (c) n-propanol, (d) isopropanol and (g) tert-butanol, single cracks or crack arrays were generated and the width of the cracks show a decreasing tendency from methanol, ethanol, to n-propanol and finally to isopropanol. However, for (e) n-butanol, (f) sec-butanol and (h) n-pentanol, the cracks show as massive crossing patterns.

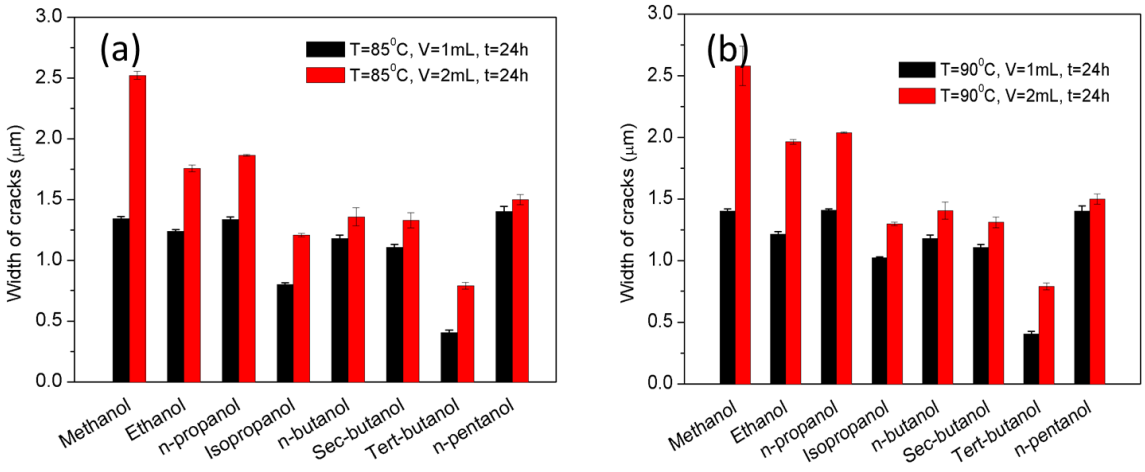

Figure 3-4 Width of the cracks fabricated by heating different kinds of alcohols after 24 hours, (a) heating temperature: T=85℃, and liquid volume V=1 mL and 2 mL; (b) heating temperature: T=90 ℃, and liquid volume V=1mL and 2mL.

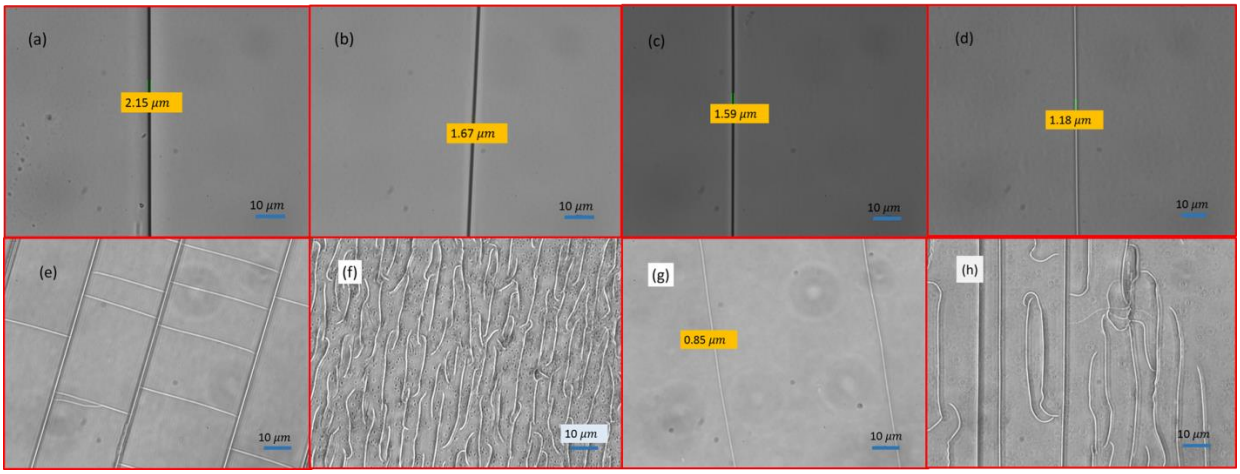

Figure 3-5 Images of nanocracks on polystyrene surfaces fabricated by heating eight kinds of alcohols at 90℃ for 12 hours, for all the cases, the volume is 2mL. (a) methanol, (b) ethanol, (c) n-propanol, (d) isopropanol, (e) n-butanol, (f) sec-butanol, (g) tert-butanol, (h) n-pentanol.

Regarding the effects of the molecule size and polar groups of alcohols on the critical stress for solvent cracking on the surface of polystyrene, Narisawa [207] reported that alcohols with larger molecular sizes would result in larger critical stress in crack initiation on polystyrene surfaces, and polar groups in the molecules result in an increase of the critical stress as well. Iisaka [208] showed that the crack initiation energy in the solvent-induced crack on polystyrene is a function of the length of

n-alcohol molecules chains, and the speed of crack initiation on the polymer surface is dependent on the diffusion coefficient of the solvent molecules. A larger diffusion coefficient will result in a smaller activation energy level for a certain crack initiation. Also, Riquet et al. [209] proved that methanol with a smaller molecular size penetrates much faster in polystyrene than ethanol at 40℃, and the diffusion coefficients are $1.9\times10^{-9}cm^2/s$ and $0.46\times10^{-9}cm^2/s$ for these two alcohols, respectively. Compared with methanol and ethanol, the diffusion coefficient for isopropanol in polystyrene is much smaller, $0.2\times10^{-9}cm^2/s$ [209].

Table 3-1 Solubility parameters and molecular volume of alcohols [44, 49, 48, 50]. The unit of δ_t , δ_d, δ_p and $\delta_h$is $(J/cm^3)^{1/2}$, and the unit of molecular volume is $cm^3/mole$.

Alcohols	δ_t	δ_d	δ_p	δ_h	Molecular volume
methanol	29.7	15.1	12.3	22.3	40.7
ethanol	26.6	15.8	8.8	19.4	58.5
n-propanol	24.5	16.0	6.8	17.4	75.2
isopropanol	23.5	15.8	6.1	16.4	76.8
n-butanol	23.1	16.0	5.7	15.8	91.5
sec-butanol	22.2	15.8	5.7	14.5	92.0
tert-butanol	21.8	15.2	5.1	14.7	95.7
n-pentanol	21.6	15.9	4.5	13.9	108.6
polystyrene	20.0	17.6	6.0	3.9	--
acetone	19.9	15.5	10.4	7.0	74.0
toluene	18.2	18.0	1.4	2.0	106.8
water	47.8	15.5	16.0	42.3	18.0

As discussed above, both the solubility parameter and the diffusion coefficient affect the crack formation. The total solubility parameter has taken the polarity, hydrogen bonds and dispersion interactions into account. With respect to the diffusion effect, since the temperature and the concentration gradients are identical for all the cases, only the molecular size should be considered. The molecular size can be expressed in terms of molecular volume. Table 3-1 shows the Hansen solubility parameter and the molecular volume of the reagents used in this study. The solubility parameter of polystyrene is 20.0 $(J/cm^3)^{1/2}$. If diffusion coefficient is not taken into account, water with a solubility parameter of 47.8 $(J/cm^3)^{1/2}$ is the weakest solvent to polystyrene (the solubility parameter difference is 27.8 $(J/cm^3)^{1/2}$), while acetone with a solubility parameter of 19.9 $(J/cm^3)^{1/2}$ is the strongest solvent for polystyrene (the solubility parameter difference is 0.1 $(J/cm^3)^{1/2}$) in the swelling process. Acetone and toluene were used to swell polystyrene surface and fabricate

nanocracks, however, they are too strong and polystyrene can be dissolved in these reagents rapidly. By contrast, water is too weak, no crack is generated on the polystyrene surface after a 48-hour heating at 90 ℃.

As shown in Table 3-1, it is clear that the difference of solubility parameter between polystyrene and the alcohols decreases with the increasing molecular volume, i. e., methanol, ethanol, n-propanol, isopropanol, n-butanol, sec-butanol, tert-butanol and n-pentanol, from large to small. Interestingly, from Figure 3-4 one can see that the width of cracks are also showing the same decreasing tendency roughly, except for n-pentanol, because the molecule of n-pentanol is too large, and it is hard for polystyrene to absorb such big molecules to initiate cracks uniformly.

In addition, for the isomers (alcohols with identical molecular formulas but different molecular structures), such as n-propanol and isopropanol, as well as n-butanol, sec-butanol and tert-butanol groups, the molecular volumes show little effects on the crack formation, the swelling process is mainly dependent on their solubility parameters. For instance, cracks created by n-propanol is larger than that created by isopropanol due to the larger solubility parameter difference between n-propanol and polystyrene, 4.5 $(J/cm^3)^{1/2}$, compared with that in the case of isopropanol, 3.5 $(J/cm^3)^{1/2}$. A larger solubility parameter difference contributes to a larger critical strain and a larger crack size, and a smaller difference of solubility parameters makes a smaller critical stain as well as a smaller crack size. However, when the critical strain is too small, crossing cracking and amorphous dissolved patterns may appear. For example, the solubility parameters of n-butanol, sec-butanol and n-pentanol are too close to that of polystyrene, which makes the initiation of cracks easily, and crossing patterns appear after the swelling process (see Figure 3-5).

Therefore, the criteria for selecting a strong cracking reagent includes: (i) a solubility parameter value close to that of polystyrene, and (ii) a small molecular volume, or both. However, when the reagent is too strong, crossing cracks will be generated. A proper reagent for nanocrack fabrication should be a chemical which does not swell the polymer greatly; in other words, the solvent should have a considerable solubility parameter value difference from that of the solid polymer and an appropriate molecular size. Therefore, considering these two factors, isopropanol is a proper agent to study the cracking on polystyrene surfaces. In the following sections, isopropanol is chosen as the testing liquid to systematically study the diffusion effects, such as heating temperature, heating time, concentration, and liquid volume.

3.3.1.3 Effects of alcohol volume and heating time

The volume of the liquid reagents affects the contacting time between the reagent liquids and the polystyrene surface directly in the swelling process when the heating temperature is constant. At a given heating temperature, a larger volume of alcohol takes a longer time to fully vaporize, which means a longer contacting time between the polystyrene surface and the alcohol. Consequently, a larger quantity of reagent molecules would diffuse into the polystyrene, and the swollen layer will be thicker and the final crack size will be larger. During the experiments, all the reagent liquids were fully vaporized before inspection. Figure 3-6presents the width of cracks fabricated by heating different volumes (from 0.5 mL to 3 mL) of isopropanol at 85℃ and 90℃ for 12 hours and 24 hours. The results show that the crack size increases gradually with the volume under a given temperature and a given heating time. As shown in this figure, under the condition of T = 85 ℃ and t = 12 hr., the cracks are about 0.5 μm wide when the volume of the liquid alcohol is 0.5 mL, and the crack width increases almost linearly with the volume of the alcohol to 1.15 μm, when the volume is 3 mL. Similarly, under the condition of T=90 ℃ and t = 12 hr., the width of the cracks increases from about 1.05 μm to almost 1.3 μm when the volume increases from 0.5 mL to 3 mL. Also seen from Figure 3-6 a higher temperature generates a larger crack size under the same liquid alcohol volume. More discussion about the temperature effects will be provided in the later section.

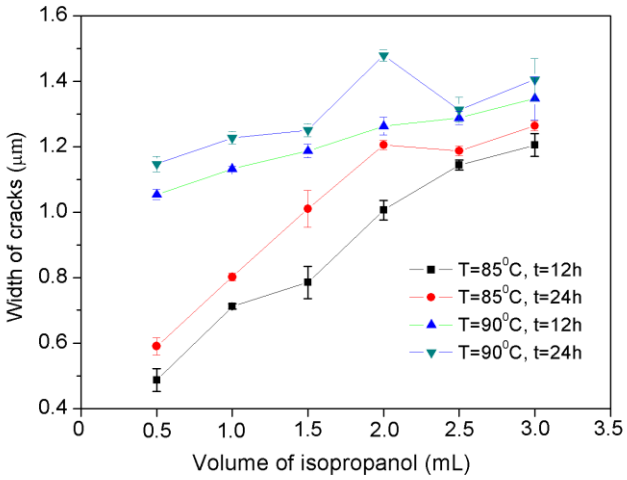

Figure 3-6 Volume effects on the cracking size. A certain volume of isopropanol (99.5%), from 0.5mL to 3mL, is heated at a fixed temperature, 85℃ and 90℃, for 12 hours and 24 hours.

The heating time is an essential parameter for the solvent-induced cracking process, including swelling, reagent releasing, crack initiation and crack propagation. The longer the reaction time, the

larger stress will be generated, which will, in turn, results in a larger crack size. Figure 3-7 shows the heating time effects on the crack size, under a constant heating temperature of 95℃, and a constant liquid alcohol volume of 1 mL. Isopropanol solutions of seven different concentrations ranging from 5% to 99.5% were tested. From the figure, one can see that the width of the cracks increases with the heating time for all the concentrations. However, it takes longer time for the cracks to initiate when the concentration becomes lower. Specifically, only about 4 hours are needed for the case of 99.5% concentration to initiate cracks. By contrast, in the cases of 10% and 15% concentrations, the cracks appear generally after 12 hours of heating. Moreover, it is obvious that the increase of crack width becomes slower after 24 hours, and the crack size is likely to level off after heating for 48 hours, because of full release of the absorbed isopropanol molecules from the swollen layer. Figure 3-8 presents the crack initiation process in detail. From the pictures, one cannot see any cracks on the polystyrene surface at 4 hours; however, after another two hours, a crack grows on a defect spot and becomes longer in half an hour.

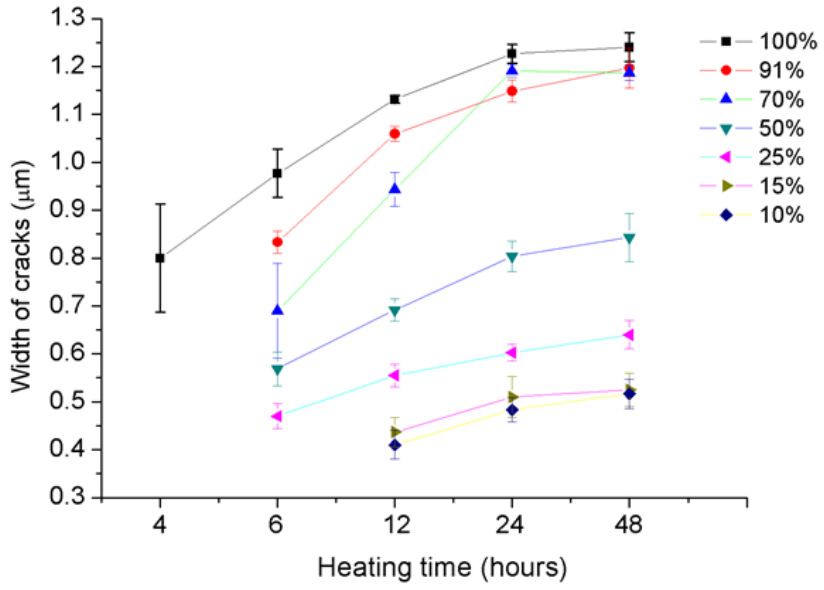

Figure 3-7 Increase in crack size with time. For all the cases, the heating temperature is 95℃; the heating time is from 4 hours to 48 hours and the volume of isopropanol solutions is 1 mL.

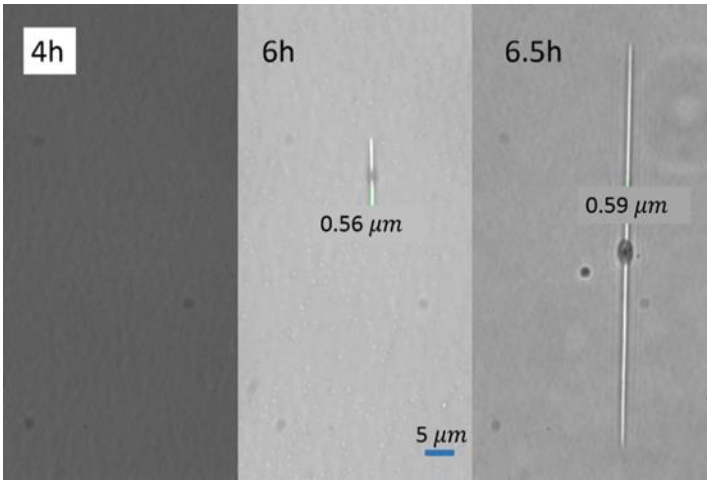

Figure 3-8 Initiation of a nanocrack on a polystyrene surface. The working condition is heating 1 mL 50% isopropanol solution at 95 ℃.

3.3.1.4 Concentration effects and the role of water

Isopropanol solutions with different concentrations from 5% to 99.5% were used to study the concentration effects on the formation of nanocracks. Figure 3-7 also shows the dependence of the width of the cracks on the concentration of isopropanol solutions. It is clear that the crack size increases with the concentration. In Figure 3-7, the smallest crack size obtained is about 0.4 μm, under the condition of heating 1 mL 10% isopropanol solution at 95℃ for 12 hours. In addition, there are no cracks when the concentration is very low, for example, lower than 10%. This is because no insufficient penetration of isopropanol molecules into the polystyrene surface, and the swollen layer is too thin to initiate cracks.

As discussed above, the solubility parameter of water is 47.8 $(J/cm^3)^{1/2}$, which is far from the solubility parameter of polystyrene, 20 $(J/cm^3)^{1/2}$, one can conclude that water is a weak reagent for the initiation of cracking on polystyrene. For example, polystyrene surfaces were exposed to 3 mL pure water at 85℃ for 48 hours. However, there were no cracks on the polystyrene surfaces. Therefore, one can conclude that water is too weak to swell polystyrene and to initiate the nanocracks. However, for water-alcohol mixtures, water plays an important role in the formation of small cracks on polystyrene surfaces. According to Fick's law, a lower concentration of isopropanol in the water film decreases the concentration gradient in the liquid-solid boundary, which slows down the diffusion process. As a consequence, the quantity of isopropanol penetrated into the swollen layer will be smaller, leading to a thinner swollen layer and a smaller crack size. The water film on the

polystyrene surface acts as a “buffering” layer and reduces the concentration gradient, giving rise to a smooth releasing process.

3.3.1.5 Temperature effects

As discussed above, the temperature is a key factor in the process of crack formation. For example, a lower temperature means a lower diffusion coefficient. Figure 3-9 shows the temperature effects on the crack size. In Figure 3-9, the temperature ranges from 70 ℃ to 105 ℃, and the concentration of the isopropanol solutions is from 10% to 99.5%. For all the cases, the heating time is 24 hours and the volume is 2 mL. It is clear that the width of the cracks increases with the temperature. However, no crack appears at all when the temperature is lower than 70 ℃, and cross-cracking appears when the temperature is higher than 105 ℃.

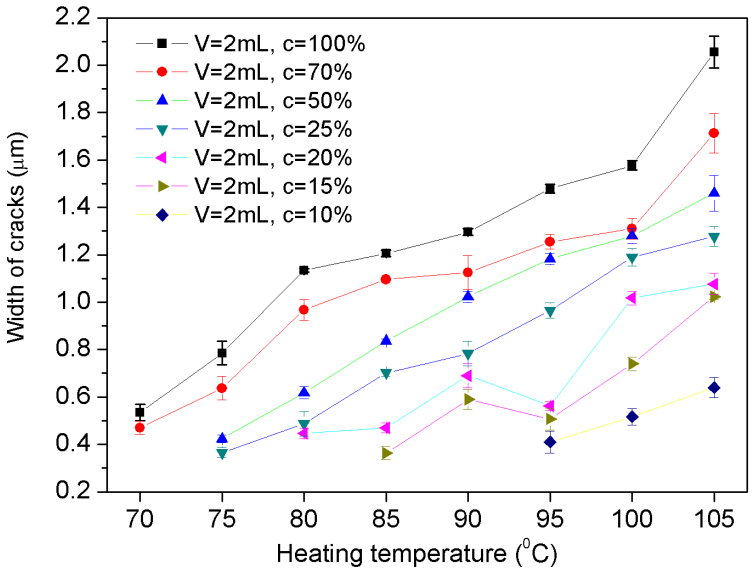

Figure 3-9 Temperature effects on crack size. The temperature ranges from 70 ℃ to105℃, and the concentration of the isopropanol solutions is from 10% to 99.5%; the heating time is 24 hours and the volume is 2 mL.

It should be noted that nanocracks may not be generated in every experiment because the formation of nanocracks depends largely on the existence of defects on the surface. It is hard to initiate cracks when there are no defects on the polystyrene surface even though the stress is large. According to the statistics of the experiments in this study, generally, the success rate of forming cracks increases with temperature as well as volume and concentration of alcohol solutions. For

example, for the cases of 1 mL, 2 mL and 24-hour heating time, when the temperature is lower than 75℃, the success rate of forming cracks is very low ($< 15\%$), and small cracks can only be obtained by chance. However, when the temperature is higher than 105℃, crossing cracks are obtained. For $80℃ < T < 100℃$, the success rate of forming cracks is generally higher than 50%, even approaches 100% when the concentration of alcohol is higher than 15%. It is also very difficult to initiate cracks when the concentration of alcohol is too low. For instance, essentially no cracks appear when the concentration is lower than 5%. However, the success rate at low concentration can still be enhanced by increasing the volume of alcohol solutions or increasing the heating temperature, or both.

3.3.1.6 Number of nanocracks

Total number of the nanocracks formed in the reaction window was recorded in this section,. Figure 3-10 shows the number of cracks created by heating 1 mL and 2 mL isopropanol solutions at various temperatures for 24 hours. From Figure 3-10 (a) and Figure 3-10 (b), one can see that the number of the cracks increases rapidly with the concentration when the concentration value is lower than 70%. However, when the concentration is higher than 70%, the number of cracks decreases. Moreover, when the concentration is lower than 15%, the number of cracks is generally smaller than 5, and the distance between the cracks is generally larger than 500 μm, even 1mm, which is large enough for making single-nanochannel nanofluidic devices. However, the locations of the nanocracks are still random. Localization of the nanocracks on polystyrene surfaces is domonstrated in the following sections.

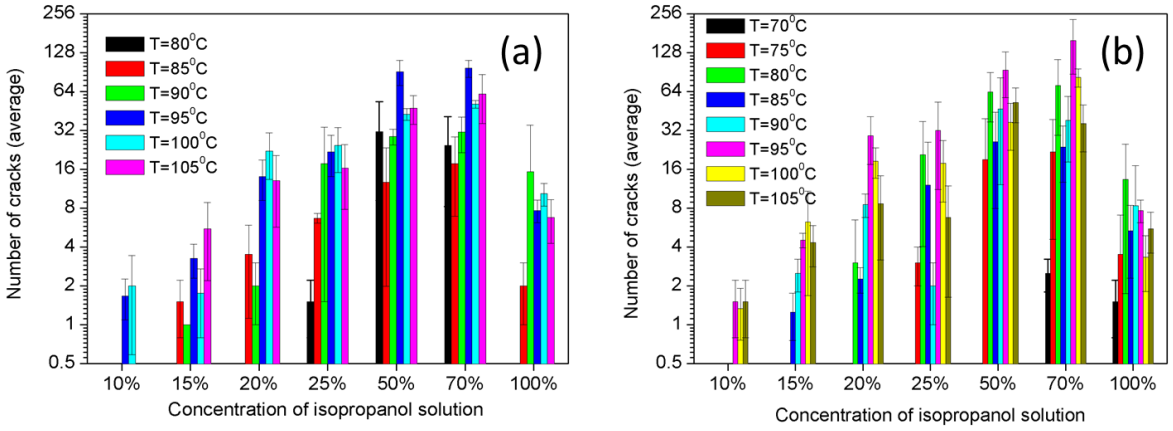

Figure 3-10 Number of nanocracks. The temperatures are 70 ℃, 75 ℃, 80 ℃, 85 ℃, 90 ℃, 95 ℃, 100 ℃, and 105 ℃, and the concentration of the isopropanol solutions are from 10% to 99.5%; the heating time is 24 hours; the volumes are (a) 1 mL and (b) 2 mL, respectively.

3.3.1.7 Fabrication of smaller nanocracks

As mentioned above, small nanochannels are essential to the nanofluidic research field. Enlightened by the results of the systematic studies described above and particularly the results shown in Figure 3-4, tert-butanol was selected to create smaller nanocracks on polystyrene surfaces, because the solubility parameter of tert-butanol (21.8 $(J/cm^3)^{1/2}$) is closer to that of polystyrene ($20(J/cm^3)^{1/2}$) than the solubility parameter of isopropanol ($23.5(J/cm^3)^{1/2}$) (see Table 3-1), and the molecular size of tert-butanol is not too large. The next step was to find an appropriate condition of crack formation. First, 1 mL 75%, 50%, 25% and 15% tert-butanol solutions were chosen to generate nanocracks. These solutions were heated at 95 ℃ for 24 hours, then the width of the cracks was measured, approximately 0.63 μm, 0.37 μm and 0.31 μm, respectively. For the case of 15% tert-butanol solution, no crack was obtained. In order to create cracks of smaller size, a lower temperature was applied. In the experiments, 1 mL 20% tert-butanol solution was heated at 80 ℃ for 8 hours to create smaller nanocracks. For example, Figure 3-11 shows a 3-D AFM image of a nanocrack generated on a PS surface by using the abonve-mentioned working parameters and a cross-section of this nanocrack about 64 nm wide and 17 nm deep.

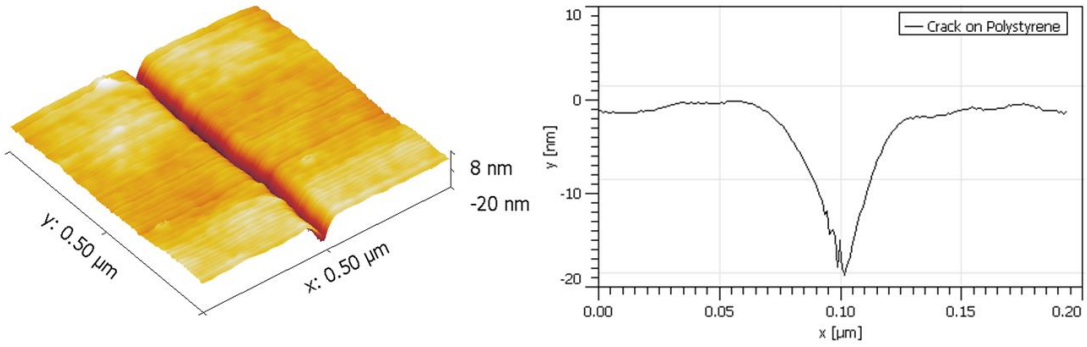

Figure 3-11 An example of small nanocrack generated on a polystyrene surface measured by AFM and a cross-section of this nanocrack of 63.72 nm wide and 17.40 nm deep. The nanocrack is created by heating 1 mL 20% tert-butanol solution at 80 ℃ for 8 hours.

3.3.2 Controlling the locations of nanocracks

As mentioned above, solvent-induced cracks always start from defects, such as sharp dents, flaws and molecular inhomogeneities. These defects are working as the stress nucleation sites during

cracking. Therefore, the idea of this section is to use artificial defects to initialize nanocracks. Figure 3-12 shows examples of polystyrene surfaces before and after nanocrack generation by the solvent-induced cracking method without artificial defects (Figure 3-12 (a1-a2)), with one artificial defect (Figure 3-12 (b1-b2)) as well as with multiple artificial defects (Figure 3-12 (c1-c2)). It is obvious that the locations of the nanocracks generated on the polystyrene surface without artificial defects are random (Figure 3-12 (a2)), and the artificial defects can control the locations of the single nanocrack and the nanocrack array precisely, as shown in Figure 3-12 (b2) and (c2).

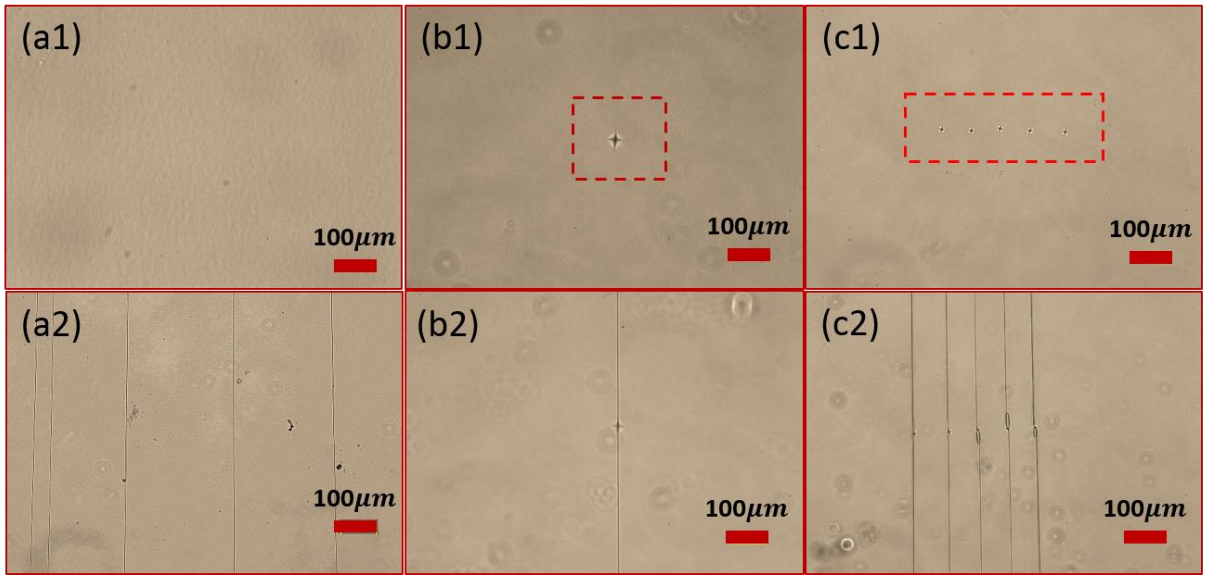

Figure 3-12 Examples of polystyrene surfaces before and after nanocrack generation under the same working condition of the solvent-induced method: (a1-a2) without artificial defects, (b1-b2) with one single artificial defect and (c1-c2) with multiple artificial defects.

3.3.2.1 Effects of defect size on the number of nanocracks

To study the defect size effects on the creation of nanocracks, different forces ranging from 10 gF to 1000 gF were applied on the indenter to create defects on polystyrene surfaces. For each polystyrene sample surface, only one defect was created; and for each force value, 7 independent samples were prepared. For all the cases, the solvent-induced working parameters were the same: heating 1 mL 90% ethanol at 90℃ for 24h. Figure 3-13 (a) and Figure 3-13 (b) summarize the size of the defects and the total number of nanocracks recorded during the experiments.

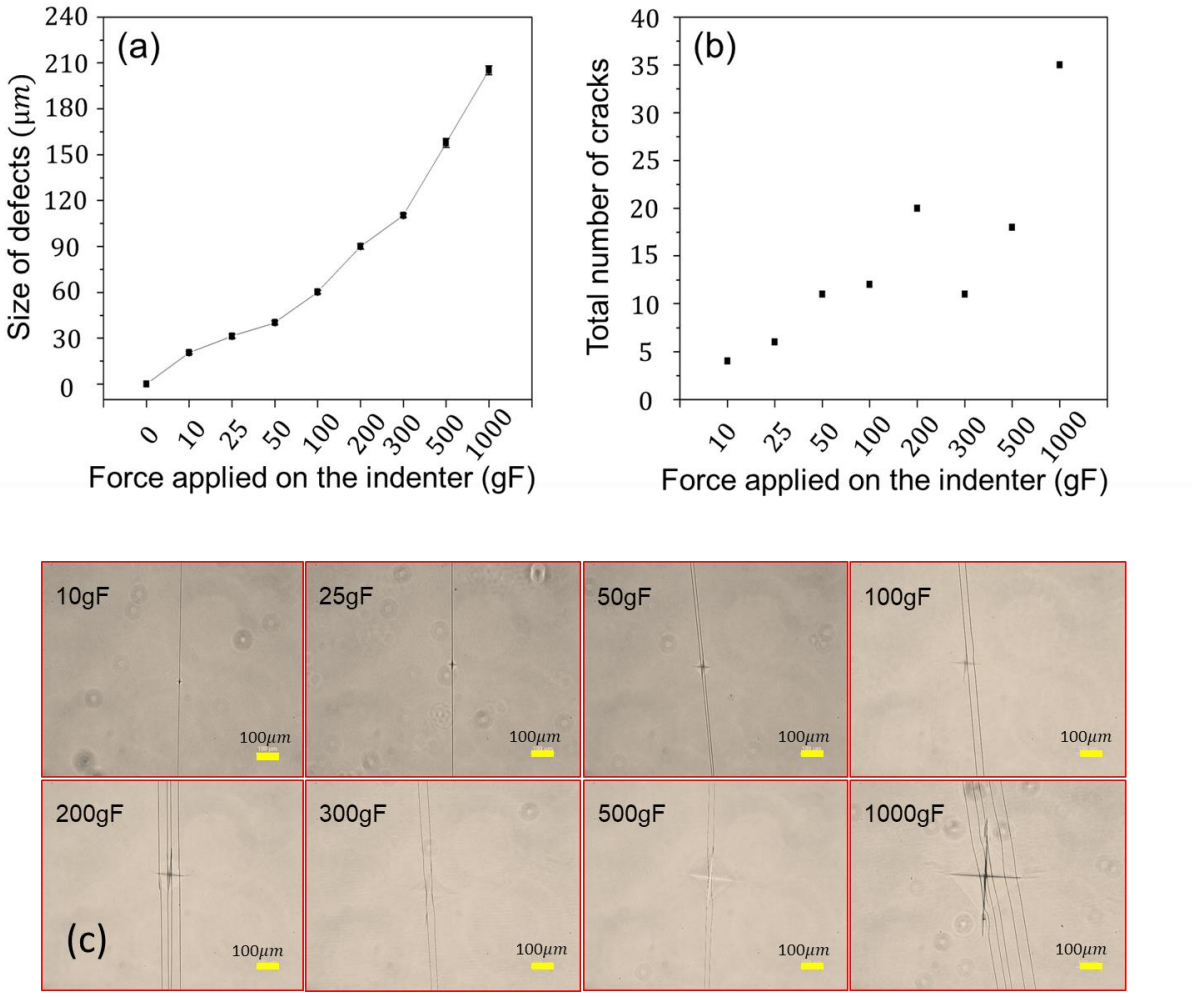

Figure 3-13 Defect size effects on the number of nanocracks. (a) The size of the defects increases with the applied force on the indenter; (b) The total number of cracks generated on the 7 defects increases with the applied force on the indenter; (c) Examples of nanocracks created on polystyrene surfaces induced by defects made by different forces.

Figure 3-13 (a) shows that the size of the defects increases with the applied force, from about 20 μm for the 10 gF case to about 210 μm for the 1000 gF. Figure 3-13 (b) depicts that the total number of nanocracks generated on these defects also increases with the magnitude of the applied force roughly. Examples of nanocracks generated on these defects created by different applied forces are demonstrated on Figure 3-13 (c). For instance, only 4 single nanocracks were generated among the 7 samples in the 10 gF cases, and 6 single nanocracks were obtained in the 7 samples of the 25 gF cases. By contrast, for other cases with larger defect sizes, more than one nanocrack was likely to appear on each defect, contributing to larger total crack numbers. For the extreme case, 1000 gF,

every defect induced 4~9 nanocracks. From Figure 3-13 one can conclude that a larger defect size makes the creation of nanocracks easier; however, more than one nanocrack may be generated on a large defect due to the intense stress concentration near the defect. On the other hand, using smaller artificial defects benefits creation of single nanocracks.

3.3.2.2 Effects of defect size on the size of nanocracks

The size of single nanocracks generated on defects made by forces ranging from 10 gF to 500 gF and under the same working condition by heating 1 mL 90% ethanol at 90℃ for 24 hours was measured. To obtain average crack size reliably, all the measurement locations are far away from the defects. The results show that both the width and the depth of the cracks increase with the heating time in the first 12 hours, and the size of the cracks is likely to level off after 12 hours. For example, for the 10 gF cases, the crack size is about 75 nm wide and 11 nm deep at 4 hours; and after another 4-hour-heating, the crack size increases to about 110 nm wide and 13 nm deep; these values reach 126 nm wide and 27 nm deep at 12 hours. However, as the heating time is as long as 24 hours, the crack size shows little change, about 138 nm wide and 26 nm deep. Figure 3-14 (a) shows the size of single nanocracks induced by single defects created with a heating time of 24 hours. It is obvious that all the cracks have an essentially the similar average size, about 140 nm wide and 28 nm deep. It is obvious that the size of the defects has little effect on the average size of fully developed nanocracks; the defects only dominate the initiation of cracking.

However, artificial defects may affect the size of cracks at positions close to the defects. For example, the nanocrack size was measured at four points separated by 50μm along a nanocrack near a defect made by a force of 200 gF, as shown in Figure 3-14 (b). The crack sizes are 338 nm in width and 68.8 nm in depth at the tip of the defect (point A), and 230 nm wide and 34.5 nm deep at point B, respectively. These values are much larger than the average crack size, 140 wide and 28 nm deep, measured where sufficiently far away from the defect. However, these values decrease to 135 nm wide and 39.4 nm deep at point C, and 147 nm wide and 34 nm deep at point D, close to the average size of the cracks. As a consquence, artificial defects do affect the size of the induced nanocracks at positions close to the defects; however, this effect becomes negligible at points which are far away from the defects.

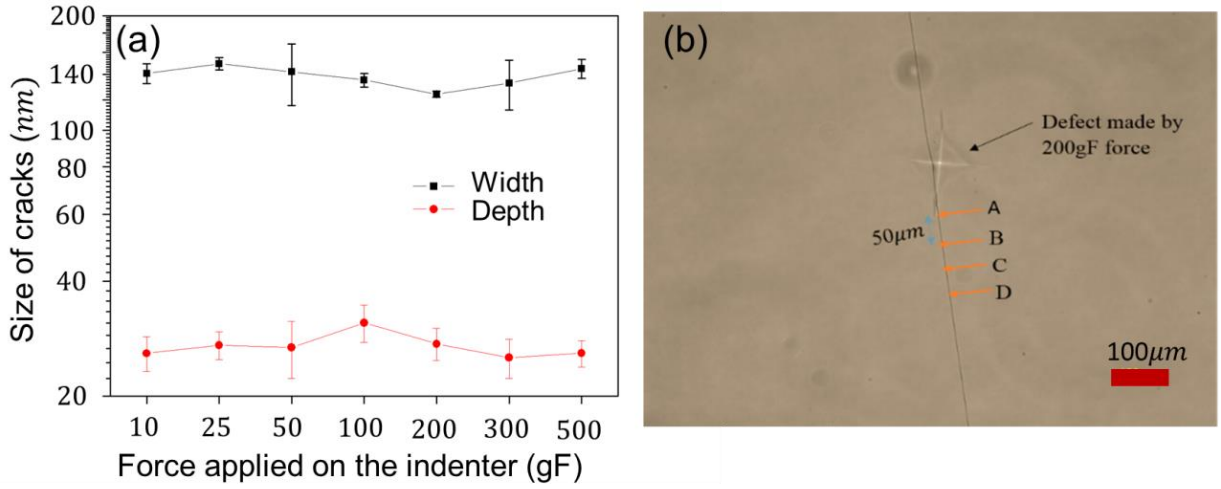

Figure 3-14 Defect size Effects on the size of the nanocracks. (a) Size of nanocracks induced by different size of defects under the same working condition. The force applied on the indenter is ranging from 10 gF to 500 gF. (b) Crack size along a single nanocrack near a defect created by 200gF. A is located at the tip of the defect and A, B, C, D are separated by a distance of about 50 μm.

3.3.2.3 Smaller single nanocrack fabrication

Single nanocracks with smaller size can be generated by using artificial defects according to the guideline mentioned above [190]. Figure 3-15 shows one of smaller single nanocracks generated on polystyrene surfaces by heating 0.8 mL 100% ethanol at 70℃ for 5.5 hours. The artificial defect was marked by 10gF. Figure 3-15 (a) is a 3D view of the nanocrack and Figure 3-15 (b) is the cross-section of this nanocrack of about 80 nm wide and 16 nm deep, as measured by the AFM.

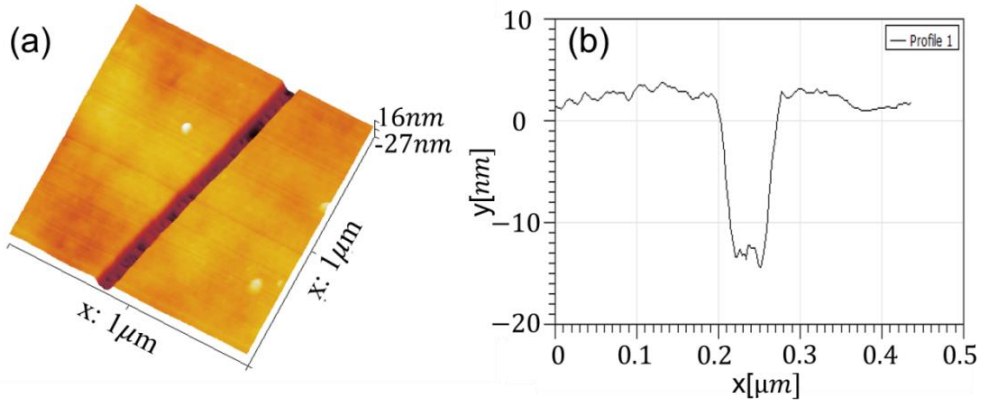

Figure 3-15 Nanocrack of 80 ±7.5 nm wide and 16 ±5 nm deep generated on a polystyrene surface by heating 0.8 mL 100% ethanol at 70 ℃ for 5.5 hours. (a) A 3D image and (b) a cross-section profile of the nanocrack measured by the AFM.

3.3.3 Fabrication of nanochannel molds by Method A: NIL by SU8 photoresist

3.3.3.1 Effects of photoresist type (solvent content)

Six kinds of photoresists (SU8 2000 series[*]) were used to replicate nanocracks from polystyrene surfaces. The nanocracks are all about 90 nm wide and 30 nm deep (see Figure 3-16 (d)), fabricated by the same working conditions. Table 3-2 shows the properties of the photoresists and the working parameters during the replication. The thickness of the photoresist layers and the standard UV exposure dose are obtained according to the datasheet of the SU8 2000 series photoresists [212], and the spin-coating time for all the cases was 60 s. The average surface roughness of the cracks and the nanochannel mold were measured by the AFM. For all the cases, the roughness values and the channel mold sizes were measured for at least 5 times under the same working conditions.

Figure 3-16 (a) shows the roughness of both the polystyrene surfaces and the SU8 nanochannel mold surfaces after replication according to the working parameters in Table 3-2. From Figure 3-16 (a) one can see that the surface roughness of both the polystyrene surfaces and the photoresist channel molds increases with the concentration of solvents in the photoresist. For example, the roughness of the original polystyrene surface is about 2.5 nm, and this value increases to approximately 5 nm in the case of SU8 2150. For SU8 2025 with the highest concentration of solvents, the surface roughness reaches approximately 25 nm. Photoresist with a higher concentration of solvents need a longer time to evaporate after coating, and the solvents swell the polystyrene surface, which in turn results in a higher level of surface roughness.

Table 3-2 Working parameters in nanochannel replication by using 6 kinds of SU8 photoresists [212].

Type of SU8	% Solvents	Viscosity (cst)	Density (g/mL)	Coating speed (rpm)	Thickness (μm)	UV dose (mJ/cm^2)
2025	31.45	4500	1.219	1200	70	200
2035	30.05	7000	1.227	1200	100	230
2050	28.35	12900	1.233	1200	150	260
2075	26.55	22000	1.236	1200	200	330
2100	25.00	45000	1.237	1500	200	330
2150	23.25	80000	1.238	3000	200	330

[*] More information about SU8 photoresist can be found: http://www.microchem.com/Prod-SU82000.htm.

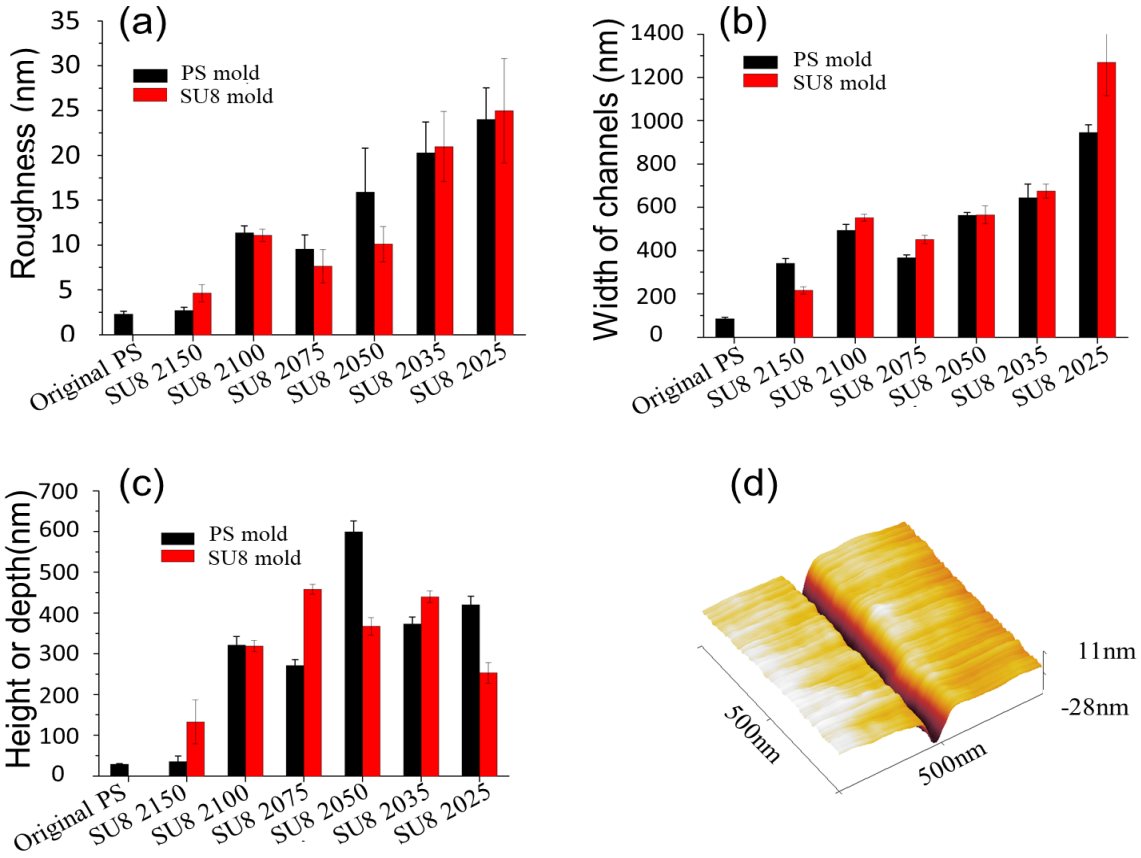

Figure 3-16 Nanochannel mold replication by using 6 kinds of SU8 photoresists. (a) Roughness of SU8 nanochannel mold surfaces and polystyrene (PS) crack surfaces after replication; (b) Width of SU8 nanochannel molds and nanocracks after replication; (c) Height of SU8 nanochannel molds and depth of nanocracks on polystyrene surfaces after replication; (d) 3D image of an original nanocrack of 90 nm wide and 30 nm deep.

Figure 3-16 (b) and Figure 3-16 (c) show the size of the nanocracks and the replicated SU8 channel molds after the replication process. It is obvious that the width of the nanocracks and the SU8 nanochannel molds increase with the solvent concentration, from about 200 nm in the case of SU8 2150 to almost 1 μm in the case of SU8 2025. The depth of the nanocracks and the height of the nanochannel molds also increase with the concentation of sovents. As mentioned above, the solvents in the photoresist would swell the polystyrene surface again and further release the residual stress in the swollen layer. As a result, in order to replicate nanochannel molds from the nanocracks on

polystyrene surfaces with a smaller size change and a smaller surface roughness, SU8 2150 is the optimal choice.

3.3.3.2 Effects of spin-coating time

The solvents in the SU8 photoresists affect not only the size of the nanochannel molds but also the uniformity of the nanochannel molds. A photoresist with a lower viscosity contributes to a better fluidity and makes the filling of the photoresist into nanocracks easier. For the reason discussed above, to replicate nanocracks with a smaller size change, SU8 2150 with a lower concentration of solvents is essential. However, the viscosity of SU8 2150 photoresist is high, it is difficult for SU8 2150 to flow into the nanocracks in a short time; as a result, one has to control the filling time of the SU8 2150 photoresist effectively.

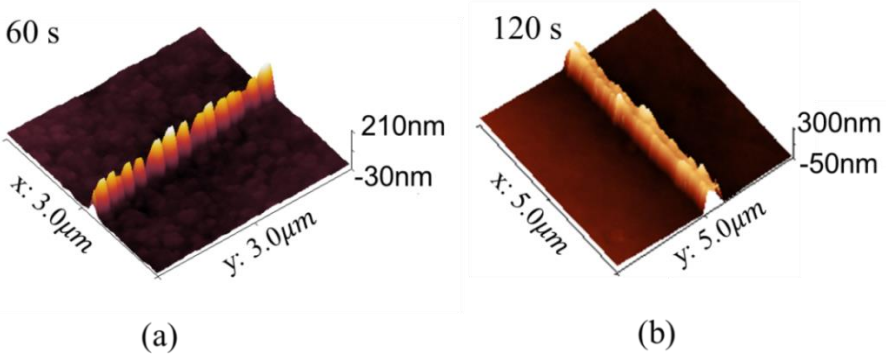

Figure 3-17 3D AFM images of nanochannel molds replicated by using SU8 2150 with a spin-coating time of (a) 60 s and (b) 120 s.

Nanochannel molds replicated by using SU8 2150 with different spin-coating time (the samples are exposed to UV light immediately after the spin-coating time) from 30 s to 120 s were examined by using the AFM. The results show that nanochannels replicated by a short spin-coating time are not consistent, i.e., the size and the shape of such a channel vary along the length direction of the channel. On the contrary, nanochannels made by a longer spin-coating time are uniform in the length direction. For instance, Figure 3-17 (a) shows a nanochannel mold replicated by 60s spin-coating time. It is obvious that the channel mold has a zigzag-shaped profile along the length direction due to the failure of filling SU8 material into the nanocrack. By contrast, the quality of nanochannel mold replicated by 120 s spin-coating time is much better, because SU8 2150 has enough time to flow into the nanocrack within such a long period of time, as shown in Figure 3-17 (b). To replicate high-quality nanochannels with smaller size change, one has to balance the spin-coating time and the

concentration of solvents in the SU8 photoresist. After extensive experimental investigations, a spin-coating time of 120s is recommended when SU8 2150 photoresist is applied.

3.3.3.3 Effects of UV exposure dose

UV light is applied to crosslink SU8 photoresist layers and to make the nanochannel molds stable. In this part, SU8 2150 was used to study the effects of UV exposure dose on the nanochannel mold replication. The thickness of the photoresist layers and the spinning coating time were about 200μm and 120 s, respectively. UV exposure dose ranging from 300mJ/cm^2 to 2700 mJ/cm^2 was studied. For a 200 μm thick photoresist layer, the standard exposure dose is around 330 mJ/cm^2 according to the SU8 photoresist manual [212].

The results show that for the underexposure cases (less than 330 mJ/cm^2), the photoresist layers are not fully cross-linked, and the photoresist layers are soft and sticky, one has to wait for several minutes before the photoresist molds are strong enough for peeling off. Therefore, the final channel mold surfaces are rough and the channel mold sizes are large due to further swelling of the polystyrene surfaces (with nanocracks). Figure 3-18 (a) is an example of the underexposure case (300 mJ/cm^2) where the mold was peeled off too early. It is clear that the nanochannel breaks and leaves some parts in the nanocrack during the peeling off process. Figure 3-18 (b) shows a nanochannel mold replicated also under the condition of underexposure (300 mJ/cm^2) with a longer peeling off time, the channel mold is intact, but the channel size is much larger (due to the further swelling of the nanocrack). In contrast, an overexposure of UV dose (larger than 1200 mJ/cm^2) is able to minimize the swelling problem. However, an overexposure UV energy level gives rise to over cross-linked photoresist layers. As a result, the channel molds become brittle and very easy to break during the peeling off process. Figure 3-18 (c) shows an example of a nanochannel mold replicated on SU8 2150 photoresist layer with an overexposure UV energy of 2700 mJ/cm^2. It is obvious that some parts of the SU8 nanochannel, in this case, are broken. Under the condition of a proper UV dose, the channel mold is strong and intact, as shown in Figure 3-17 (b). Based on the extensive experimental studies, we found that to make durable and intact nanochannel molds of 200μm thick by using SU8 2150 photoresist, a proper exposure UV dose should be around 800 mJ/cm^2.

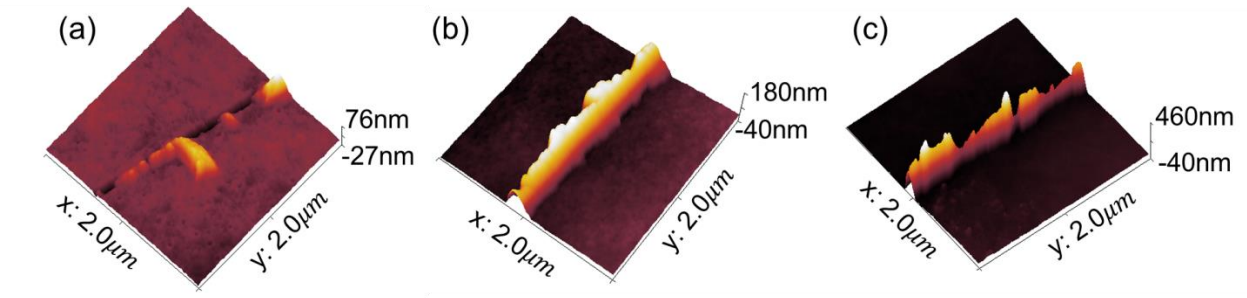

Figure 3-18 AFM images of nanochannel molds: (a) A broken SU8 mold during peeling off due to underexposure of UV light and insufficient evaporation time. (b) An example of nanochannel mold replicated by SU8 2150 with an underexposure energy of 300 mJ/cm; (c) A nanochannel mold replicated by SU8 2150 photoresist with an overexposure UV energy of 2700 mJ/cm^2.

3.3.3.4 Thickness of the photoresist layer

The thickness of SU8 photoresist layers also affects the size and the quality of the replicated nanochannel molds. To examine this factor, a series of photoresist layers from 80 μm to 650 μm obtained by spin-coating SU8 2150 at different spin coating speed ranging from 1000 rpm to 8000 rpm for 120 seconds were used to replicate nanochannel molds. To minimize the time of solidification, all the samples were overexposed to UV light for 40 s (1200 mJ/cm^2).

Figure 3-19 (a) compares the size of nanochannels replicated with different thicknesses of SU8 photoresist layers. The original nanocracks were fabricated under the same condition with an average size of 15.6 nm in width and 47.7 nm in depth. Figure 3-19 (a) shows the channel mold size after duplication as a function of the spin-coating speed. From Figure 3-19 (a), one can see that both the width and the height of the nanochannel molds decrease with increasing spin-coating speed. For example, when the spin-coating speed is 1000 rpm, the thickness of the SU8 layer is about 650 μm and the corresponding channel size is about 2208 nm in width and 2388 nm in height. When the spin-coating speed increases to 8000 rpm, the thickness of the SU8 layer is only about 80 μm and the channel size is approximately 541 nm in width and 134 nm in height, which is much smaller than that of the 1000 rpm case. The channel mold size decreases with the thickness of the SU8 layer, because, on one hand, a thicker SU8 layer would generate more heat during the cross-linking process, which will reheat the nanocrack and trigger a larger crack size; on the other hand, a thicker layer of SU8 photoresist contains more solvents, making the time of evaporation longer; consequently, the solvents would further swell the polystyrene surface and lead to a larger crack size. Figure 3-19 (b) shows 3D images of the nanochannel molds replicated under different spin-coating speeds. It is

obvious that the size of the channels decreases with the increasing spin-coating speed. In addition, the uniformity of the channel molds improves with the spin-coating speed. Consequently, for SU8 2150 photoresist, the higher the spin-coating speed the higher the nanochannel mold quality.

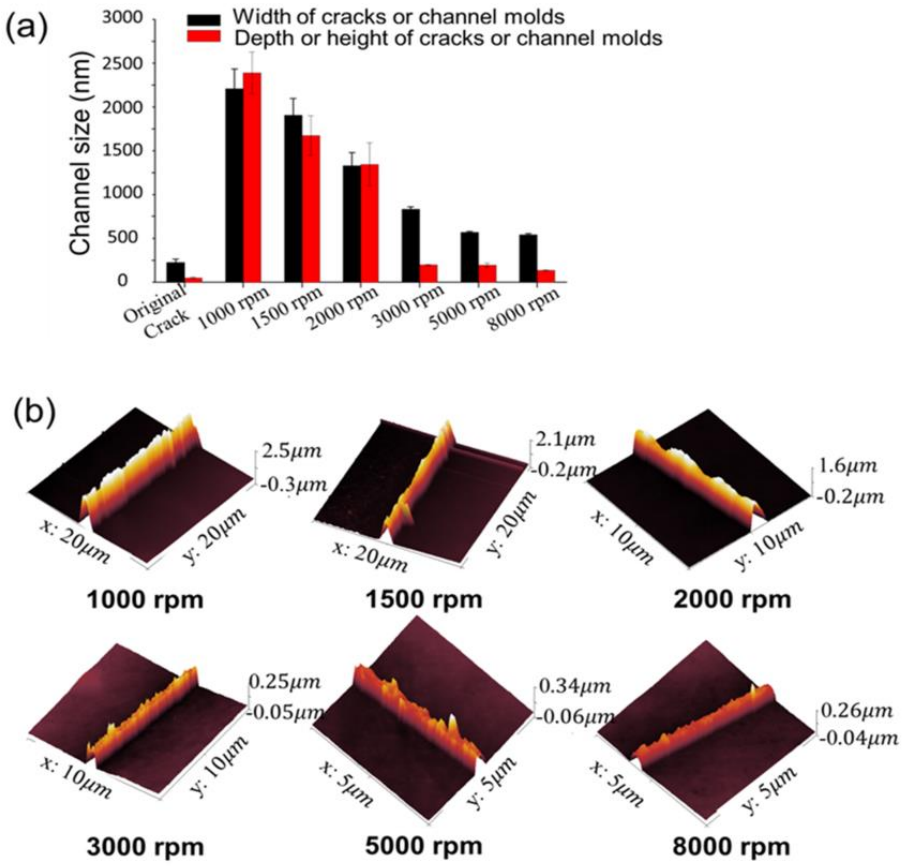

Figure 3-19 (a) Size of nanochannels replicated from nanocracks with an average size of 215.6 nm in width and 47.4 nm in depth for different spin-coating speeds ranging from 1000 rpm to 8000 rpm. (b) 3D images of nanochannels replicated at different spin-coating speeds, 1000 rpm, 1500 rpm, 2000 rpm, 3000 rpm, 5000 rpm and 8000 rpm, and the corresponding channel sizes are 2208 ×2388 nm, 1860×1692 nm, 1320 ×1331 nm, 802 ×173 nm, 562 ×164nm and 541 ×134 nm, respectively.

3.3.4 Fabrication of nanochannel molds by Method B: NIL by Smooth cast

3.3.4.1 Effects of the type of smooth cast

Three kinds of smooth cast materials, i.e., smooth cast 300, smooth cast 305 and TASK 4 were used to replicate nanocracks. Smooth cast 300 can cure in 10 minutes at room temperature and generate a large amount of heat, which increases the size of the nanocracks significantly. It is also hard to control the replication process precisely due to the fast curing process. TASK 4 has a higher

concentration of solvents and a lower viscosity, and TASK 4 can replicate the finest details; however, the high concentration of solvents will further swell the polystyrene surfaces and enlarge the unstable cracks. Compared with Smooth cast 300 and TASK 4, Smooth cast 305 has a moderate curing time and moderate solvent contents and is suitable for nanocrack replication.

To improve the fidelity of the nanoimprint technique by using Smooth cast 305, one needs to handle at least four parameters. The first one is the pre-curing time, which denotes the period of time from the mixing of part A and part B of smooth cast 305 to the start of the nanocrack imprint. After the pre-curing time, the rubber-like smooth cast layer is attached to a polystyrene surface with nanocracks. The applied pressure and the pressurized time are critical parameters during the nanoimprint. The last parameter is the peeling off time, which is the time from the moment of mixing of part A and part B of the smooth cast to the moment of peeling off of the smooth cast layer from the polystyrene surface. Peeling off time dominates integrity of nanochannel molds.

3.3.4.2 Pre-curing time

Pre-curing time affects the nanoimprint process in three aspects. Firstly, pre-curing time determines the fluidity of the smooth cast layer. The longer the pre-curing time, the harder the material will be, and a larger pressure has to be applied on the smooth cast material during the imprint in order to obtain nanochannels identical to the nanocracks. Secondly, the pre-curing time controls the solvent content of the smooth cast layer, which affects the swelling level of the polystyrene surface during replication. The longer the pre-curing time, the lower concentration of solvents in the smooth cast layer and the lower swelling effects will be. Lastly, the pre-curing time decides the temperature of the smooth cast layer. The heat generated in the smooth cast layer due to chemical reactions and crosslinking of molecules will provide more energy to the nanocracks and results in a larger channel size. As the pre-curing time becomes longer, the smooth cast cools down, and the temperature effect is minimized.

During the experiments, a pre-curing time from 17 min, 20 min, 23 min, 25 min, 27 min, 30 min, 35 min to 40 min was tested to replicate nanocracks of about 300 nm in width and 60 nm in depth. For all the cases, the peeling-off time was 60 min and the pressurized time was 60 s. The pressure values were different for different cases due to the fluidity of the smooth cast layers. Specifically, for the 17 min and 20 min cases, no pressure was applied, because the pre-curing smooth cast layers were too soft; for the 23 min and 25 min cases, only 0.5 MPa was applied. The pressure applied to

the 27 min case was 5 MPa, and for the other cases with longer pre-curing time, the pressure value was 10 MPa.

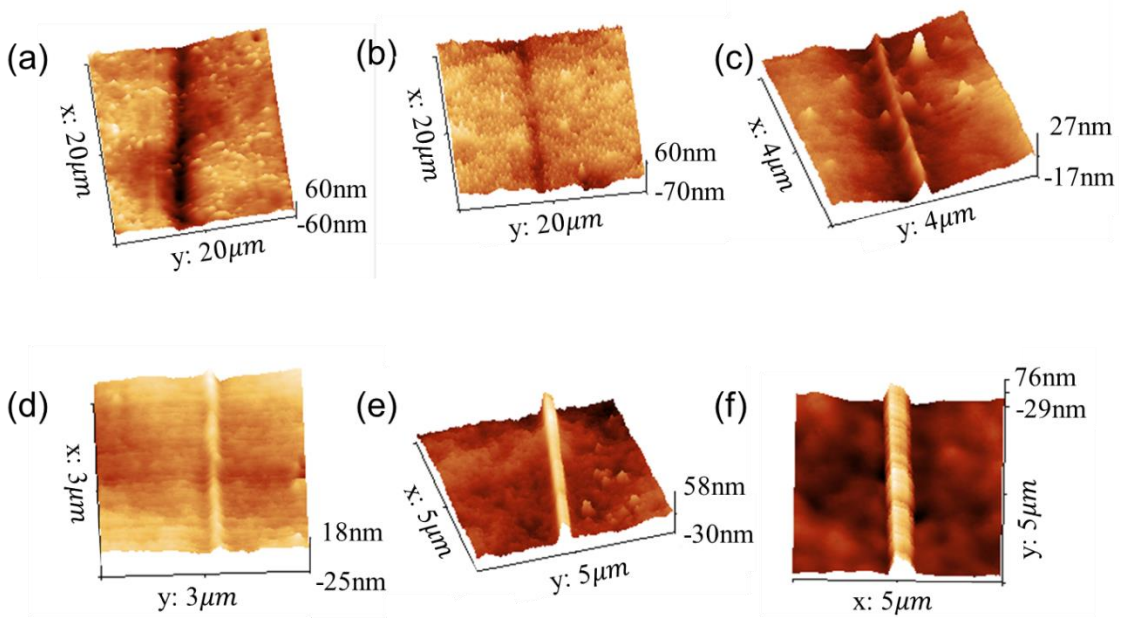

Figure 3-20 AFM 3D images of nanochannel molds replicated with different pre-curing time; (a) 17 min, (b) 20 min, (c) 23 min, (d) 25 min, (e) 27 min, (f) 30 min. For all the cases, the peeling off time is 60 min. The original nanocrack size is about 300 nm wide and 60 nm deep.

The results show that when the pre-curing time is shorter than 23 min, the surfaces of the smooth cast layers are wet and soft; as a result, the solvents in the smooth cast layer destroys the nanocracks easily. However, as the pre-curing time becomes too long, the smooth cast layers are dry and hard, therefore, a high pressure is needed during the nanoimprint, which also triggers further cracking of the nanocracks. Figure 3-20 shows examples of nanochannels replicated by using a pre-curing time from 17 min to 30 min. It is obvious that a longer pre-curing time contributes to a better channel mold quality. However, as the pre-curing time becomes too long (longer than 30 min), the smooth cast layer becomes too hard, and a higher pressure is needed, which deforms or breaks the polystyrene nanocracks. Based on a large number of tests conducted in this study, a recommended pre-curing time for smooth cast 305 is around 25~30 min, under the condition of room temperature of 23℃. A higher room temperature would speed up the crosslinking process of the smooth cast and give rise to a shorter pre-curing time.

3.3.4.3 Effects of pressure

Pressure is an essential parameter for the nanoimprint. If the pressure is too high, the nanocracks on polystyrene surfaces are likely to deform or break up, and the size of the nanocracks becomes larger. On the other hand, if the pressure is too low, the smooth cast material cannot flow into the nanocracks and fully fill the nanocracks; consequently, the channel molds may be shallower than the original nanocracks, or even no positive nanochannels can be produced at all. To study the pressure effects, nanocracks with an average size of 300 nm in width and 60 nm in depth on polystyrene surfaces were replicated onto smooth cast layers with pressure values ranging from 0.25 MPa to 5 MPa. For all these cases, the pre-curing time was 25 min and the pressurized time was 30 s with a peeling off time of 60 min. Figure 3-21 shows the size and 3D images of the nanochannel molds.

From Figure 3-21 (a), one can see that the width of these channel molds is almost constant when the pressure is lower than 2 MPa, about 300 nm, which is similar to that of the original nanocracks, because the nanocracks on polystyrene surfaces are relatively stable (i.e., no further cracking is induced) when a low pressure is applied. However, for the higher pressure values, 2.5 MPa and 3 MPa, the width of these channel molds increases dramatically due to further cracking of the nanocracks. In the experimental investigations, a pressure as high as 5 MPa was also tested; however, it was found that a lot of new fractures were generated on the polystyrene surfaces under such a high pressure. Figure 3-21 (b) shows that the height of the channel molds is about 24 nm when the pressure is 0.25 MPa, and this value increases to 30 nm as the pressure increases to 0.5 MPa. This is because the cracks are partly filled with the smooth cast material when the pressure is lower than 0.5 MPa. When the pressure increases from 0.75 MPa to 1.5 MPa, the height of the channels reaches about 60 nm due to fully filling of the smooth cast material in the nanocracks. However, as the pressure is higher than 2 MPa, both the width and height of the channel molds increase dramatically due to further cracking of the nanocracks as mentioned above. For example, for the 2 MPa and 2.5 MPa cases, the channel molds become 280 nm wide and 370 nm high, and 414 nm wide and 354 nm high, respectively, which are much larger than the original crack size. Figure 3-21 (c) demonstrates 3D images of these positive nanochannels with detail. From these results, one can conclude that the optimal pressure value for the nanoimprint by smooth cast 305 is around 0.5~1.5 MPa under the condition of 25 min pre-curing time.

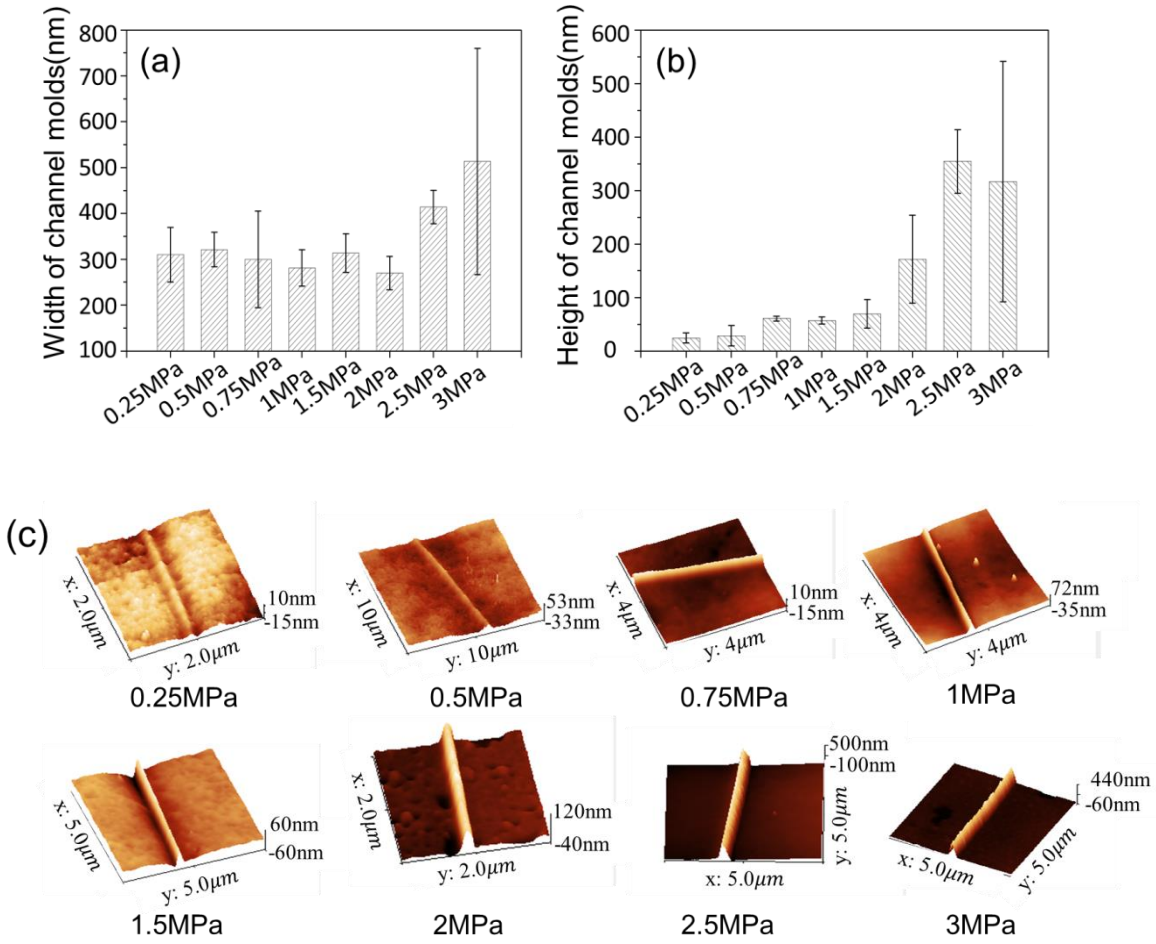

Figure 3-21 Nanochannels replicated by Smooth cast 305 with different pressure applied from 0.25 MPa to 3 MPa. (a) The width of the nanochannel molds and (b) The height of the nanochannel molds. (c) 3D images of nanochannels replicated under different pressures.

3.3.4.4 Pressurized time

The pressurized time and the pressure are critical to the filling of the Smooth cast in the nanocracks during replication. Pressurized time from 5s to 10 min was studied. The original nanocracks were about 300 nm wide and 60 nm deep. In all the cases, the pre-curing time was 25 min, the pressure applied was 1 MPa, and the peeling off time was 60 min.

Experimental results show that the width of the channel molds changes by very little when the pressurized time increases from 5 s to 5 min. However, the depth of the channels increases with the increasing pressurized time, from about 20 nm to nearly 50 nm when the pressurized time increases from 40 s to 1 min. A longer pressurized time allows more material flowing into the nanocracks.

When the pressurized time is longer than 3 min, a higher chance of further cracking will take place; and for the extreme case of 10 min pressurized time, no positive channel was found on the smooth cast surface. This is because when the pressurized time is too long, the smooth cast material inside the nanocrack is deeply cross-linked and becomes brittle, and the shear force applied in the peeling off process would break the positive channels, leaving the cross-linked material inside the nanocracks. On the other hand, a pressurized time shorter than 15 s would result in a higher degree of surface roughness and a lower success ratio of replication. Figure 3-22 shows 3D images of nanochannels replicated with (a) 10 s, (b) 1 min and (c) 5 min pressurized time, respectively. It is obvious that the nanochannel mold replicated with 10 s pressurized time is not so smooth, and the channel mold replicated with 1 min pressurized time is much better than that of the 10 s case. For the 5 min case, the channel mold is not straight due to detaching action of the smooth cast layer with the crack during the solidifying process. A suitable pressurized time for smooth cast 305 should be around 1 min when the pre-curing time is 25 min and the pressure value is 1MPa.

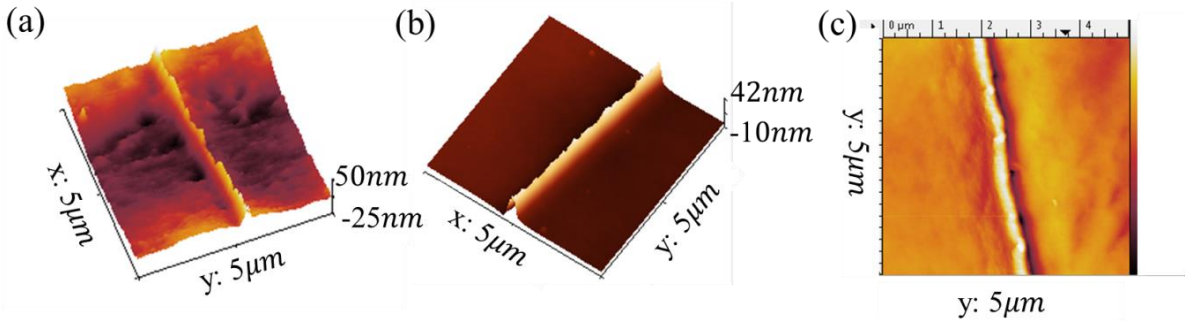

Figure 3-22 Images of nanochannels replicated by Smooth cast 305 with a different pressurized time of (a) 10 s, (b) 1 min and (c) 5min. For all the cases, the pre-curing time is 25 min, the pressure is 1 MPa and the peeling off time is 60 min.

3.3.4.5 Peeling off time

The peeling off time is also an important parameter for the nanoimprint in the smooth cast-polystyrene system. Peeling off earlier can minimize the contacting time between the smooth cast layers and the nanocracks and reduce the swelling of the polystyrene surfaces; however, the smooth cast material squeezed in the nanocracks would be still soft and sticky, consequently, the channel molds are likely to be deformed or broken during the peeling off process.

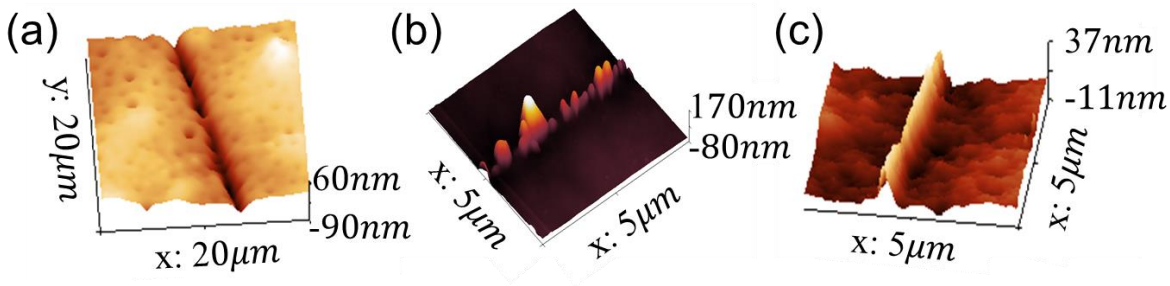

Figure 3-23 Examples of nanochannel molds replicated by Smooth cast 305 with different peeling off time. (a) 25 min, (b) 40 min, (c) 100 min. For all the cases, the pre-curing time is 25 min, the pressure is 1MPa and the pressurized time is 60 s.

Peeling off time from 35 min to 100 min was studied experimentally. In the experiments, the pre-curing time was 25 min and the pressure value was 1 MPa with the pressurized time of 1 min. Figure 3-23 (a) and Figure 3-23 (b) show examples of nanochannels replicated by peeling off too early with peeling off time of 25 min and 40 min, respectively. It is clear that the channel mold becomes negative (should be positive) in Figure 3-23 (a) and zigzag-like in Figure 3-23 (b) due to the failure of peeling off. On the other hand, when the peeling off time is too long, the contacting time between the smooth cast and the polystyrene surface becomes longer, which would enhance the swelling of the polystyrene surface. As shown in Figure 3-23 (c), in this case, the peeling off time is 100 min and the channel mold surface is much rougher than that in Figure 3-22 (b) in which the peeling off time is 60min. Based on the results of the extensive experimental investigation, a proper peeling off time is recommended as 60min.

3.3.4.6 Fabrication of nanochannel molds with optimal parameters

Based on the experiments demonstrated above, high-quality nanochannel molds replicated by using smooth cast 305 can be obtained by the following working procedures. Firstly, 1 g part A and 0.9 g part B of smooth cast 305 is well mixed in a petri dish and degassed in a vacuum oven for 5 min. Then, the smooth cast layer is peeled off from the petri dish and attached to a nanocrack sample surface with a pre-curing time of 25~30 min. Thirdly, the smooth cast-polystyrene system is sandwiched by a pressure gauge with about 1 MPa pressure applied for 1 min. After the pressure is released, the smooth cast layer is peeled off from the polystyrene surface at 60 min counting from the mixing of part A and part B. Figure 3-24 shows (a) a 3D view of a nanochannel mold and (b) profiles of different cross-sections of this nanochannel mold. It is clear that the mold surface is smooth and the channel size is also uniform along the length direction (see Figure 3-24 (b)), about 350 nm wide

and 80 nm high, which is slightly larger than the original nanocrack, about 300 nm wide and 60 nm deep. Fine adjustment of the operating parameters can further improve the fidelity of the mold to the original nanocrack.

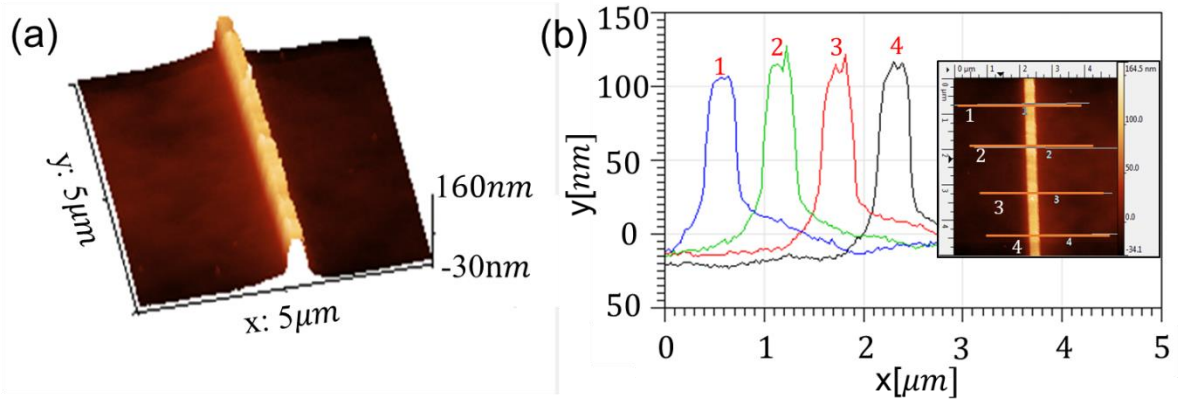

Figure 3-24 A nanochannel mold replicated on a Smooth cast layer by the optimal parameters. (a) A 3D image of the nanochannel mold, (b) Profiles of different cross-sections along the nanochannel.

3.3.5 Comparison of method A and method B

Overall, both SU8 and smooth cast can be used to replicate nanocracks from polystyrene surfaces. Figure 3-25 compares positive nanochannel molds replicated by smooth cast 305 and SU8 2150 from nanocracks of similar size, about 570 nm in width and 160 nm in depth. Figure 3-25 (a) is the nanochannel mold replicated by SU8 2150, the nanochannel is $1021 \pm 31nm$ in width and 362 ± 18 nm in height (as shown in Figure 3-25 (b)). Figure 3-25 (c) shows the nanochannel mold replicated by Smooth cast, the channel size is 616 ± 15 nm in width and 232 ± 9nm in height (Figure 3-25 (d)). One can see that the nanochannel mold replicated by smooth cast has a smaller size and a smoother surface compared with that replicated by SU8 2150 photoresist owing to the higher solvent concentration in the SU8 2150. A higher concentration of solvent would further swell and dissolve the nanocracks on the polystyrene surface and give rise to a larger replicated channel size. Table 3-3 summarizes the optimal working parameters for both methods and evaluates both methods by comparing the facilities, cost, durability, channel quality and so on. From Table 3-3 one can see that the major advantage of using SU8 is the significantly short processing time, and the disadvantage is that the replicated channel size is much larger than the size of the original nanocrack. While using the smooth cast method, the processes take much longer time than those of the SU8 method; however, the replicated channel size is similar to the size of the original nanocrack.

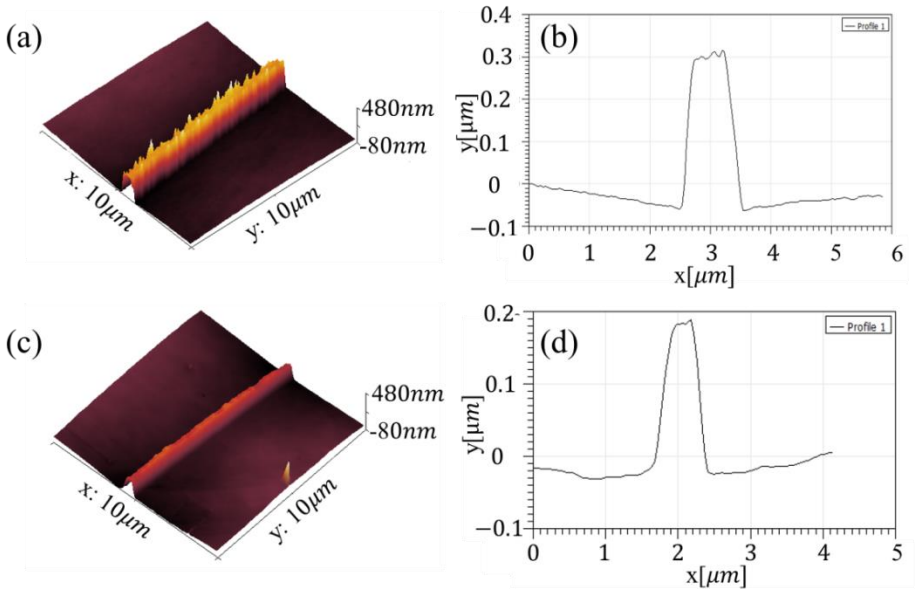

Figure 3-25 Comparison of positive nanochannel molds replicated by using smooth cast 305 and SU8 2150 from nanocracks of similar size, 570 nm in width and 160 nm in depth. (a) Nanochannel mold replicated by SU8 2150, the channel size is 1021±31nm in width and 362±18 nm in height. (b) A cross-section of the nanochannel in (a). (c) Nanochannel mold replicated by smooth cast 305, the channel size is 616±15 nm in width and 232±9nm in height. (d) A cross-section of the nanochannel in (c)

Table 3-3 Summary and evaluation of SU8 method and Smooth cast method.

	SU8	**Smooth cast**
Optimal working parameters	Photoresist type: SU8 2150 Photoresist layer: 80μm @8000rpm Coating time: 120s UV exposure dose: 600~1500 mJ/cm^2	Smooth cast type: Smooth cast 305 Pre-curing time: 25~27 min Pressure: 1 MPa Pressurized time: 1~3 min Peeling off time: 60 min
Facilities	Spin-coater, UV exposure machine,	Micro-hardness testing system, pressure gauge, vacuum oven
Materials	SU8 2150, PMMA slab	Smooth cast 305
Time cost	5~10 min	60~100 min
Price	Medium	Very low
Channel quality	Channel size is generally much larger than that of the original cracks. The roughness of the channel mold surfaces is about 5 nm.	Channel size is generally larger than that of the original cracks by 10% ~ 20%. Surface roughness is about 2~3 nm, similar to that of the original polystyrene surface.

3.3.6 Fabrication of PDMS nanochannels

3.3.6.1 The durability of nanochannel molds

PDMS nanochannels can be made from these nanochannel molds by following the procedures of fabricating bi-layer PDMS nanochannels described in the previous section. However, durable nanochannel molds are crucial for fabrication of sealed PDMS nanochannel chips with high repeatability. The durability of both SU8 photoresist nanochannel molds and smooth cast nanochannel molds were studied by duplicating bi-layer PDMS nanochannels from each mold for at least 6 times. Figure 3-26 (a) shows the average sizes of PDMS nanochannels replicated from a single SU8 nanochannel mold for 6 times, and Figure 3-26 (b) shows a 3D image of a PDMS nanochannel replicated from the SU8 nanochannel mold and a cross-section profile of this channel. Clearly, all the channels are about 715 nm wide and 90 nm deep, with 1.5% and 11% deviation in the width and depth directions, respectively. Figure 3-26 (c) shows that the sizes of PDMS channels replicated from one smooth cast nanochannel mold for 7 times; all these channels are about 220 nm wide and 40 nm deep, with 12% and 9.5% deviation in the width and depth directions, respectively. Figure 3-26 (d) shows an AFM 3D image of the PDMS nanochannel replicated from the nanochannel mold duplicated by the smooth cast and a cross-section profile of this channel. In conclusion, both smooth cast nanochannel molds and SU8 photoresist nanochannel molds are sufficiently durable for replicating of PDMS nanochannels with little size change.

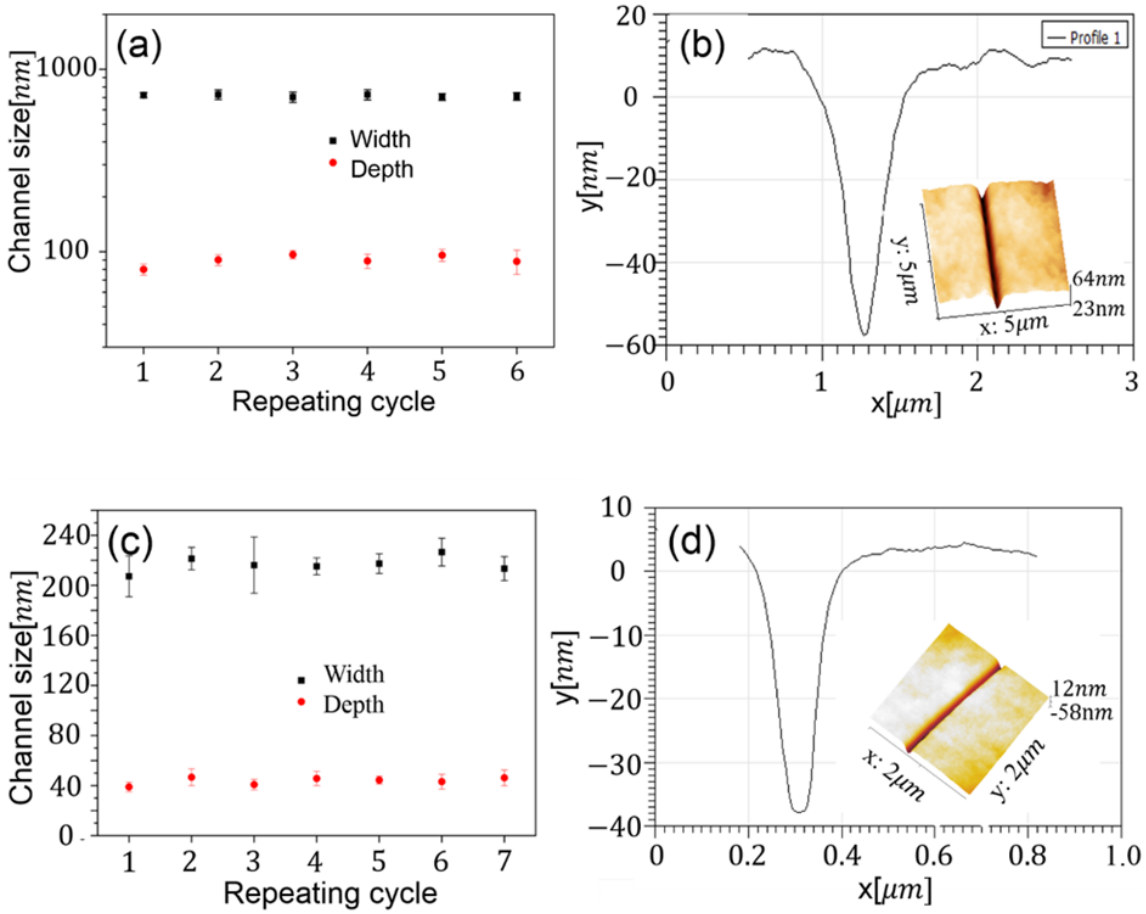

Figure 3-26 (a) Size of PDMS nanochannels replicated from a SU8 single nanochannel mold for 6 times. (b) 3D view of a PDMS nanochannel replicated from the nanochannel mold and a cross-section profile of this nanochannel, about 715nm wide and 90 nm deep.(c) Size of nanochannels replicated from a smooth cast nanochannel mold for 7 times. (d) 3D view of a nanochannel replicated from the nanochannel mold made of smooth cast and a cross-section profile of this channel, about 220 nm wide and 40 nm deep.

3.3.6.2 Fabrication of smaller PDMS nanochannels

As mentioned above, the Smooth cast material works better in smaller nanocrack replication compared with photoresist. Figure 3-27 shows AFM images and profiles of a smaller PDMS nanochannel fabricated by using a smooth cast nanochannel mold. Figure 3-27 (a) is an original nanocrack on a polystyrene surface with a size of approximately $95\pm10\ nm$ in width and $35\pm4\ nm$ in depth. Figure 3-27 (b) is a positive nanochannel on smooth cast replicated from this nanocrack (a), and the channel size is $104\pm12\ nm$ in width and $43\pm5\ nm$ in height. Figure 3-27 (c) is a PDMS nanochannel replicated from this nanochannel mold (b); the nanochannel size is approximately

106±10 *nm* in width and 40±7nm in depth. The nanocrack on the polystyrene surface was created by heating 1 mL 90% ethanol at 85℃ for 3.5 hours. The defect on the polystyrene surface was marked by the indenter tip with an applied force of 50gF. The smooth cast nanochannel mold was fabricated with the following operating parameters: a pre-curing time of 27 min and a pressure of 1 MPa with a pressurized time of 1 min, and a peeling off time of 60 min. The smooth cast method is able to produce smaller nanochannels. For example, Figure 3-28 shows (a) a 3D view of a smaller PDMS nanochannel replicated from a smooth cast nanochannel mold and (b) a cross section profile of this nanochannel of approximately 60 nm in width and 20 nm in depth.

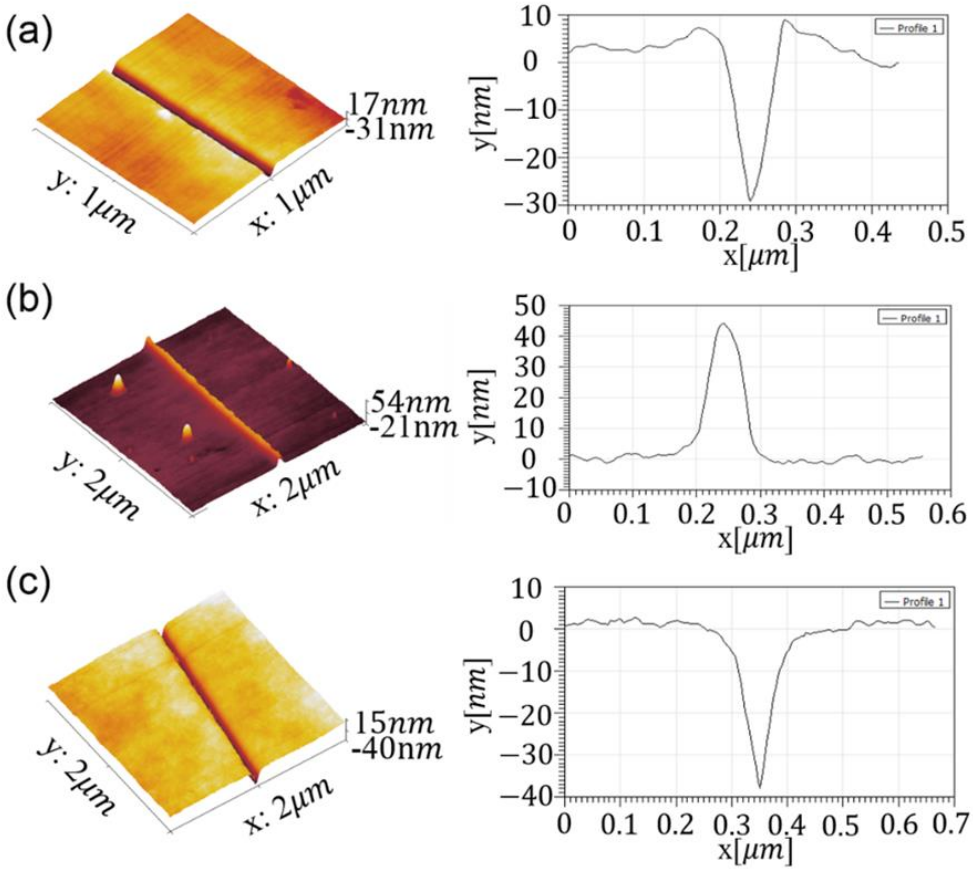

Figure 3-27 Fabrication of a smaller PDMS nanochannel. (a) A negative nanocrack on polystyrene surface (95±10 nm wide and 35±4 nm deep),(b) A positive nanochannel mold on smooth cast (104±12 nm wide and 43±5 nm high) replicated from (a), (c) A negative nanochannel on PDMS (106±10 nm wide and 40±7nm deep) replicated from the smooth cast channel mold (b).

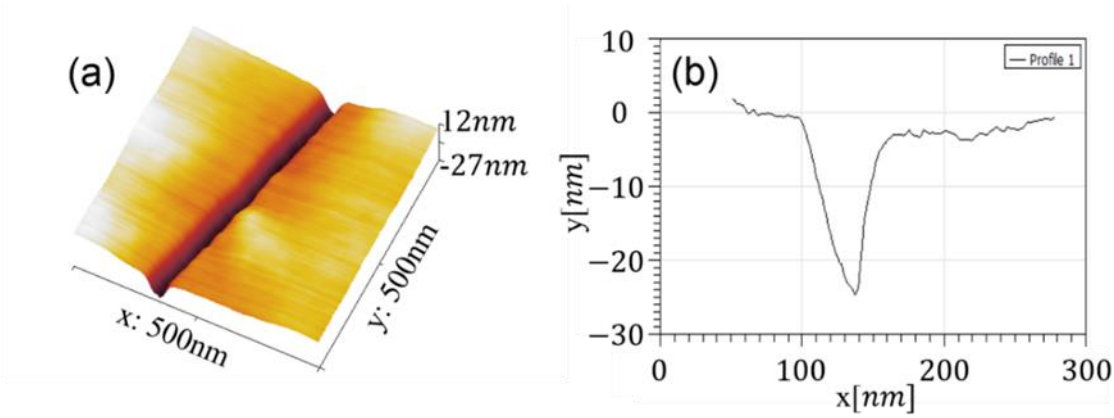

Figure 3-28 (a) A 3D image of a smaller PDMS nanochannel of 60±8nm in width and 20±6 nm in depth replicated from a nanochannel mold made of Smooth cast and (b) a cross-section profile of this nanochannel.

3.3.7 Chip alignment and bonding

X-PDMS and h-PDMS have similar properties of regular PDMS and can form sealed chips by plasma bonding. First, a bi-layer PDMS nanochannel slab and a bi-layer PDMS microchannel slab are prepared. Four wells are punched on the microchannel slab to work as sample reservoirs. Afterward, the two slabs are placed in the plasma cleaner chamber and treated with plasma for 30 s. After the treatment, the surfaces can be bonded together by using the homemade alignment system (Figure 3-3). Figure 3-29 shows (a) a nanofluidic chip with single nanochannel after bonding and (b) a nanofluidic chip with parallel nanochannels after bonding. Figure 3-29 (c) is an example of the final nanofluidic chip. Figure 3-29 (d) shows a cross-section of the bi-layer PDMS nanochannel after bonding and Figure 3-29 (e) is a zoomed-in view of this nanochannel cross-section measured by the AFM. To make sure these nanochannels are open after bonding, these nanochannels were filled with an electrolyte solution. An electric field was applied along the channels and the electrical current inside the nanochannel was monitored by an electrometer. The results show that PDMS nanochannels as small as 20 nm deep were still open after bonding.

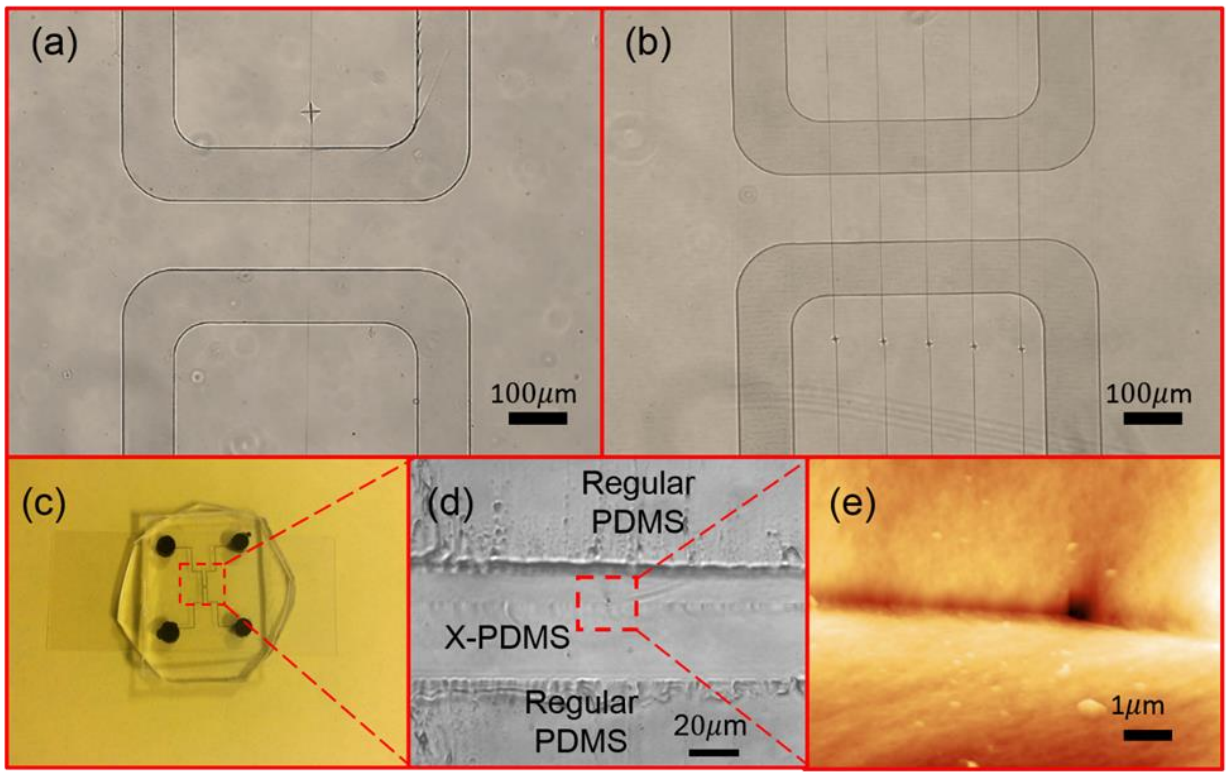

Figure 3-29 Nanofluidic chip after bonding. (a) A PDMS nanofluidic chip with single nanochannel; (b) A PDMS nanofluidic chip with parallel nanochannels; (c) An example of final PDMS nanofluidic chip; (d) A cross-section of the bi-layer PDMS nanochannel; (e) A Zoomed-in view of the cross section measured by the AFM.

3.4 Conclusion

This chapter presents a novel method to fabricate PDMS nanofluidic chips with single nanochannels or multiple nanochannels of controllable channel size and spacing. Long nanochannels of sub-100 nm in width and depth can be obtained by this method. Artificial defects marked on polystyrene surfaces by a hardness testing indenter are used to position nanocracks created by the solvent-induced cracking method. To fully understand the solvent-induced cracking method, a systematic experimental study is performed to investigate the formation of nanocracks on polystyrene surfaces. The solubility parameter and the diffusion coefficient were taken into account. The size of cracks increases with heating temperature, heating time, volume and concentration of alcohol solutions. Nanocracks are replicated onto either SU8 photoresist layers or smooth cast layers by nanoimprint technique to work as nanochannel molds. Based on the extensive experimental investigations, two sets of optimal working parameters for both the SU8 and the smooth cast methods

are developed. X-PDMS or h-PDMS supported by regular PDMS is used to replicate nanochannels from the channel molds to avoid the collapse of channel roofs during device bonding. Nanochannel-based nanofluidic devices are obtained by bonding a PDMS nanochannel slab onto a PDMS microchannel slab. The method described in this chapter provides an effective tool for fabricating disposable and inexpensive PDMS nanofluidic devices with single or multiple nanochannels with high reliability. The method of fabricating nanofluidic devices as developed in this chapter can be applied in almost every lab and greatly facilitates fundamental studies of transport phenomena at the nanoscale and enable further development of nanofluidic-based applications[*].

[*] Experimental results of additional electrical current and overlimting current behavoir in single nanochannels can be found in Appendix B.

CHAPTER 4 Fundamental Research I: Electroosmotic Flow in Single PDMS Nanochannels*

4.1 Introduction

Electroosmotic flow (EOF) describes the electrokinetically driven liquid motion due to the existence of electric double layer (EDL). EOF in microchannels plays an important role in microfluidics and has been studied comprehensively. In microchannels, the thickness of EDL is generally negligible in comparison with the channel size, as mentioned in CHAPTER 2. However, as the dimensions of nanochannels are comparable to the thickness of EDL, EDLs get overlapped and consequently many new transport phenomena such as current rectification [213–216], ion enrichment and depletion [217], new dynamics of pressure driven flow [218–220] have been discovered. These new transport phenomena facilitate various novel applications and studies of the nanofluidics [221–224]. Theoretically, in nanochannels with overlapped EDLs, traditional P-B equation and H-S equation used in the microchannel systems are not applicable anymore [4]. For the case of extremely small nanochannels, even the continuum hypothesis can hardly survive when the channel size is in the order of the interaction length (or free path) of the fluid molecules [224].

Analytical and Numerical Studies. Over the past few decades, a series of analytical and numerical models have been developed to study the effects of overlap of EDLs [223,225–231], ionic size [232], ionic valence [233,234], viscosity [235,236] and pH value [237,238] of the solutions, surface roughness [239,240] and surface charge density [4,227,241–243] of channel walls, as well as channel size [4,244] on the electroosmotic flow in nanochannels. Qu and Li [225] derived an overlapped EDL model to calculate electrical potential and ion distribution in the diffuse layer based on the Debye-Huckel approximation. Baldessari [230,245] also set a new model to predict electric potential distribution in overlapped EDLs with the consideration of ion mobility and pH of the solution. In recent years, molecular dynamics (MD) method combining with continuum theory has also been used to simulate ion distributions in EDLs and EOF in nanochannels, finding that ion size of the solvent strongly affects the ion distribution near the channel surfaces [244]. Qiao [235] argued that the electroosmotic mobility in nanochannels increases with the surface charge of the channel surfaces, however, the speed is slower than that predicted by the continuum theory due to the increased viscosity in the interfacial layer. Liu

* A similar version of this chapter was published as:
Peng, R.; Li, D. Electroosmotic Flow in Single PDMS Nanochannels. Nanoscale 2016, 12237–12246.
http://pubs.rsc.org/-/content/articlehtml/2016/nr/c6nr02937j .

and Sofos [239,240] studied the channel roughness effects upon the EOF in nanochannels numerically, showing that even a small roughness value can reduce the EOF velocity dramatically and give rise to a non-Newtonian behavior of the fluid. Pennathur and Santiago [234,246] studied EOF and ion transport in nanochannels theoretically, proved that when the thickness of the EDL is comparable to the channel size, the electroosmotic flow velocity profile in the nanochannel is nonuniform, and a decrement of EOF velocity occurs when EDLs get overlapped. Bhattacharyya [229] investigated EOF in nanochannels in which the channel height and channel width are all on the order of the thickness of EDL and predicted that the Debye-length is not a good parameter to estimate the actual thickness of EDL. Modeling and simulation of ionic currents in 3D nanomembrane connected with microchannels were performed by Chatterjee et al [247], showing that electrokinetic flow in a hybrid micro-nanofluidic system is dependent on the capacitance of the nanomembrane and the surface charge of the nanoarrays. Movahed and Li [4] presented a 3-D model of EOF in nanochannels, showing that flow field, electrical field and ionic concentration field in nanochannels are all dependent on the channel size.

Experimental Studies. Experimental results of mass transfer in nanochannels are very limited. Stein [248] explored ion transport in silica nanochannels of 70 nm in height and $50\mu m$ in width. Their work found that the conductance of the nanochannels saturates at the dilute limit, and the conductance of the nanochannels is independent of the ion concentration. Ion transport properties in nanochannels are dominated by the surface charge. Ion transport in nanochannels of 2 nm deep was conducted by Duan and Majumdar [249], it was also found that ion transport is dominated by the surface charge when the ionic concentration of the buffer solution is lower than 100 mM. However, little attention has been paid to the flow in these studies.

Jacobson et al. [250] measured EOF velocity in nanochannels as small as 98 nm deep by using fluorescent dye (Rhodamine B), showing a 35% decrease of the electroosmotic mobility compared with that in microchannels. Hug[81] developed a new method to fabricate nanofluidic chips based on silicon dioxide wafers and measured EOF velocity in both microchannels and nanochannels; however, the smallest channel size is just 200 nm which is not sufficient to study any unique transport phenomena at nanoscale, because there is essentially no overlap of EDLs in such a large nanochannel. Pennathur and Santiago [246] investigated electrokinetic transport phenomena in two nanochannels of 40 nm deep and 100 nm deep experimentally by using both the current monitoring method and the fluorescence imaging method. However, the width of these channels is about $1\mu m$, which is not in the nanoscale. These nanochannels were fabricated by conventional photolithography

and dry etching method on quartz wafers. Haywood et al. [251] measured EOF velocity in three glass nanochannels of 530 nm wide and 54 nm, 108 nm, 216 nm deep respectively fabricated by combining photolithography, chemical etching, FIB techniques and so on. Both Pennathur's and Haywood's results prove that EOF velocity in nanochannels decreases as EDLs get overlapped. Table 4-1 reviews the the experimental results in detail.

Table 4-1 Summary of experimental results of electrokinetic transport of ions and fluids in nanochannels.

References	**Channel size**	**Channel material**	**Measurement Method**	**Focus**
Stein et al. [248],	70 nm deep and $50\mu m$ wide	Fused silica	Conductance	Ion transport
Duan and Majumdar [249]	2 nm deep and $50\mu m$ wide	Silicon-glass	Conductance	Ion transport
Jacobson et al. [250]	98 nm and 300 nm deep	Not mentioned	Confocal fluorescence detection	EOF mobility
Mela et al. [252]	200 nm high and $7.2\mu m$ wide	Silicon-based	Current monitoring	EOF flow rate
Hug et al. [81]	Larger than 200 nm deep and 200 nm wide	Silicon-silicon	Current monitoring	Channel fabrication and conductance
Pennathur and Santiago [246]	40 nm, 100 nm deep and $1\mu m$ wide	Quartz	Current monitoring method and Fluorescent dye imaging	Ion transport and flow transport
Haywood et al.[251]	54 nm, 108 nm, 216 nm deep and 530 nm wide	Glass	Fluorescent dye imaging method	Ion transport and flow transport

As reviewed above, even though several experimental studies have been conducted to investigate EOF in nanochannels, few of them worked on channels made by Polydimethylsiloxane (PDMS) which is the most widely used materials in microfluidic and nanofluidic research; furthermore, few of them worked with channel sizes smaller than 40 nm where significant EDL overlap may occur, especially in two dimensions. In the literature reviewed above, results of the channel size effects on EOF velocity in nanochannels are very limited. Therefore, the objective of this chapter is to systematically investigate EOF in smaller single nanochannels made of PDMS and to provide a better understanding of the electrokinetic transport of fluids in PDMS nanochannels.

In this chapter, nanofluidic chips with single nanochannels are fabricated on PDMS platforms. EOF velocity in single PDMS nanochannels with one-dimensional size ranging from 20 to about 250 nm is measured systematically by the current slope method. The effects of the channel size, the

concentration of electrolyte solution as well as the applied electric field on EOF velocity in nanochannels are studied. Zeta potential of the PDMS channel surfaces is also measured by using the current slope method. For comparison, corresponding analytical and numerical studies of EOF velocity in nanochannels are also presented in this chapter.

4.2 Methods

4.2.1 Analytical model

EOF in nanochannels with overlapped EDLs can be estimated by the following analytical solution [228] theoretically. Assuming that EOF transport between two sufficient large parallel plates separated by a distance of $2d$, the electric potential distribution in the y direction of the channel (perpendicular to the channel wall, and $y = 0$ at the middle plane) with a small degree of EDL overlapping can be written as [228]:

$$\Psi(y) = \frac{4k_bT}{ze}\left\{tanh^{-1}\left[\tanh\left(\frac{ze\zeta_w}{4k_bT}\right)\exp\left(-k_d(y+d)\right)\right]\right\} + \frac{4k_bT}{ze}\left\{tanh^{-1}\left[\tanh\left(\frac{ze\zeta_w}{4k_bT}\right)\exp\left(-k_d(d-y)\right)\right]\right\} \quad (4\text{-}1)$$

where k_b is the Boltzmann constant, T is the temperature, e is the unit charge, z is the valence of the buffer solution ($z = z^+ = -z^- = 1$ for KCl) and ${k_d}^{-1}$ is the Debye length which is a function of the ionic concentration, k_d is also referred as the Debye-Huckel parameter [3].

$${k_d}^{-1} = \lambda_D = \sqrt{\frac{\varepsilon_0\varepsilon_r k_b\, T}{2n_{i\infty}\,(ze)^2}} \quad (4\text{-}2)$$

Here, $n_{i\infty}$ is the number density of ions in the bulk solution. ε_0 is the permittivity of vacuum and ε_r is the dielectric constant of the electrolyte solution. Combining the Stokes equation under the condition of laminar flow, the EOF velocity distribution along the y direction can be calculated by:

$$\boldsymbol{V_{EOF}}(\boldsymbol{y}) = -\frac{\varepsilon_0\varepsilon_r\zeta_w\boldsymbol{E_{ex}}}{\mu}\left(1 - \frac{\Psi(y)}{\zeta_w}\right) \quad (4\text{-}3)$$

where $\boldsymbol{E_{ex}}$ is the externally applied electric field, ζ_w is the zeta potential of the channel wall and μ is the viscosity of the electrolyte solution. In microchannels, the thickness of the EDL is negligible compared with the channel size, therefore, $\Psi(y)$ becomes zero and Equation (4-3) becomes the famous Helmholtz-Smoluchowski equation [3] (Equation (2-4)). Based on the profile of the EOF

velocity, one can easily get the average velocity in the nanochannel by integrating the velocity in the y direction:

$$\boldsymbol{V_{av}} = \frac{1}{2d}\int_{-d}^{d} \boldsymbol{V_{EOF}}(\boldsymbol{y})dy \qquad (4\text{-}4)$$

However, for a very large degree of EDL interactions or high channel wall zeta potential, $\frac{ze\Psi_u}{k_bT} \gg 1$, the potential along the y direction of the channel can be calculated by;

$$\Psi(y) = \Psi_u - \frac{2k_bT}{ze} ln\, cos\left\{cos^{-1}\, exp\left[\frac{ze}{2k_bT}(\Psi_u - \zeta_w)\right] - \frac{k_d(y+d)}{2} exp(\frac{ze}{2k_bT}\Psi_u)\right\} \qquad (4\text{-}5)$$

where Ψ_u is the potential at the middle plane which can be calculated by applying the boundary condition: y=0, and the the following equation [228]:

$$cos\left[\frac{k_d(y+d)}{2} exp(\frac{ze}{2k_bT}\Psi_u)\right] = exp\left[\frac{ze}{2k_bT}(\Psi_u - \zeta_w)\right] \qquad (4\text{-}6)$$

The analytical solutions can be used to predict EOF velocity profiles in nanochannels directly by using Matlab. Figure 4-1 is an example of EOF profile plotted according to the analytical solution in a nanochannel of 104 nm high with 10^{-3} M KCl solution loaded under an electric field of 25 V/cm. The corresponding Matlab codes are listed in Appendix C.

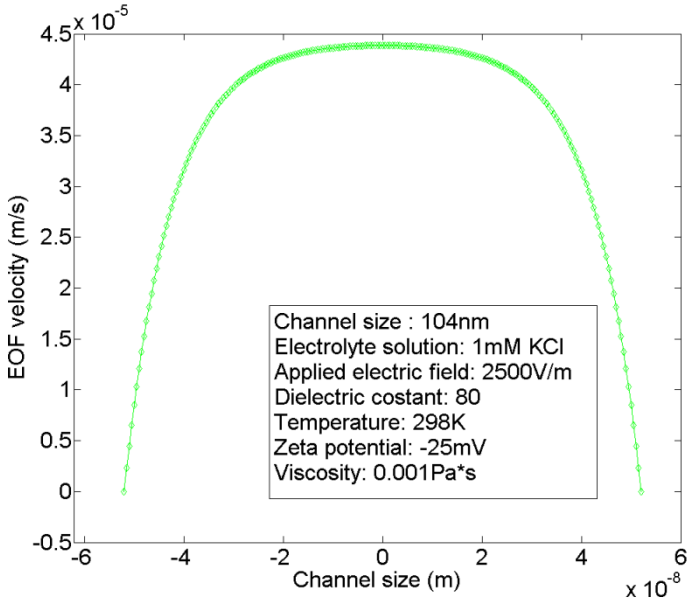

Figure 4-1 An example of EOF velocity profile in a nanochannel of 104 nm high with 10^{-3}M KCl solution loaded under an electric field of 25 V/cm plotted based on the analytical model by Matlab software.

4.2.2 Numerical simulation

Figure 4-2 shows a 2D computational domain of the numerical study with a channel height of 2d and a channel length of L. AB is the entrance of the nanochannel and CD is the outlet boundary, AD and BC are the channel walls. An electric is applied on the nanochannel with electric potentials applied on AB and CD. The governing equations and boundaries are listed in the following sections.

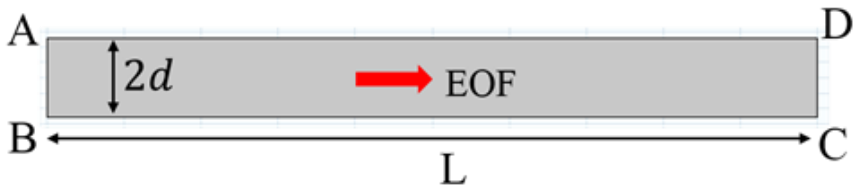

Figure 4-2 Schematic of modeling EOF in a nanochannel. The nanochannel is 2d in height and L in length. Electric potential is applied between the entrance and outlet of the nanochannel.

4.2.2.1 Electric field

Electric Field in EDL In the nanochannel area, Poisson equation must be solved in order to calculate the electric potential distribution in the EDL:

$$-\nabla(\varepsilon_0\varepsilon_r\nabla\Psi) = \rho_e \qquad (4\text{-}7)$$

$$\rho_e = F\sum_i c_i z_i \qquad (4\text{-}8)$$

where Ψ is the electric potential and ρ_e is the net charge density, F is the Faraday constant. c_i and z_i are the ionic concentration and valence of $K^+$and Cl^-respectively. The boundary conditions are:

$$\boldsymbol{n}\cdot(\varepsilon_0\varepsilon_r(-\nabla\Psi)) = 0 \text{ at AB and CD} \qquad (4\text{-}9)$$

$$\Psi = \zeta_w \text{ at channel wall AD and BC} \qquad (4\text{-}10)$$

Externally Applied Electric Field In the nanochannel area, the externally applied electric field is assumed to be independent of the EDL and the applied electric field. The externally applied electric field must also be governed by Poisson equation,

$$\nabla(\varepsilon_0 \varepsilon_r \nabla\Phi) = 0 \qquad (4\text{-}11)$$

where Φ is the externally applied electrical potential, the boundary conditions are

$$\boldsymbol{n} \cdot \boldsymbol{D} = 0 \text{ at AD and BC} \qquad (4\text{-}12)$$

$$\Phi = V1 \text{ at AB} \qquad (4\text{-}13)$$

$$\Phi = 0 \text{ at CD} \qquad (4\text{-}14)$$

4.2.2.2 Ionic concentration field

The thickness of EDL is comparable to the size of the channel and EDLs are likely to get overlapped in nanochannels, consequently, Nernst-Plank equation should be applied to study the ionic concentration field.

$$\nabla \boldsymbol{N_i} = 0 \qquad (4\text{-}15)$$

$$\boldsymbol{N_i} = -D_i \nabla c_i - z_i \mu_i c_i \nabla\Psi + c_i \boldsymbol{V_{EOF}} \qquad (4\text{-}16)$$

$$\mu_i = \frac{D_i}{RT} \qquad (4\text{-}17)$$

where $\boldsymbol{N_i}$, D_i, μ_i are the flux, diffusion coefficient and ion mobility of K^+or Cl^- respectively. $\boldsymbol{V_{EOF}}$ is the EOF velocity inside the nanochannel, R is the gas constant. The following boundary conditions are applied in the concentration field:

$$\boldsymbol{n} \cdot \boldsymbol{N_i} = 0 \text{ at AD and BC} \qquad (4\text{-}18)$$

$$c_i = c_{i\infty} \text{ at AB and CD} \qquad (4\text{-}19)$$

Here $c_{i\infty}$ is the concentration of the bulk solution.

4.2.2.3 Flow field

Stokes equation and the continuity equation are solved in order to calculate the flow field inside the nanochannel. Here, we assume that the fluid is incompressible and the flow inside the

nanochannel is laminar flow due to the low Re number, and no pressure is applied between the entrance and the outlet of the nanochannel.

$$-\nabla P + \mu\nabla^2 \boldsymbol{V_{EOF}} - \rho_e \nabla\Phi = 0 \qquad (4\text{-}20)$$

$$\nabla \cdot \boldsymbol{V_{EOF}} = 0 \qquad (4\text{-}21)$$

where P is the pressure, μ is the dynamic viscosity of the electrolyte solution. The boundary conditions at channel walls are nonslip due to the viscos effect and no pressure applied at the channel ends:

$$\boldsymbol{V_{EOF}} = 0 \text{ at AD and BC} \qquad (4\text{-}22)$$

$$P = 0 \text{ at AB and CD} \qquad (4\text{-}23)$$

The channel size effect, ionic concentration effect and the applied electric field effect on the EOF velocity in nanochannels are studied systematically by using this model. Table 4-2 lists the parameters and constants used in the simulation. In the numerical studies, ionic concentration from $10^{-4}M$ to 0.5 M, channel height from 20 nm to 300 nm, externally applied electric field ranging from 12.5 V/cm to 50 V/cm were tried. The relative zeta potential values were from the experimental results.

Table 4-2 Constants and parameters used in the example simulation.

Parameter	Description	Value and unit
$\boldsymbol{\mu}$	Viscosity of electrolyte	0.9×10^{-3} [Pa*s]
$\boldsymbol{\rho}$	Density of water	1000 [kg/m^3]
$\boldsymbol{\zeta_w}$	Zeta potential of channel wall	-25 [mV]
$\boldsymbol{\varepsilon_r}$	Dielectric constant of water	80[1]
$\boldsymbol{\varepsilon_0}$	Permittivity of vacuum	8.854×10^{-12} [F/m]
L	Length of channel	1000 [nm]
W	Width of channel	50 [nm]
$\boldsymbol{V1}$	Electric potential applied on the entrance	25 [mV]
$\boldsymbol{c_{inf}}$	Bulk concentration	1[mol/m^3]
$\boldsymbol{z_1}$	Valence of K^+	1[1]
$\boldsymbol{z_2}$	Valence of Cl^-	-1[1]
e	Unit charge	1.602×10^{-19} [C]
F	Faraday Constant	9649 [C/mol]
$\boldsymbol{D_1}$	Diffusion coefficient of K^+	1.957×10^{-9} [m^2/s]
$\boldsymbol{D_2}$	Diffusion coefficient of Cl^-	2.032×10^{-9} [m^2/s]

R	Gas constant	8.314[J/mol/K]
k_b	Boltzmann constant	1.381×10^{23} [J/K]
T	Temperature	298[K]

Figure 4-3 is an example of the flow field inside a nanochannel of 104 nm high with 10^{-3}M KCl solution loaded under an electric field of 25 V/cm. The color scale and the arrow in Figure 4-3 (a) depict the velocity field, and Figure 4-3 (b) shows a velocity profile at the cross-section of this nanochannel. From Figure 4-1 and Figure 4-3 one can see that the velocity profiles are almost identical, revealing that the direct numerical models are reliable.

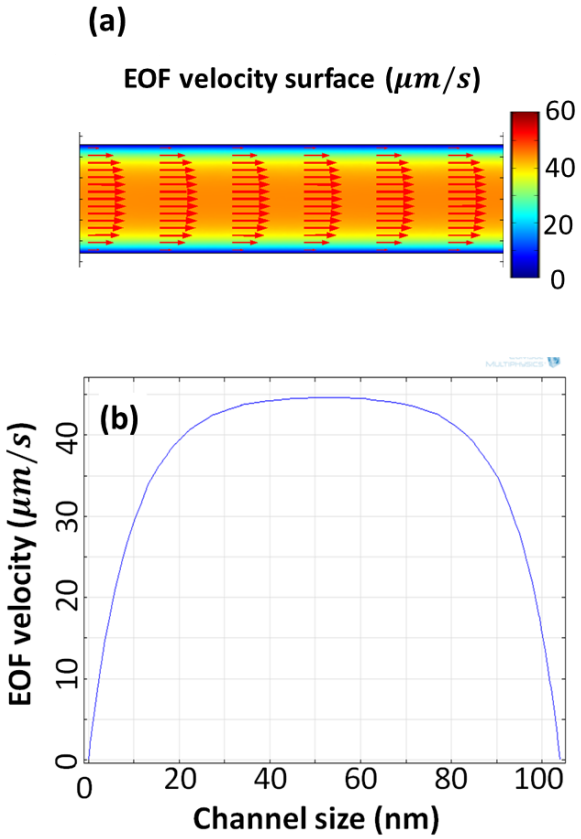

Figure 4-3 EOF field inside a nanochannel of 104 nm high with 10^{-3}M KCl solution loaded under an electric field of 25 V/cm. (a) EOF velocity plotted by color surface and arrows (b) a velocity profile at the cross-section of this nanochannel.

4.2.3 Experimental system

4.2.3.1 Fabrication of single-channel nanofluidic devices

In this chapter, PDMS nanofluidic chips with single nanochannels were made by following the working procedures presented in CHAPTER 3. Figure 4-4 (a) shows an example of a PDMS nanochannel replicated from a smooth cast nanochannel mold and Figure 4-4 (b) illustrates a cross-section of this nanochannel measured by the AFM. Figure 4-4 (c) is an example of the micro-nanofluidic chip after bonding, and Figure 4-4 (d) shows a cross-section of the nanochannel after bonding captured by the optical microscope and a zoomed-in view of this cross-section measured by the AFM. In this chapter, the microchannel system is composed of a pair of "U" shaped microchannels with a cross-section of 150 μm in width and 30 μm in depth. The two "U" shape microchannels are separated by 100 or 200 μm which are bridged by nanochannels.

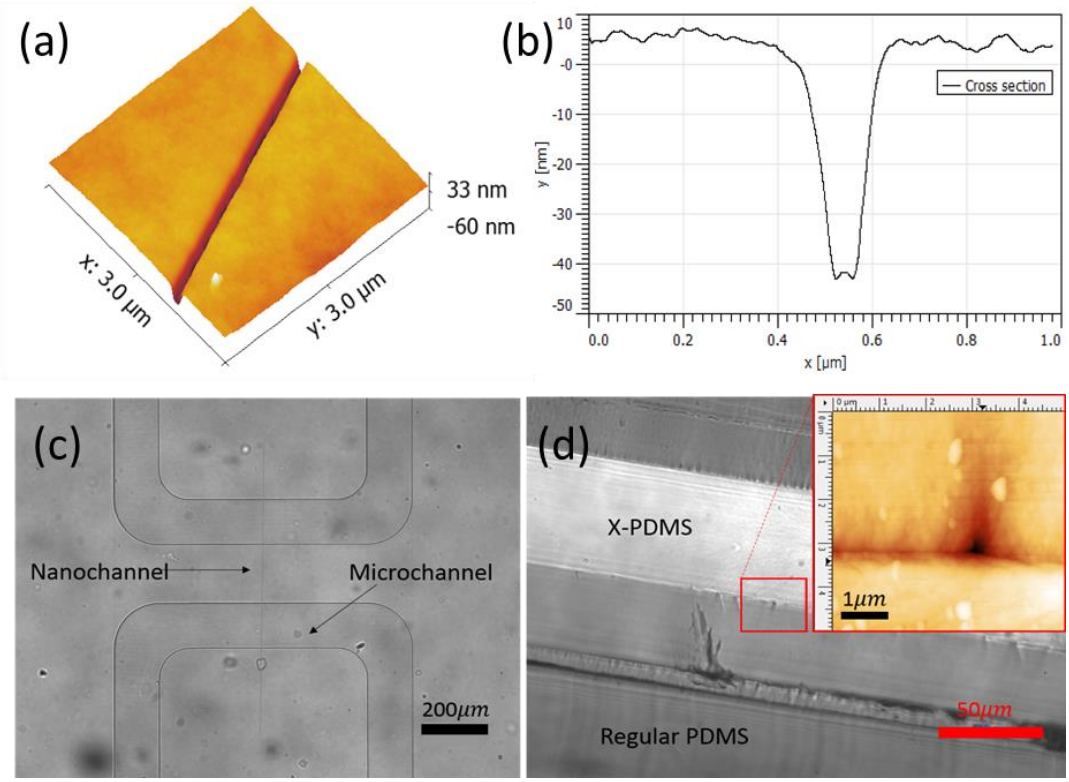

Figure 4-4 Examples of a PDMS nanochannel and a PDMS nanofluidic chip. (a) A single nanochannel replicated on PDMS; (b) A cross section of this nanochannel of 183±11 nm in width and 42±6 nm in depth as measured by AFM; (c) Picture of a single-nanochannel nanofluidic chip; (d) A zoomed-in view of the cross-section of the single nanochannel after bonding.

4.2.3.2 EOF velocity measurement by the current slope method

To measure EOF velocity in microchannels or in nanochannels, several methods have been developed, and these methods can be divided into two categories: imaging tracing method and current monitoring method. For the imaging tracing method, fluorescence dye or nanoparticles are diluted or mixed into electrolyte solutions to make the movements of the fluids visible. A camera or a photodetector will record the movements of the fluorescent dye or particles. For example, Sadr et al. [253] studied EOF in rectangular channels by using nanoparticles; Jacobson et al. [250,251] measured EOF velocity through nanochannels by using Rhodamine dye. EOF in single nanochannels was also investigated by Pennathur and Santiago by imaging Rhodamine B [246]. Fluorescence imaging makes the velocity visible; however, diffusion of the fluorescent dye results in a blurring boundary of the flow profile and inaccuracy timing. Also, the fluorescent dye molecules and nanoparticles carry electrostatic charges, which make them subject to additional electrophoretic motion, and may affect the electric field in the nanochannel. These side effects must be considered and corrected in order to obtain the true EOF velocity by these methods.

The electrical current monitoring method can measure EOF velocity by monitoring the electrical current change during replacement between two electrolyte solutions of slightly different conductivity. As a low conductivity solution replaces a high conductivity solution in a channel by EOF, the electrical current decreases from an initial higher current value and eventually reaches a lower constant value when the high conductivity solution is completely replaced by the low conductivity solution in the channel. Ren et al [254] improved the current monitoring method by using the slope of the current change to minimize the inaccuracy involved in determining the starting time and the ending time of the current change. This improved method is also called the current slope method. The current slope method does not need the exact starting time and ending time of the solution displacement, and the average velocity can be calculated by the following equation:

$$\boldsymbol{V_{av}} = \frac{k_{slope} \cdot L}{\boldsymbol{E_{ex}} A(\lambda_2 - \lambda_1)} \qquad (4\text{-}24)$$

where $\boldsymbol{V_{av}}$ is the average velocity of the EOF, k_{slope} is the slope of the linear part of the current change curve, A is the cross section of the channel, L is the length of the channel, λ_1 and λ_2 are the conductivity of the higher ionic concentration solution and lower ionic concentration solution, respectively.

In the single nanochannel chips used in this work, the length of the nanochannels is short, and it is easy to measure the stable electric current values when the channel is filled with either the higher ionic concentration solution or the lower ionic concentration solution. As a consequence, Equation (4-24) can be re-written into the following form to calculate the EOF velocity in single nanochannels:

$$V_{av} = \frac{k_{slope} \cdot L}{I_2 - I_1} \qquad (4\text{-}25)$$

where I_1 and I_2 are the electrical current in the nanochannel filled with the higher ionic concentration solution and the slightly lower ionic concentration solution, respectively.

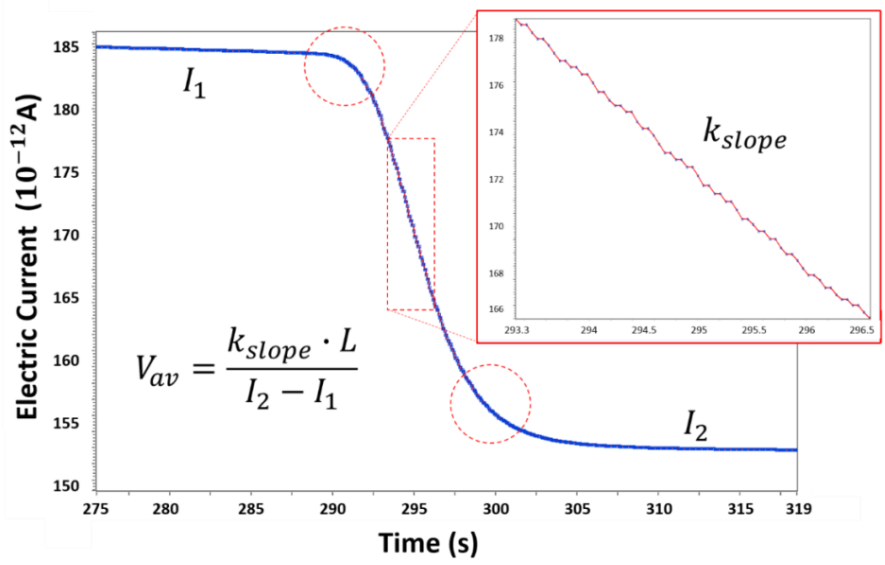

Figure 4-5 An example of EOF velocity measurement in nanochannels by the current slope method. The current change is measured by replacing 100% 10^{-2} M KCl solution with 90% 10^{-2} M KCl solution with 25 V/cm electric field applied in an 804 nm wide and 215 nm deep nanochannel.

Figure 4-5 shows an example of the current change curve measured by replacing 100% 10^{-2}M KCl solution with 90% 10^{-2}M KCl solution under 25 V/cm electric field in an 804 ± 13 nm wide and 215 ± 7 nm deep nanochannel. At the beginning, only 100% 10^{-2}M KCl solution flows in the nanochannel, and the current is constant, I_1. After the 100% solution is replaced by the 90% concentration solution, the current decreases gradually and eventually reaches a constant lower current value, I_2, when the higher concentration solution is completely replaced by the lower concentration solution(see Figure 4-5), due to the conductivity change. The most linear part of the current slope is magnified in the up-right corner of Figure 4-5, which is used to represent the slope of

the current change during the entire displacement process. The nonlinear parts in the red circulars are caused by mixing and dispersion of the solutions at the starting and ending of the displacement.

Figure 4-6 shows the layout of the current monitoring system. A DC power (Keithley, Model 6517A, Voltage module) is used to provide an electric potential to the nanofluidic chip reservoirs through Platinum electrodes (Sigma-Aldrich®). Electrometer (Keithley, Model 6517A) connecting to the computer is used to record the current by Labview programs (National Instruments Corp.). To reduce the noises during the current measurement, a hand-made Faraday case is covered on the power switch and the nanofluidic chip.

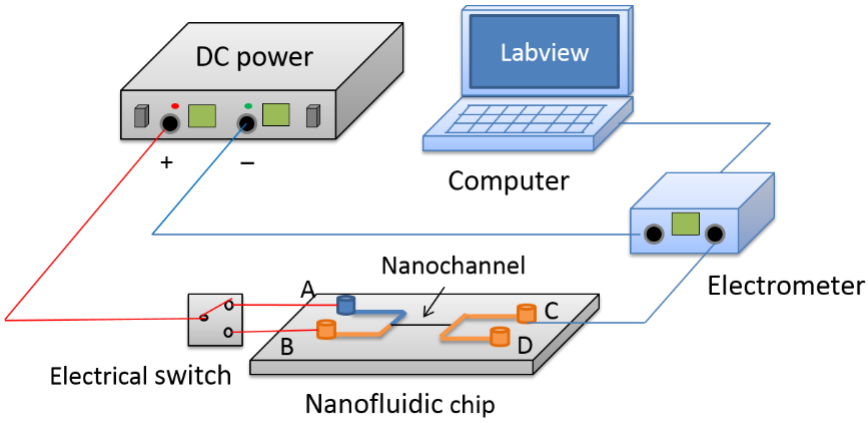

Figure 4-6 Schematic of the current slope measurement system.

For each set of measurement, a fresh nanofluidic chip was initially loaded with KCl solution of a given ionic concentration, ranging from 10^{-4} M to 0.5 M in the experiments. The electrolyte solutions were prepared by dissolving KCl (Fisher Scientific®) in pure water (Mini Q, Direct-Q 3) with a resistivity of 18.2 MΩ · cm at 25 ℃. Then, the DC power was applied on the nanochannel through reservoirs A and C (see Figure 4-6), and the current was recorded by the computer simultaneously. After the current became constant, the solution in reservoir B was replaced by another kind of KCl solution with a slightly lower concentration. An electric field was applied through reservoirs B and C. Under the applied electrical field, the solution from reservoir B would be pumped into the microchannel and then into the nanochannel because of the electroosmotic flow. As a consequence, the solution with a higher concentration in the nanochannel would be replaced by the lower concentration solution gradually by EOF, and the electrical current would decrease gradually until reaching another plateau. Moreover, when an electric field is applied on the nanochannel, ion polarization may occur at the micro-nanochannel conjunctions. In this work, the electric field applied in the experiments was lower than 50 V/cm and the ion concentration polarization is very weak, also

Joule heating effects can be negligible.* In addition, the period of time of the electrolyte displacement was only a few seconds which is much shorter than that of the propagation process of the ion concentration polarization. As a consequence, in this work, the ion concentration polarization effect is assumed to be negligible. Similar assumptions have been applied and proved by Haywood et al [251].

It should be noted that the electrical current value in nanochannels decreases with the ionic concentration of the solutions, which makes the current measurement harder for lower concentrations solutions. In this paper, 5% concentration difference was applied for both 0.5 M and 0.1 M concentration cases; 10% concentration difference was used for 0.01 M and 10^{-3} M cases; and 20% concentration difference was utilized in the case of 10^{-4} M solution during the displacements. For each working condition, i.e. one given solution, one given electric field and one given nanochannel size, the current slope measurement was repeated for at least 5 times in independent new chips. EOF velocity was calculated by using Equation (4-25).

Table 4-3 List of nanochannels used in the EOF velocity measurement. (H_D: Hydraulic diameter).

Channel No.	Depth (nm)	Width (nm)	H_D	Cross area (nm^2)
1	241±11	867±20	225	104570
2	215±7	804±13	201	86811
3	183±12	798±19	174	73115
4	149±15	795±18	144	59315
5	130±16	714±19	126	46630
6	114±17	716±21	111	40907
7	104±9	757±25	101.5	39417
8	94±11	609±9	92	28343
9	89±2	626±17	87	27857
10	81±5	532±9	79	21546
11	67±7	640±22	66	21440
12	58±2	404±15	57	11716
13	50±2.5	232±11	39	5800
14	42±5.6	183±11	40	3843
15	32±4	106±9	29	1696
16	20±5	63±10	18.3	630

* Calculation of the Joule heating effects and experimental results of Joule heating effects in a single nanochannel can be found in Appendix D.

In this chapter, 16 nanochannels with different sizes ranging from approximately 60 nm to 860 nm in width and about 20 nm to 241 nm in depth were tested. Table 4-3 gives the geometric parameters of these nanochannels, including the width, depth, hydraulic diameter and the cross-section area values. The length of the nanochannels connecting the two "U" shape microchannels in the nanofluidic chips is 200μm for channel 1 to channel 12, and 100μm for channel 13 to channel 16. All the PDMS nanochannels were measured by the AFM for at least 5 times to characterize the channel size. A microchannel of 5 μm deep, 50 μm wide and 1 cm long fabricated by conventional photolithography method was also used to study the EOF velocity in microchannels and to measure the zeta potentials of x-PDMS channel surfaces. All the experiments were conducted at room temperature of about 25 ^{o}C.

4.3 Results and discussion

4.3.1 Zeta potential measurement in microchannels

Zeta potential is used to predict EOF velocity in microchannels by Helmholtz-Smoluchowski equation. As a comparison work, EOF velocity of 0.5 M, 0.1 M, 10^{-2}M, 10^{-3} M and 10^{-4}M KCl solution in an x-PDMS microchannel was also measured by the current slope method. Zeta potential of the channel surface at each concentration was calculated by using the H-S equation (Equation (2-5)) and the measured EOF velocity. During the calculation, the permittivity and viscosity of the solutions were treated as constants, and the zeta potential is fitted as a function of the ionic concentration (as shown in Figure 4-7):

$$y[mV] = -8.27448 + 2.13367 * \ln(c[M] - 3.42286 * 10^{-5}) \qquad (4\text{-}26)$$

Zeta potential of the x-PDMS channel surfaces under the condition of any ionic concentration between 10^{-4} M and 0.5 M in the simulation part of this chapter was calculated by using Equation (4-26). Here, the assumption is that the zeta potential is dominated by the concentration and does not change with the overlapping of EDLs. To be noted, overlapping of EDLs affects zeta potential of nanochannel surfaces, and a more accurate model has been developed by Ma et al. [238] The model shows that the deviation of zeta potential for the cases of high degree EDL interactions under the condition of low pH values (for example pH=4) is significant [238]. However, in our cases, the pH values are about 5.7, and the interactions between EDLs are much weaker in comparison with that of

Ma's model with large deviation of zeta potential, indicating that the deviation of the zeta potential due to channel size in our work is very small and negligible.

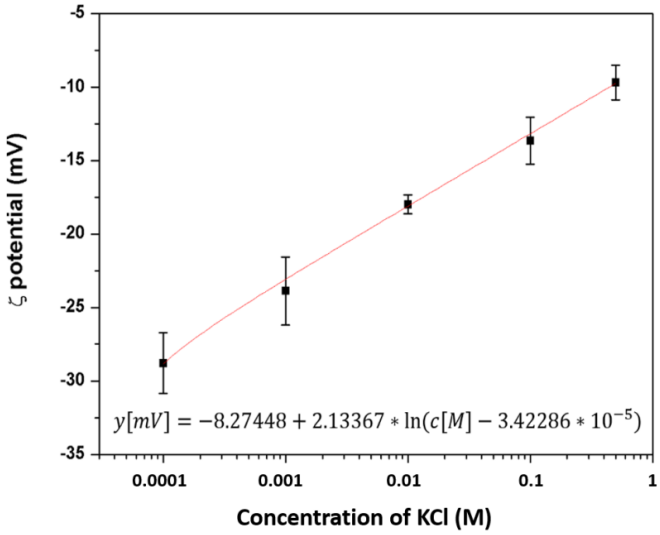

Figure 4-7 Zeta potential of x-PDMS channel surface contacting with different KCl solutions ranging from 10^{-4} M to 0.5 M measured by the current slope method and calculated by the H-S equation.

4.3.2 Channel size effects

Single PDMS nanochannels with depth ranging from 20 nm to 241 nm as well as a microchannel of a cross-section 50×5 μm were used to study the channel size effects upon the EOF velocity in nanochannels. During the experiments, all the channels initially were filled with 100% 10^{-2}M KCl solution and 100% 10^{-3} M KCl solution; and then the initial solutions were replaced by 90% 10^{-2} M and 90% 10^{-3}M KCl solutions under 25 V/cm electric field. Figure 4-8 shows the experimental results and the numerical simulation results. To simplify the figures, only the smallest dimension (the depth) of the channels is plotted as the x-axis in these figures, the width of the channels is labeled above or below the error bars (see Figure 4-8 (a)). Numerical simulation results are also plotted on Figure 4-8 (a), in which the red dashed line depicts the simulation results of the 10-3 M cases and the black dashed line is the simulation results of the 10-2 M cases. From Figure 4-8 (a), it is obvious that, in relatively large nanochannels, i.e., when the depth (the smallest dimension) is larger than 100 nm for the case of 10^{-3}M solution or larger than 50 nm for the case of 10^{-2}M solution, the EOF velocity values are independent of the channel size, about 40 $\mu m/s$ and approximate 30 $\mu m/s$, respectively. However, when the channel size becomes smaller, i.e., when the

depth (the smallest dimension) is smaller than 100 nm for the case of 10^{-3} M solution or smaller than 50 nm for the case of 10^{-2}M solution, EOF velocity in the nanochannels for both concentration values becomes size dependent and decreases with the channel size. The experimental results in Figure 4-8 agree with the numerical simulation results well. The profiles of the EOF velocity in the nanochannels for both 10^{-2} M cases and 10^{-3} M cases are plotted in Figure 4-8 (b) and Figure 4-8 (c) by the numerical method.

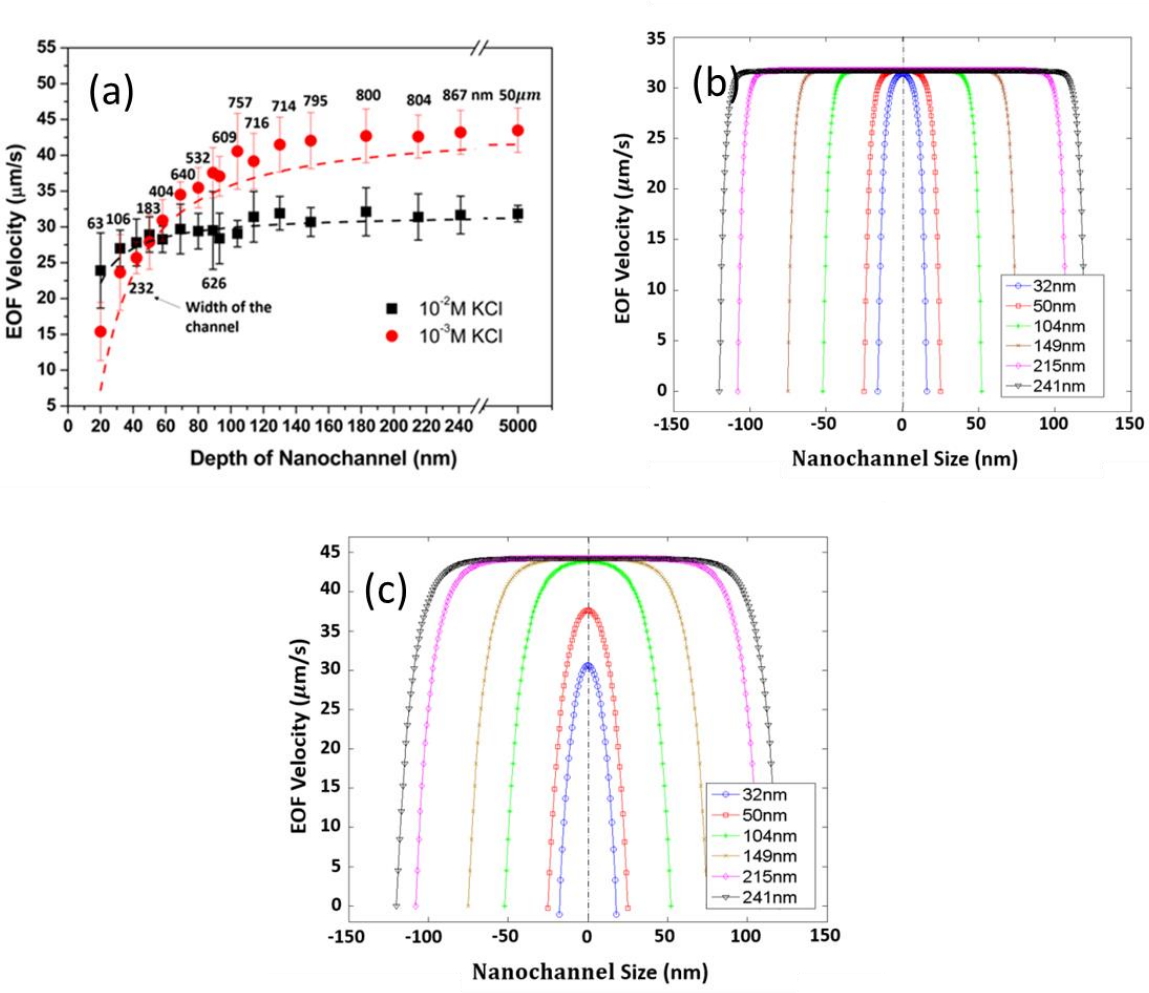

Figure 4-8 Channel size effects on the EOF velocity in nanochannels. (a) In the experiments, EOF velocity of 10^{-2} M KCl and 10^{-3} M KCl solutions in 16 nanochannels with depth ranging from 20 nm to 241 nm and a microchannel are measured under the electric field of 25 V/cm. The widths of the channels are labeled near the error bars of each data point. The red dashed line depicts the simulation results of 10^{-3} M cases and the black dashed line is the simulation results of 10^{-2} M cases;

(b) EOF velocity profiles in nanochannels with 10^{-2}M KCl solution; (c) EOF velocity profiles in nanochannels with 10^{-3}M KCl solution.

For the 10^{-2} M cases, EOF velocity in all the larger nanochannels is essentially constant, about 30 $\mu m/s$, which is identical with the velocity in the microchannel (see Figure 4-8 (a)). Channel size has little effect on the EOF velocity, because the EDL is very thin in comparison with the relatively large nanochannel size. For 10^{-2} M KCl solution, the Debye length $\lambda_D(1/k_d)$ is only about 3 nm, and the thickness of the diffuse layer is usually 3 to 5 times of λ_D [3], 10~15 nm, which means no overlap of EDLs occurs in nanochannel larger than 30 nm. Therefore, the EOF velocity in these nanochannels is just as large as that in the microchannels, and H-S equation is still applicable. However, in reality, the average EOF velocity still shows a slightly decreasing trend when the channels size becomes smaller than, for example, 50 nm, as showing in Figure 4-8 (a). This is because the percentage of the nanochannel cross-section occupied by the EDL increases when the channel size becomes smaller. When the channel size is smaller than 30 nm, for example, in the 20 nm deep nanochannel, a weak degree of overlap of EDLs occurs, which will further reduce the EOF velocity to about 24$\mu m/s$.

Similarly, for the 10^{-3} M cases, λ_D is about 10 nm and the thickness of the diffuse layer of the electric double layer is about 30 ~50 nm. Consequently, EDLs are likely to get overlapped in the nanochannels with sia ze smaller than 100 nm and the EOF velocity will decrease accordingly. As expected, from Figure 4-8 (a) one can see that EOF velocity in nanochannels with 10^{-3}M solution decreases gradually as the channels size becomes smaller than 100 nm. The velocity profiles in Figure 4-8 (c) also show that the maximum velocity value in the 104 nm deep nanochannel is slightly smaller than that in the microchannel as shown in Figure 4-8 (a). In addition, in most cases of this chapter, the nanochannel size in the width direction is much larger than that in the depth direction; therefore, it is impossible for the EDLs to get overlapped in the channel width direction; consequently, the channel width has little effect on the EOF velocity. However, for the smallest nanochannel studied in this work, the channel is 20 nm deep and 63 nm wide. In this case, EDLs can get overlapped weakly in the width direction in addition to the depth direction. As shown in Figure 4-8 (a), the EOF velocity is approximate 15 $\mu m/s$, only about one third of that in the microchannel.

4.3.3 Concentration effects

Figure 4-9 shows the experimental results (solid points with error bars) and numerical simulation results (dashed lines) of ionic concentration effects on the EOF velocity in 6 nanochannels

and one microchannel. KCl solutions with concentration ranging from 0.5 M to 10^{-4} M were studied in these channels. The applied electric field for all the cases is 25 V/cm. Apparently, EOF velocities of the 0.5 M solution in all the nanochannels and the microchannel are essentially the same, about $17\mu m/s$, because, at this high ionic concentration, the thickness of the EDL is extreme thin ($\lambda_D \approx 0.43\ nm$) and there is no overlap of EDLs in all the channels. As the ionic concentration decreases to 0.1 M and 10^{-2} M, EOF velocity in the channels increases with the concentration inversely due to the increasing zeta potential as shown in Figure 4-7. However, a lower ionic concentration will also contribute to a thicker EDL, which will in turn give rise to overlapped EDLs in smaller nanochannels and consequently a smaller EOF velocity. As the ionic concentration decreases further to $10^{-3}M$ and$10^{-4}\ M$, nanochannels of different size behavior differently in terms of the EOF velocity. For example, in the microchannel, EOF velocity keeps increasing from about 42 $\mu m/s$ to almost 53 $\mu m/s$ while the ionic concentration decreases from 10^{-3} M to $10^{-4}\ M$, following the trend of the zeta potential in Figure 4-7. For the 241 nm deep and 149 nm deep nanochannels, the velocity still increases with the concentration inversely for the 10^{-3} M case, but decreases slightly for the 10^{-4} M case due to weak overlap of EDLs. For nanochannels smaller than 89 nm, overlapping of EDLs dominates the EOF transport, and the EOF velocity decreases dramatically even though the ionic concentration decreases. For example, in the nanochannel of 20 nm deep and 63 nm wide with 10^{-4} M solution, $\lambda_D \approx 30$ nm, EDLs are overlapped in both the depth direction and the width direction; consequently, EOF velocity is reduced to only about 1/9 of that in the microchannel under the same applied electric field. It is obvious that the experimental results and the numerical simulation results in Figure 4-9 show the similar trend and from both figures one can conclude that: in relatively larger nanochannels without overlapped EDLs, the EOF velocity depends on the ionic concentration; in smaller nanochannels with overlapped EDLs, the EOF velocity depends on both the ionic concentration and the channel size.

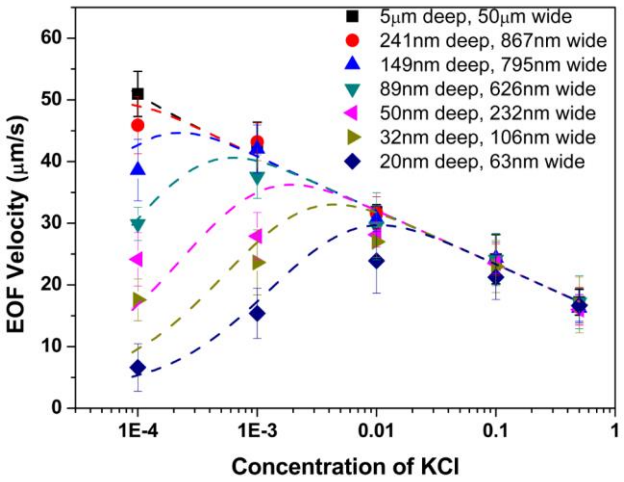

Figure 4-9 Concentration effects on the EOF velocity. EOF velocity of 10^{-4} M, 10^{-3} M, 0.01 M, 0.1 M and 0.5 M KCl solutions in five nanochannels and a microchannel were measured systematically. The applied electric field for all the cases is 25 V/cm. The solid points with error bars are the experimental results and the dashed lines illustrate the corresponding simulation results.

From the results, one can see that EOF velocity in PDMS nanochannels depends highly on the ionic concentration. Similar properties of EOF in glass nanochannels have also been proved experimentally by Pennathur[246] and Haywood et al [251], and the electroosmotic mobility values in their works are higher than that in the present cases under the conditions of same concentration values and channel sizes due to the surface property difference between glass and x-PDMS material. However, all the results follow the EDL overlapping theory, as a result, one can also predict EOF transport in nanochannels, nanomembranes, nanoporous made of other materials such as silicon, polycarbonate and so on accordingly, which is essential to the applications of nanofluidics.

4.3.4 Effects of applied voltage

Figure 4-10 shows the electric field effects on the EOF velocity in nanochannels. In the experiments, EOF velocities of 10^{-2}M KCl solution and 10^{-3}M KCl solution in 5 nanochannels as well as in a microchannel with applied electric fields ranging from 12.5 V/cm to 50 V/cm were studied. As shown in both Figure 4-10 (a) and Figure 4-10 (b), EOF velocity in both the microchannel and the nanochannels increases linearly with the applied electric field. The slope of the velocity *vs* electric field curve is the electroosmotic mobility. From Figure 4-10 (a), one can see that the electroosmotic mobility decreases by a little with the decreasing channel size even though no overlap of EDLs exists. As discussed above, the slight decrease of the electroosmotic mobility in the

small nanochannels is due to the increase in the percentage of the channel cross-section occupied by EDLs when the channel size becomes smaller. For 10^{-3}M KCl solution, no overlap of EDLs occurs in nanochannels larger than 100 nm, as shown in Figure 4-10 (b), EOF velocity in the nanochannels larger than 104 nm is essentially the same as that in the microchannel under the same applied electric field. However, Figure 4-10 (b) shows that the electroosmotic mobility decreases when the channel size becomes smaller than 104 nm, because EDLs get overlapped. This is evident in the case of 50 nm deep nanochannels.

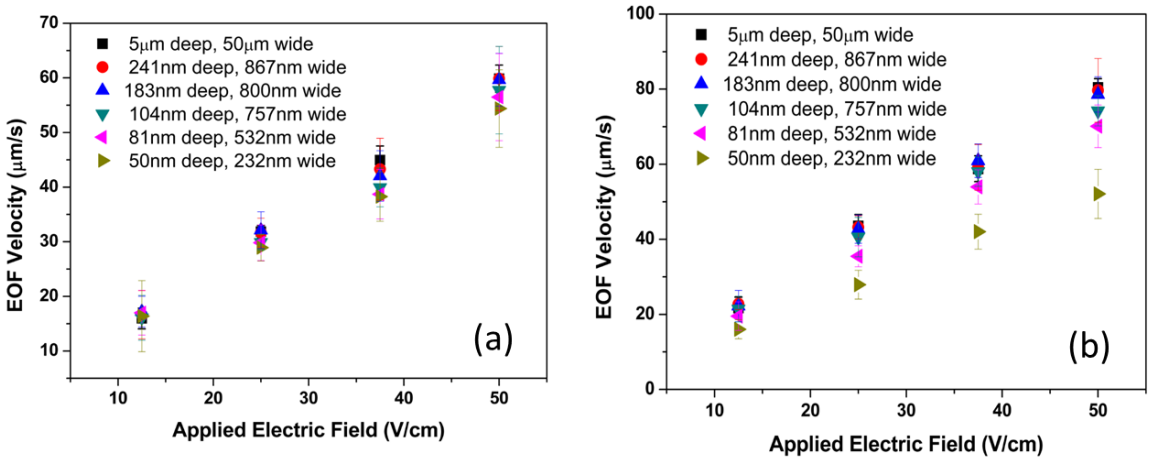

Figure 4-10 Electric field effects on the EOF velocity. In the experiments, EOF velocity of (a) 10^{-2} M KCl solution and (b) 10^{-3} M KCl solution in 5 nanochannels and one microchannel are measured. The applied electric fields are 12.5 V/cm, 25 V/cm, 37.5 V/cm and 50 V/cm respectively.

4.4 Conclusion

This chapter presents a systematic study of electroosmotic flow (EOF) in single PDMS nanochannels with one dimension as small as 20 nm by using the current slope method. Sixteen nanochannels with different sizes as well as a microchannel were tested in the experiments. Zeta potentials of the x-PDMS microchannel surfaces contacting with KCl solutions of different concentrations were also measured by the current slope method. The results show that EOF velocity in nanochannels increases with the applied electric filed linearly, and EOF velocity in nanochannels with overlapped EDLs is smaller than that in microchannels under the same applied electric field. EOF velocity in relatively large nanochannels without overlapped EDLs is independent of channel size and can be calculated by Helmholtz-Smoluchowski equation. However, EOF velocity in smaller nanochannels with overlapped EDLs is strongly dependent on both the nanochannel size and the ionic concentration of the electrolyte solution. The experimental results and numerical simulation

results presented in this chapter provide an improved understanding of electrokinetically driven fluids through nanochannels.

CHAPTER 5 Fundamental Research II: Electrokinetic Motion of Single Nanoparticles in Single Nanochannels*

5.1 Introduction

The phenomenon of electrophoresis describes the motion of charged colloidal particles suspended in electrolyte solutions in response to externally applied electric fields [3,6]. Electrophoresis has long been applied to separate a mixture of charged particles or molecules practically by using porous media, such as gels [255]. The development of nanofabrication techniques today makes manipulation and transport of individual molecules and particles in nanofluidic platforms possible [2,256,257]. For example, stretching, separation and direct observation of individual DNAs [258–263] and proteins [264,265], sizing and detection of single nanoparticles [266–268] by electrokinetically driven force on nanofluidics devices have been reported recently. However, to make full use of these techniques with high performance and efficiency, it is crucial to fully understand the mechanism of electrokinetic motion of nanoparticles or molecules in the nanospace, such as in straight nanochannels.

5.1.1 Analytical and numerical models

A large number of numerical and analytical models have been developed to study electrophoresis behavior since the last century, and these models are based on different limiting assumptions and working conditions, such as domain boundary, particle shape and surface zeta potential, type of electrolyte solution, and thickness of electric double layer (EDL). In the early years, Helmholtz-Smoluchowski and Debye-Huckel models were developed to evaluate electrophoresis of particles in stationary liquids under the conditions of thin EDL($k_d a \gg 1$) and thick EDL ($k_d a \ll 1$), respectively [269,270], where a is the radius of the particle, and ${k_d}^{-1}$ is the Debye length. Two general formulas for the electrophoretic mobility of charged particles in concentrated electrolyte solutions and in extremely diluted electrolyte solutions were derived [6], as reviewed in CHAPTER 2. These two formulas are bridged by Henry's function valid for arbitrary $k_d a$ [271] and further improved by Ohshima et al [272–274].

* A similar version of this chapter was published as:
Peng, R.; Li, D. Electrokinetic Motion of Single Nanoparticles in Single PDMS Nanochannels. Microfluid. Nanofluidics, 2017, 21 (1), 12. https://link.springer.com/article/10.1007/s10404-017-1848-0.

Modern theories focusing on the other working parameters and conditions have also been developed. These conditions can be divided into two branches, including the above-mentioned unbounded environment [275–277] and the bonded domain which investigates the channel wall effects on the electrophoretic motion of particles. Particle motions near a flat plane [278–280], in rectangular channels [281,282], cylindrical channels [283,284] under the conditions of thick EDL limit [285–287], thin EDL limit [278,279,288,289] and arbitrary EDL thickness [290–292] have been studied. The thickness of EDL is dominated by the ionic concentration of the buffer solutions [3], however, pH values [293,294] and symmetry or asymmetry property of the ions [282,295–297] also affect the electrophoretic behavior. For the cases of particle motion in cylindrical channels, generally, the particles move along the centerlines of the channels [280,283,298], however, the off-axis effect has also been investigated [292,299,300]. Zeta potential of the particle surfaces is another key parameter in the electrophoresis. Besides the general low zeta potential assumption [280,285,286], particles with high zeta potential [277,282,296], arbitrary zeta potential [290] and particles with non-uniform zeta potential distribution [301,302] have also been studied. In addition, electrophoresis models involving neutral particles, dielectric particles [280,287] and particles made of soft materials [288,291,298,303,304], porous media [305,306] as well as air bubbles [307] have been investigated. It is also a fact that in practical applications, the shape of the particles is diverse. As a result, modeling of electrophoresis of spherical [277,278,280,282,283,285,287], cylindrical [288,308], rectangular [281,309] and spheroidal [310] particles has been conducted. These models are summarized in Table 5-1, and details about these modern models are documented as follows.

Keh and Anderson [278] studied boundary effects on the electrophoretic motion of colloidal spheres with infinite $k_d a$. Boundary conditions of single flat wall, two parallel walls and long circular tube are studied, showing that: firstly, the electrophoretic velocity is changed by the interactions between the particles and the boundaries; and secondly, the fluid around the particle slows down the electrophoretic velocity due to the retardation effects; thirdly, electroosmotic flow caused by the boundary gives rise to deviation of the electrophoretic motion velocity. Keh and Chen [279] investigated the electrophoretic motion of dielectric sphere particles with bonded boundaries and got similar analytical solutions, providing that the electrophoretic motion is affected by the electroosmotic flow, the squeezed electric field lines around the particles (speeding up effects), and the viscous retardation caused by the channel wall. Electrophoresis of two particles with different particle size and zeta potential has been investigated by Chen and Keh [276], they proved that when the two particles share the same zeta potential, these two particles will not interact with each other. For

the case of electrophoresis of suspension of particles with arbitrary size but same zeta potential, the volume fraction dominates the electrophoretic mobility of the particles.

Yoon and Kim[310] gave exact solutions to the EDL around spheroids at a low zeta potential. Their work shows that the orientation of the spheroids affects the electrophoretic mobility significantly and the value of the electrophoretic mobility shows a minimum as the particle size is comparable to the thickness of the EDL. In 1992, Mangelsdorf and White [311] studied the electrophoretic mobility of a spherical particle in an oscillating electric field and proved a function to describe the magnitude and phase of the electrophoretic mobility based on the zeta potential, frequency, particle size and the concentration of electrolyte solution. In 1994, Ohshima [272] improved Henry's function and proved a simple expression for the retardation effect in the calculation of electrophoresis of spherical particles. The electrophoretic motion of an infinitely long cylindrical particle has also been studied [273].

Ennis and Anderson [285] in 1997 worked on the electrophoretic motion of charged particles with rigid boundary and low zeta potential, in which EDLs get overlapped but not significantly. The results showed that when EDLs get overlapped, the electrophoretic velocity is not proportional to the zeta potential difference between the particle and the boundary, and the velocity increases significantly as $k_d a$ is smaller than 10. Shugai and Carnie [280] investigated the electrophoretic motion of spherical particles with thick EDLs in confined boundaries numerically and proved the analytical results developed by Keh and Anderson et al. [278] [285]

Ohshima [312] also derived general expressions and approximate expressions of electrophoretic motion of spherical particles in a salt-free medium, predicting the existence of a critical value of the particle surface charge. When the surface charge is lower than the critical value, the velocity is proportional to the zeta potential and when the surface charge is higher than the critical value, the velocity becomes independent of the surface charge due to condensation of counterions near the particle surface. A corresponding numerical work has also been conducted [313]. An approximate analytical solution for the electrophoretic motion of charged spherical particles in general electrolyte solutions was also derived, in which the relaxation effects and arbitrary zeta potential at the condition of large $k_d a$ are considered [314].

Hsu, Ku and Kao [286] focused on the effects of electroosmotic flow on the electrophoretic motion of particles in cylindrical pores. Their numerical simulation results show that the surface potential of the pore affects the electrophoretic mobility significantly, and if the surface potential is too high or

too low, reversal of the particle motion would not occur; and when the surface potential is located in a medium level, reversal motion may occur for twice. Hsu and Chen [284] improved this model and took the effects of double layer polarization into account afterward. A new expression to evaluate the electric force acting on the particle during the electrophoresis under the condition of weak electric fields was derived by Hus, Yeh and Ku [315]. The new expression is based on the Maxwell stress tensor and is applicable to both rigid and soft particles and various surface conditions.

Khair and Squires [316] studied the electrophoretic motion of spherical particles with hydrodynamic slip, showing that in the case of thick diffuse layer $k_d a \ll 1$, the slip boundary will enhance the electrophoretic mobility, however, for thin diffuse layer ($k_d a \gg 1$), the enhancement depends on the zeta potential of the particle surface. In the low to moderate range zeta potential, the mobility increases with the zeta potential, and for the larger zeta potential, the mobility decreases and becomes independent of the zeta potential due to the nonunifrom conductivity inside the EDL. Swan and Furst [274] provided a simpler expression for Henry's function, in which slipping boundary condition is also applied.

Miloh and Boymelgreen [287] investigated the dipolophoresis of ideally polarizable nanoparticles with overlapping EDL in cylindrical nanopores. In this work, EDLs of the nanoparticle and the channel wall get overlapped. The nanoparticle is ideally polarizable, as a result, induced charge electroosmotic flow is also considered in this model. The result shows that both the background EOF and the electrophoretic mobility of the particle depend on the frequency of the applied electric field.

Lee et al [317] combined the electrophoretic motion and the diffusiophoresis and studied the motion of nanoparticles in nanopores. In nanochannels, when the EDL thickness is comparable to the particle size, the diffusiophoresis is dominated by the induced electrophoresis driven by the electric field arising from the polarization of the EDL. In the case of small $k_d a$, the diffusiophoresis is dominated by the second kind of the induced electrophoresis [317].

Movahed and Li [281] studiedthe the electrophoretic motion of rectangular nanoparticles in cylindrical nanochannels and indicated that as the channel size is fixed, a nanoparticle with a larger size will move faster than a smaller one under the same condition. Hsu et al [288] [293,318]pointed out the importance of the boundary conditions of electrophoresis of soft cylindrical particles. The influence of the EOF [293] and the ionic polarization [318] on the electrophoretic mobility of rigid spheres in a charge regulated cylindrical pore filled with multiple ionic species were also investigated. Electrophoresis of a deformable particle in nanochannels has also been studied by Tseng et al. [298] In

2016, Liu and Pennathur [292,319] simulated electrophoretic motion of nanoparticles in nanochannels with overlapped EDLs and found that the mobility of the nanoparticles is affected by the confined channel size significantly.

Table 5-1 Summary of electrophoresis theory.

	Particle property	**Electric field**	**Zeta potential range**	**Thickness of the EDL**	**Boundaries or channel type**	**Equations**	**mobility**	**Additional inf**
Wiersema and Overbeek 1966 [277]	Rigid sphere, single non-conducting, uniform dielectric constant particle	Moderate (in the order of few V/cm)	Moderate zeta	$0.2 < k_d a < 50$	Open, the viscosity and dielectric constant of fluid is independent of position	Relaxation effect of the EDL is considered	Direct numerical, no approximation	Brown motion is negligible
O'Brien and White [296]	Solid colloidal particle		Large range		Unbounded		Direct numerical, no approximation	
O'Brien and Hunter [289]	Large Particles		Large zeta potential	Large $k_d a$ $k_d a$ >150 Thin EDL	Polarizable double layer		Analytical solutions	
Ohshima, Healy and White [275]	Spherical colloidal particle		All value of zeta	Large $k_d a$ $k_d a$ >10	Open			
Keh and Anderson 1985 [278]	No conducting Spherical single, particle (dilute solution)	weak	Uniformly charged particle	Thin EDL $k_d a \rightarrow \infty$	Bonded boundaries: Single flat wall, parallel walls and long circular tube with EDL overlap	P-N-P equation With angular velocity	Analytical solutions	
Keh and Chen [279]	Dielectric sphere	Parallel and uniform	Uniformly charged particle	Thin EDL $k_d a \rightarrow \infty$	Single non-conducting plane	P-N-P equation With angular velocity	Analytical solutions	
Chen and Keh [276]	Non-conducting sphere 2 particles		2 particle with different zeta potential and size	Thin EDL $k_d a \rightarrow \infty$	Open boundary	Stokes equation and Laplace equation	Analytical solutions	
Yoon and Kim[310]	Spheroids and oblate spheroids	Low potential	Constant surface potential	Low ka $k_d a \approx 1$	Open boundary	Linearized P-B equation	Analytical solutions	

Mangelsdorf and White [311]	Solid spherical colloidal particles, large particle size	Oscillating electric field of 10^5 Hz	Constant and uniform surface potential Arbitrary value	Large range (Arbitrary value)	Open boundary	N-S equation with inertial term and colloidal-particle force balance equations	Numerical solution	Brownian motion is negligible
Ohshima [272 273]	Solid spherical colloidal particles [272], solid cylindrical particle [273] and Soft particle [304 303]		Low zeta	Arbitrary value (all $k_d a$)	Open boundary		Analytical solutions	
Ennis and Anderson 1997 [285]	Spherical particle	Low	Low zeta	Arbitrary value (all $k_d a$)	Single flat wall, slit and circular tube No significant EDL overlap	P-N-P equation and N-S equation	Analytical approximation solutions	
Shugai and Carnie [280]	Spherical particle	Low	Low zeta	Arbitrary thickness of EDL	Single flat wall, slit, and circular tube, with EDL, overlapped		Numerical solution	
Ohshima [312 313]	Spherical particle	Low	High and low (existence of critical surface charge)	Thick EDL (salt-free medium)	Open boundary	P-B equation	Analytical solutions and numerical solutions	
Ohsihma[314]	Spherical particle	Low	All value	Large ka $k_d a > 30$	Open boundary	P-N-P equation and approximate method	Analytical solutions	
Hsu, Ku and Kao [286]	Spherical particle	Low	Low	Thick EDL	In cylindrical pore with a charged surface	Linearized P-B equation and N-S equation	Numerical solution	With EOF considered
Hsu and Chen [284]	Spherical particle	Low	Polarized EDL	Thick EDL	In cylindrical pore with a charged surface	Linearized P-B equation and N-S equation	Numerical solution	With both EOF and polarized EDL considered
Liu, Qian, and Bau 2007 [320]	Cylindrical particles	Low	Uniform charge density	arbitrary EDL thickness;	Nanopore boundary	P-N-P equation and N-S equation	Numerical solution	Multi-ion model with polarized EDL considered

Khair and Squires [316]	Spherical particle	low	Uniform charge density Various values	$k_d a \gg 1$ and$k_d a \ll 1$	Bounded boundaries with hydrodynamic slip	P-N-P equation and N-S equation	Numerical solution and analytical solutions	The enhancement of electrophoretic mobility depends on zeta
Swan and Furst [274]	Spherical particle		Low zeta potential	Various value	Open boundary with slipping boundary surface	Based on Henry's function	Analytical solution	With slipping surface
Lee et al [317]	Spherical nanoparticle	Low	Various value	Various value	Nanopore	P-N-P equation, Strokes equation	Numerical solution	With concentration gradient into account
Movahed and Li [281]	Rectangular nanoparticle		Various value	Various value	Bounded nanochannel	P-N-P equation, N-S equation	Numerical solution	
Tseng et al. [298]	Deformable nanoparticle	Low	Various value	Various value	Cylindrical nanochannel	P-N-P equation, N-S equation	Numerical solution	Electroosmotic retardation flow is considered
Liu and Pennathur [292,319]	Spherical nanoparticle	Weak	100mV	$0.1 < k_d a < 100$	Confined nanochannel (20, 50 and 100nm)	P-N-P equation, N-S equation	Numerical solution	

5.1.2 Experiments

Experimental studies of the electrokinetic motion of single particles provide a fundamental understanding of electrokinetic transport phenomena. For example, the channel wall effects on the electrokinetic motion of individual spherical microbeads in PDMS microchannels have been studied by Xuan et al. [321,322]. For transport of single nanoparticles in nanochannels, several numerical models [292,323] were presented recently; however, systematic studies of the electrokinetic motion of nanoparticles in nanopores or in straight nanochannels by experiments are very limited [267,324–326]. One possible reason is that the nanochannels used in these studies are made of silicon, glass [267,325] or thermal plastics, consequently, high-cost equipment and complicated procedures are required for the device fabrication. In addition, the nanochannels used in these works are nano-slits that have only one dimension in the nanometer scale, while other dimensions of these nano-slits are larger than 5 μm [325,326]. Obviously, in these nano-slits, the nanoscale channel wall can influence the nanoparticle motion just in one dimension. Furthermore, because the other dimensions are in the micron scale, such a nano-slit allows transport of multiple nanoparticles through the same cross-section of the channel simultaneously. Interactions between these nanoparticles may affect the electrophoretic mobility of the particles. [327–331] Also, the ionic concentration of the buffer solutions is limited in a small range in these works, which is not sufficient to study the ionic concentration effects on the electrokinetic motion of nanoparticles. Electrophoresis of spherical nanoparticles in nanochannels with a particle-to-nanochannel size ratio larger than 0.67 [326] is still a mystery.

This chapter investigates the electrokinetic motion of single polystyrene nanoparticles in single PDMS nanochannels systematically. A novel method to fabricate PDMS-glass micro-nanochannel chips with single nanochannels smaller than 70 nm deep is deomonstrated. All the nanochannels used in this study are in sub-micron in both the width and the depth dimensions. Electrokinetic motion of single fluorescent nanoparticles diluted in LiBr aqueous solutions from 10^{-5}M to 10^{-2} M in single nanochannels is measured by a fluorescent particle tracking system. Ionic concentration effect, particle size to channel size ratio effect, and electric field effect on the motion of single nanoparticles are investigated quantitatively. An extreme case of large size ratio (as large as 0.9) is examed and a numerical model is also created to simulate the electrokinetic motion of single particles in single nanochannels.

5.2 Materials and Methods

5.2.1 Numerical simulation

In the numerical simulation section, 3D models are reduced to 2D in order to reduce the computational cost, and the models are solved by Comsol software (SOMSOL 4.3b). Figure 5-1(a) shows an example of a 3D model, a single nanoparticle translocating in a rectangular nanochannel, and Figure 5-1(b) shows a simplified model in 2D. Poisson-Nernst-Planck equation and Navier-Stokes equation are coupled to solve the flow field, ionic concentration field as well as the electric field in the nanochannel.

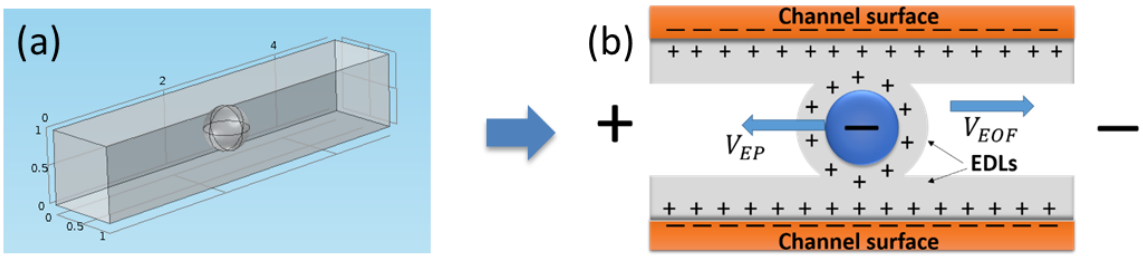

Figure 5-1 Modeling of electrophoretic motion of a nanoparticle in a nanochannel. (a) A 3D model of the simulation; (b) A simplified 2D model.

5.2.1.1 Physical modeling

Figure 5-2 illustrates the computational domain for electrophoresis of a single nanoparticle in a single nanochannel. The nanochannel is 2d in width and L in length, and the nanoparticle is *a* in radius locating at the middle of the nanochannel initially. The nanochannel is filled with LiBr buffer solution. An electric potential is applied between the entrance and the exit of the nanochannel to drive the liquid and the nanoparticle. ABCD is the computational domain of the nanochannel and Γ is the boundary of the nanoparticle. Governing equations and boundary conditions are listed as follows:

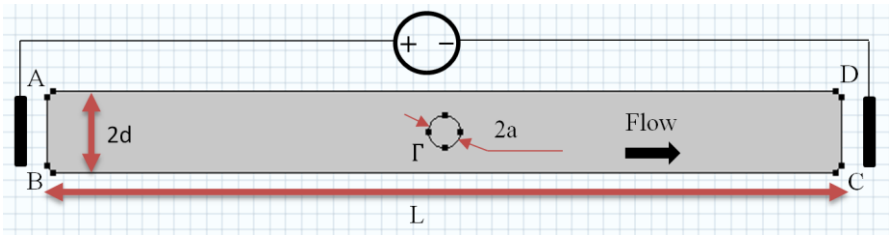

Figure 5-2 Modeling of electrophoresis of a single nanoparticle in a single nanochannel.

5.2.1.2 Electric field

Electric Field in EDL. During the modeling, uniform surface zeta potentials are considered for both the channel wall and the nanoparticle. The Poisson equation is applied to calculate the electric potential distribution in the computational domain.

$$-\nabla(\varepsilon_0\varepsilon_r\nabla\Psi) = \rho_e \quad (5\text{-}1)$$

$$\rho_e = F\sum_i c_i z_i \quad (5\text{-}2)$$

where Ψ is the electric potential of the channel surface or the nanoparticle, and ρ_e is the net charge density, F is the Faraday constant. c_i and z_i are the ionic concentration and valence of Li^+ and Br^-respectively. The boundary conditions are:

$$\boldsymbol{n}\cdot(\varepsilon_0\varepsilon_r(-\nabla\Psi)) = 0 \text{ at AB and CD} \quad (5\text{-}3)$$

$$\Psi = \zeta_w \text{ at channel wall AD and BC} \quad (5\text{-}4)$$

$$\Psi = \zeta_p \text{ at the particle surface } \Gamma \quad (5\text{-}5)$$

Externally Applied Electric Field. In the nanochannel area, the externally applied electric field is weak and assumed to be independent to the EDL, and the applied electric field is also governed by Poisson equation,

$$-\nabla(\varepsilon_0\varepsilon_r\nabla\Phi) = 0 \quad (5\text{-}6)$$

where Φ is the externally applied electrical voltage, the boundary conditions are

$$\boldsymbol{n}\cdot\boldsymbol{D} = 0 \text{ at AD and BC and } \Gamma \quad (5\text{-}7)$$

$$\Phi = V1 \text{ at AB} \quad (5\text{-}8)$$

$$\Phi = 0 \text{ at CD} \quad (5\text{-}9)$$

5.2.1.3 Flow field

Stokes equation and the continuity equation are solved in order to calculate the flow field inside the nanochannel. Here, we assumed that the fluid is incompressible and the flow inside the nanochannel is laminar flow due to the low Re number, and no pressure is applied between the entrance and the outlet of the nanochannel.

$$\rho_w \frac{\partial \boldsymbol{V_{EOF}}}{\partial \mathrm{t}} = -\nabla P + \mu \nabla^2 \boldsymbol{V_{EOF}} - \rho_e \nabla \Phi \quad (5\text{-}10)$$

$$\nabla \cdot \boldsymbol{V_{EOF}} = 0 \quad (5\text{-}11)$$

where ρ_w is the density, P is the pressure, μ is the dynamic viscosity of the electrolyte solution. The boundary conditions at channel walls are nonslip due to the viscos effect and no pressure at the channel ends. Here, in order to save the computational cost, we set the original point of the coordinate system at the center of the nanoparticle, and a relative slipping veloicty (EK velocity of the nanoparticle, but opposite direction) is setted on the nanochannel walls as a slip boundary. As a result, the boundary conditions are:

$$\boldsymbol{V_{EOF}} = -\boldsymbol{V_{EK}} \text{ at AD and BC} \quad (5\text{-}12)$$

$$P = 0 \text{ at AB and CD} \quad (5\text{-}13)$$

$$\boldsymbol{V_{EOF}} = \boldsymbol{0} \text{ at the surface of nanoparticle } \Gamma \quad (5\text{-}14)$$

5.2.1.4 Ionic concentration field

The thickness of EDL is comparable to the channels size and electric double layers are likely to get overlapped in nanochannels, consequently, N-P equation is applied.

$$\nabla \boldsymbol{N_i} = 0 \quad (5\text{-}15)$$

$$\boldsymbol{N_i} = -D_i \nabla c_i - z_i \mu_i c_i \nabla \Psi + c_i \boldsymbol{V_{EOF}} \quad (5\text{-}16)$$

$$\mu_i = \frac{D_i}{RT} \quad (5\text{-}17)$$

where $\boldsymbol{N_i}$, D_i, μ_i are the flux, diffusion coefficient and ion mobility of Li^+or Br^- respectively. $\boldsymbol{V_{EOF}}$ is the fluid velocity inside the nanochannel, R is the gas constant. And the following boundary conditions are applied:

$$\boldsymbol{n} \cdot \boldsymbol{N_i} = 0 \text{ at AD and BC} \quad (5\text{-}18)$$

$$c_i = c_{i\infty} \text{ at AB and CD} \quad (5\text{-}19)$$

$$\boldsymbol{n} \cdot \boldsymbol{N_i} = \boldsymbol{n} \cdot (c_i \cdot \boldsymbol{V_P}) \text{ at the surface of nanoparticle } \Gamma \quad (5\text{-}20)$$

Here $c_{i\infty}$ is the concentration of the bulk solution.

5.2.1.5 Particle motion

The nanoparticle is subjected to an electrostatic force due to the negatively charged surface (F_{ep}), a hydrodynamic force (F_{hd}) owing to friction between the particle and electroosmotic motion and a dielectrophoresis force (F_{dep}) caused by the nonlinearly distributed electric field and the polarizable property of the nanoparticle. However, in this simulation, the DEP force is neglected and the nanoparticle is treated as nonpolarizable. Therefore, the total force acting on the nanoparticle is:

$$\boldsymbol{F_t} = \boldsymbol{F_{ep}} + \boldsymbol{F_{hd}} \tag{5-21}$$

The electrophoretic force and the hydrodynamic force can be calculated by:

$$\boldsymbol{F_{ep}} = \iint \boldsymbol{T} \cdot d\boldsymbol{s} \tag{5-22}$$

$$\boldsymbol{T} = \varepsilon_0 \varepsilon_r \left(E_i E_j - \frac{1}{2} \delta_{ij} |E|^2 \right) \tag{5-23}$$

$$\boldsymbol{F_{hd}} = \iint \boldsymbol{n} \cdot (-\boldsymbol{PI}) + \mu[\nabla \boldsymbol{V_{EOF}} + (\nabla \boldsymbol{V_{EOF}})^T] d\boldsymbol{s} \tag{5-24}$$

where $\boldsymbol{T}$ is the Maxwell stress tensor of the applied electric field and $\boldsymbol{I}$ is the unit tensor. The velocity of particles can be calculated by using the Newton's second law for each step:

$$\boldsymbol{F_t} = m_p \frac{d\boldsymbol{V_{EK}}}{dt} \tag{5-25}$$

where $m_p$is the mass of the nanoparticle,

$$m_p = \rho_p \frac{4\pi a^3}{3} \tag{5-26}$$

Where ρ_p is the density of particle, and the velocity of the particle $\boldsymbol{V_{EK}}$ is obtained until the total force reaches zero.

5.2.1.6 Numerical method and examples of results

The Poisson equation, N-P equation, N-S equation and continuity equation are fully coupled to calculate the electric field, ionic concentration field, and the flow field. Table 5-2 lists the parameters and constant values used in this simulation. Here the variables such as channel size (500 nm×50 nm), particle size (30 nm in diameter), concentration of electrolyte solution (0.1 mM), applied electric field (100 V/cm) zeta potential of the channel surface ($-50\,mV$) and zeta potential of the partilce

surface ($-50\,mV$) etc. are setted in an example model. During the systematic study, these values were changed as needed, and the results of the example model simulated by using the parameters listed in Table 5-2 are demonstrated as follows.

Table 5-2 Constants and parameters used in the simulation.

Parameter	Description	Value and unit
$\boldsymbol{\mu_w}$	Viscosity of electrolyte	0.9×10^{-3} [Pa*s]
$\boldsymbol{\rho_w}$	Density of water	1000 [kg/m^3]
$\boldsymbol{\rho_p}$	Density of particle	1190 [kg/m^3]
$\boldsymbol{\zeta_w}$	Zeta potential of channel wall	-50 [mV]
$\boldsymbol{\zeta_p}$	Zeta potential of particle	-50 [mV]
$\boldsymbol{\varepsilon_r}$	Dielectric constant of water	80[1]
$\boldsymbol{\varepsilon_0}$	Permittivity of vacuum	8.854×10^{-12} [F/m]
$\boldsymbol{a}$	Radius of particle	15 [nm]
L	Length of channel	500 [nm]
W	Width of channel	50 [nm]
$\boldsymbol{V_1}$	Electric potential applied on the entrance	5 [mV]
$\boldsymbol{c_{inf}}$	Bulk concentration	0.1[mol/m^3]
$\boldsymbol{z_1}$	Valence of Li^+	1[1]
$\boldsymbol{z_2}$	Valence of Br^-	-1[1]
e	Unit charge	1.602×10^{-19} [C]
NA	Avogadro constant	6.022×10^{23} [1/mol]
F	Faraday Constant	9649 [C/mol]
$\boldsymbol{D_1}$	Diffusion coefficient of Li^+	1.03×10^{-9} [m^2/s]
$\boldsymbol{D_2}$	Diffusion coefficient of Br^-	2.084×10^{-9} [m^2/s]
R	Gas constant	8.314[J/mol/K]
$\boldsymbol{k_b}$	Boltzmann constant	1.381×10^{23} [J/K]
T	Temperature	293[K]

Figure 5-3 shows the electric potential distribution in the nanochannel and around the nanoparticle. Here the externally applied electric field is neglected because the electric field inside the EDL is several magnitudes stronger than that of the externally applied electric field. For example, in this case, the electric field inside the EDLs (in the width direction) is in the order of $10^4\ V/cm$ and the external electric field in the length direction is only about $100\ V/cm$. The surface plot in Figure 5-3 shows the electric field distribution inside the nanochannel. Obviously, EDLs get overlapped inside the nanochannel and the electric potential at the middle plane of the nanochannel is nonzero.

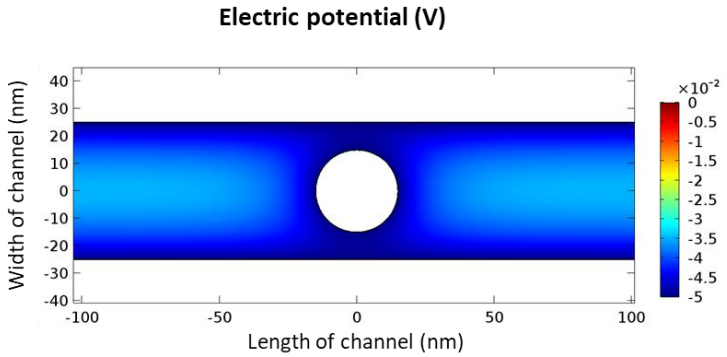

Figure 5-3 Electric field distribution in the nanochannel and around the nanoparticle. The zeta potential of both the channel wall and the nanoparticle surface is –50 mV.

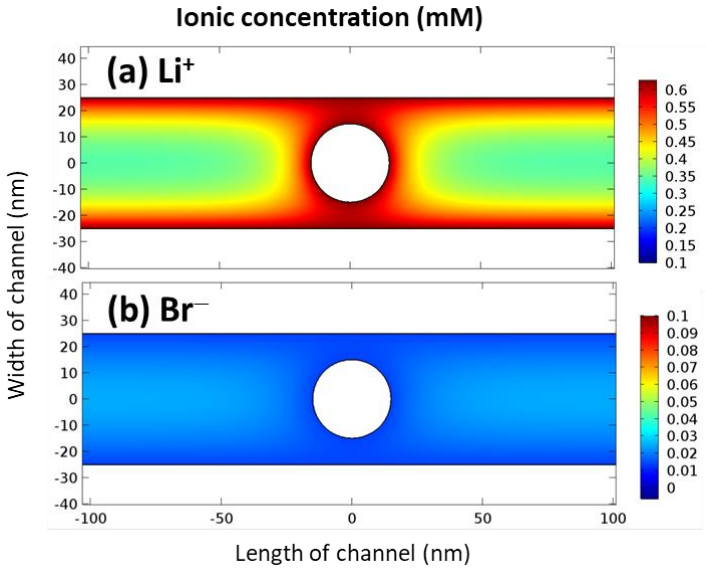

Figure 5-4 Ionic concentration distribution of (a) Li^+ and (b) Br^- in the nanochannel and around the nanoparticle. EDLs get overlapped inside the nanochannel. The applied electric field is 100 V/cm, and the zeta potential of both the channel wall and the nanoparticle is -50 mV.

Figure 5-4 shows the concentration of both $Li^+$and Br^- inside the nanochannel and around the nanoparticle. The concentration of both $Li^+$and Br^- in the bulk solution at the entrance and outlet of the nanochannel is 0.1 mM. The corresponding Debye length is about 30 nm, and EDLs get overlapped in the nanochannel. From Figure 5-4 one can see that the channel is occupied by Li^+, and the concentration of Br^-inside the nanochannel is extremely low due to the electrostatic repulsion force between the negatively charged Br^- ions and the negatively charged channel surface/particle surface. Figure 5-5 shows flow field inside the nanochannel, the surface plot shows the flow field and

the arrow surface depicts the velocity profile. The calculated velocity of the nanoparticle is about 85.9 $\mu m/s$.

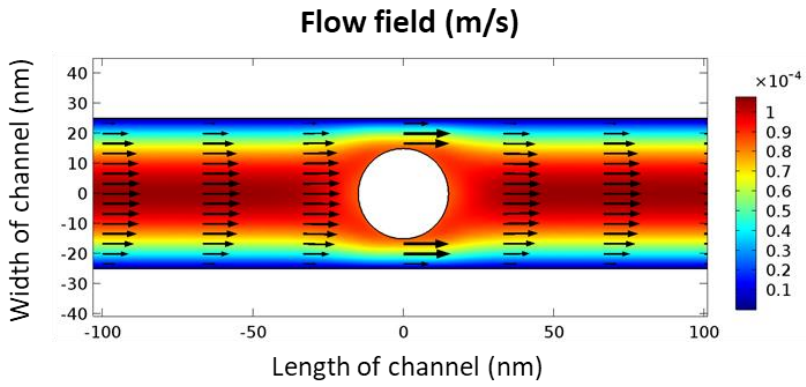

Figure 5-5 Flow filed inside the nanochannel. The applied electric field is 100 V/cm. The surface plot shows the flow field and the arrow plot depicts the profile of the flow field.

5.2.2 Experimental setup

5.2.2.1 Fabrication of nanofluidic chips

Reliable and reproducible micro-nanofluidic chips are essential to the experimental studies of the electrokinetic motion of nanoparticles in nanochannels. PDMS nanochannels were fabricated by following the working procedures listed in CHAPTER 3 and integrating microchannels and nanochannels into one channel mold is demonstrated in Appendix G. Figure 5-6 (a) shows an example of the micro-nanochannel chips and Figure 5-6 (b) is a zoomed-in view of the nanochannel section. Figure 5-6 (c) and Figure 5-6 (d) are a 3D image of the nanochannel and three cross-sections of this nanochannel measured by the AFM, respectively.

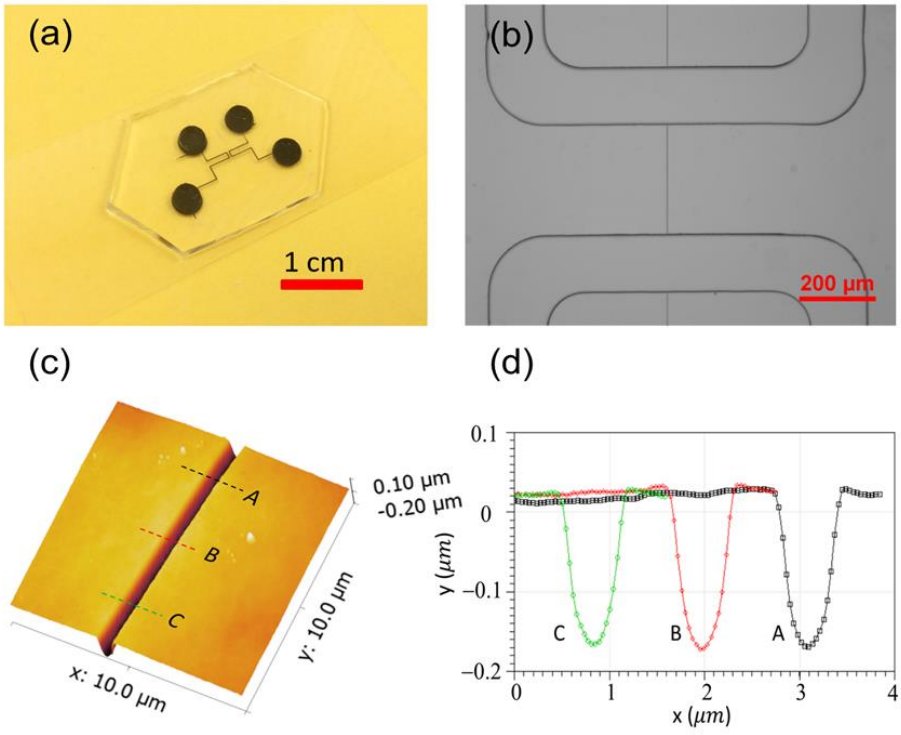

Figure 5-6 (a) An example of the PDMS-glass micro-nanochannel chips, (b) a zoomed-in view of the micro-nanochannel conjunctions of the micro-nanochannel chip, (c) a 3D image of the nanochannel and (d) three cross-sections A, B and C of this nanochannel, separated by 3 μm measured by the AFM.

5.2.2.2 Fluorescent nanoparticle tracking system

The most direct way to determine the velocity of a fluorescent nanoparticle is to track the motion of the fluorescent nanoparticle by using a fluorescent microscope. Figure 5-7 (a) shows a schematic diagram of the nanoparticle tracking system used in this study. This system is composed of a fluorescent microscope (Nikon Ti-E), a PDMS-glass micro-nanofluidic chip, a DC power source and a computer with image processing software (NIS-Elements BR). The fluorescent microscope is equipped with a 100× oil immersion objective lens (Apo λ, NA=1.45), a blue laser source (λ =488 nm) and a CCD camera (Q-imaging, Retiga 2000R). During the experiments, the nanofluidic chip was located on the working stage of the microscope with the nanochannel section on the focal point of the oil lens. Nanoparticle samples were loaded into the microchannels and the nanochannel through the channel wells. A DC electric field (Keithley, 6517A) was applied along the single nanochannel through two Platinum electrodes inserted in the channel wells. By this way, nanoparticles were loaded into the nanochannel by electroosmotic flow. As nanoparticles moved in

the nanochannels under the electric fields, the CCD camera recorded the motion of the nanoparticles and the software calculated the apparent velocity of the particles. Figure 5-7 (b) shows an example of the trajectory of a 140 nm particle in a 340 nm deep nanochannel under an electric field of 20 V/cm. The nanoparticle is suspended in 10^{-4} M LiBr solution, and the average apparent velocity of this nanoparticle is 68.5 $\mu m/s$.

In this work, in order to study the electrokinetic motion of single nanoparticles in single nanochannels, only one single nanoparticle was introduced into the nanochannel each time. However, for most cases, both the PDMS nanochannel wall and the nanoparticles are negatively charged. As a result, the nanoparticles can hardly flow into the nanochannel freely even an external electric field (for example, 20 V/cm in the experiments) was applied along the nanochannel due to electrostatic repulsion between the channel wall and the nanoparticles. However, nanoparticles would accumulate at the entrance of the nanochannel due to the electrostatic attraction force. To "push" the nanoparticles into the nanochannel, a very strong electric field pulse (duration of less than 0.5 s) was applied to the nanochannel; consequently, one or more nanoparticles were introduced into the nanochannel in a very short time due to the strong electrostatic force along the axis of the nanochannel. In the case of more than one nanoparticle was loaded into the nanochannel, a weak electric field was applied on the nanochannel to drive the nanoparticles and release some of them, finally leaving only one inside the channel. It should be noted that, because the nanochannels used are in nanoscale in both the depth and the width directions, the nanoparticles inside the nanochannel would line up automatically due to the above-mentioned electrostatic repulsion force between the channel wall and the nanoparticles. As a result, the extra particles can be released precisely. As only one nanoparticle was left in the channel, we switched the direction of the electric field back and forth to drive or manipulate the single nanoparticle and to measure the electrokinetic velocity, generally, for 10 times or more. After that, this particle was released, and another one was loaded, and so on and so forth.

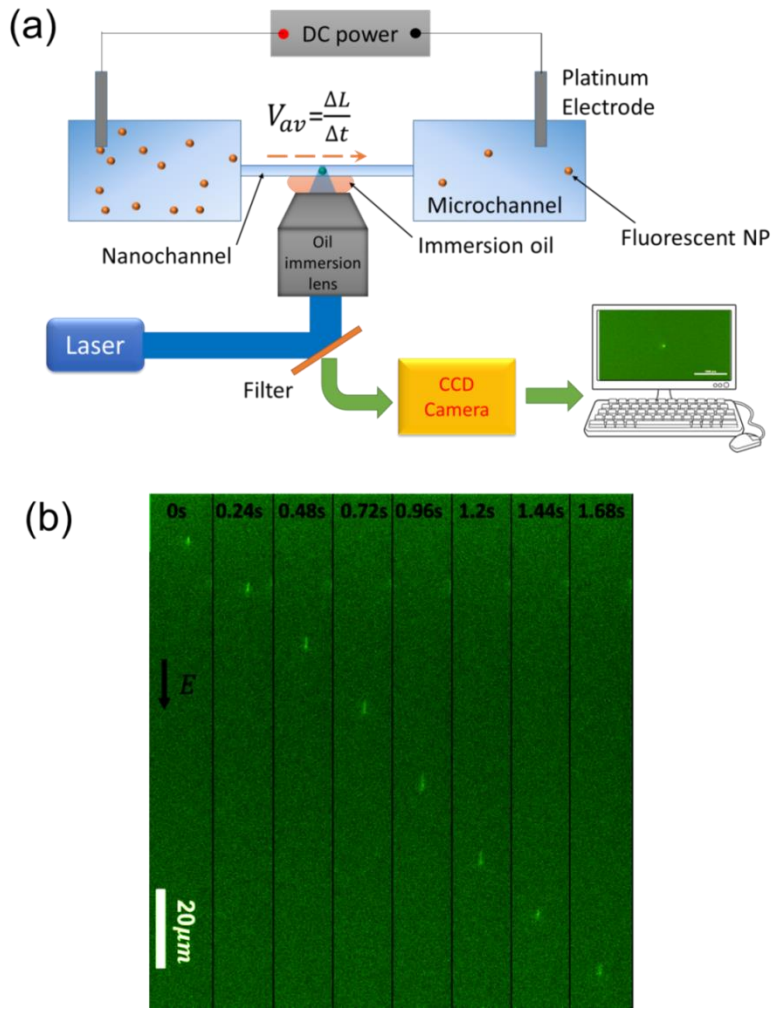

Figure 5-7 (a) Schematic of the fluorescent particle tracking system, and (b) an example of the electrokinetic motion of a 140 nm particle in a 340 nm deep nanochannel under 20 V/cm electric field. The video was captured by a CCD camera with an exposure time setting of 80 ms.

5.2.2.3 Chemical reagents and experimental procedures

The particle-solution samples were prepared by diluting carboxylated polystyrene fluorescent nanoparticles (Bangs Laboratories Inc.) into LiBr solutions. The particle concentration used in the experiments was diluted to about 10^9/mL. Three sizes of nanoparticles, 60 nm, 83 nm and 140 nm, were used in this study. The ionic concentrations of LiBr solutions used in this work were 10^{-5} M, 10^{-4} M, 10^{-3} M, and 10^{-2} M. The buffer solutions were obtained by dissolving LiBr (Fisher Scientific) into pure water (Mini Q, Direct-Q3, 18.2 MΩ·cm). The length of the nanochannels was about 300 μm. DC electric fields from 10 V/cm to 100 V/cm were applied over the 300 μm long nanochannels. To study the particle-to-channel size ratio effects on the electrokinetic motion of

nanoparticles, 6 nanochannels and 2 straight microchannels were fabricated. Table 5-3 gives the details of the channels.

Table 5-3 Sizes of the PDMS-glass microchannels and the PDMS-glass nanochannels.

Channel No.	Width (w)	Depth (b)
1	$50\mu m$	$25\mu m$
2	$10\mu m$	$5\ \mu m$
3	$501 \pm 24nm$	$340 \pm 17nm$
4	$460 \pm 15nm$	$157 \pm 13.5nm$
5	$436 \pm 18nm$	$102 \pm 5.6nm$
6	$596 \pm 11nm$	$91 \pm 5nm$
7	$450 \pm 25nm$	$83 \pm 6.5nm$
8	$507 \pm 11nm$	$67 \pm 3nm$

Chip conditioning was conducted by loading LiBr solutions into the fresh channels for 15 minutes before nanoparticle samples were loaded. It should be noted that the buffer solution used for the chip conditioning was the same as that of the nanoparticle sample solutions. For each working condition, i.e. one channel size, one particle size, one ionic concentration and one electric field, the experiments were repeated for at least three times on three independent fresh chips; and for each chip, the motion of the nanoparticles was tracked for at least 10 times. The motion of these nanoparticles was captured by the CCD camera with an exposure time setting of 80~150 ms. For large nanoparticles, for example, 140 nm nanoparticles, the fluorescent light intensity is high and the exposure time setting was relatively short, 80 ms; however, for smaller nanoparticles, for example, 60 nm nanoparticles, the exposure time was 150 ms to make sure the accuracy of the measurement. All the experiments were conducted at room temperature of about 23 ℃. For all the cases, only the apparent velocity was measured. The apparent velocity is the combined velocity of the electrophoresis of the particle and the the electroosmotic flow of the fluid inside the channel, and genreally speaking the aparent velocity is more useful for practical applications.

5.3 Results and discussion

5.3.1 Ionic concentration effects

Nanoparticles of 60 nm and 140 nm in diameter diluted in 10^{-2} M, 10^{-3} M, 10^{-4} M and 10^{-5} M LiBr solutions were tested in two nanochannels with cross-sections of 340 × 501 nm and 157 ×

460 nm, respectively, as well as in a microchannel of 25×50 μm. The applied electric field for all the cases was 20 V/cm. The apparent velocity of the 60 nm and 140 nm nanoparticles is shown in Figure 5-8, in which a is the diameter of the nanoparticles and b is the depth of the channels. From Figure 5-8 one can see that in the microchannel, the apparent velocity of 140 nm nanoparticles increases with the decreasing ionic concentration from 45 $\mu m/s$ to 110 $\mu m/s$, which is consistent with the dependence of the electroomostic flow on the ionic concentration [332]. The increase of the EOF is due to the increase in zeta potential of the microchannel wall surfaces. However, the zeta potential of the nanoparticles also increases with the decreasing ionic concentration. From the results one can conclude that the influence of the increasing zeta potential of the nanoparticle is minor and the apparent velocity of the nanoparticles is dominated by the electroosmotic flow in the channel.

In the two nanochannels, the apparent velocity of both 60 nm and 140 nm nanoparticles increases as the ionic concentration decreases from 10^{-2} M to 10^{-3} M. However, as the ionic concentration decreases further, the velocity of both the 60 nm and 140 nm nanoparticles experiences a decreasing trend, which is opposite to that in the microchannel. Obviously, for the cases of 10^{-2} M and 10^{-3} M solutions in nanochannels, the thickness of the EDL is very thin, about 10 nm and 40 nm, respectively; as a result, there is no overlap of EDLs in these two nanochannels, the electroosmotic flow in these two nanochannels is the same as that in the microchannel, increasing with the decrease in ionic concentration, similar to that in the microchannel as mentioned above. By contrast, as the ionic concentration decreases further, to 10^{-4}M and 10^{-5} M, the thickness of the EDL adjacent to the channel walls increases dramatically, to about 120 nm and 400 nm respectively; as a consequence, EDLs are overlapped in the two nanochannels, resulting in decreasing EOF velocities inside the nanochannels. The effects of overlap of EDLs on the electroomotic flow in nanochannels has been demonstrated in CHAPTER 4. In addition, as the ionic concentration decreases, the increase of zeta potential of the polystyrene nanoparticles will also give rise to larger electrophoretic mobility values of these nanoparticles, but in the opposite direction of the electroosmotic flow. As a result, the apparent velocity of 60 nm particles decreases further, to about 38 $\mu m/s$ and 55 $\mu m/s$ in the 157 nm deep and 340 nm deep nanochannels filled with 10^{-5} M ionic concentration solution.

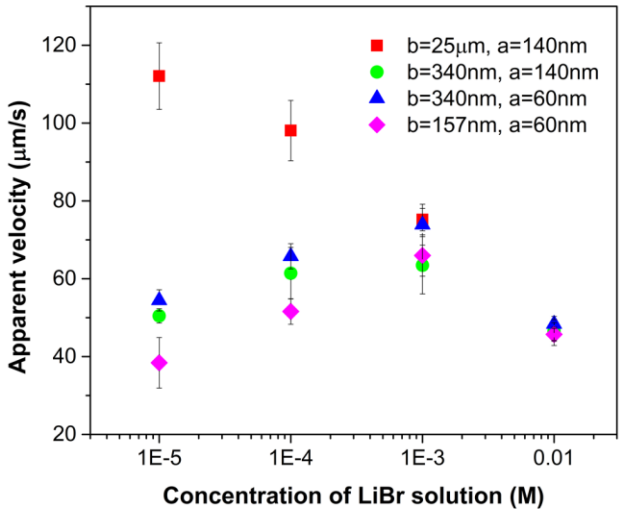

Figure 5-8 Concentration effects on the electrokinetic velocity of single nanoparticles in single nanochannels. Apparent velocity of 60 nm particles and 140 nm nanoparticles in single nanochannels of 340 × 501 nm cross section and, 157 × 460 nm cross section, and in a microchannel of 25 × 50 μm was measured by the particle tracking system. For all these cases, the electric field applied over the nanochannels and the microchannel is 20 V/cm and the ionic concentrations of the LiBr solutions are 10^{-2} M, 10^{-3} M, 10^{-4} M and 10^{-5} M. In this figure, a is the diameter of the nanoparticles, and b is the depth of channels.

Interactions of EDLs between the nanochannels and the nanoparticles affect the apparent velocity of the nanoparticles. As the ionic concentration decreases, the thickness of EDL near both the nanochannel walls and the nanoparticle surface increases, and EDLs may overlap in the gaps between the nanochannel walls and the nanoparticles easily, especially for the large particle-to-channel size ratio systems. For example, in the case of 157 nm nanochannel loaded with 60 nm nanoparticles diluted in 10^{-3} M LiBr solution, no overlap of EDL between the channel walls, because the thickness of the EDL is about 40 nm which is much smaller than the half depth of the nanochannel, about 80 nm. However, if a 60 nm nanoparticle was loaded in this nanochannel, the gap between the nanoparticle surface and the channel wall should be around 50 nm, assuming that the nanoparticle is located in the centerline of the nanochannel due to EDL repulsion [292]. Consequently, the thickness of the EDL, 40 nm, is larger than the half length of the gap, 25 nm, which means EDLs get overlapped between the nanoparticle and the nanochannel walls. For the cases of particle motion in overlapped EDLs, it is hard to find an analytical solution for the

nanoparticle transport behavior due to the sophisticated interactions between the particle and the channel wall. However, from Figure 5-8 one can see that the apparent velocity of the 60 nm nanoparticles is smaller than that in the microchannel. Compared with the cases without overlap of EDLs mentioned above, the zeta potential changes are the same. The only difference is that in the nanochannels, EDLs are overlapped. Consequently, we can predict that the electrokinetic motion of nanoparticles in nanochannels filled with diluted ionic solutions is dominated by the overlap of EDLs.

5.3.2 Particle-to-channel size ratio effects

Figure 5-9 depicts the channel size effects on the electrokinetic motion of 60 nm nanoparticles. Nanochnanels of 340 nm, 157 nm, 102 nm, 91 nm and 84 nm in depth as well as microchannels of 25 μm and 5 μm in depth were tested. During the experiments, nanopartilces were diluted in 10^{-2} M and 10^{-5}M LiBr solutions and loaded in these channels. The applied electric field for all the cases was 20 V/cm. In Figure 5-9, the size ratio a/b is plotted as the x-axis, where a is the diameter of the nanoparticle and b is the depth of the channels. It is obvious that the apparent velocity of the nanoparticles decreases with the size ratio for both concentration values. For instance, for the 10^{-2} M cases, the apparent velocity of the 60 nm nanoparticles in the microchannels ($a/b \approx 0$) and the large nanochannel (340 nm deep nanochannel, $a/b = 0.18$) is about $50 \mu m/s$; however, as the channel size decreases to 84 nm deep ($a/b = 0.71$), the apparent velocity decreases gradually to about 22 $\mu m/s$.

Similarly, for the cases of 10^{-5} M ionic concentration, the velocity of the 60 nm nanoparticles in the microchannels is about 110 $\mu m/s$; however, when the channel size decreases down to nanometer scale ($a/b > 0.18$ in Figure 5-9), the apparent velocity of the nanoparticles decreases dramatically due to the interactions between EDLs. In Figure 5-9, the thickness of the EDL for the 10^{-5} M case is very large, about 400 nm, and EDLs are overlapped between the nanochannel walls and also between the nanochannel walls and the nanoparticles. When EDLs get overlapped, the electroosmotic flow in the nanochannel decreases, and interactions between the nanoparticles and the channel walls also become stronger, consequently, the apparent velocity decreases rapidly with the channel size. For example, the velocity of the 60 nm nanoparticles is about 55 $\mu m/s$ in the 340 nm deep nanochannel ($a/b = 0.18$), and this value decreases to about 20 $\mu m/s$ as the channel size decreases to 91 nm ($a/b = 0.66$), in which EDLs get overlapped strongly. It can be concluded that, as the channel size becomes smaller, the size ratio becomes larger and interactions between the EDLs

is stronger. Strong interactions between EDLs dominate the electrokinetic motion of the nanoparticles inside a small nanochannel and result in a decrement in the apparent velocity.

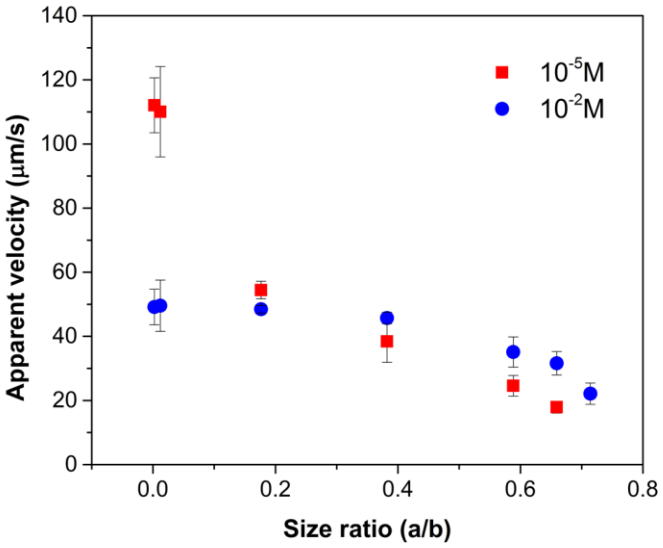

Figure 5-9 Particle-to-channel size ratio effects on the apparent velocity of 60 nm nanoparticles. Nanochannels of 340 nm, 157 nm, 102 nm, 91 nm and 84 nm in depth as well as microchannels of 25 μm and 5 μm in depth are tested. The paricles are diluted in 10^{-2} M and 10^{-5} M LiBr solutions. The applied electric field is 20 V/cm m for all the cases. In this Figure, a is the diameter of the nanoparticles and b is the depth of the channels.

It should be noted, under the condition of strong EDL interactions, for instance, for the case of 60 nm nanoparticles in an 84 nm deep nanochannel (a/b = 0.71) filled with 10^{-5} M LiBr solution, the nanoparticles can hardly move under low electric fields. Aggregation occurs in the nanochannel due to the strong particle-nanochannel electrostatic interactions. An example of 60 nm nanoparticles trapped in an 84 nm deep nanochannel is shown in Figure 5-10 (a). The nanoparticles can only be removed with very high electric field ($10^4 V/cm$ or higher). Trapping of DNAs inside nanopores under the condition of low electric field has also been reported. [333] Attempt of transporting 60 nm nanoparticles in a 67 nm deep nanochannel ($a/b \approx 0.9$) indicates that it is extremely hard to load 60 nm nanoparticles into such a small nanochannel by electroosmotic flow due to strong DEP (dielectrophoresis) force at the channel entrance [334] and the electrostatic repulsion force between the nanoparticles and the channel wall surfaces. Generally, 60 nm nanoparticles are stuck at the entrance of the 67 nm nanochannel, as shown in Figure 5-10 (b).

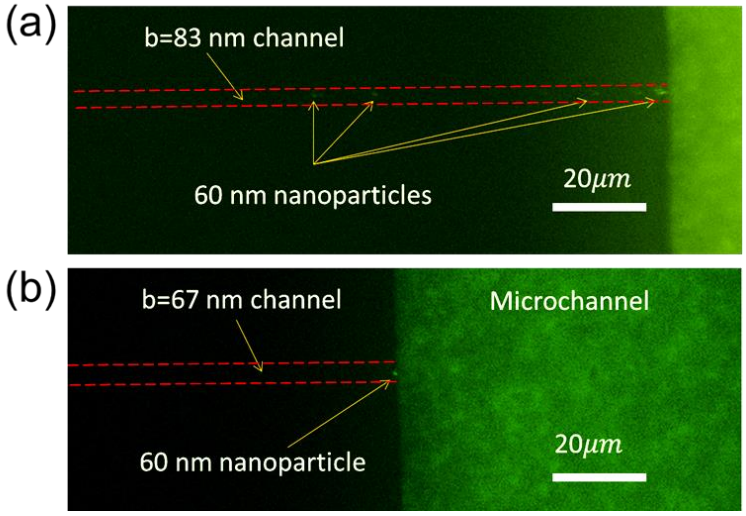

Figure 5-10 (a) Trapping of 60 nm nanoparticles inside an 84 nm deep nanochannel filled with 10^{-5} M LiBr solution, the applied electric field is 20 V/cm, (b) An example of 60 nm nanoparticles stuck at the entrance of a 67 nm deep nanochannel.

5.3.3 Effects of applied electric field

Figure 5-11 demonstrates the electric field effects on the apparent velocity of nanoparticles. Three cases are demonstrated in Figure 5-11: transport of 60 nm nanoparticles in a 157 nm deep nanochannel filled with 10^{-2} M solution, 140 nm particles in a 25 μm deep microchannel filled with 10^{-2} M solution, and 140 nm particles in a 340 nm deep nanochannel loaded with 10^{-3} M LiBr solution. The electric field ranges from 10 V/cm to 100 V/cm for all these cases. It is obvious that the apparent velocity of the nanoparticles increases almost linearly with the applied electric field for all the cases. The slopes of these curves indicate the mobility values of these particles. From Figure 5-11 one can see that for the 10^{-2} M LiBr solution cases, the mobility of 60 nm nanoparticles in the 157 nm deep nanochannel is smaller than that of the 140 nm particles in the 25 μm deep microchannel due to the interactions of the overlapped EDLs as mentioned above.

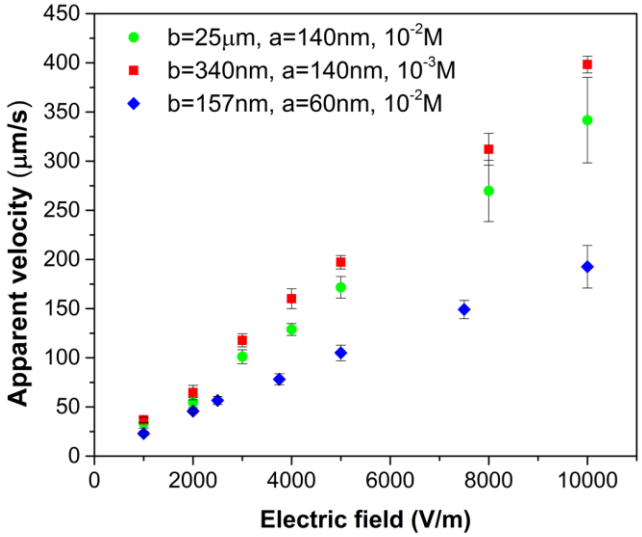

Figure 5-11 Electric field effects on the apparent velocity of nanoparticles. Three cases were tested: 60 nm nanoparticles in a 157 nm deep nanochannel filled with 10^{-2} M LiBr solution; 140 nm nanoparticles in a 25 μm deep microchannel filled with 10^{-2} M LiBr solution; and 140 nm particle in a 340 nm deep nanochannel filled with 10^{-3} M LiBr solution.

In addition, electrokinetic motion of 140 nm nanoparticles in the 25 μm deep microchannel filled with 10^{-2} M LiBr solution is smaller than that in the 340 nm deep nanochannel filled with 10^{-3} M LiBr solution. This is because the mobility of the nanoparticles in channels without overlapped EDLs is dominiated by the EOF. In Figure 5-11, under the condition of higher electric fields, the error bars of the measured velocity are larger compared with that of the low electric field cases because the limitation of the fluorescent tracking system. Under the condition of a high electric field, the velocity of the fluorescent particles is high and a sufficient exposure time is needed to observe the nanoparticles clearly. However, a longe exposure time makes the trajectories of the nanoparticles blurring and results in larger errors during the velocity calculation. “Stick/slip” motion of the nanoparticles under the conditions of low electric field and large size ratio was also observed during the experiments. The “stick/slip” motion was previously observed in the experimental studies of translocation of DNAs through nanochannels probably due to strong electrostatic interactions between the negatively charged DNAs and the positively charged channel wall [335]. However, in this case, both the nanochannel wall and the nanoparticles are negatively charged, the "stick/slip" behaviour may be caused by strong inhomogeneous electric field inside the channel due to the surface roughness of the nanochannel wall.

5.4 Conclusion

This chapter presents a systematical study of electrokinetic motion of single nanoparticles in single nanochannels. PDMS nanofluidic chips with single nanochannels are developed. The effects of ionic concentration, particle-to-channel size ratio (a/b), and electric field on the electrokinetic velocity of fluorescent nanoparticles in six nanochannels and two microchannels by the particle tracing method are investigated. The results show that the electrokinetic velocity of nanoparticles in small single nanochannels increases with the ionic concentration in diluted solutions and decreases with the ionic concentration in concentrated solutions. The apparent velocity of single nanoparticles in single nanochannels decreases with increasing particle size to channel size ratio (a/b) due to the interactions of the overlapped EDLs inside the nanochannels. Under the condition of a proper electric field range, the apparent velocity increases with the applied electric field linearly. “Stick-slip” motion and stuck of nanoparticles in single nanochannels under the conditions of large size ratio and low electric field were also observed. The experimental study presented in this chapter provides an improved understanding of electrokinetic motion of nanoparticles in a confined nanospace and is potentially valuable for the future applications of nanofluidics.

CHAPTER 6 Application I: Detection of Nanoparticles and DNAs by Resistive Pulse Sensing Method on PDMS Nanofluidic Chips [*]

6.1 Introduction

Resistive Pulse Sensing (RPS) technique has been a traditional approach to characterize properties of particles made of metals [336–338], polymers [339,340], semiconductors [341], and particle-like objects like cells [342], proteins [343], viruses [267,340,344,345], bacteria [346] even individual molecules [347] as well as soft particles such as oil droplets [348] and liposomes [341,349,350]. Detecting and sequencing of individual DNA molecules on nanofluidic devices based on the RPS technique [260,351–354], for example, direct observation of DNA knots by using solid-state nanopores [260] and precisely controlled DNA sequencing through α-hemoinlysin nanopores [353] have been reported recently. Furthermore, RPS has also been applied to measure zeta potential or surface charge of nanometer-sized objects, [355–357] to study transport phenomena in confined nanospaces [267,358], to investigate deformation of soft nanoparticles [349] and even to predict the substructure of nanopores [359]. In order to expand the ability of the RPS technique in practical applications, a simple and cost-effective platform with high sensitivity and resolution for nanoscale objects is highly desirable.

A traditional design of an RPS testing device is the "capillary-in-tank" style [337,340,360,361], as reviewed in CHAPTER 2. Specifically, a capillary with a small orifice (the sensing gate) is immersed in a tank of electrolyte solution, and an electric potential difference is applied between the two ends of the orifice. As particles pass through the sensing gate one by one and partially displace the electrolyte solution in the sensing gate, the electric current inside the sensing gate area changes accordingly, generating "pulse" signals which are recorded by an Ammeter. This design was initially developed for cell counting and detection [362], and a large quantity of samples are needed during the measurement. To detect nanoparticles by the traditional design, tiny small nano-orifices or nanopores and a high sensitivity Ammeter are required. However, fabrication of nano-scaled orifices is a difficult task. For example, fabricating nano-pipettes as the sensing gate [337,340,360,361] involves melting and pulling micro-capillaries followed by post-processes such as sanding and etching [336,338]. This

[*] A similar version of this chapter was submitted or published as:
(a) Peng, R.; Li, D. Detection and Sizing of Nanoparticles and DNA on PDMS Nanofluidic Chips Based on Differential Resistive Pulse Sensing. Nanoscale 2017, 9, 5964–5974. http://pubs.rsc.org/en/content/articlehtml/2017/nr/c7nr00488e.
(b) Peng, Ran, and Dongqing Li. "Particle Detection on Microfluidic Chips by Differential Resistive Pulse Sensing (RPS) Method." Talanta 2018, https://doi.org/10.1016/j.talanta.2018.03.023.

method is complicated and can hardly ensure the repeatability of the production. Additionally, observation and characterization of nano-pipette cross-sections are also tricky problems technically [363]. Fabrication of solid-state nanopores by using the techniques of the semiconductor industry, for example, FIB [266,267], and RIE [364] requires expensive nanofabrication facilities and professional fabrication skills [345,352]. In addition, RPS signals generated by the nano-pipettes are asymmetric due to the conical [337,340,360,361] or pyramidal [357] shaped RPS gates, and the velocity of nanoparticles in these RPS gates is not constant. Consequently, it is not accurate to investigate translocations of individual nanoparticles by using the asymmetric RPS gates. Furthermore, the sensitivity of an orifice-based sensing gate is highly dependent on the instrumental sampling rate due to the very short sensing gate and the high moving speed of particles [365]. For the traditional design, Brownian motion of nanoparticles outside the conical-shaped sensing gate may contribute a high level of background noise to the detecting system, which has a huge effect on the resolution and sensitivity of the RPS detecting system. By using the traditional RPS devices, distinguishing nanoparticles of 80 nm and 160 nm [361], and nanoparticles of 57 nm and 101 nm [266] have been claimed. However, these resolutions are not high enough for the nanoparticle research field. Although small nanoparticles detected by the RPS method has been reported [340,366–368], the SNR is too low for reliable signal identification. For example, the smallest spherical-shaped virus detected by the RPS method declared by Terejanszky in 2014 was 26 nm, and the SNR is only about 2 [340].

Microfluidic and Lab-on-a-Chip techniques have emerged in the last decades as a powerful tool for minimization of detecting systems and development of user-friendly devices. An RPS detection system developed on a nanofluidic chip can minimize the traditional bulky RPS systems on one hand, and save the samples on the other hand. A nanochannel-based sensing gate can generate symmetric RPS signals and enables investigation of individual particles precisely. For instance, nanochannel-based RPS nanofluidic chips fabricated by quartz [351,364] and carbon nanotubes (CNTs) [347,369,370] have been developed for characterization of individual DNA molecules and nanoparticles. However, the finely printed electrodes, [364] complicated nanofluidic channel systems [351] and difficulties in fabrication and assembling of the nanofluidic chips stop these devices from practical applications. PDMS-based RPS chips are cost-effective, reproducible, productive and can reduce the background noises effectively [369], which have been developed for biomarker, molecule, and nanoparticle detection [352,371,372]. A key advancement in this area is the differential microfluidic RPS systems on PDMS chips. This method can significantly minimize the surrounding noises and enhance the sensitivity of the RPS detection [339,346]. However, the smallest nanoparticle detected by such a

differential RPS chip was only 220 nm [339] when the width of the sensing gate is about 740 nm. A smaller nanochannel-based sensing gate is likely to enhance the detection limit and the sensitivity of a differential RPS chip significantly. As a result, smaller nanochannels fabricated on polystyrene surfaces and PDMS slabs demonstrated in CHAPTER 3 can be potential candidates for making RPS sensing gates. In addition, in order to fully utilize the advantages of the differential RPS technique developed on these kinds of nanofluidic chips and to improve the sensitivity and SNR in nano-sized or submicron-sized objects detection, a systematic study is needed to fully understand the working parameters involved in the detection.

This chapter presents a newly designed PDMS nanofluidic chips for nanoparticle characterization and DNA detection based on differential RPS technique. The nanofluidic chip is composed of two PDMS slabs with a short nanochannel on the bottom layer connecting two microchannel systems on the top layer. RPS signals are acquired through two detecting fluidic channels and amplified by a single-stage differential amplifier. The amplitude and the duration of the RPS signals are analyzed to study the size and velocity of the nanoparticles. Nanoparticles of 23 nm in diameter were detected by the differential RPS device with an SNR of approximately 8. This is one of the smallest particle size ever measured by the differential RPS method. The resolution of the differential RPS chip was also studied by detecting a mixture of 60 nm and 83 nm nanoparticles. The results obtained by the RPS method are compared with data obtained from a DLS (dynamic light scattering) system. Detection of dsDNA molecules by using the differential RPS chip is also presented.

In the last section of this chapter, working parameters in detecting submicron-sized particles by the differential RPS method on nanofluidic chips are studied systematically. Particle-to-pore size ratio effects are investigated by detecting polystyrene particles of different size ranging from 83 nm to 1 μm by one RPS sensor. KCl solutions ranging from 0.1 mM to 2 M are applied in detecting 140 nm, 500 nm and 5 μm particles to study the ionic concentration effects. Influences of pH of the electrolyte and the applied electric field on the SNR in detecting both submicron-sized particles micron-sized particles are also investigated. Particle loading frequency effects and particle loading trajectory effects on the channel-based differential RPS method are discussed.

6.2 Materials and methods

6.2.1 Mathematical model for single-gate differential RPS sensors

Figure 6-1 (a) illustrates the working principle of the differential RPS system. The upstream and downstream sections of the main channel are connected by a nanochannel, and the system is powered by a DC electric field. Two symmetric microchannels located adjacent to the RPS gate work as the electrodes for differential signal acquisition. Figure 6-1 (b) is an equivalent electrical circuit of the detection system, where R_1 and R_3 are the electrical resistances of the upstream and the downstream of the main channel filled with electrolyte solution, and R_2 and ΔR are the electrical resistances of the nano-RPS gate and the resistance change of the RPS sensor due to passing through of particles. R_a and R_d are the electrical resistances of the amplifier circuits and the detecting channel. Assuming that the length of the RPS gate is L and the hydraulic diameter of the RPS gate is D, in which $\mathrm{D} = (4S/\pi)^{1/2}$. S is the cross area of the RPS gate.

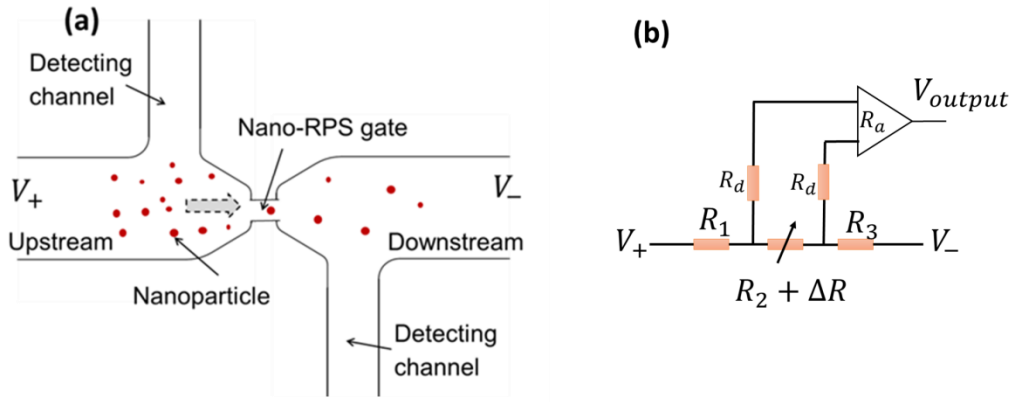

Figure 6-1 Working principle of a nanochannel-based differential RPS chip. (a) Layout and mechanism of the differential RPS chip design. The upstream and downstream of the microchannel is connected by a submicron channel. The channels are filled with electrolyte solution. A DC electric field is applied along the main channel. Two detection channels located at the two ends of the RPS gate work as the differential signal acquisition electrodes. (b) An equivalent electrical circuit of the differential RPS design.

As a particle passes through the RPS gate, the electric potential change between the RPS gate can be calculated by

$$\Delta V_{sensor} = \frac{R_m}{R_m + R_2} \cdot \frac{\Delta R}{R_m + R_2 + \Delta R} \Delta V \qquad (6\text{-}1)$$

R_m is the total electrical resistance of the main channel, $R_m = R_1 + R_3$, and the electric potential difference ΔV applied along the main channel is constant, $\Delta V = V_+ - V_-$. Assuming that the resistance change due to the particle is much smaller than that of the detecting system, and $R_m = kR_2$, the electric potential change of the sensor gate can be rewritten as:

$$\Delta V_{sensor} = \frac{k}{(k+1)^2} \cdot \frac{\Delta R}{R_2} \Delta V \qquad (6\text{-}2)$$

On the other hand, ΔV_{sensor} provides the signal source to the differential amplifier through the two detection channels. Assume that the resistance of both detection channels is R_d and the inner resistance of the amplifier is R_a, as a result one can get the input electric potential change to the amplifier is:

$$\Delta V_{input} = \frac{R_a}{R_a + 2R_d} \Delta V_{sensor} \qquad (6\text{-}3)$$

As a result, the output of the differential amplifier due to the electric potential change can be calculated by:

$$\Delta V_{output} = A\left(\eta_{up} - \eta_{down}\right) + A\Delta V_{input} \qquad (6\text{-}4)$$

Here A is the amplification factor of the amplifier, $\eta_{up}$and η_{down} are the noises coming from the upstream section and downstream section of the detecting channels. The first term on the right-hand side, $\eta_{up} \approx \eta_{down}$ due the symmetrical design of the detecting channels, consequently, the first term ideally can be cancelled [373]. That is also the mechanism why differential RPS method has lower noise level compared to that of the traditional design. Consequently, Equation (6-4) can be simplified as

$$\Delta V_{output} = A\Delta V_{input} \qquad (6\text{-}5)$$

For the resistance of the detecting channel R_d, one can get it by

$$R_d = \frac{1}{\sigma} \frac{L_d}{HW} \qquad (6\text{-}6)$$

In which L_d is the length of the detection channels, H and W are the width and depth of the detection channels. In this thesis, the size ratios *(d/D)* are smaller than 0.5 in almost all the cases. As a result Equation (2-14) is applied. Combining Equation (6-2), (6-3), (6-5), (6-6) one can get

$$\Delta V_{output} = A \frac{R_a}{R_a + 2R_d} \cdot \frac{k}{(k+1)^2} \cdot \frac{d^3}{D^2 L} \cdot \left[\frac{D^2}{2L^2} + \frac{1}{\sqrt{1 + (D/L)^2}}\right] F\left(\frac{d^3}{D^3}\right) \Delta V \qquad (6\text{-}7)$$

Equation (6-7) can be rewritten as

$$\Delta V_{output} = A\frac{k}{(k+1)^2}\cdot\left[\frac{D^2}{2L^2}+\frac{1}{\sqrt{1+(D/L)^2}}\right]\cdot\left[\frac{\sigma R_a HW/L_d}{\sigma R_a HW/L_d+2}\right]\cdot\frac{3}{2}\gamma F\left(\frac{2L}{3D}\gamma\right)\Delta V \qquad (6\text{-}8)$$

where γ is the particle-to-sensor volume ratio,

$$\gamma = \frac{2}{3}\frac{d^3}{D^2 L} \qquad (6\text{-}9)$$

For infinite small particles, the output of the RPS signals can be calculated by combining Equation (6-2), (6-3), (6-5), (6-9) and Equation (2-13),

$$\Delta V_{output} = A\frac{3k}{2(k+1)^2}\cdot\frac{R_a}{R_a+2R_d}\gamma \qquad (6\text{-}10)$$

However, in this study, experimental data are not correlated to these mathematical models quantitatively due to the complexity and practicability of these equations. For practical applications of an RPS sizing system, a numerical fitting curve is commonly used.

6.2.2 RPS detection system

Figure 6-2 shows a sketch of the RPS detection system developed in this chapter. A differential RPS chip with microchannels connected by a nanochannel is fabricated on a PDMS platform. A DC power is applied to the upstream and downstream of the main channel through two reservoirs. Electrical pulse signals generated by the particles are detected by the two differential detecting channels through Pt electrodes and transferred to the differential amplifier. A data acquisition card and a self-compiled LabVIEW program are applied to collect the amplified signals. To minimize noises from the surroundings, shielding cables and a shielding box were applied during the experiments. It is to be noted that battery is applied here to minimize the nosises as demonstrated in Appendix E.

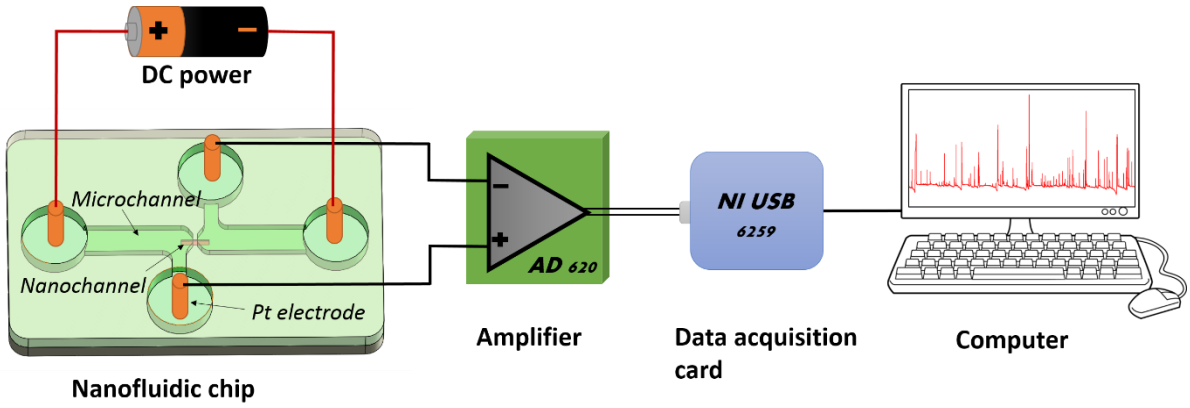

Figure 6-2 A diagram of the nano-RPS testing system. The system is composed of a nanofluidic chip, a DC power supply, a differential amplification circuit, a data acquisition card and a computer installed with LabVIEW program to control the data acquisition. A shielding box and shielding cables are used to reduce the noises from the surroundings.

6.2.3 Fabrication of RPS nanofluidic chips

The PDMS-PDMS nanofluidic chip is composed of two layers of PDMS. The top layer consists of the microchannel system and a nanochannel on the bottom layer, as shown in Figure 6-3 (a). The depth of the microchannel is about 5μm and the gap between the upstream microchannel and the downstream microchannel is about 6.4 μm, which will be bridged by the nanochannel on the bottom PDMS layer. The upstream and the downstream microchannels are about 1 cm long and 100 μm wide, and the detecting channels are about 0.7 cm long and 50 μm wide. The nanofluidic chips are fabricated by following the working procedures presented in CHAPTER 3.

Figure 6-3 (b) and Figure 6-3 (c) show an example of the microfluidic chip after bonding and a zoomed-in view of the RPS sensing area, respectively. The size of submicron channels used in this study was measured by an AFM (Multimode™SPM, Digital Instruments) at five locations and average values are presented in this article. It should be noted that PDMS channels replicated from one positive channel mold have the same size, as a result, the size of PDMS channels replicated from one certain channel mold was measured for only once on one PDMS channel. Figure 6-3 (d) and Figure 6-3 (e) illustrate an example of a submicron channel replicated on a PDMS surface and a cross-section of this channel. It is difficult to have a one-fits-all chip for all different nanoparticles. Nanofluidic chips with different sizes of sensing gates on the bottom layer are applied to detect nanoparticles of various sizes. However, for all these chips, the microchannels on the top layer are the same, and the sensing gates are all about 6.4 μm long.

In this last section of this chapter, three chips with three different RPS gates were developed to investigate the working parameters involved in the nanochannel-based differential RPS method. An RPS gate of 2.4 μm in width and 2.5 μm in depth was used to study the particle-to-sensor volume ratio effects by detecting 1 μm, 500 nm, 220 nm, 140 nm, and 83 nm particles. An RPS gate of 455 nm in width and 430 nm in depth was used to investigate the ionic concentration effects, the pH effects and the applied voltage effects by detecting 140 nm nanoparticles. As a comparison work, a 16 μm wide and 15 μm deep micron-sized RPS gate was utilized to detect 5 μm particles.

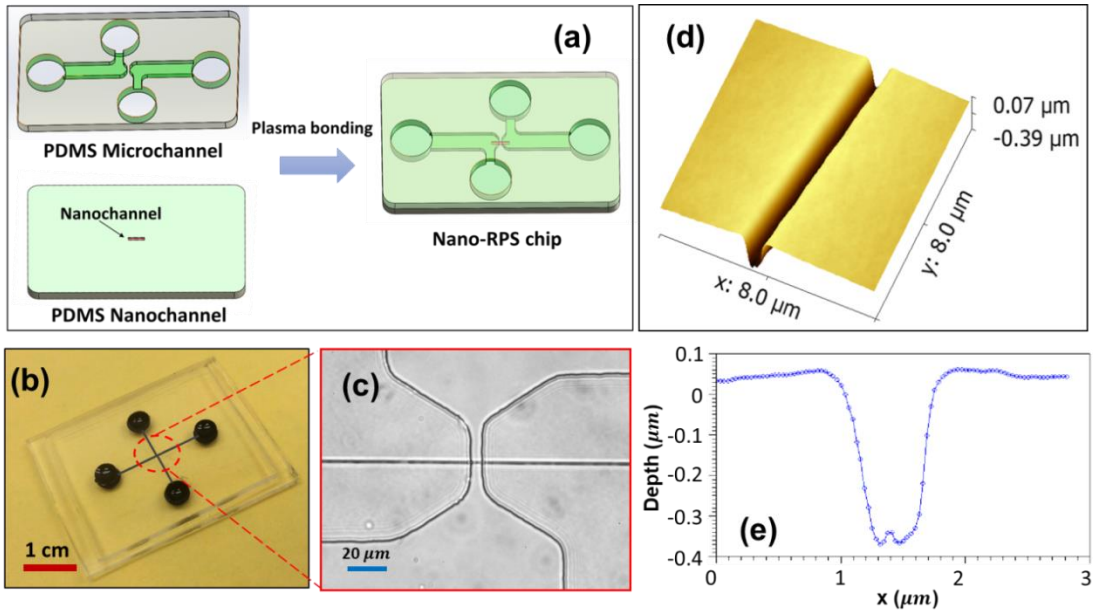

Figure 6-3 Fabrication of differential RPS nanofluidic chips for nanoparticle detection. (a) Components of a PDMS microfluidic chip, with a microchannel system on the top layer a single sensing channel on the bottom layer. (b) An example of RPS chip after bonding. (c) A zoomed-in view of the RPS gate area. (d) A 3-D image of the sensing gate and (e) a cross-section of this sensing gate.

6.2.4 Chemical reagents and materials

KCl solutions ranging from 0.1 mM to 2 M were prepared by dissolving KCl (Fisher Scientific) into pure water (Mini Q, Direct-Q3, 18.2 MΩ·cm, pH 6.5). Triton X-100 (0.1% (v/v)) was applied in all the solutions to avoid aggregation of nanoparticles. Acidic and alkaline solutions (0.5 M HCl and 0.5 M KOH) were used to adjust the pH value of the KCl solutions. Particles of 5 μm (PS05N) 1 μm (PS04N), 500 nm (PS02N) and 220 nm (FC02F) in diameter were bought from Bangs Laboratories (10% solids, w/v), and polystyrene particles of 140 nm (G140) and 83 nm (G85B) in diameter were purchased from Thermo Fisher Scientific (1% solids, w/v). Before each test, the polystyrene particles

were diluted in a specific electrolyte solution by 1000 times. The sample solutions were initially dispersed by using a vortex mixer for 30 s and further mixed by using an ultrasonic mixer (Fisher Scientific) for at least 2 min. For each electrolyte solution, the conductivity and the pH value were measured for at least 3 times (Omega PHH-128). The sizes of particles were also measured by DLS (Zetasizer Nano ZS90, Malvern). DsDNA (λ DNA, 10% concentration, Sigma-Aldrich) was diluted in 2 M KCl solution by 10^4 times. During the experiments, the DC power (AJC Brand® Battery) was applied on the nanofluidic chip through Pt electrodes (Sigma-Aldrich), and the amplification factor of the single stage differential amplifier (AD620, Digi-Key) was from 100 to 1000.[†] The signals were recorded by the data acquisition card (USB 6259) working at 1~4 kHz sampling frequency. Zeta potential of the nanoparticles was also characterized by the DLS.

6.2.5 Experimental procedures and data processing

During RPS detection, the PDMS chip was filled with one kind of pure KCl electrolyte solution for 15 minutes prior to loading the particle samples or DNA samples. Afterwards, Pt electrodes were inserted into the channel reservoirs, and a DC power was applied to the electrodes. The RPS signals were detected by the differential detecting channels and amplified by the differential amplifier then recorded by a self-complied LabVIEW program simultaneously. A low pass Bessel filter working at 30~50 Hz was applied to remove high-frequency noises from the original data. It should be noted that 1~4 kHz sampling rate is sufficient for this study because the duration time of the RPS events for all the cases was around 50~200 ms. Additionally, for each case, i.e., one kind of solution, one RPS gate size, and one applied voltage, at least three fresh chips were prepared and the experiments were conducted on these chips independently. All the experiments were conducted at room temperature around 23℃.

During the data processing, moving average technique was applied to evaluate the baseline of the raw data. This technique has been reported by Plesa and Dekker [374]. For each case, at least 50 RPS events were analyzed. To avoid errors in evaluating dwelling time of the RPS events, FWHM (Full Width at Half Maximum) durations of the RPS signals were calculated, and the FWHM dwelling time is applied in this chapter. Average values and standard derivations of the amplitudes and the duration of the RPS events are evaluated and presented. In the last section, working parameter effects on the signal-to-noise ratio (SNR) of the differential RPS method were investigated. The SNR was calculated by

[†] The electrical circuit of the amplifer can be found in http://www.analog.com/media/en/technical-documentation/data-sheets/AD620.pdf.

$$SNR = \Delta V_{output}/\delta \qquad (6\text{-}11)$$

where the noise level (δ) of each case was obtained by calculating the standard deviation of 1000 data points without RPS events. In addition, for each case, the experiments were repeated for at least three times on three chips. However, for each chip, the noise level varies due to the uncertainty in the chip bonding process and variability in surface charge of the PDMS channels, etc. An average noise level was obtained to evaluate the SNR. It should be noted that the widely accepted threshold is 3~5 times of the noise level. In this article, for most cases, thresholds of 3~20 times of the noise level were applied to identify RPS events. However, for only extreme cases, the SNRs were very low and a value of 3 times of the noise level failed to identify RPS events, as a result, a minimum value of 1.5 times of the noise level was used to identify RPS events to obtain comprehensive trends of the data.

6.3 Results and discussion

6.3.1 Determination of particle aggregation

An RPS chip with a relatively large RPS sensing gate is used to detect submicron particles. Figure 6-4 shows the results of detecting $1\mu m$, 500 nm and 220 nm particles by using the nanochannel-based RPS detecting chip with a RPS sensing gate of 2.4 μm wide, 2.5 μm deep and 6.4 μm long. The applied electric voltage along the main channel was 3V. RPS signals of $1\mu m$, 500 nm and 220 nm particles are shown in Figure 6-4 (a), (c) and (d), respectively. As mentioned above, a lot of information can be obtained from these signals. For example, one can get the number of the particles, the velocity of the particles and the size of the particles by analyzing the RPS signals. Besides, according to the signals, we can also determine aggregation of particles and so on.

Figure 6-4 (a) shows RPS signals of 1 μm particles. It is obvious that for most signals, the amplitude is about 0.35 V. However, the magnitudes of some signals are almost doubled or tripled, and there are apparent "bands" between these signals. It is suspected that these "bands" are due to aggregation of particles. For most cases, only individual particles pass through the RPS sensing gate, as a result, most signals have similar values and are located in the "I" area, as shown in Figure 6-4 (a). However, as two particles aggregate and pass the sensing gate together, the signals are almost doubled, because RPS signals are approximately proportional to the volume of the particles according to the working principle of the RPS technique explained above. These signals are clearly seen in the "II" area. For the cases of aggregation of three particles, the amplitude of the RPS signals is almost tripled, and the signals appear in the "III" area. It is reported that the signal "bands" have

been applied in label-free biomarker detection [372] and also DNA folding analysis [375]. RPS signals of 500 nm and 220 nm nanoparticles detected by the same chip under the same condition are shown in Figure 6-4 (c) and Figure 6-4 (d). From these figures one can see that for well dispersed nanoparticle samples, the RPS signals are quite uniform. The amplitudes reveal the sizes of these particles and will be discussed in the following section.

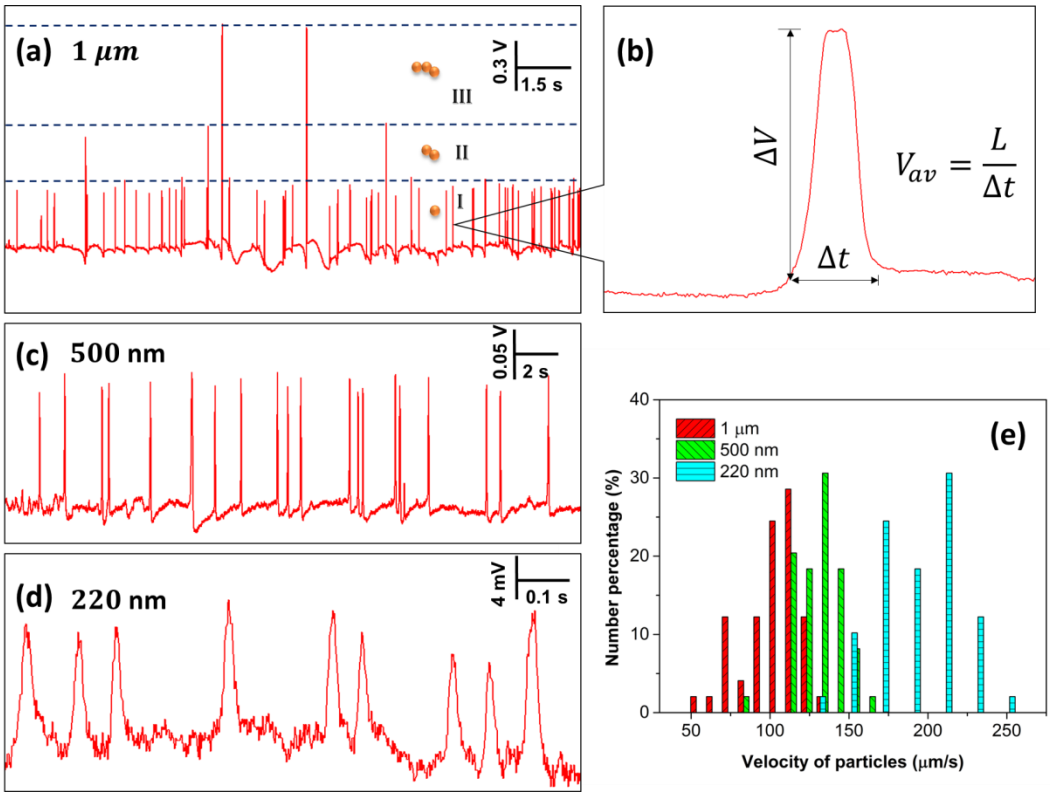

Figure 6-4 Detection and characterization of 1 μm, 500 nm and 220 nm particles by using a nanochannel-based RPS detection chip. The applied electric voltage along the main-channel is 3 V. The RPS sensing gate is about 2.4 μm wide, 2.5 μm deep and 6.4 μm long. (a) Typical RPS signals of 1 μm particles, the symbols "I", "II" and "III" denote the signal "bands" due to aggregation of the particles; (b) A zoomed-in view of the RPS signal of a 1 μm particle, where ΔV is the amplitude of the RPS signal, L is the length of the RPS gate, Δt is the duration of the signal and V_{av} is the mean velocity of the particle; (c) Typical RPS signals of 500 nm particles; (d) Typical RPS signals of 220 nm particles; (e) Velocity of 1 μm, 500 nm and 220 nm particles measured by the RPS chip

6.3.2 Dynamic motion of particles

RPS technique is well known for the ability of counting and sizing particles. However, RPS method can also be used to study the dynamic motion of particles. For example, translocations of DNA modified nanoparticles [376], HIV and EBV viruses [357] investigated by RPS method have been reported. Based on the apparent velocity, surface properties of the nanoparticles such as zeta potential can also be derived [356]. However, the sensing gates used in these works are conical shaped, and the velocity of the nanoparticles inside the sensing gates changes with the location of the particles. A nanochannel based sensing gate is more suitable for investigating the motion of particles due to the symmetric RPS signals and constant velocity as mentioned in the introduction section. Figure 6-4 (b) shows a zoomed-in view of an RPS signal of a 1 μm particle displayed in Figure 6-4 (a). Here L is the length of the sensing gate measured by the microscope, ΔV and Δt are the amplitude and duration of the RPS signal, $V_{av}$is the mean velocity of the particle. The mean velocity of this particle can be calculated by:

$$V_{av} = \frac{L}{\Delta t} \qquad (6\text{-}12)$$

It should be noted that here the dwelling time is the full-width time. For other cases in this thesis, FWHM is applied. Figure 6-4 (g) shows the results of statistic data of velocity distribution of 1μm, 500 nm and 220 nm particles measured by the RPS device. From Figure 6-4 (g) one can easily reach a conclusion that small particles move faster than large ones in the same sensing gate under the same applied electric fields. Specifically, the mean velocity of the 220 nm particles is about 200 $\mu m/s$, while the mean velocity of the 500 nm and the 1μm particles are 135 $\mu m/s$ and 105 $\mu m/s$, respectively. The zeta potentials of the 1 μm, 500 nm and 220 nm particles measured by the DLS method are about $-12.7\ mV, -11.83\ mV$ and $-10.75\ mV$ in average, indicating that larger particles have a little bit higher zeta potential. As a result we may predict that the reduction of the velocity with the increase of particle size is possibly due to higher zeta potential of the larger particles and stronger interactions between the channel walls and the larger particles [377].

6.3.3 Resolution of the nano-RPS chips

To distinguish nanoparticles with a smaller size difference, a nano-RPS chip with a smaller sensing gate of approximately 6.4 μm long, 680 nm wide and 330 nm deep was developed. The electric potential difference applied between the two ends of the main channel was 1.5 V, and the amplification factor of the amplifier was 1000. A sample mixture of 60 nm and 83 nm nanoparticles

passed through the sensing gate. Figure 6-5 (a) shows the RPS signals of these nanoparticles. From Figure 6-5 (a) one can see that there is an apparent "band" between the amplitudes of the signals, and the amplitude of the smaller signals is about 0.27 V and the amplitude of the larger signals is approximately 0.56 V. It is assumed that the larger signals come from passing through of the 83 nm nanoparticles and the smaller ones are the signals of the 60 nm particles. To verify our assumption, sample solutions containing only 60 nm and 83 nm nanoparticles were detected by using both the DLS method and this nano-RPS chip, separately. The results of the DLS data and RPS data are shown in Figure 6-5 (b) and Figure 6-5 (c).

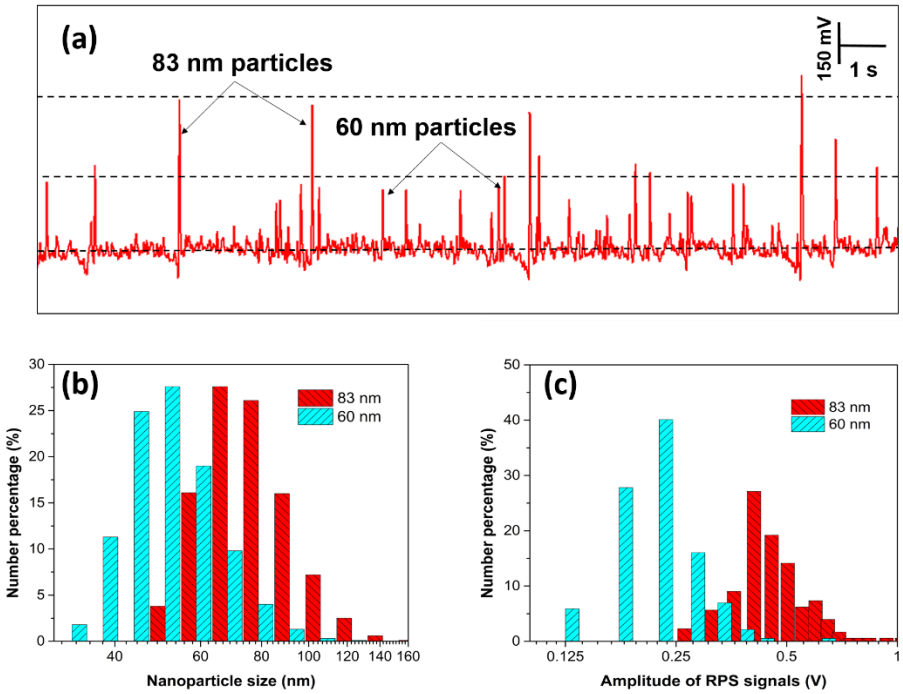

Figure 6-5 (a) RPS signals of a sample mixture of 60 nm and 83 nm nanoparticles diluted in 1 M KBr solution. The RPS sensing gate is about 6.4 μm long, 680 nm wide and 330 nm deep. (b) Size distribution of 60 nm and 83 nm nanoparticles diluted in 1 M KBr solution containing 0.5% Tween 20 measured by the DLS; (c) Amplitude distribution of RPS signals of the 60 nm and 83 nm nanoparticles measured by the RPS chip.

It is obvious that in Figure 6-5 (a) the size distributions of the 60 nm nanoparticles and the 83 nm nanoparticles measured by the DLS are heavily overlapped, indicating that the DLS can hardly tell the difference between 60 nm and 83 nm nanoparticles. However, for the RPS data, as shown in Figure 6-5 (c), there are two obvious peaks in these two amplitude distributions, 230 mV and 440 mV, respectively. It is much easier to distinguish 60 nm and 83 nm nanoparticles by using the RPS

device than that by using the DLS system. In addition, the signal amplitude of the 83 nm particles is almost twice of that of the 60 nm particles, which agree well with the working principle mentioned above (infinite small particle case), the output of the signals is almost proportional to the volume of the particles. To be noted, the 23 nm resolution is obtained by the experiments. In theory, the resolution can be much smaller because according to Equation (6-10), the amplitude of the signals increases with the volume of the particles, as long as the signal difference is larger than the surrounding noise, the difference is distinguishable. However, in reality, determining the resolution by experiments is limited by the quality of samples. For example, we tried to distinguish nanoparticles of 50 nm and 60 nm in average diameter; however, the real sizes of these two kinds of particles overlap heavily due to the particle manufacturing accuracy. Consequently, it was hard to tell the difference between these two samples by using the nano-RPS chip or any other facilities.

6.3.4 Sensitivity of the nano-RPS chips

Sensitivity is another key parameter in particle characterization. According to Equation (6-10), a smaller sensing gate (smaller D) is able to enhance the sensitivity of the nano-RPS chips and to detect smaller nanoparticles. Figure 6-6 shows examples of RPS signals of 140 nm and 23 nm nanoparticles measured by using smaller RPS sensing gates. Figure 6-6 (a) shows RPS signals of 140 nm nanoparticles detected by using an RPS sensing gate of 6.4 μm long, 875 nm wide and 607 nm deep. The electric field applied along the main channel was 6 V/cm, and the amplification factor of the amplifier was 100. The amplitude of the signals is about 55 mV, and the SNR is still larger than 10. The few larger signals in Figure 6-6 (a) are probably due to aggregation of the nanoparticles as mentioned above. Figure 6-6 (b) illustrates RPS signals of 23 nm nanoparticles. The size of the RPS sensing gate used in this chip was 6.4 μm long, 510 nm wide and 80 nm deep, and the electric field applied along the main channel was 0.75 V/cm, which is much lower than the previous experiments, 6 V/cm. A lower electric field is able to reduce the dielectrophoresis (DEP) force at the sensing gate entrance, making the sample loading easier especially for small RPS sensing gates. The amplitude of the 23 nm nanoparticle signals is about 0.7 V and the SNR is over 8, which is high enough for identification of individual nanoparticles. Surfactant molecules with long tails may affect the hydrodynamic diameter of the 23 nm nanoparticles and give rise to so large signals. To confirm the effects of the surfactant on the particle size, 23 nm nanoparticles were diluted in both pure water without surfactant and in 1 M KBr solution with 0.5% Tween 20, and measured by the DLS. The results show that the mean sizes of the 23 nm nanoparticle samples prepared in pure water without

surfactant and in 1 M KBr solution with 0.5% surfactant are about 25 nm and 27 nm, respectively, revealing that the surfactant has little effect on the particle size.

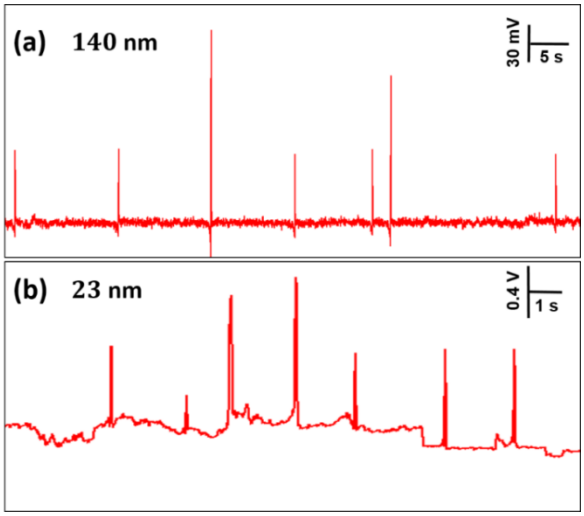

Figure 6-6 RPS signals of 140 nm and 23 nm nanoparticles diluted in 1 M KBr solution. (a) RPS signals of 140 nm nanoparticles detected by using an RPS sensing gate of 6.4 μm long, 875 nm wide and 607 nm deep. The electric field applied along the main channel is 6 V/cm and the amplification factor of the amplifier is 100; (b) RPS signals of 23 nm nanoparticles. The size of the RPS sensor gate is about 6.4 μm long, 500 nm wide and 80 nm deep. The electric field applied along the main channel is 0.75 V/cm, and the amplification factor of the amplifier is 1000.

Based on the current experimental results, it is believed that the nano-RPS chips developed in this chapter are applicable for smaller nanoparticle detection. Theoretically, the sensitivity can be calculated by setting a fixed SNR. For example, we assume that an SNR of 2 is enough for particle identification. In Figure 6-6 (b), the signal of the 23 nm nanoparticles is about 0.7 V and the noise level is about 0.09 V. As a result, the smallest detectable signal is about 0.18 V. On the other hand, the amplitude of the RPS signal is proportional to the volume of the particle, as a consequent, we can get the smallest particle can be detected by this chip is about 15 nm. However, the sensitivity of the RPS chip can be further improved by minimize the RPS gate. For example, carbon nanotubes with smaller inner diameters are applied in single molecule detection in CHAPTER 7.

6.3.5 An application: dsDNA detection and analysis

Nanofluidics provides a powerful tool for DNA detecting, sequencing, and mapping. In this section, detection of dsDNA molecules by using the PDMS differential RPS chips is conducted. The size of the nanochannel-based sensing gate is about 500 nm wide and 80 nm deep. During this

experiment, 10% concentration λ dsDNA (125-23130 bp) were diluted in 2M KCl solution by 10^4 times without adding any surfactant. The amplification factor of the amplifier was 1000. The electric field applied along the main channel of the RPS chip was 1.5 V/cm. Here, a higher ionic concentration of the buffer solution (2 M KCl) benefits higher quality data acquisition [260], as demonstrated in Equation (6-10).

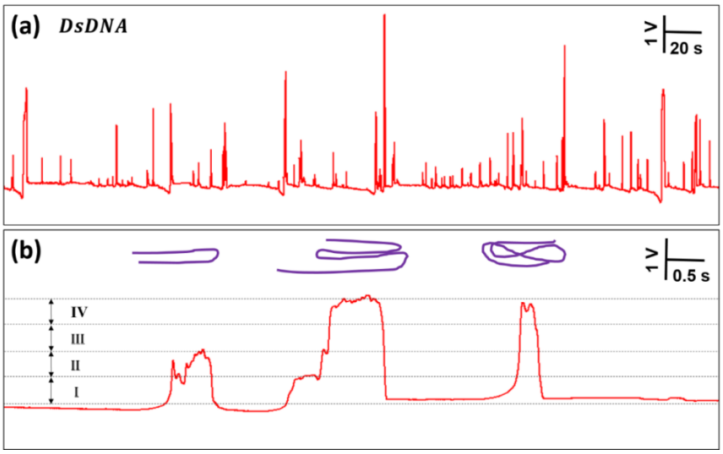

Figure 6-7 RPS signals of dsDNA molecules. 10% concentration dsDNA molecules are diluted in 2M KCl solution by 10^4 times. The amplification factor of the amplifier is 1000. The applied electric voltage along the RPS chip is 3 V.

Figure 6-7 (a) shows the RPS signals of the dsDNA molecules, one can see that the amplitude of the signals is not uniform, ranging from 0.3 V to 5.2 V, and the noise level is about 0.2 V, as a result, the SNR is ranging from 1.5 to 26. The mean SNR is still higher than 10, which is high enough for reliable data analysis. A zoomed-in view of the signals is shown in Figure 6-7 (b). It's obvious that one can read the amplitudes and the duration of the signals from the figure easily. It is reported recently that the amplitude of RPS signals can be used to predict the state of DNA molecules, for instance, folding and knotting of the DNA chains [260]. The mechanism is as follows. It is widely accepted that DNA molecular chains can self-entangle by knotting or folding due to the flexibility of the chains. As a DNA polymer chain passes through an RPS sensing gate, the spherical particle model mentioned in the section 6.2.1 cannot be used anymore. One has to take the shape factor into consideration. For example, as the DNA chain is much longer than its diameter, we can assume that the molecule chain is a long cylindrical rod, and the amplitude of the RPS signal is not proportional to the volume of the object anymore. The cross-section area blocked by the insulator rod may dominate the amplitude of the RPS signal. For example, the amplitude of the RPS signal of a double-folded DNA should be twice compared to that of a single-folded DNA, and so on and so forth.

Consequently, one can also predict the status of the DNA molecules roughly based on the RPS signals. For example, in Figure 6-7 (b), there are four "bands" in Figure 6-7 (b), I, II, II and IV, which stand for the folding number of the DNAs. The sketches above the signal peaks illustrate the possible situations of the folding and knotting of the DNA chains. For example, for the first peak on the left side of Figure 6-7 (b), the amplitude is about two-band high, as a result, one can predict that the DNA chain is double folded. As the DNA molecule chains become longer, there are higher possibilities of heavy folding and knotting, resulting in higher amplitudes of RPS signals. For instance, the amplitudes of the second and third peaks in Figure 6-7 (b) are about 4-band high, revealing that these DNA chains are four times folded or knotted. In addition, the duration of the signals gives information of the translocation of the DNA chains, leading to the velocity, the length of the DNA molecules and so on. For example, in Figure 6-7 (b), the duration of the peaks is 0.3~1.5 s; as a result, one can predict the velocity of the DNA molecules is 4~20$\mu m/s$. The deviation in the velocity may be caused by the length and the folding of the DNA molecule chains. The duration of the DNA translocation is critical to the nanopore-based DNA sequencing, and a longer translocation time enables a higher detecting resolution [353]. The duration of the translocation in this experiment is on the magnitude of second level which is much longer than that measured by the nanopore-based sensing gates, are on the order of millisecond [352,375,378,379]. As a result, the nanochannel-based RPS gates are potentially used to slow down the motion of DNAs and enable higher resolution DNA sequencing and detection.

6.3.6 Working parameters in differential RPS detection

6.3.6.1 Particle-to-sensor volume ratio and particle sizing

According to Maxwell's theory [177], the magnitude of an RPS signal generated by a non-conducting particle is proportional to the electrical resistance change of the sensor, while the electrical resistance change of the sensor is dominated by the particle-to-sensor volume ratio [365], as demonstrated in Equation (6-9) and (6-10). To study the particle-to-sensor volume ratio effects on particle detection by the differential RPS method, particles of 1 μm, 500 nm, 220 nm, 140 nm and 83 nm were diluted in 0.5 M KCl solution and detected by one RPS gate. The RPS gate is about 6.4 μm long, 2.4 μm wide and 2.5 μm deep. The corresponding particle-to-sensor volume ratios (γ) are 0.012, 1.5×10^{-3}, 1.3×10^{-4}, 3.2×10^{-5} and 6.1×10^{-6}, respectively. For all the cases, a 6 V DC voltage was applied to the main channel during the experiments. The experimental results are illustrated in Figure 6-8. Figure 6-8 (a) demonstrates the number percentage distributions of the RPS

signals detected by using this RPS gate under the above-mentioned conditions. For this specific sensing gate, 83 nm nanoparticles were too small to be detected. Figure 6-8 (b) illustrates the particle-to-sensor volume ratio effects on the amplitude and the SNR of the RPS signals by detecting 1 µm, 500 nm, 220 nm and 140 nm particles. Examples of RPS signals of 1 µm, 500 nm, 220 nm and 140 nm particles are demonstrated in Figure 6-8 (c)-(f), respectively.

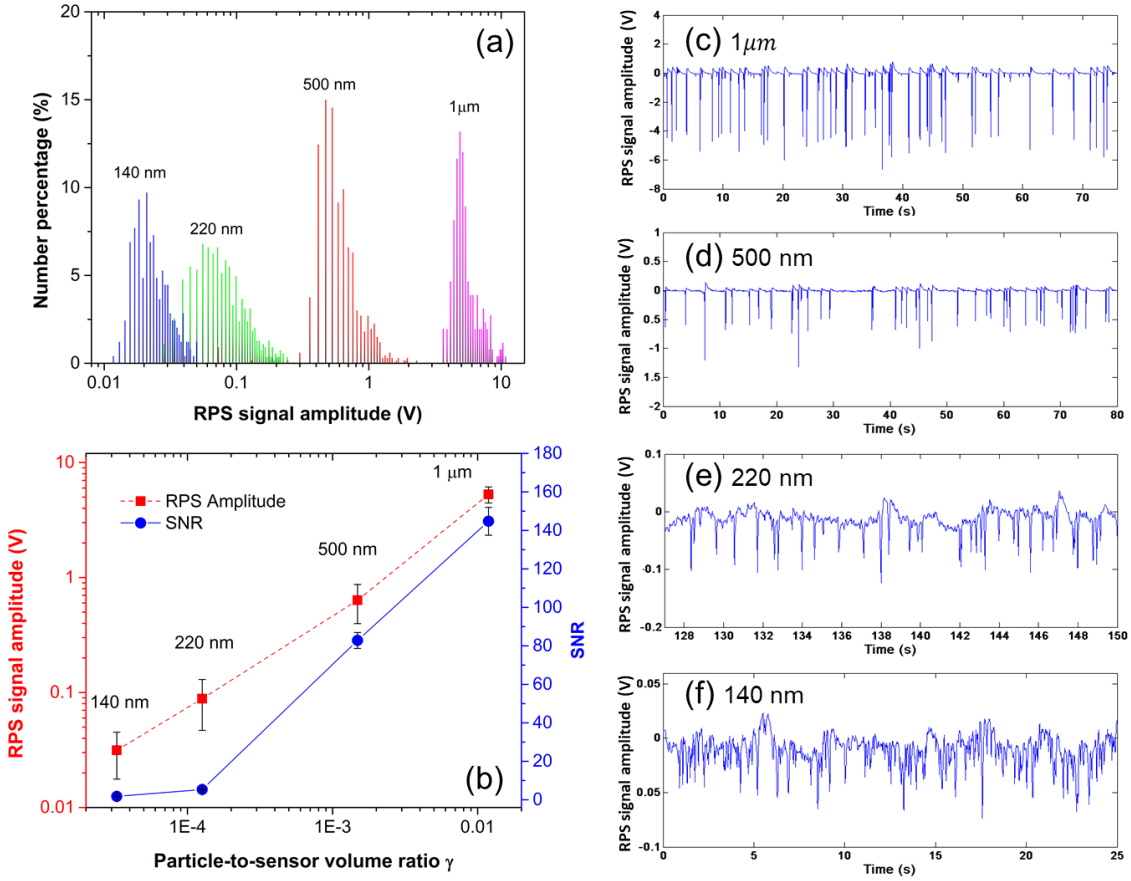

Figure 6-8 Particle-to-sensor volume ratio γ effects on particle detection by the differential RPS method. The RPS sensor was about 6.4 µm long, 2.4 µm wide and 2.5 µm deep, and the applied voltage was 6 V. Particles of 1 µm, 500 nm, 220 nm and 140 nm in diameter were dispersed in 0.5 M KCl solution. (a) RPS amplitudes of 1µm, 500 nm, 220 nm and 140 nm particles. (b) Volume ratio effects on the RPS signal amplitudes and SNRs. (c)-(f) Examples of RPS events of 1 µm, 500 nm, 220 nm and 140 nm particles detected by the RPS chip.

DLS is one of the most commonly used techniques for nanoparticle sizing and characterization, which has been a standard tool in nanoparticle research [336]. In this study, the particle samples were measured by both the DLS and the RPS method, and the results of the RPS method are compared with that of the DLS system. From Figure 6-8 (a) one can see that the distributions of these RPS

magnitudes are well distinguished, showing superior resolution than that of the DLS method (see Figure 6-9 for the DLS data), in which the sizes of the particles are heavily overlapped. As a result, one can conclude that the RPS method developed in this chapter has a higher detecting resolution compared with that of the DLS system, and is more reliable for particle sizing.

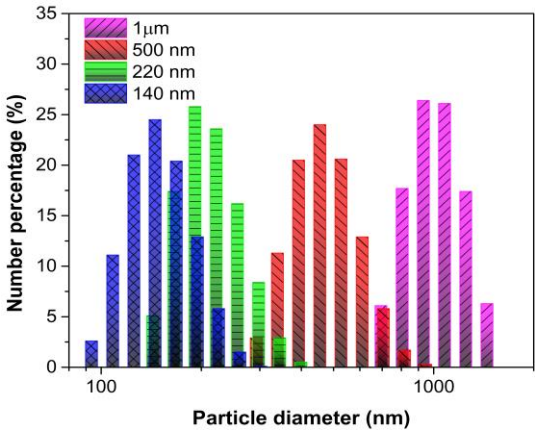

Figure 6-9 Size distribution of 1 *μm, 500 nm, 220 nm, and 140 nm particles measured by the dynamic laser scattering (DLS)method. The polystyrene particles were diluted in 0.5 M KCl solution (pH 6.5) by 1000 times and the size of the particles was evaluated by the average number-weighted values*

The average RPS amplitudes of the 1 μm, 500 nm, 220 nm and 140 nm particles are around 5 V, 0.5 V, 0.09 and 0.03 V, respectively, as shown in Figure 6-8 (b) (the red dashed line), and the corresponding spans of the bins are illustrated in Figure 6-8 (a). From Figure 6-8 (b) one can find that the relation between the RPS signal amplitude and the particle-to-sensor volume ratio γ is not linear. According to the theory, when the particle is infinitely small in comparison with the pore diameter, the resistance change is a linear function of the particle volume [177], however, as the particle diameter relative to the diameter of the sensing gate becomes large, the relationship between the electrical resistance change and the particle volume becomes increasingly nonlinear [178,180,380]. Similarly, the SNR of the RPS signals also increases with γ dramatically, as shown in Figure 6-8 (b), indicating that a larger size ratio γ gives rise to a higher SNR which is beneficial to the reliability of the particle detection. Examples of RPS signals of 1 μm, 500 nm, 220 nm and 140 nm particles are demonstrated in Figure 6-8 (c)-(f). Apparently, both the amplitude and the SNR of the RPS events in Figure 6-8 (c) are much higher than that in Figure 6-8 (d), (e) and (f). RPS events detected under the condition of high γ are more recognizable than those of the low γ cases. For instance, one can see the RPS signals clearly in Figure 6-8 (c) but can hardly recognize the events in Figure 6-8 (e). As mentioned above,

83 nm nanoparticles were also detected by this chip under the same working conditions, but the signals of the particles were immersed in the background noises due to the extremely low size ratio γ. Theoretically speaking, a large γ would improve the sensitivity and the SNR of the RPS detection efficiently, however, the upper limit is dependent on the sensor's physical size, because an extremely high γ may trigger problems in sample loading. As a result, a suitable γ is very important for nanoparticle detection by the differential RPS method.

6.3.6.2 Ionic concentration effects

Generally speaking, the RPS method works well with highly conductive electrolyte solutions and it is difficult to detect RPS events by using an electrolyte solution with an extremely low conductivity. The conductivity of an electrolyte solution is dominated by both the mobility and concentration of the ions. In this section, KCl solutions ranging from 0.1 mM to 2 M were applied to detect both 140 nm and 5 μm particles by using two RPS gates of different sizes, 2.5 μm × 2.4 μm × 6.4 μm, and 16 μm × 15 μm × 20 μm, respectively. For the 140 nm particle cases, the particles were diluted in the above-mentioned KCl solutions, and a 1.5 V electric potential was applied along the main channel. For the 5 μm particle cases, a 9 V electric voltage was applied. It should be noted that in order to obtain reliable RPS signals, different electric fields were applied in the 140 nm cases and the 5 μm cases, and the electric field effects will be discussed in the following sections. Figure 6-10 shows the experimental results in detail. Figure 6-10 (a) illustrates the distributions of the RPS amplitude of the 140 nm particles detected by using 0.01 M, 0.1 M, 0.5 M and 1 M KCl solutions, and the corresponding examples of RPS signals are presented in Figure 6-10 (b). The conductivity of the electrolyte solutions and the ionic concentration effects on the signal amplitude and the SNR of 140 nm and 5 μm particle cases are shown in Figure 6-10 (c) and Figure 6-10 (d), respectively.

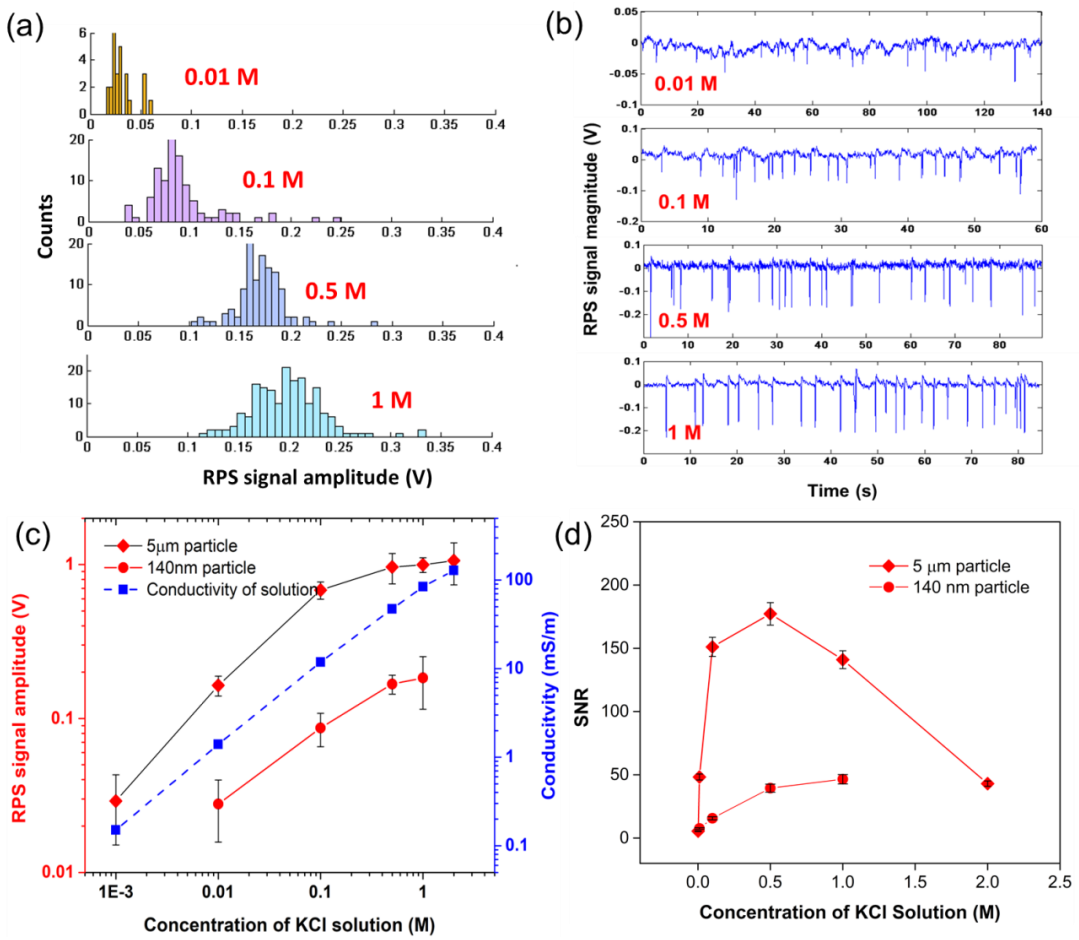

Figure 6-10 Ionic concentration effects on the amplitude and the SNR in particle detection by the differential RPS method. (a) Distributions of RPS amplitudes of 140 nm particles detected by using 0.01 M，0.1 M, 0.5 M and 1 M KCl solutions. (b) Examples of RPS signals of 140 nm particles detected by using 0.01 M，0.1 M, 0.5 M and 1 M KCl solutions, respectively. (c) The conductivity of the solutions and ionic concentration effects on the RPS signal amplitudes of 140 nm and 5 μm particles. Error bars of the conductivity are too small in comparison with the symbols which are neglected in this figure. (d) Ionic concentration effects on the SNR in detecting 140 nm and 5 μm particles by the differential RPS method.

From Figure 6-10 (a) and (b), one can see that both the amplitude and the SNR of the RPS signals increase with the ionic concentration. RPS events detected by using a high concentration solution, such as 1 M KCl, is more recognizable than that detected by utilizing a low concentration solution, 0.01 M KCl, because the conductivity of the high concentration solution is higher than that of the low one. As shown in Figure 6-10 (c), the conductivity of the KCl solution increases with the

ionic concentration dramatically, for instance, as the concentration increases from 0.1 mM to the 2 M, the conductivity increases from 0.15 mS/m to about 125 mS/m. The amplitudes of the RPS signals for both the 140 nm particles and the 5 μm particles follow the trend of the conductivity curve, which coincides with the model presented in Equation (6-9). The conductivity of electrolyte solution dominates the electrical resistance of the detecting channels R_d, which affects the input of the RPS signals (Equation (6-3)). From Equation (6-3), apparently, one can get a conclusion that a higher concentration electrolyte solution with a higher electric conductivity is beneficial for smaller particle detection by obtaining an RPS signal with larger amplitude. The conductivity effect on the magnitude of RPS signals was also verified by using other 5 kinds of electrolyte solutions (as shown in Figure 6-11). From Figure 6-11 one can also conclude that the amplitude of the RPS signals follows the trend of the conductivity roughly.

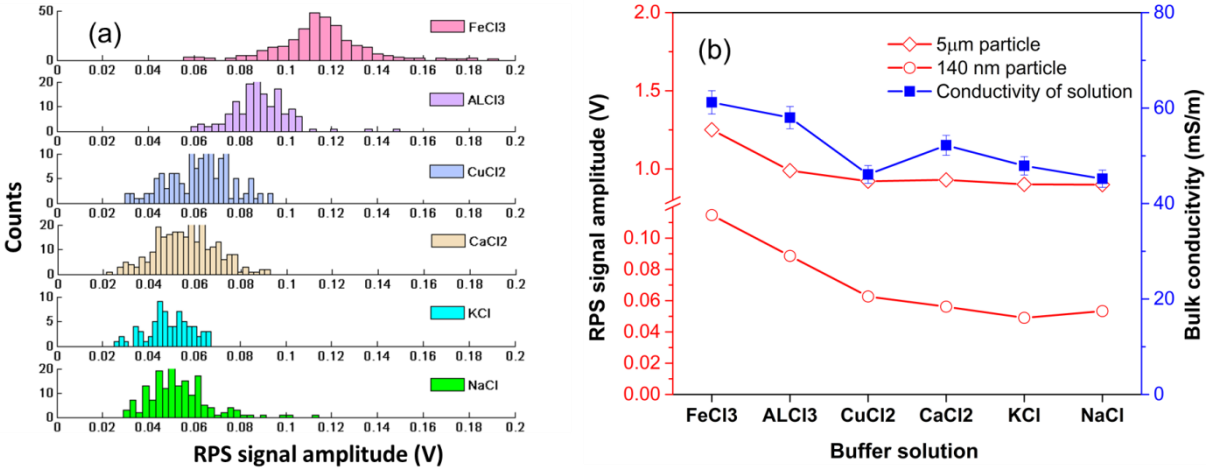

Figure 6-11 (a) Distributions of RPS signal amplitudes of 140 nm particles detected by using $FeCl_3$, $AlCl_3$, $CuCl_2$, $CaCl_2$, KCl and NaCl solutions. The concentration of all the solutions was 0.5 M, and the applied voltage was 3 V. (b) RPS amplitudes of 5 um and 140 nm particles obtained by using the six kinds of electrolyte solutions and the conductivity of these solutions.

Ionic concentration affects the SNR of the RPS detection by the same way. From Figure 6-10 (d), one can see that the SNR of the 140 nm cases increases with the ionic concentration gradually from 7.6 to about 47 as the ionic concentration increases from 0.01 M to 1 M. For the 0.01 M case, it is difficult to identify 140 nm particles by RPS events due to the low SNR; however, for the 2 M case (not presented in the figure), 140 nm particles get aggregated in such a high ionic strength environment, consequently, it is also hard to detect reliable RPS events due to the blockage of the RPS gate. Examples of RPS signals of aggregated nanoparticles and blockage of the RPS gate due to

high ionic concentration are demonstrated in Figure 6-12. It should be noted that polarization of ions at the entrance of RPS gate also affects loading of samples by increasing the ionic concentration at the entrance area. A high ionic concentration environment would trigger aggregation of nanoparticles and blockage of RPS gates. However, the polarization issue only becomes appreciable at a high applied voltage and under the condition of very long conditioning time. As a result, polarization effects on the nanoparticle detection by RPS method are not considered in the thesis. As a comparison case, the SNR of the 5 μm particle cases also increases with the ionic concentration in the range of 1 mM to 0.5 M, as shown in Figure 6-10 (d); however, the SNR decreases rapidly when the concentration increases further, while the amplitude of the RPS signals still increases with the ionic concentration (see Figure 6-10 (c)). One possible reason for the decrease of the SNR at high concentration is the electrolysis of water under the condition of the high conductivity of the electrolyte and the high electric voltage applied along the main channel. Electrolysis of water would generate small air bubbles at the electrodes and change the pH value of the electrolyte solution, resulting in fluctuations of current in the main channel and giving rise to a higher level of background noise. The effects of the pH value and the applied voltage will be discussed in the following sections.

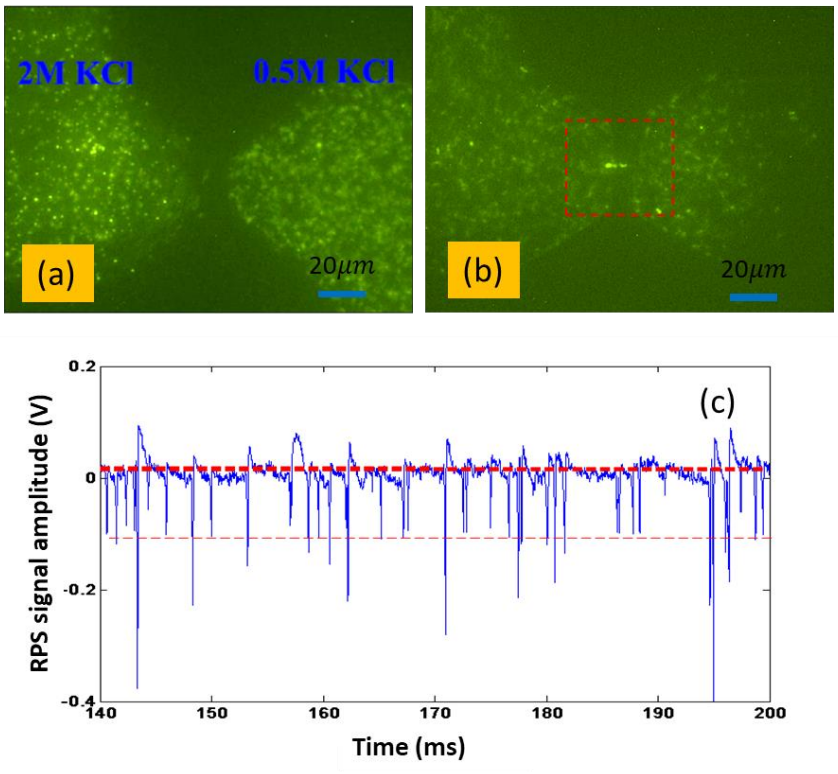

Figure 6-12 (a) An example of aggregation of 140 nm particles due to high ionic strength (left-hand side 2 M KCl). (b) An example of blockage of an RPS gate due to aggregation of 140 nm particles (in the red rectangular). (c) An example of non-uniform RPS signals due to aggregation of 140 nm particles.

6.3.6.3 Applied voltage effects

The DC power applied to the main channel provides driven forces for the loading of particles through electrophoresis and electroosmosis on one hand and generates basic current and detectable signals on the other hand. However, the magnitude of the applied voltage affects the particle detection processes significantly. An electric voltage ranging from 1 V to 9 V was applied to investigate the electric field effects on detecting 140 nm particles by the differential RPS method. As comparison cases, 500 nm and 5 μm particles were also detected by using larger RPS gates. All the particles were diluted in 0.5 M KCl solution (pH4). Figure 6-13 shows the experimental results in detail. Figure 6-13 (a) illustrates the distributions of the RPS amplitudes of 140 nm particles detected by applying 1 V, 1.5 V, 3 V, 6 V and 9 V electric voltages. From Figure 6-13 (a) one can see that the amplitude of the RPS signals increases with the applied voltage gradually. Figure 6-13 (b) and Figure 6-13 (c) illustrate the effects of the applied voltage on the amplitude and the SNR of the RPS signals for all these three particle cases.

Form Figure 6-13 (b) one can see that the amplitudes of the RPS signals are almost linear with the applied voltage for all three particle cases, which coincides with the model derived in Equation (6-9), where the output of the RPS amplitude is proportional to the applied electric voltage when the other parameters are identical, i. e., the same electrolyte solution, and the same particle-to-sensor volume ratio. Consequently, to obtain RPS signals with larger amplitudes, a higher applied voltage is essential. However, a high SNR is more desirable for recognizable RPS signals. Figure 6-13 (c) shows the applied voltage effects on the SNR of the differential RPS detection. The SNRs of these three particle cases increase with the applied voltage at low voltages and then decrease after reaching critical values. For instance, the SNR of the 5 μm case increases from 27 to about 85 when the applied voltage increases from 1.5 V to 6 V; however, the SNR value decreases to about 70 as the voltage increases to 9 V. The 500 nm case shows a similar trend. For the 140 nm particle case, the SNR is about 3 at 1 V and increases gradually to around 18 at 3 V and then reduces to about 6 when the applied voltage increases to 9 V.

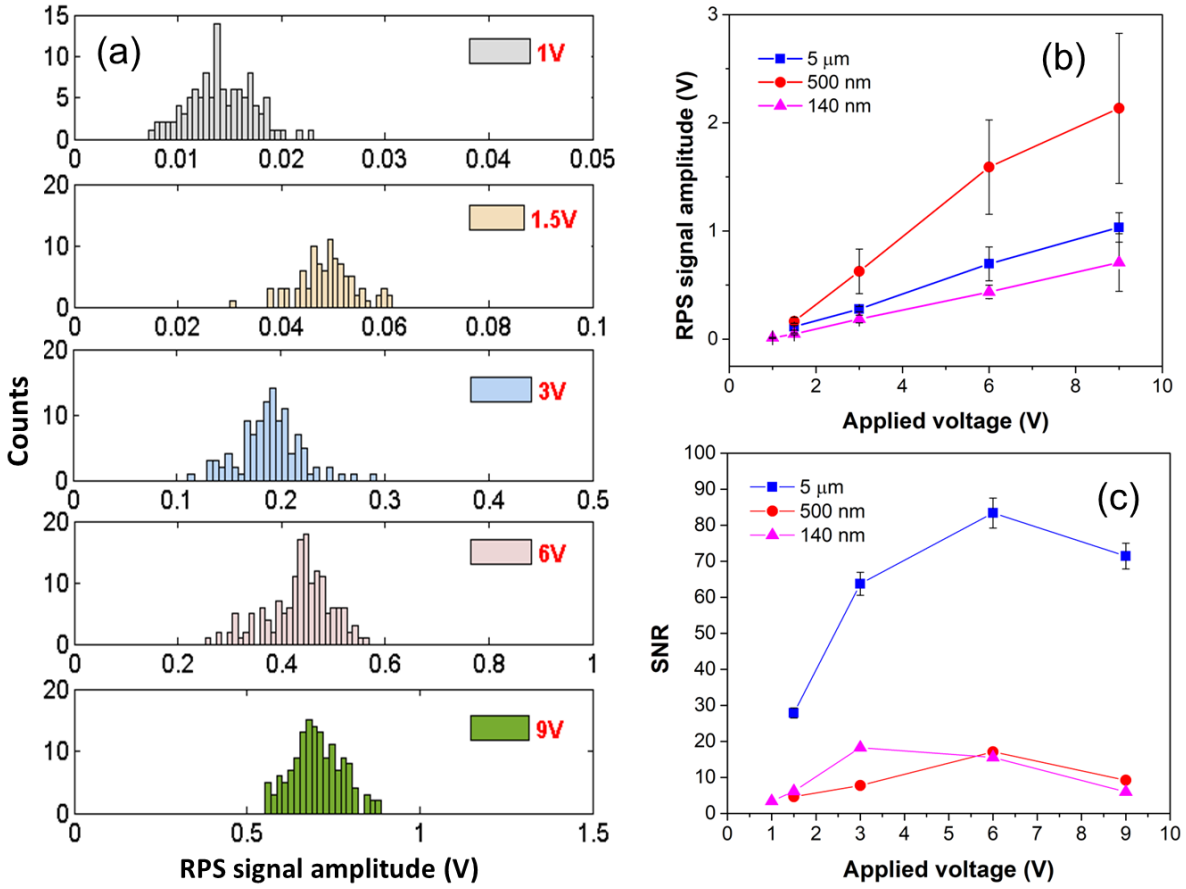

Figure 6-13 Applied voltage effects on detecting particles by the differential RPS method. (a) Distributions of the RPS amplitudes of 140 nm nanoparticles detected by applying 1 V, 1.5 V, 3 V, 6 V, 9 V electric voltages, respectively. (b) Applied voltage effects on the RPS amplitude in detecting 5 μm, 500 nm and 140 nm particles. (c) Applied voltage effects on the SNR in detecting 5μm, 500 nm and 140 nm particles. Error bars smaller than the symbols (500 nm and 140 nm cases) are neglected.

Apparently, the increment of the SNR at low voltages is due to the increasing RPS signal amplitude as shown in Figure 6-13 (b). However, when the applied voltage becomes higher, new phenomena occur and affect the SNR. As mentioned above, a high voltage is likely to trigger electrolysis of water which gives rise to air bubbles and changing of pH value of the electrolyte media. These factors contribute to a higher level of background noise. In addition, the dynamic motion of particles is stronger under the condition of higher electric fields. Collisions between the particles and collisions between the particles and the channel walls also give rise to a higher noise level. Moreover, when a high electric field is applied to a small RPS gate, vortices are likely to be generated at the entrance and the exit of the sensing gate due to polarization of ions, electroosmotic flow of the second kind, induced-charge effects and so on [381–386]. The vortices induce fluctuations of

the electrical current in the main channel and result in a higher noise level during RPS detection, especially for nano-sized RPS gates. For example, the SNR of detecting 140 nm particles at 3 V is about 18, and this value decreases by two-thirds to around 6 as 9 V is applied. Consequently, to obtain RPS signals with large amplitudes and high SNRs, a suitable applied voltage is crucial. Many published papers have been studied the applied voltage effects on the RPS detection [267,387], however, in these papers, the effects of applied voltage on the SNR of the RPS detection have not been investigated.

6.3.6.4 pH effects

It is widely accepted that pH affects the surface charge properties of solid surfaces, and surface charges dominate electrokinetic transport behaviors in both microfluidic and nanofluidic systems. However, particle samples are usually required to be suspended in a specific pH environment, and to the best of our knowledge, the effects of the pH environment on small particle detection by the differential RPS method have seldom been studied. Also, it should be noted that PDMS material could be damaged in extreme environments, such as extreme high pH values, due to hygroscopic and hydrolytic degradation [388]. However, these effects only become appreciable at very long exposure time and extreme pH values. In this chapter, the PDMS chips were used for only once, and the working life of each chip was generally shorter than 30 min. As a result, the effects of hygroscopicity of the PDMS material on the RPS detection were not considered in this study. In this section, KCl solutions with various pH values were applied to study the pH effects on the particle detection. Particles of 5 μm, 500 nm, and 140 nm were diluted in these solutions, and 9 V, 6 V, and 3 V electric voltages were applied along the main channels in these three particle cases, respectively. Figure 6-14 illustrates the pH effects on the particle detection in detail. Figure 6-14 (a) describes the conductivity of KCl solutions with pH values ranging from 1 to 13 and the amplitude of RPS signals of 5 μm, 500 nm, and 140 nm particles detected by using these solutions. Figure 6-14 (b) gives the pH effects on the SNR of the RPS signals in detecting 140 nm particles, and Figure 6-14 (c) demonstrates the distributions of the RPS amplitude of the 140 nm particles. Examples of RPS signals recorded during detecting 140 nm particles by using pH 1, pH 4, pH 6 and pH 10 KCl solutions are demonstrated in Figure 6-14 (d).

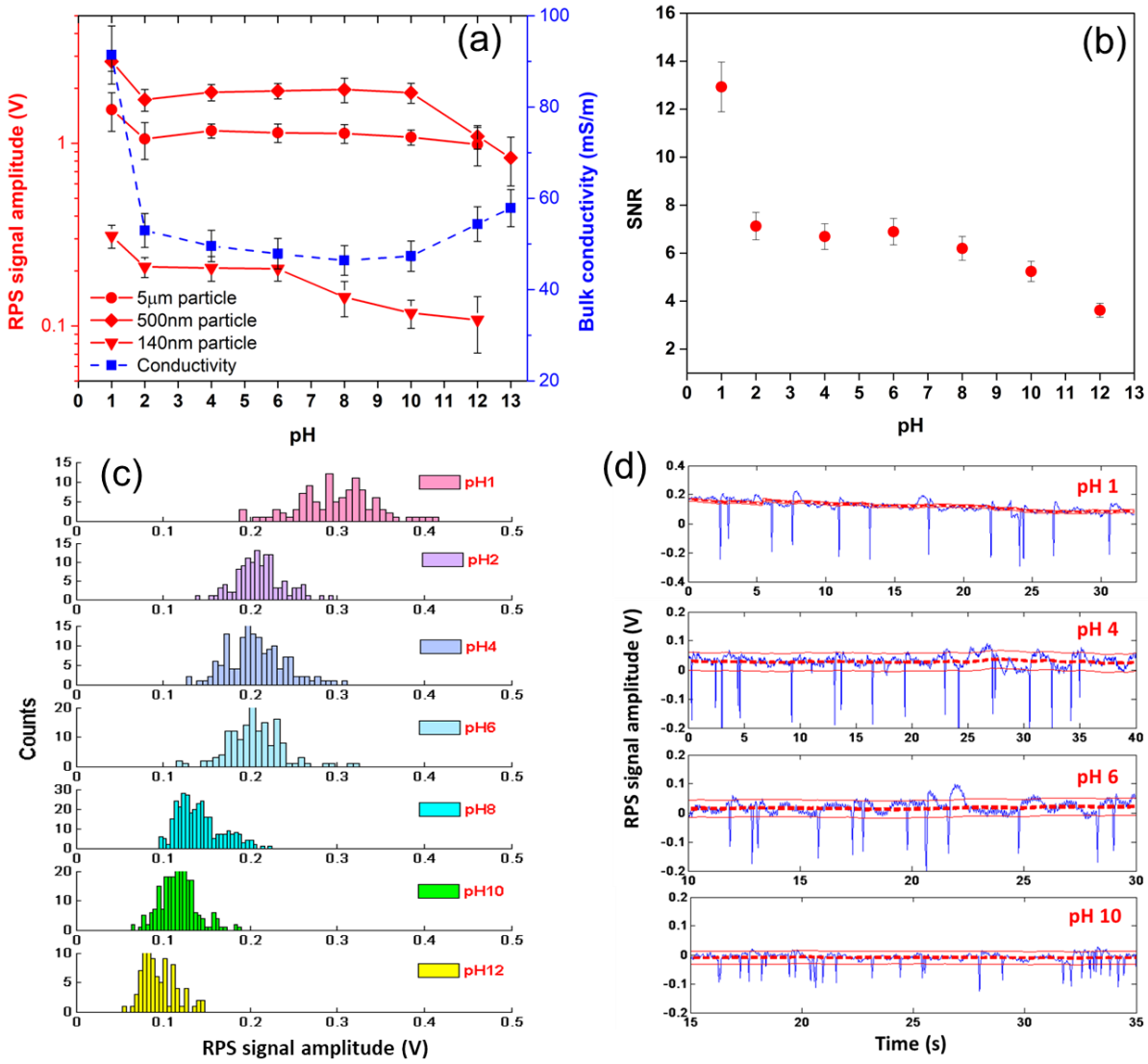

Figure 6-14 pH effects on particle detection by the differential RPS method. The particles were diluted in 0.5 M KCl solution, and 9 V, 6 V and 3 V electric voltages were applied in the 5 μm, 500 nm and 140 nm particle cases, respectively. (a) Conductivity of 0.5 M KCl solutions with pH ranging from pH 1 to pH 13 and RPS amplitudes of 5 μm, 500 nm and, 140 nm particles detected by using these solutions. (b) pH effects on the SNR in detecting 140 nm particles. (c) Distributions of RPS amplitudes in 140 nm particle detection and (d) RPS signals of 140 nm particles detected by using pH 1, pH 4, pH 6 and pH 10 KCl solutions.

From Figure 6-14 (a) one can see that the RPS amplitude for all three particle cases decreases with increasing pH sharply at low pH followed by a plateau in the middle and experiences a decreasing trend at high pH. The conductivity of the solutions decreases with increasing pH at low

pH and arrives at a plateau in the mediate pH, however, increases again when the pH value is higher than 10, as shown in Figure 6-14 (a). The high conductivity at low and high pH values is due to the high ionic mobility of H^+ and OH^- ions [6]. It is obvious that the amplitudes of the RPS signals for all these three particle cases are dominated by the conductivity of the electrolyte media and follow the trend of the conductivity curve at low pH values. However, when the pH value becomes higher, the conductivity effects are less important, and the RPS amplitudes are mostly affected by the pH.

For instance, for the 140 nm particle cases, when the pH value increases from 1 to 2, the conductivity decreases from about 90 mS/m to around 53 mS/m while the signal amplitude decreases from 0.3 V to about 0.2 V. However, when the pH increases further from 6 to 12, the conductivity also increases from 47 mS/m to 55 mS/m, but the amplitude or the RPS signals decreases from about 0.2 V to 0.1 V. The trend of the SNR in Figure 6-14 (b) is almost identical with the signal amplitude curve in Figure 6-14 (a). However, the calculated background noise levels for all these cases are of the same magnitude, about 0.02 V. As a result, one can conclude that pH has little effect on the background noise but affects the amplitude of the RPS signals at high pH, as intuitively shown in Figure 6-14 (d). From Figure 6-14 (d) one can see that RPS signals detected by using pH 1 solution are more recognizable than those by using higher pH solutions. On the other hand, from Figure 6-14 (a) one can see that the decrease of the RPS amplitude at high pH is more evident in the 140 nm particle case. One probable reason is that the charge effect on the RPS amplitude in the 140 nm particle case is more obvious than that in the 5 μm and 500 nm particle cases, because a small particle has a larger surface-to-volume ratio compared with large particles. Under the condition of high pH, small particles are highly negatively charged; as a result, the charges on the particles contribute partial conductivity to the RPS gate and reduce the amplitude of the RPS signals. While in the model presented in this chapter, the particles are assumed to be perfectly non-conducting and pH has no effects on the amplitude of the RPS signals. However, in practical particle detection, to obtain RPS signals with large amplitudes and high SNRs, it is crucial to find a right electrolyte with a suitable pH value.

In addition, pH of the electrolyte solution plays an important role in sample loading and stabilization of particle suspensions in particle detection by affecting the surface charges of the RPS gate and the particles. In electrokinetic sample loading, the surface charges on the RPS gate and the particles combining with the externally applied electric field provide the driven forces for the fluid and the particles. However, at a specific pH value, sample loading by electroosmotic flow and electrophoresis may fail because the surface charges may become zero at this pH value, which is

called PZC (point of zero charge) or isoelectric point. For example, during the experiments of this section, reversal of moving direction of the particles at a pH around 10 was observed. As a result, at pH 10, the velocity of the particles was very slow. Furthermore, the repulsion force between the entrance of the RPS gate and the particles at high pH will stop the particles from entering the RPS gate, which is also a problem in particle loading sometimes. To conclude, the pH of the electrolyte media affects the efficiency of electrokinetic sample loading, the duration time and amplitude of the RPS events, stability of the particle suspensions by dominating the surface charges of the RPS gates and the particles.

6.3.6.5 Particle concentration and loading trajectory effects

One can get the dynamic motion and the concentration of particles by evaluating the duration time and the frequency of the RPS signals, and for a channel-based RPS sensor, the dynamic motion of the particles is affected by the concentration and the trajectory of the particles. For example, when two successive particles are too close to each other, they affect the motion of each other when passing through the RPS gate due to the electrostatic repulsion force between them. In addition, simultaneous translocation of two or more particles will generate larger RPS signals in comparison with those of the single particle cases, as mentioned above. The trajectory of a particle inside an RPS sensor also affects the shape of the RPS signal. For example, off-axis translocations of particles may generate larger RPS signals compared with those of the on-axis cases [389–391] due to the non-uniform electric field inside the RPS gate. Additionally, RPS signals are induced even before the entry of the particles [389,392,393]. As a result, attention should be paid to the trajectories of the particles during RPS detection.

Figure 6-15 demonstrates an example of grouping of RPS signals due to off-axis particle loading and interactions between the channel walls and the particles. In this case, 500 nm particles were diluted in 0.5 M KCl solution (pH 2) by 500 times and detected by applying 9 V along the main channel. To be noted, the trajectory effects may happen at any circumstance and the working condition demonstrated in part is just an example. Figure 6-15 (a) is a scatter diagram of the RPS signals. From Figure 6-15 (a) one can see that the signals are separated into two apparent groups. The amplitudes of the two groups of RPS signals are similar, as shown in Figure 6-15 (b), however, the signals are separated into two groups by different durations (Figure 6-15 (c)). Figure 6-15 (d) is a zoomed-in view of the first-group RPS signals, and the distributions of the amplitude and the duration time of these signals. A similar example of grouping of RPS signals detected by the differential RPS method is demonstrated in Figure 6-16.

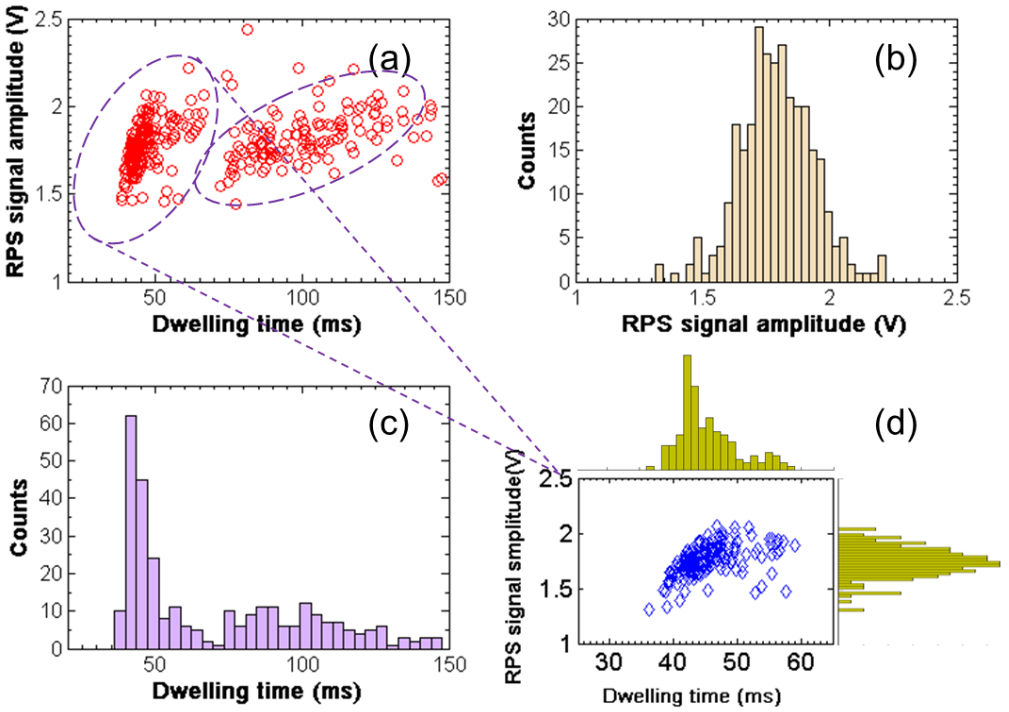

Figure 6-15 An example of grouping RPS signals caused by off-axis particle loading and particle-wall interactions. (a) Scatter diagram of RPS signals of 500 nm particles detected by the differential RPS; (b) Distribution of the RPS signal amplitude in (a); (c) Distribution of dwelling time of the RPS signals in (a); (d) A zoomed-in view of the first-group RPS signals.

Grouping of RPS signals by amplitude has been reported previously [389], and a variation in amplitude ranging from 10% ~ 35% has been presented [390,391]. However, in Figure 6-15 (a), the difference in the amplitude of these two groups of events is not so obvious, and the events are mainly grouped by duration time. The discrepancy in the grouping style is considered to be caused by the shape of the RPS gate and the interactions between the particles and the RPS gate. In Figure 6-15 (a), the RPS gate is a long channel and the electric field inside the channel is relatively uniform, as a result, off-axis translocations of particles will not contribute large amplitude changes in the RPS detection. However, as the particle size is comparable to the inner diameter of the RPS gate, off-axis particles are likely to touch the RPS gate walls and interact with the channel walls, resulting in a low transport speed and a long duration time. On the contrary, particles loaded along the central axis will pass through the RPS gate smoothly without any interactions, and the speed is high while the duration time is short. Consequently, the events of the translocations are divided into two apparent groups, one group with a shorter duration time and without channel wall-particle interactions and one

group with a longer duration time due to the interactions between the channel walls and the particles, as shown in Figure 6-15 (a). Consequently, one may predict that for long channel-based RPS gates, the grouping behavior is dominated by the particle-wall interactions, and the RPS events are mainly grouped by duration time, for example, more than 50% in difference as illustrated in Figure 6-15 (a). The uniformity of the RPS gate and the setting of the microchannel-nanochannel conjunction dominate the number of groups, as shown in Figure 6-16 (a). From Figure 6-16 (a) one can predict that there are four groups of sampling trajectories.

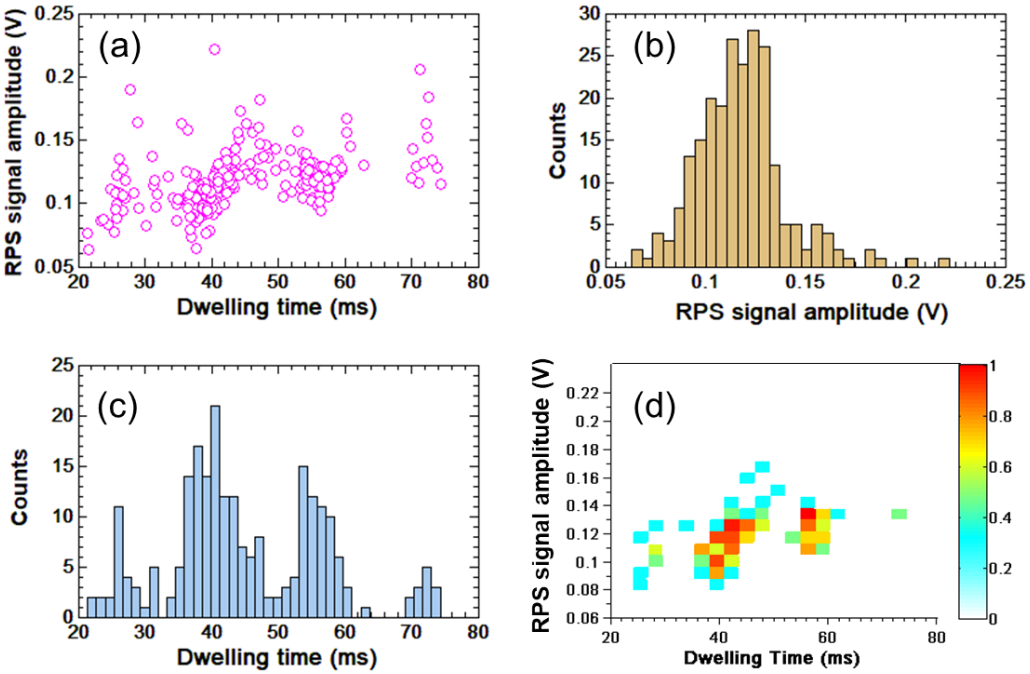

Figure 6-16 Grouping of RPS signals of 140 nm particles detected by the differential RPS. 140 nm particles were diluted in 0.5 M KCl (pH 4) and a 3 V electric voltage was applied along the main channel. The signals fall into four groups. (a) Scatter diagram of RPS signals. (b) Distribution of the RPS amplitude. (c) Distribution of the dwelling time. (d) Heat map of the RPS signals.

It is impossible to avoid the circumstance of simultaneous loading of particles theoretically. Entering of two particles into the RPS gate at once would generate a larger RPS signal compared with that of a single particle case. An example of simultaneous transport of particles is demonstrated in Figure 6-12 (c). However, the possibility of the simultaneous loading situation can be minimized by controlling the concentration of the particle samples. In theory, the highest particle concentration (volume ratio v/v) that an RPS system can handle by a one-by-one detection style is the same as that

of the particle-to-sensor volume ratio (γ). In the experiments, the particle samples are usually diluted to make sure the one-by-one detection process.

6.4 Conclusion

In conclusion, in this chapter, we developed nanofluidic chips with single nanochannels working as RPS gates for detecting and characterizing nano-sized objects. The nanochannel-based differential RPS detection system is simple, cost-effective and has the merits of high resolution and high sensitivity. The nano-RPS chips were used to detect aggregation of nanoparticles, electrokinetic motion of particles and dsDNA molecules. The results obtained by the nano-RPS chips are compared with that obtained by the DLS method, showing superior performance. Detecting nanoparticles of 23 nm with high SNR by using the differential nano-RPS chips was achieved. The differential nano-RPS device was also used to detect a mixture sample of 60 nm and 83 nm nanoparticles, showing an excellent detecting resolution. An application of detecting dsDNA molecules by the nano-RPS device with high SNR was also demonstrated.

To investigate the key working parameters in the differential RPS method in nanoparticle detection, the effects of particle-to-sensor size ratio, ionic concentration and pH of the electrolyte solution, applied voltage, as well as the particle loading trajectory on the differential RPS method are studied systematically. The results show that both the amplitude and the SNR of the RPS signals increase with the particle-to-sensor size ratio and the conductivity of the electrolyte media. The amplitude of RPS signals also increases with the applied voltage. However, the SNR increases with the applied voltage only when the voltage is lower than a critical value, and when the applied voltage is higher than the critical value, the SNR decreases with the voltage gradually. pH has little effect on the background noise of the differential RPS detection but reduces the amplitude of the RPS signals at high pH. In nanochannel-based differential RPS detection, the RPS events could be divided into groups due to the interactions between the channel walls and the particles. Aggregation of small particles under the condition of extremely high ionic strength, extremely low pH, instability of electric current through the RPS gate at a high driven electric field are also investigated.

This chapter provides a framework for the working principle, working procedures as well as applications of the differential RPS method in nano-sized object detection. Detection of nanoparticles by the differential RPS method can be enhanced by optimizing the working parameters. In addition, based on the systematic study presented in this chapter, the device also offers potential applications in the fundamental research areas such as microfluidics, nanofluidics as well as interfacial sciences

by analyzing the shape, amplitude, duration of the RPS signals. The potential applications may include investigating electrokinetic transport of particles in a confined space, detecting surface charge of particles, capturing and manipulating of particles, and detecting deformation of targets and so forth. Detecting smaller objects requires even smaller nanochannels; however, it is difficult to fabricate PDMS nanochannels smaller than 20 nm due to the collapse of channel roofs after bonding. In the next chapter, the PDMS nanochannels are replaced by CNTs, which enables detecting smaller objects.

CHAPTER 7 Application II: Detection of Single Molecules and Ions by Carbon Nanotube-based Differential Resistive Pulse Sensor [‡]

7.1 Introduction

Driven by the development of nanofabrication technologies, nanoscale resistive pulse sensing (RPS) technique has received increasing attention and been widely applied in detection of cations [394–397], nanoparticles [339,340,398], DNAs [260,353,399–402], proteins and viruses [343,403–406] as well as single molecules [347,395] due to its simplicity, high versatility and sensitivity. A typical nano-RPS system includes a small nano-orifice separating two reservoirs filled with electrolyte solution. An electric field is applied across the orifice to build up a steady electric current through the orifice. As nano-sized objects pass through the nano-orifice and disturb the steady electric current, detectable signals are generated. From the amplitude, frequency and dwelling time of the signals, one can obtain the size, number, concentration, shape, velocity, and surface charge properties of these nano-sized objects. As a key component of a nano-RPS system, the nano-orifice can be a solid-state nanopore [266,345,349,352], a biological nanopore [353], an elastic polymer-based nanopore [378,407,408], a nanochannel [398] or a confined nano-space made of unconventional nanomaterials such as a piece of nanomembrane [409] or a nanotube [113,410–413].

Carbon nanotube (CNT) has been used in RPS systems due to its superior properties over other materials. For example, the controllable inner diameter (a few nm or less than 1 nm) of CNTs is comparable to the size of single molecules, which provides an excellent platform for detecting and manipulating single nano-sized objects such as cations [394,396,397], DNAs [410,412–414], small organic molecules [347,395] and solid nanoparticles [415]. The uniformity of long CNTs facilitates transport mechanisms unique in nanospace, such as ultra-fast transport of molecules due to the superhydrophobic interior surface of CNTs and special phase transition of water in nanotubes [416–418]. The TPa-level Young's modulus and high chemical inertness properties are favorable to practical applications preventing mechanical deformation and chemical deterioration [419]. Furthermore, synthesis of ultra-long CNTs by methods such as chemical vapor deposition (CVD) is more productive and less expensive than that of the solid-state nanopores. In addition, CNT-based devices

[‡] A similar version of this chapter was submitted to a journal for publicaiton:
Peng, R.; Li, D. Detecting of Individual Molecules and Ions by Carbon Nanotube-based Differential Resistive Pulse Sensor, Small. (Accepted), http://onlinelibrary.wiley.com/journal/10.1002/(ISSN)1613-6829.

are easier to fabricate compared to biological nanopores, which are sensitive to temperature, pH and salt concentration. Chemical properties of CNT orifice can be modified by using covalent or non-covalent molecular bonding, especially at the tube ends, enabling detection of specific species. Due to these merits, increasing efforts have been made to develop CNT-based RPS devices. However, there are significant challenges.

Nanofluidic devices with a single CNT or multiple CNTs working as fluidic pathways have been reported, and these devices can be divided into two branches, i.e. vertical CNT channels and horizontal CNT channels. The first vertical CNT pathway chip incorporating an isolated CNT was reported by Crooks et al [369]. An isolated CNT was embedded into epoxy and microtomed into thin slices. These slices with identical nanopores were further mounted onto freestanding membrane supports to form the final devices. As a result, a lot of identical chips can be fabricated at a time, which is productive. However, the inner diameter of the CNT (> 50 nm) is too large to detect single molecules. Another strategy to fabricate vertical CNT channels is to insert well dispersed ultra-short CNTs into a lipid membrane [410,414]. However, the sonication-assisted cutting process would produce defects on CNT walls, and the lipid layers are not as mechanically stable as that of solid state devices and epoxy chips.

Planar fluidic pathways using CNTs were developed by Lindsay's group [347,412,413] and Strano's group, et al. [394,396,397,420] During the fabrication process, CNTs were localized on a substrate horizontally and covered by a layer of photoresist. Electron-beam or conventional optical lithography was applied to generate reservoirs and patterns following by cutting and uncapping of CNTs by plasma. The length of the CNT channels was well controlled by the photolithography process. However, cutting or uncapping of CNTs by plasma was not so efficient (about 80% success ratio reported by Liu et al. [412]), especially for multiwall carbon nanotube (MWNT). The planar design of nanofluidic chips can enable simultaneous optical and electrical probing. However, most devices mentioned-above are not optically transparent. Additionally, the current monitoring method required by the traditional RPS method by using voltage clamp is relatively complicated. Though cations [394,396,397], DNAs [410–414] and organic molecules [395] have been detected by the horizontal CNT channels, the smallest ssDNA detected by CNT-based RPS device as reported in the literature was 60 nucleotides (60-nt) [411] to the best of our knowledge, and no evidence ever showed that the CNT-based RPS device can distinguish ssDNAs of different lengths which is essential to DNA sequencing.

To solve the above-mentioned problems in the current differential RPS method and the CNT-based RPS devices, in this chapter, CNT-based differential RPS nanofluidic chips are developed on

glass slides. A novel method to uncap and cut CNTs by mechanical shear force is developed. The planar layout of the nanofluidic chip is optically transparent which enables optical and electrical probing simultaneously. The differential RPS design can minimize the background noise dramatically. Cations, rhodamine B molecules as well as ssDNAs are detected by using this system with high signal-to-noise ratio. Distinguishing 15-nt and 30-nt ssDNAs by using the CNT-based differential RPS nanofluidic chips is also achieved.

7.2 Materials and Methods

7.2.1 Design and fabrication of CNT-based RPS nanofluidic chips

Differential RPS was initially developed by Wu et al. [421] on microfluidic devices to detect micron-sized objects such as microparticles and blood cells. In comparison with the traditional RPS design, there are two symmetrically positioned detecting channels at the two ends of the RPS orifice to collect the voltage change signals across the RPS orifice (or called the RPS gate). The signals collected from these two detecting channels are fed to a differential amplifier circuit. In this way, the background noise is reduced efficiently [421]. Thereafter, the differential configuration was improved and applied in nanoparticle detection and sizing on PDMS nanofluidic chips [398], showing potential capabilities in CNT-based RPS detection. Figure 7-1 illustrates the CNT-based differential RPS nanofluidic chip. A CNT channel is connected by two microchannels, and an electric voltage difference ($V_+ - V_-$) is applied along the main channels as the driving source for liquid flow and particle transport in the chip. Two detecting channels are located in the vicinity of the CNT symmetrically. The change of the electric potential difference between the CNT channel $V_{up} - V_{dn}$ is collected by the two detecting channels and amplfied by a differential signal amplifer. Here, the inner diameter of CNT is on the order of several nanometers, which enables detection of individual molecules on the nanometer level.

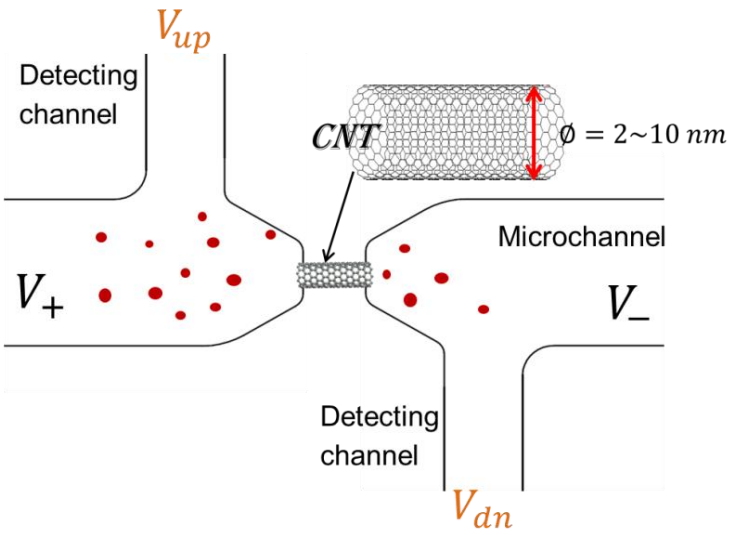

Figure 7-1 Schematic of a differential CNT-based RPS nanofluidic chip. A single CNT channel is connected by two straight microchannels for sample loading and collecting under an externally applied electric field. Two symmetrically positioned detecting channels are used to acquire voltage changes as nano-objects pass through the CNT channel.

The CNT-based differential RPS chip is composed of a bottom layer and a top layer. The bottom layer with microchannel systems connected by a CNT channel is fabricated on a glass slide, and the top layer made of a piece of PDMS slab with liquid reservoirs are covered on the bottom part to form the sealed chip. Figure 7-2 elucidates the device fabrication processes in detail. Firstly, a thin layer of positive photoresist is spin-coated on a dehydrated glass slide (Figure 7-2 (a)) followed by anchoring a single CNT on the surface of the sticky photoresist layer, as illustrated in Figure 7-2 (b). Thereafter, another layer of photoresist is spin-coated onto the first layer and embeds the CNT followed by a soft baking process to vaporize the solvent (Figure 7-2 (c)). A photomask is applied to generate microchannels on the photoresist layer by exposing the system to UV light (Figure 7-2 (d)) followed by a developing process. After the developing process, the ends of the CNT are exposed in the air as shown in Figure 7-2 (e). Figure 7-3 (a) and Figure 7-3 (b) show images of a photoresist layer after UV exposure and developing, in which the microchannels are bridged by several CNT channels. It should be noted that both positive photoresist and negative photoresist are applicable, depending on the photomask.

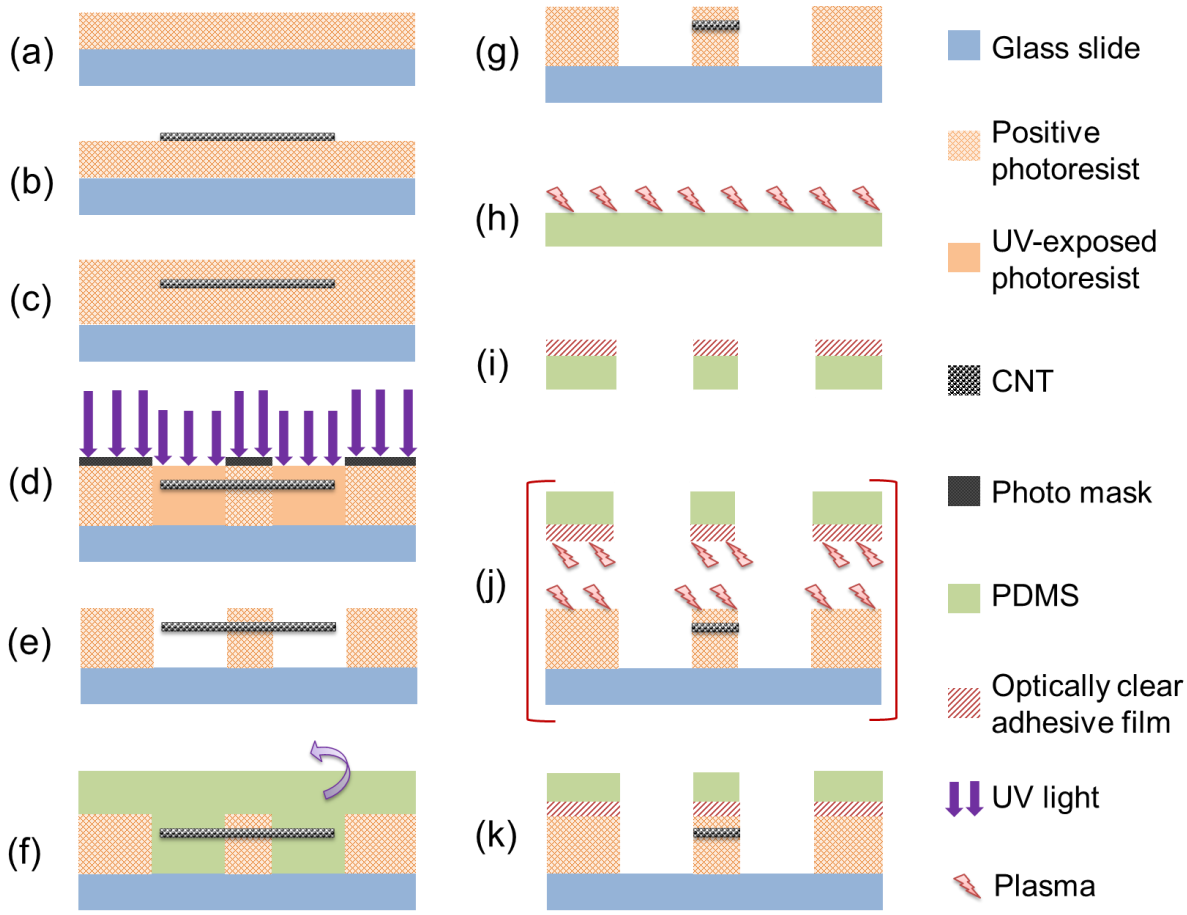

Figure 7-2 Fabrication of CNT-based RPS nanofluidic chips. (a)-(c) Embed a CNT into a layer of photoresist (d) Exposure to UV light (e) Developing of the photoresist layer (f)-(g) Cutting and uncapping of CNT (h)-(k) Boning of PDMS-photoresist nanofluidic chip.

To obtain an open CNT channel, a cutting or uncapping process is needed. Figure 7-2 (f) and Figure 7-2 (g) show the working principle of the cutting in detail. Firstly, liquid form pre-curing PDMS is cast onto the photoresist device mold and the ends of the CNT (the sections exposed in the air in Figure 7-2 (e)) are cast into the PDMS. Peeling off the solidified PDMS layer mechanically can remove the ends of the CNT directly, leaving an open CNT channel connecting two microchannels as shown in Figure 7-2 (g) and Figure 7-3 (c). An example of cutting a large number of MWNTs by this method can be found in Figure 7-4. Cutting CNTs by the above-mentioned mechanical force maintains the integrity of CNTs.

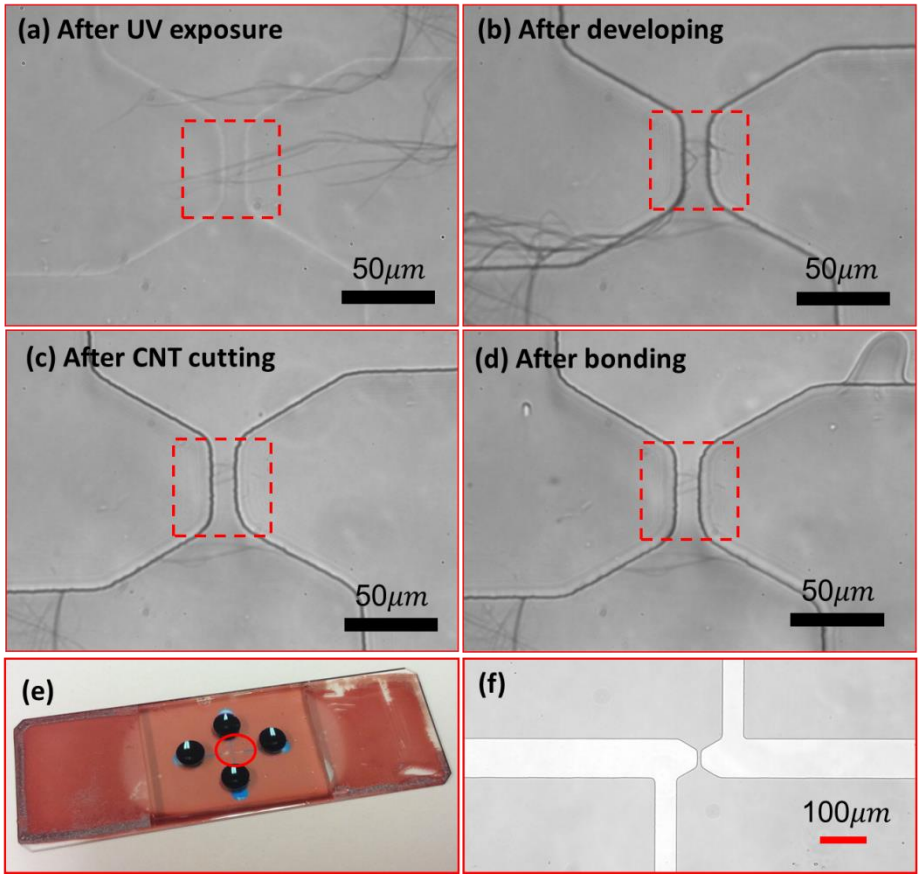

Figure 7-3 Pictures captured during chip fabrication. (a) Photoresist layer after UV exposure. The microchannel systems are connected by several CNTs. (b) The UV-exposed microchannel systems are removed by developing and the ends of CNTs are exposed to air. (c) CNT cutting by casting and peeling off of PDMS. (d) CNT-based RPS chip after bonding. (e) An image of CNT-based RPS chip after bonding and (f) a zoomed-in view of the RPS sensing area of the nanofluidic chip.

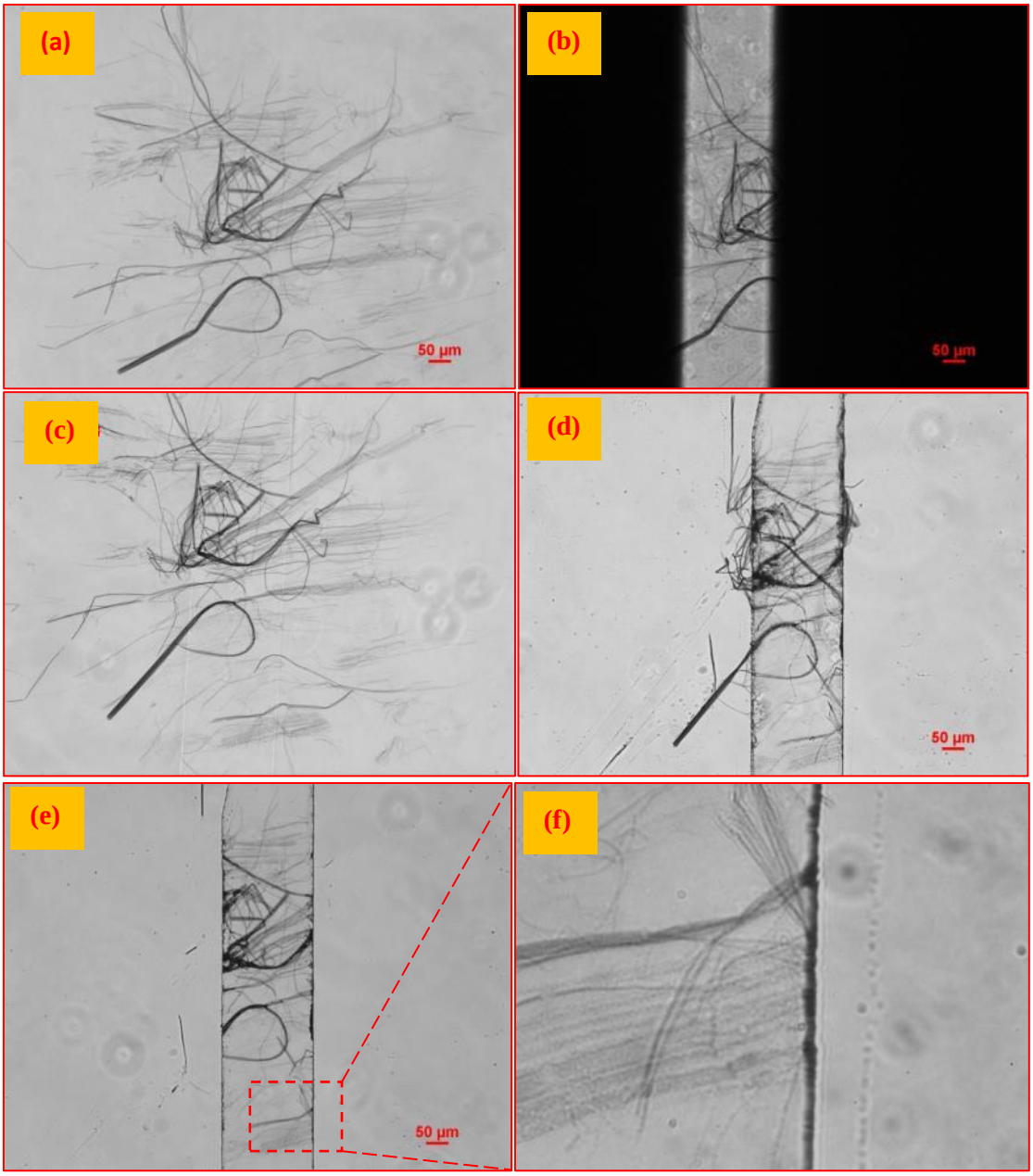

Figure 7-4 Images of cutting MWNTs by an unconventional method. (a) CNTs dispersed on a PDMS surface and transferred into a photoresist layer. (b) The photoresist layer is covered with a photomask. The transparent area will be exposed to UV light. (c) Photoresist layer after exposure to UV. (d) Photoresist layer after developing. The unexposed area is removed. And the redundant sections of the CNTs are exposed in the air. (e) Redundant sections of the CNTs are removed by peeling off of PDMS. (f) A zoomed-in view of CNTs after removing the redundant sections.

To obtain a sealed nanofluidic device, an optically clear adhesive film (Polyacrylic acid) and plasma treatment are applied during the bonding process. Specifically, an adhesive film is placed onto a piece of plasma treated PDMS slab (Figure 7-2 (h)) followed by punching of liquid reservoirs (Figure 7-2 (i)). Afterward, the PDMS-adhesive film cover and the glass-photoresist bottom are bonded together with the help of plasma treatment (Figure 7-2 (j)) and an alignment of the channels and reservoirs (Figure 7-2 (k)). Figure 7-3 (d) shows a photo of the CNT-based nanofluidic chip captured after bonding. A photo of the real device is shown in Figure 7-3 (e) with a zoomed-in view of the sensing area demonstrated in Figure 7-3 (f).

7.2.2 Chemical reagents and instruments

KCl solution (2 M) was prepared by dissolving KCl powder (Fisher Scientific) into pure water (Mini Q, Direct-Q3, 18.2 MΩ·cm, pH 6.5). 15-nt (T) and 30-nt (T) ssDNA (IDT, Integrated DNA technologies) were diluted in the 2 M KCl solution to 10 nM before loading. Rhodamine B (Sigma Aldrich) was also diluted in the 2 M KCl electrolyte to 5 nM before RPS testing. Pre-curing PDMS (Sylgard 184) was prepared by mixing PDMS base with curing agent at a ratio of 10:1. The photomask for photolithography was designed by AutoCAD and printed at a resolution of 5 μm (CAD/Art services, Inc.). Nanofluidic chips were developed on glass slides (Fisher Scientific, 25 mm $\times$ 76 mm). Positive photoresist (AZ1512) and developer (AZ 300 MIF Developer) were purchased from MicroChemicals. Plasma (Harrick plasma®, PDC-32G) and optically clear adhesive film (3M, 8172) were used in chip bonding. Characterization of microchannels and CNTs were conducted using optical microscopy (Nikon, TE2000), atomic force microscopy (AFM) (Multimode™SPM, Digital Instruments) and high-resolution transmission electron microscopy (HR-TEM). DC power (AJC Brand® Battery) was applied on the nanofluidic chip through Pt electrodes (Sigma-Aldrich). During the experiments, the amplification factor of the single stage differential amplifier (AD620, Digi-Key) was 500, and the signals were recorded by the data acquisition card (USB 6259) working at 4 kHz sampling frequency. A homemade Faraday case and shielding cables were applied during the experiments to minimize the surrounding noises.

7.2.3 Synthesis and isolation of MWNTs

Vertically-aligned MWNT forests were synthesized on silicon substrates by following the procedures as previously reported [422,423]. A 4 nm thick Fe layer was deposited on the silicon wafer to work as the catalyst. Vertical-aligned MWNTs were grown on the catalyst by using CVD method at a temperature of 725 ˚C. During the synthesis, ethylene together with argon and hydrogen (70:70:70

sccm) were mixed in a furnace tube of 25 mm in diameter (Lindberg) to supply the carbon source. The length of the MWNTs can be well controlled by the growth time. MWNTs of about 1.5 mm in length were used in this study. The diameter of the MWNTs was characterized by HR-TEM. The MWNTs are all cylindrical tubes with 10-15 wall layers. The tubes are geometrically smooth with an inner diameter range of 2~10 nm as shown in Figure 7-5 (d) [422].

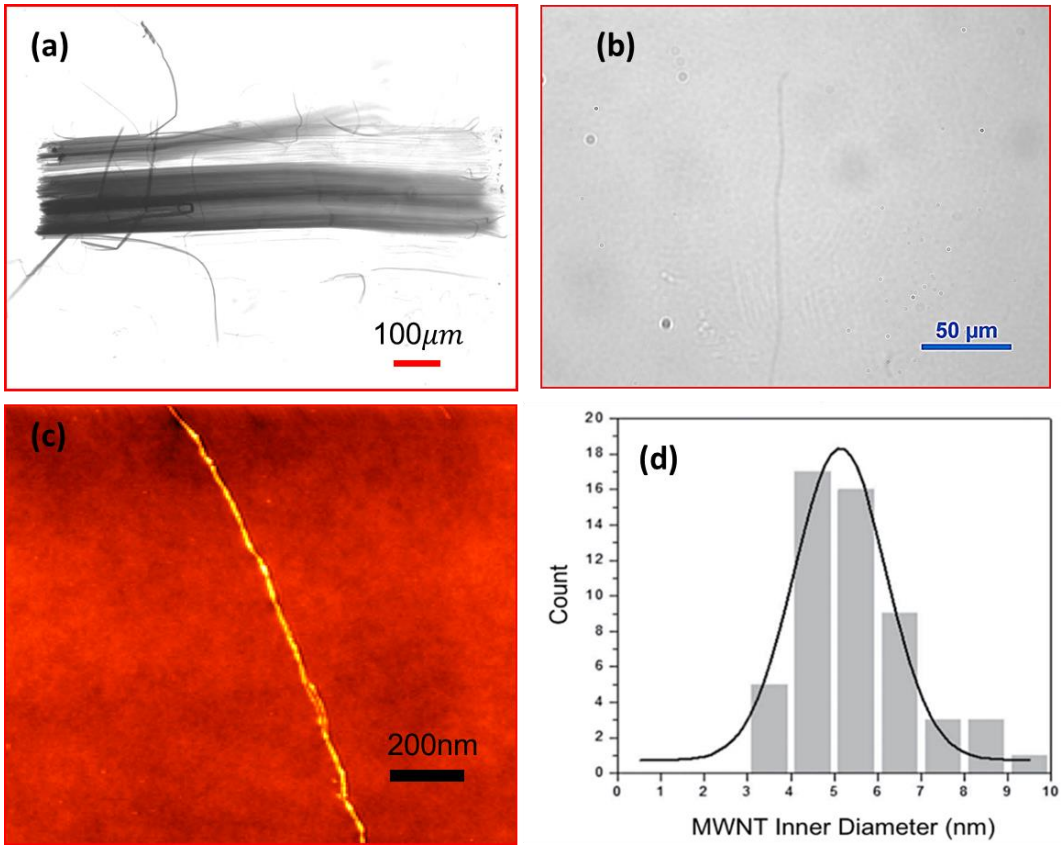

Figure 7-5 Characterization of MWNTs. Examples of (a) a bundle of CNTs transferred onto a piece of PDMS slab, (b) isolated CNTs on a PDMS surface after 'sticking and detaching' and (c) isolated CNTs measured by AFM. (d) Histogram of CNT inner diameter [422].

It is difficult to obtain isolated CNTs from a CNT forest physically. Inspired by the 'sticking and detaching' method which has been used to isolate graphene [424], in this study, single CNTs or small bundles of CNTs were isolated from the forest by a similar way. Firstly, a piece of adhesive tape was used to detach a bundle of CNTs from the CNT forest which has grown on a silicon wafer. Thereafter, the bundle of CNTs was transferred onto a piece of soft PDMS slab surface. Figure 4a shows a picture of CNTs on a piece of PDMS slab, which may include thousands of individual CNTs. However, most of these CNTs were removed by the following rounds of 'sticking and detaching' using a scotch tape, until isolated CNTs were obtained (Figure 7-5 (b)). Figure 7-5 (c) shows an

example of the isolated CNTs scanned by AFM. The isolated CNTs can be transferred onto a photoresist layer as described above and bridge the microchannels to assemble the final RPS device. It should be noted that the isolated bundle of CNTs may still contain several individual CNTs and some of them may be blocked by the amorphous carbon or the iron catalyst (see Figure 7-6 for the example of blocked CNT channels). In the chip fabrication processes, only the most uniform CNTs were selected. It is hard to ensure that every chip is good for RPS detection, due to the blockage of the CNTs or failure in cutting, as well as multi-CNT-channels. Therefore, only devices offer uniform RPS signals and translocations of single molecules through one single CNT were considered.

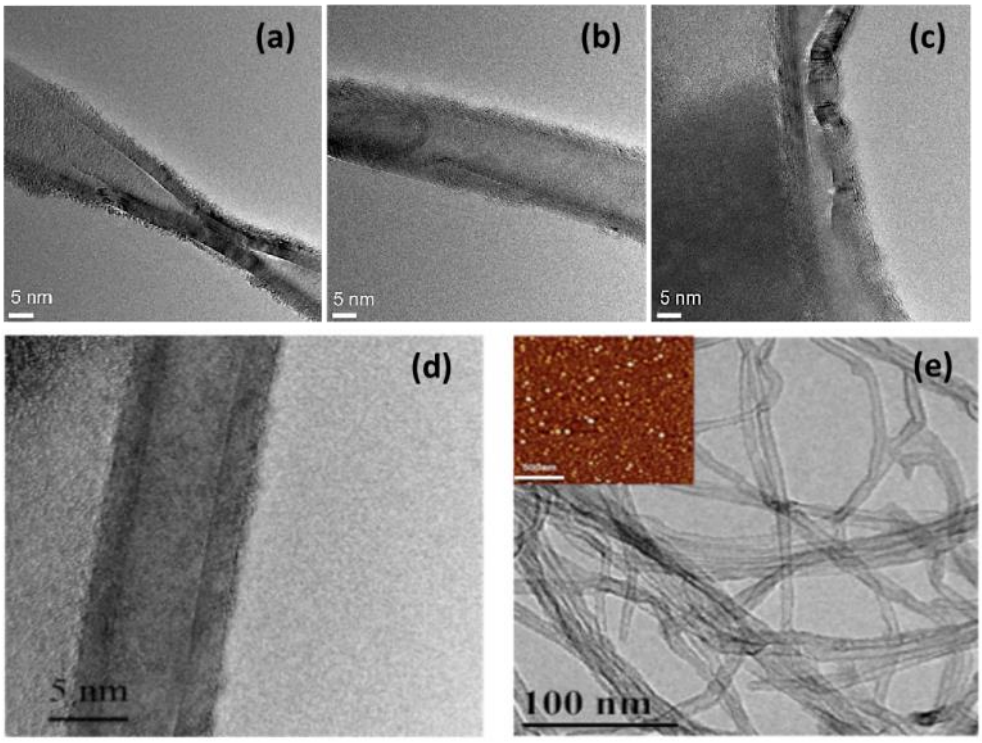

Figure 7-6 Characterization of CNTs. (a-c) HR-TEM images of multi-walled carbon nanotubes show example structural defects causing blocked CNT channels. (d) HR-TEM of a single CNT showing the multiple walls and an inner diameter around 5 nm. (e) TEM image of CNTs with diameters well correlated to Fe Catalyst particle sizes, as shown in the AFM image (inset, scale bar is 500 nm). [422]

7.2.4 Experimental procedures and data processing

Conditioning of the CNT-based nanofluidic chip was conducted by filling the channels with 2 M KCl solution for 10 min prior to loading the samples. After loading the ssDNA or rhodamine B samples, a DC electric field was applied to the main channels through Pt electrodes by simply inserting the electrodes into the liquid reservoirs. The signals were detected by the differential

detecting channels also through Pt electrodes and amplified by 500 times then recorded by a self-complied LabVIEW program. As mentioned above, it is hard to isolate single CNTs for every chip and it is impossible to guarantee an identical size of CNTs in all the RPS chips. As a result, in this work, a mathematical model is created to consider the multi-CNT-channels on a chip and to identify translocation of single targets. Only the chips with uniform and stable detecting signals were considered in the following sections.

Generally, the data presented in this study were obtained from one individual chip. However, for each case, the experiments were repeated on at least 10 fresh chips to verify the reliability. For the cases of detecting multiple samples on one chip, the chip was flushed by using fresh 2 M KCl solution for at least 5 times to remove residual samples from the previous experiments. The original data were acquired at a frequency of 4 kHz and a Bessel low pass filter was applied to remove the high-frequency noises. During the data processing, moving average technique [374] as mentioned in the previous chapter was applied to evaluate the baseline of the raw data. The noise level of the RPS data was obtained by calculating the standard deviation of 4000 data points without any RPS events, and a minimum signal-to-noise ratio (SNR) threshold of 2 was applied to identify the RPS events. The amplitude and the FWHM (Full Width at Half Maximum) dwelling time of the RPS events were plotted into histograms. All the experiments were conducted at room temperature.

7.3 Results and discussion

7.3.1 Mathematical model for single molecule detection by multiple-CNT-channel RPS

As mentioned above, CNTs created by the CVD method are usually in the form of bundles. It is essential to isolate single CNTs for the RPS chips. However, in most cases, more than one CNTs bridge the upstream and downstream microchannels, as shown in Figure 7-3 (d). This section aims to develop a mathematical model for such a multi-channel RPS detection system. Figure 7-7 (a) shows a sketch of a multi-CNT channel RPS system and Figure Figure 7-7 (b) is an equivalent electrical circuit of the detection system.

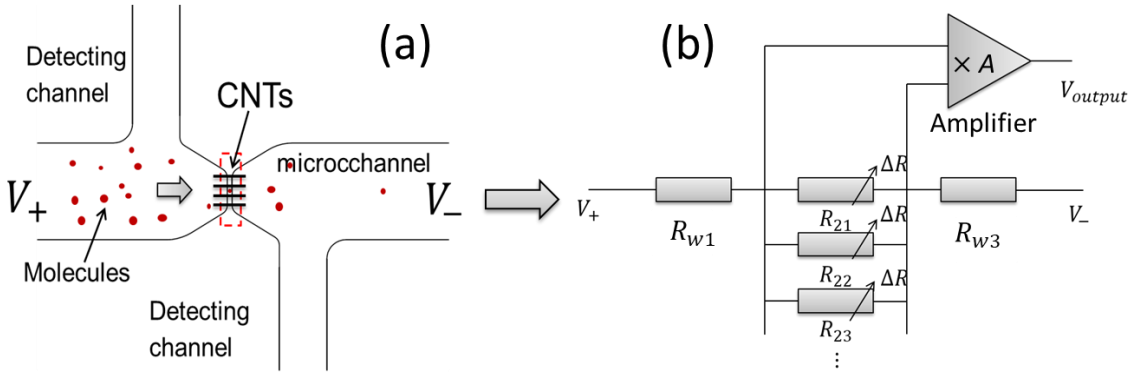

Figure 7-7 (a) Working principle of a differential RPS detection system containing multiple CNT channels and (b) an equivalent electrical circuit of the RPS system. R_2 is the electrical resistance of each CNT filled with electrolyte solution. R_1 and R_3 are the resistances of the upstream and the downstream microchannels and ΔR is the electrical resistance change of each CNT due to one single object passing through. A is the amplification factor of the amplifier.

As shown in Figure 7-7 (a) and Figure 7-7 (b), there are several parallel CNTs working as RPS sensors. A DC electric voltage difference of ΔV ($\Delta V = V_+ - V_-$) is applied along the main channel. Assume that these CNTs have the same diameter. The electrical resistance for each CNT filled with electrolyte solution is R_2. The resistances of the upstream and the downstream of the main channel are R_{w1} and R_{w3}, respectively. ΔR is the electrical resistance change of each CNT due to one single object passing through. The total electrical resistance of the parallel CNTs filled with electrolyte and without any targets passing through is given by

$$R_{2t} = \frac{R_2}{n} \tag{7-1}$$

where n is the number of the parallel CNTs. When m targets pass through n CNTs simultaneously ($m < n$), the total electrical resistance of the CNTs is given by

$$R'_{2t} = \frac{R_2(R_2 + \Delta R)}{n(R_2 + \Delta R) - m\Delta R} \tag{7-2}$$

According to Ohm's law, the electric potential difference across the CNTs without any objects passing through is

$$V_1 = \frac{R_2}{R_2 + nR_w}\Delta V \tag{7-3}$$

where R_w is the total electrical resistanc of the main channels, $R_w = R_{w1} + R_{w3}$, and the electric potential difference across the CNT channels while m targets passing through is

$$V_2 = \frac{R_2(R_2 + \Delta R)}{R_2(R_2 + \Delta R) + nR_w(R_2 + \Delta R) - mR_w\Delta R}\Delta V \qquad (7\text{-}4)$$

Assuming that the electrical resistance of the detecting channels is negligible, the output of the differential RPS signal can be simplified as

$$\Delta V_{output} = A\left(\eta_{up} - \eta_{down}\right) + A(V_2 - V_1) \qquad (7\text{-}5)$$

which can be rewritten as

$$\Delta V_{output} = A\left(\eta_{up} - \eta_{down}\right) + A\frac{km\alpha}{(k+n)^2 - m\alpha(k+n)}\Delta V \qquad (7\text{-}6)$$

where A is the amplification factor, $k = \frac{R_2}{R_w}$ is the electrical resistance ratio between the sensor gate and that of the main channel, which is constant for a fixed system, and $\alpha = \frac{\Delta R}{R_2 + \Delta R}$ is the relative resistance change of an individual CNT due to translocation of a single target through a single CNT. For the differential RPS, the noises coming from the upstream detecting channel η_{up} and the noises coming from the downstream channel η_{dn} can be canceled due to the symmetric design of the detecting channels. Consequently, the amplitude of the output signals can be rewritten as

$$\Delta V_{output} = A\frac{km\alpha}{(k+n)^2 - m\alpha(k+n)}\Delta V \qquad (7\text{-}7)$$

because the electrical resistance of the main channel is much smaller than that of the nano-sized CNTs, $k = \frac{R_2}{R_w}$ (as defined above) is a large number and is much larger than the limited number of the parallel CNTs, n, i.e., $k \gg n$. As $k \gg m\alpha$ (m is a small integer), a simplified equation for the case of m targets passing through m out of n CNT channels ($m < n$) simultaneously can be obtained as:

$$\Delta V_{output} = A\frac{m\alpha}{k}\Delta V \qquad (7\text{-}8)$$

As a consequence, one can conclude that for a given RPS device containing n parallel CNT channels, the output of the RPS signals is proportional to the number of target m, the relative resistance change of an individual CNT due to translocation of a single target(α), as well as the

externally applied voltage ΔV. In Equation (7-8), the parameter $\alpha = \frac{\Delta R}{R_2+\Delta R}$ can be positive or negative, revealing increase or decrease of the electrical resistance of the CNT channel (ΔR) due to translocations of different objects. Consequently, the output of the signals ΔV_{output} can also be positive peaks or negative peaks. For instance, the signals in Figure 7-8 (a) and Figure 7-8 (b) are upward peaks, indicating the increase of electrical resistance of the CNT sensors when rhodamine B molecules or potassium ions passing through the CNT channels. On the contrary, the downward peaks in Figure 7-8 (c) caused by translocations of 30-nt ssDNAs indicate the decrease in electrical resistance of the CNT channels. This is due to the large number of counter ions shielding the negatively charged ssDNA chain, which yield a positive contribution to the conductivity of the CNT channels. The conductance change highly depends on the ionic concentration of the electrolyte solution, the length of the ssDNA and the inner diameter of the CNT [113,411,425,426]. In addition, both m and ΔR affects the amplitude of the RPS signals. For example, under the conditions of $m > 1$ in multi-species detection, the RPS signals will not be uniform. Figure 7-8 (a) shows an example of RPS signals of rhodamine B molecules diluted in 2 M KCl solution detected by a CNT-based RPS chip. The applied voltage was constant at 1 V. One can only define the gaps between the RPS signals by experience, as highlighted by the dashed lines. The three gaps are assumed to be caused by passing through multiple molecules, as shown in Equation (7-8), in which m can be 1, 2 or 3. The Gaussian fitting curves illustrated in Figure 7-8 (a) predict the three cases mentioned above. However, it not reliable to evaluate the molecules by using these non-uniform signals. As a consequence, in this paper only uniform RPS signals are considered in the following sections, in which each RPS peak is assumed to be caused by translocation of one single object through one single CNT channel and m is assumed to be 1. Examples of uniform RPS signals of potassium ions and 30-nt ssDNAs are demonstrated on Figure 6b and Figure 6c. As $m = 1$, Equation (7-8) can be simplified as

$$\Delta V_{output} = \frac{A\alpha}{k}\Delta V \qquad (7\text{-}9)$$

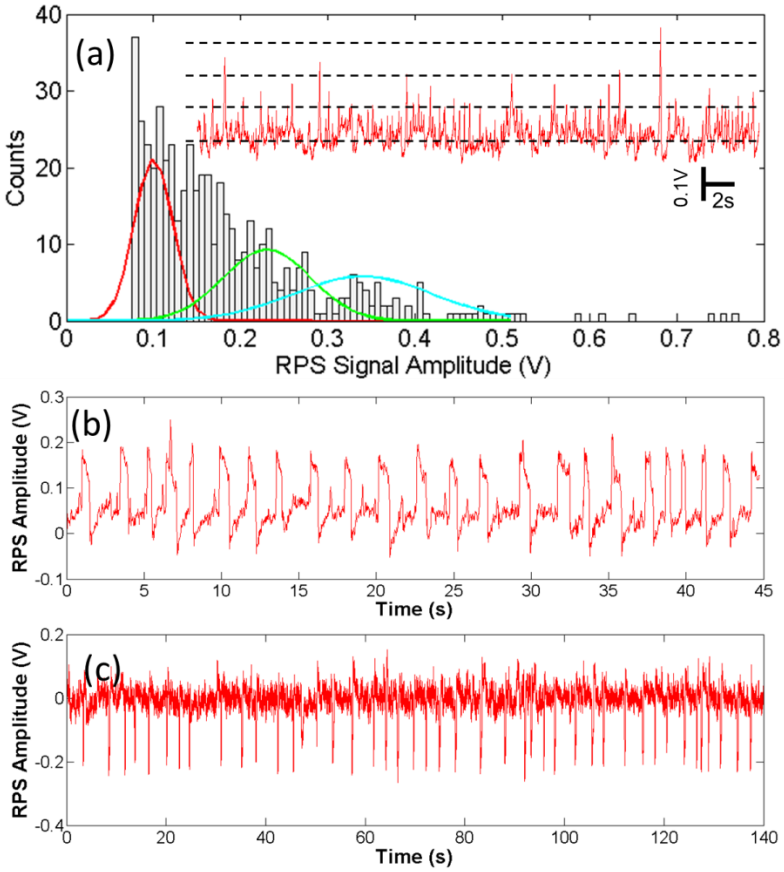

Figure 7-8 Examples of RPS signals detected by using a CNT-based RPS nanofluidic device. (a) An example of RPS signals of rhodamine B molecules detected by a CNT RPS device and a histogram of the RPS signal amplitudes. The applied voltage was 1 V. There are apparent gaps between the RPS signals (N=507, N is the number of RPS events). (b) An example of RPS signals of individual potassium ions detected by using a CNT-based RPS nanofluidic chip with 1 V applied voltage. (c) RPS signals of detecting 30-nt ssDNAs by using a CNT-based RPS device.

7.3.2 Detection of potassium ions

Transport and detection of individual cations in single CNT channels have been reported by Strano's group [394–397]. It has been proven that in CNT-based RPS detection, the baseline current is solely contributed by the transport of protons [394]. When the applied electric field is higher than the threshold of the barrier energy, cations are partitioned into the CNT channel and give rise to the peaks. In this study, translocations of individual potassium ions were also detected by the CNT-based differential RPS chips developed under various electric fields. Figure 7-9 shows RPS signals of potassium ions detected by applying 1 V, 1.5 V and 3 V electric voltages. During the experiments, 2 M KCl solution was loaded in a fresh nanofluidic chip followed by data acquisition. As mentioned in

the references [394,396,397], a critical driving electric field and a conditioning time were essential to start the translocation of molecules through CNTs. For instance, no stable RPS peaks were observed in the initial 20 minutes when the applied voltage was lower than 0.5 V. However, RPS signals appeared in about 15 minutes when 1 V voltage was applied, as shown in Figure 7-9 (a). When the applied voltage became higher, for example, to 1.5V, stable and uniform RPS signals were obtained (see Figure 7-9 (b)). When the applied voltage was as high as 3V, there were still detectable RPS signals, however, the signals were not uniform in amplitude anymore, as shown in Figure 7-9 (c). This is because the translocations of the potassium ions are not continuous, and there are large scatters in the magnitude of the signals. In-depth discussions are given in the next paragraph.

Energy barrier in sample loading through CNT has been reported previously [394,395,412,427]. The threshold is established based on several possible mechanisms, such as translocation of charged objects from a high dielectric environment to a low dielectric space, electrostatic repulsion force between the charged objects and the charged CNT entrance, as well as partial shedding of hydration shells for charged objects to enter the super-hydrophobic interior of CNTs [397]. Here, the CNT entrance is negatively charged due to the existence of carboxylic acid groups. As a result, negatively charged ions such as chloride and hydroxyl ions can hardly get into the CNT channel due to the electrostatic repulsion. Thus, the energy barrier for translocation of anions is much higher than that of the cations such as the basic current carriers (protons [394]) and the potassium ions. Consequently, when the applied voltage is high enough to overcome the energy barrier for the potassium ions to get into the CNT channel and generate RPS signals, chloride ions may not. The rhythmical repeating of the RPS signals is due to the successive translocation of potassium ions. When an electric field is applied across the CNT channel, a constant proton flux is generated in the interior of the CNT, which leads to the base current as mentioned above, while potassium ions and protons are concentrated at the CNT entrance due to polarization. However, as a potassium ion enters the CNT channel driven by the externally applied electric field, the proton flux is obstructed, resulting in a higher electrical resistance of the CNT channel. Once the potassium ion leaves the CNT channel from the exiting side, the electrical resistance of the CNT channel recovers due to the high concentration of protons at the entrance of the CNT channel [396]. Repetition of these processes gives rise to oscillation of the RPS signals.

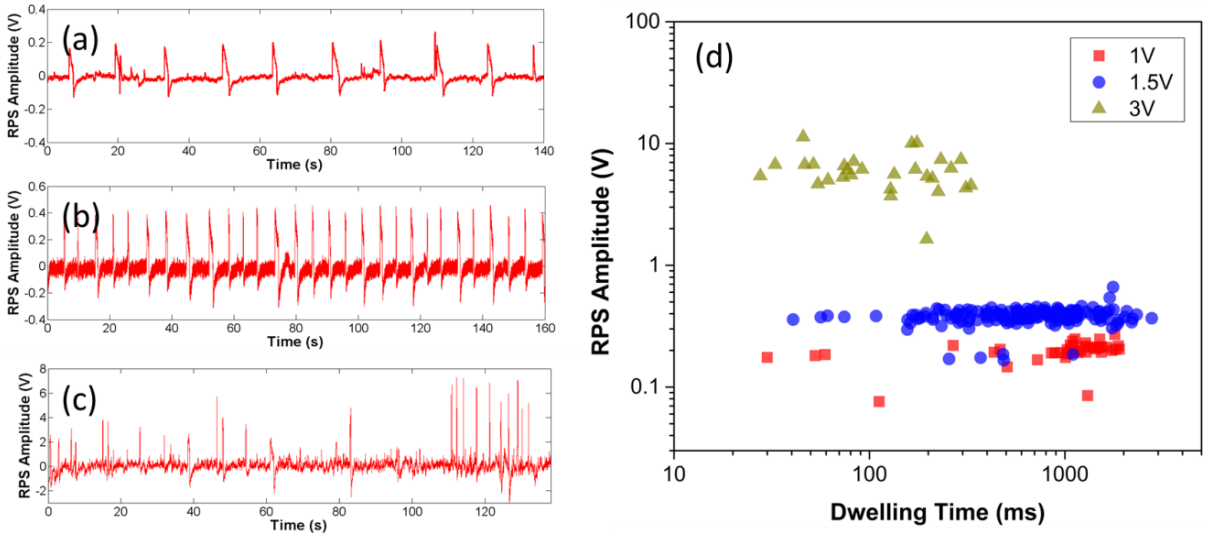

Figure 7-9 RPS signals of potassium ions detected by a CNT-based RPS device. Examples of RPS signals showing potassium ion translocation events by applying (a) 1 V, (b) 1.5 V and, (c) 3 V voltage. (d) Distribution of potassium ion signals detected by applying 1 V (N=65), 1.5 V (N=144) and 3 V (N=33) electric voltages.

Figure 7-9 (d) shows the distribution of the amplitudes and durations of the RPS events at 1V, 1.5V and 3 V respectively. It is obvious that, as the applied voltage increases, the duration time of the RPS events decreases while the amplitude increases. This observation coincides with the prediction of the mathematical model, as shown in Equation (7-9). The shorter duration time of the RPS events at higher applied voltage is due to the increase in electrophoretic mobility of the potassium ions. Since the potassium ions move faster under high voltage, the frequency of the RPS events also increases with the applied voltage. From the examples in Figure 7-9 (a) and Figure 7-9 (b), one can see that the number of the RPS signals generated in the time window (about 140s) increases as the applied voltage increases from 1 V to 1.5 V. However, as the applied voltage increases to 3 V, the oscillation of the RPS signals breaks down, as shown in Figure 7-9 (c). The breaking down of oscillation is assumed to be caused by simultaneous translocation of cations and anions. Simultaneous translocation of cations and anions would block the CNT channel and stop the successive cations loading. On the other hand, when the applied voltage is higher than the critical value to overcome the energy barriers for anions to enter the CNT channel, the translocation of chloride ions can also generate RPS signals. The opposite moving directions or alternative translocation of the positively charged ions and the negatively charged ions lead to less regular RPS signals. Figure 7-9 (c) is a possible case of the above-mentioned situation, in which the signals are

not successive and the amplitude of these signals is not uniform. However, the signal-to-noise ratio (SNR) is still very high. SNR is one of the most important indicators in evaluating the performance of a lab-on-a-chip sensing device, but it was not mentioned in the limited number of references [394–397]. The calculated SNR during the on-chip cation detection presented in the study is around 5 for almost all the cases, which is high enough for recognizing individual RPS events. In comparison with the traditional RPS design, both the differential detecting fluid channels and the low noise level of the PDMS material [369] contributed to the high SNR and reliable event identification.

7.3.3 Detection of 30-nt and 15-nt ssDNAs

It is difficult to identify short ssDNAs by CNT-based RPS, and to the best of our knowledge, the shortest ssDNA detected by CNT-based methods was about 60-nt [411]. Till now it is still a challenging problem to identify nucleotides of different lengths and different types. In this study, ssDNAs of 15-nt and 30-nt were detected by a CNT-based differential RPS device successfully with an applied voltage of 1 V. The results show that the differential RPS device can distinguish these two lengths of ssDNA chains clearly, as shown in Figure 7-10. Figure 7-10 (a) is a scatter plot of the RPS signals from these two lengths of ssDNAs. The difference between the 15-nt ssDNAs (black square) and the 30-nt ssDNAs (red cycle) is obvious. Figure 7-10 (b) and Figure 7-10 (c) are the histograms of the RPS amplitude and dwelling time of these two lengths of DNAs. It is clearly shown that translocation of 30-nt ssDNAs leads to a larger signal amplitude and a shorter duration time compared with that of 15-nt ssDNAs. For example, the average amplitude of an RPS event for 30-nt ssDNAs is about 0.26 V which is much larger than that for the 15-nt ssDNAs, approximately 0.08 V (see Figure 7-10 (b)). As shown in Figure 7-10 (c), the average duration time of an RPS event for 15-nt ssDNAs is much shorter than that for the 30-nt ssDNAs, indicating a faster-moving speed of the shorter ssDNAs. More specifically, the average speed of the 15-nt ssDNAs is about 200 $\mu m/s$ which is much higher than the 65 $\mu m/s$ of the 30-nt ssDNAs. The average speed of the ssDNA was calculated using the average dwelling time and the length of the CNT channel. Figure 7-10 (d) shows an example of RPS signal acquired when no ssDNA sample was added, in which no detectable RPS events were obtained. Figure 7-10 (e) and Figure 7-10 (f) show two examples of RPS signals detected after 15-nt and 30-nt ssDNA samples were loaded, indicating that the RPS events are indeed generated by the ssDNAs.

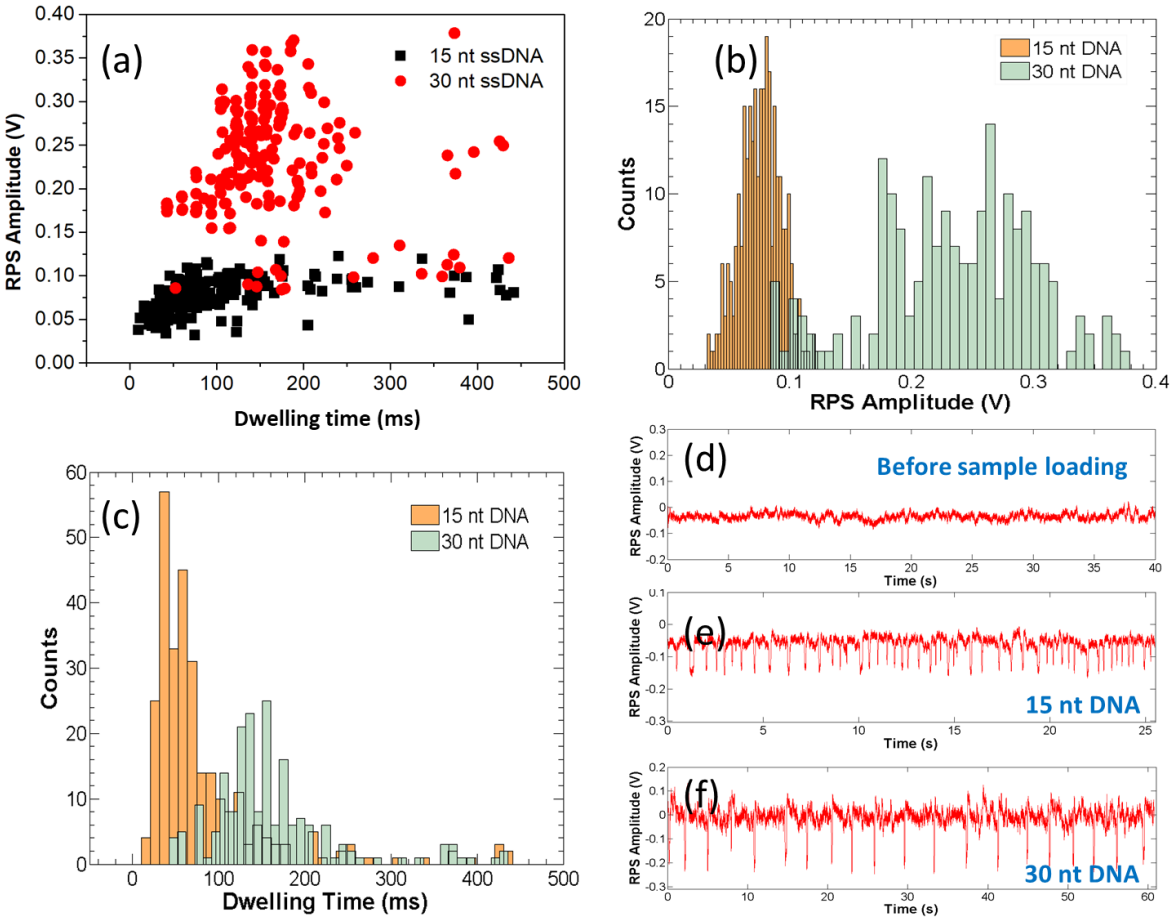

Figure 7-10 RPS signals of 15-nt ssDNAs and 30-nt ssDNAs detected by a CNT-based RPS device. The applied voltage was 1 V. (a) Scatter plot of RPS signals of 15-nt (N=447) and 30-nt (N=276) ssDNAs. (b) Histogram of the amplitude of the RPS signals of 15-nt and 30-nt ssDNAs. (c) Histogram of the duration time of the 15-nt and 30-nt ssDNAs. Example of RPS signals detected while (d) no ssDNAs were loaded, (b) 15-nt ssDNAs was loaded and (c) 30-nt ssDNAs were loaded.

The differences in the amplitude and duration time of RPS events generated by these two ssDNAs are essentially due to the difference between their electrostatic charges. It has been reported that translocation of DNAs with a large number of nucleotides through a CNT may decrease the electrical resistance of the CNT channel [411–413] and give rise to conductive pulses. As mentioned in the modeling section, the conductive pulse is caused by the counterions shielding the strongly charged ssDNAs by providing more current carriers [113,411,425,426]. Each 30-nt ssDNA has double the units of charge compared to a 15-nt ssDNA molecule. Consequently, 30-nt ssDNAs would supply double the quantity of current carriers in comparison with that of 15-nt ssDNAs and are more likely to generate larger conductive changes (ΔR) in the CNT channels. Also shown in Equation (7-9) that

the output voltage (i.e. RPS signal) is proportional to α which increases with ΔR. Both the electrostatic charge and the length of a ssDNA affect its electrokinetic motion in a CNT. For example, a longer ssDNA with more electrostatic charges would be subjected to a larger electrostatic force in comparison with that of a shorter one under the same external electric field, and the longer ssDNA should moves faster than the short one according to the machansm of the gel electrophoresis [428]. However, from Figure 7-10 (c) one can see that the average duration time of 15-nt ssDNAs is shorter than that of 30-nt ssDNAs. The possible reasons are as following. Firstly, longer ssDNAs are more likely to interact with the charges at the CNT entrance and exit, which may slow down the sample loading and exiting processes of longer ssDNAs. Translocation of molcues inside a CNT has been reported to be near-perfect slip due to the atomic smoothness of the graphiteic surface of the CNT channel [417,418], as a result, the average duration time of the RPS events is dominated by the entering and exiting processes. In addition, electroosmotic flow in the opposite direction may slow down the longer ssDNAs by hydrolic drag froce. Similar results has been report by He et al. [413] On the other hand, the extended entering and exiting time of longer ssDNAs also decreases the frequecny of the RPS events during longer ssDNA detection due to the partioning effect [422]; for instance, the density of RPS events of 15-nt ssDNAs is much higher than that 30-nt ssDNAs, as shown in Figure 7-10 (e) and Figure 7-10 (f). It should be pointed out that the resolution of the RPS detection system to distinguish ssDNAs of different lengths also depends on other working parameters, such as physical and chemical properties of the CNTs.

The energy barrier always plays an important role in ssDNA sample loading during CNT-based RPS detection. When the applied voltage is lower than a critical value (depends on the length of DNA and the properties of the CNT chip), ssDNA can hardly get into the CNT channel. The energy barrier [394,395,412,427] for translocation of ssDNAs in CNTs is not only due to electrostatic charge at the entrance of CNT [412], and the entropy barrier [411,414], but also the folding and tangling of the ssDNA chains [429]. Regarding the applied voltage, when the externally applied electric field is weak, the negatively charged carboxylic acid groups at the entrance of the CNT channel will repel the negatively charged ssDNAs, stopping the ssDNAs from entering the CNT channel. The magnitude of the electrostatic repulsion force is dependent on the number of carboxylic acid groups at the CNT entrance as well as the number of nucleotides in the ssDNA chains. However, for ssDNAs with a fixed number of nucleotides, when the externally applied electric field is high enough, the electrostatic driving force will overcome the electrostatic repulsion force and other energy barriers and load the ssDNAs into the CNT channel. On the other hand, the high applied electric field will

also help the positively charged potassium ions overcome the energy barriers; consequently, translocation of potassium ions and ssDNA may happen simultaneously in a CNT channel. However, due to the steric hindrance effects in the CNT channel and the oppositely moving direction of the ssDNAs and the potassium ions, translocation of ssDNAs and potassium ions in a single CNT may happen alternatively. For instance, when a 1 V voltage was applied to a CNT-based RPS chip to detect 30-nt ssDNAs which were diluted in 2 M KCl solution, at the beginning, stable and uniform conductive events were obtained; however, after about 20 min, the RPS signal became abnormal, as shown in Figure 7-11. The abnormality of the signals may be caused by the alternative translocation of the potassium ions and the ssDNAs.

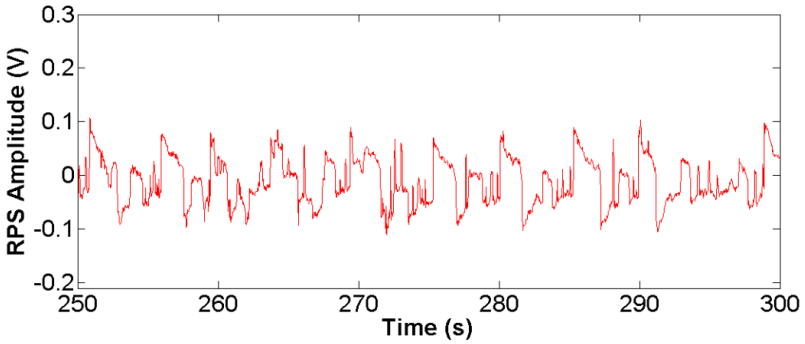

Figure 7-11 Abnormal RPS signals possibly due to alternative translocation of potassium ions and 30-nt ssDNAs.

The CNT-based differential RPS device developed in this study is essential for the high-resolution detection. As mentioned above, the differential detection channels can minimize the noises efficiently in comparison with that of the traditional design. Differentiation of ssDNAs with 30-nt and 15-nt can be achieved because of the combination of using the MWNT as the RPS sensing gate and employing the differential RPS strategy.

7.4 Conclusion

This chapter reports a novel CNT-based differential RPS nanofluidic chip for sensing single molecules, cations, and ssDNAs. A novel method for cutting CNTs with precise-controlled length is developed. This method does not need any chemical etching processes, which well keeps the originality of the CNT channels. The processes to fabricate RPS nanofluidic chip are simple and cost-effective. To identify signals of individual ions or molecules, a mathematical model is developed for the multi-CNT channel RPS detection system. Translocation and sensing of individual

molecules, potassium ions as wells as ssDNAs through CNT channels are demonstrated. The results suggest that translocation of ssDNAs with a large number of nucleotides through a CNT channel decreases the electrical resistance of the CNT channels while translocation of cations and rhodamine B molecules increases the electrical resistance of the CNT channels. It is demonstrated that 15-nt and 30-nt ssDNAs can be differentiated by the amplitude and the duration time of the RPS signals, which provides a potential avenue for DNA sequencing. The CNT-based RPS nanofluidic chip also offers a platform for fundamental research such as electrokinetic transport phenomena in CNTs, capture and manipulation of single molecules, detection of heavy metal ions in drinking water.

CHAPTER 8 Conclusions and Future Work

This chapter presents an overall summary of this thesis. Contributions of this thesis are also listed below. Based on these conclusions, future directions in nanofluidic device fabrication, electrokinetic transport phenomena at the nanoscale, as well as potential applications of the nanochannel-based nanofluidic systems are recommended.

8.1 Conclusions and contributions

This thesis starts with fabrication of nanochannel-based nanofluidic devices on PDMS material. Based on these nanochannel-based nanofluidic devices, two fundamental research projects are conducted to investigate electrokinetic transport phenomena in nanochannels and two applications are developed to detect nanoparticles and molecules. In the nanochannel fabrication part, a novel method to create nanocracks with controllable size and spacing on polystyrene surfaces is provided. Nanocracks as small as sub 100 nm wide and 20 nm deep can be obtained according to the optimal working guideline. Nanochannel mold duplication by nanoimprint technique is also investigated systematically. A comprehensive guideline for nanochannel-based PDMS nanofluidic device fabrication by such an easy approach is provided. The fundamental research projects investigate EOF transport in single nanochannels and EK motion of single nanoparticles in single nanochannels numerically and experimentally, providing a better understanding of electrokinetic transport phenomena in PDMS nanochannels, especially under the condition of overlapped EDLs. The effects of overlapped EDLs on these transport behaviors are elucidated. In the two application projects, differential RPS detection systems are developed on PDMS-nanochannel-based or CNT-channel-based nanofluidic chips for detection and characterization of individual particles, cations and DNA molecules. Working parameters involved in the differential RPS detection are studied systematically. Additionally, a detailed procedure for fabricating CNT-based nanofluidic devices is demonstrated. Overall, based on the studies presented in the previous chapters, major contributions of this research are briefly summarized as follows:

1) We developed a novel method to generate nanocracks on polystyrene surfaces with controllable locations and sizes. A guideline to create smaller nanocracks is provided.

2) Regarding nanochannel mold fabrication, Smooth cast and SU8 photoresist are applied to duplicate nanochannel molds from unstable nanocracks by nanoimprint technology. For both strategies, optimal working parameters are investigated.

3) We provide a cost-effective, reproducible, reliable and simple method to fabricate bi-layer PDMS nanochannel-based nanofluidic devices with comprehensive working procedures for the nanofluidic research community. We believe that the disposable PDMS nanofluidic device would benefit the nanofluidics field in the future.

4) We developed a hand-made alignment system based on an inverted optical microscope, and the resolution of the alignment system is high enough for general microfluidic applications.

5) We measured EOF velocity in single PDMS nanochannels. The channel size effect upon EOF velocity in nanochannels was studied by using 16 nanochannels comprehensively. The experimental results expand our understanding of the EDL theory and EOF in nanochannels.

6) We developed a reliable experimental system for single particle monitoring based on an optical microscope. Single nanoparticle transport in single nanochannels with overlapped EDLs was investigated.

7) We demonstrated the effects of ionic concentration and particle-to-channel size ratio (a/b) on the apparent velocity of nanoparticles inside single nanochannels by experiments systematically.

8) We developed a single-nanochannel-based differential RPS detection system based on PDMS nanofluidic chips and we provided comprehensive mathematical models for the single-gate differential RPS system.

9) The performance of the PDMS differential RPS chips, including resolution (23 nm), sensitivity (23 nm), capability of detecting aggregation of particles and predicting folding and knotting of DNA molecule chains is demonstrated.

10) We studied buffer solution (concentration, pH value and conductivity) effects on the amplitude and the signal-to-noise ratio (SNR) of RPS signals detected by single-channel-based differential RPS chips.

11) Sample loading trajectory effects on the channel-based RPS detection system and grouping of RPS events are demonstrated.

12) We developed a CNT-channel-based differential RPS detection system, and a comprehensive working procedure for fabricating CNT-channel-based differential RPS nanofluidic chips is provided.

13) We demonstrated novel strategies in CNT isolation and CNT cutting, providing the CNT research field with effective methods in handling CNTs

14) We solved a critical problem in PDMS-photoresist system bonding effectively by using an adhesive film.

15) We developed a mathematical model for multi-CNT channel RPS devices.

16) The CNT-channel-based differential RPS chips developed in this thesis are capable of detecting individual cations and molecules and distinguishing 15-nt ssDNA and 30-nt ssDNA with high resolution.

8.2 Recommendations and future research

Possible directions and extensions of the present work are as follows.

8.2.1 Fabrication of nanofluidic devices

The nanofluidic chips presented in this thesis are easy-to-make and cost-effective; however, improvements are still needed for practical applications, including:

a. The nanocracks were generated on polystyrene surfaces and the width of the cracks is generally larger than 100 nm. Polymers with different molecular structures such as PMMA or PC may be used to produce smaller nanocracks or complicated patterns by nature.

b. The nanocracks on the polystyrene surfaces are not stable during replication due to the solvent in the replicas. A proper material for nanochannel mold replication from these unstable nanocracks without size change is urgently needed.

c. PDMS is too soft for nanofluidic devices, especially when the structural size is smaller than 50 nm. The collapse of channel roofs would block the nanochannels and result in failures in nanofabrication. x-PDMS can solve this problem in most cases, however, preparing x-PDMS is complicated and time-consuming. As a result, a ready-to-use material with high Young's modulus is highly demanded.

d. The PDMS-PDMS nanofluidic chip presented in this thesis needs alignment during bonding. Integrating the nanochannels and the microchannels onto one channel mold would get rid of the alignment process and benefit the repeatability of the nanofluidic device fabrication. To be noted, a proof-of-concept experiment has been demonstrated in Appendix G.

e. The solvent-induced carking method can also generate special structures which can be used to integrate nanofluidic chips for special applications, such as mimicking blood capillaries in human bodies.

f. The working procedure developed for fabricating CNT-channel-based RPS nanofluidic devices can also be applied to other nanomaterials, such as ZnO_2 nanowires, nanoribbons. For example, the strategies developed for isolating and cutting CNT channels can also be applied in these nanomaterials.

8.2.2 Electrokinetically driven transport at the nanoscale

In this thesis we only studied the most common cases: EOF in nanochannels and EK motion of single nanoparticles in single nanochannels, and the working parameters we studied are very limited. More experiments are needed to explore these transport behaviors:

g. The classical EDL theory does not consider the ion size effects on the electric potential distribution, but in reality, the size of ions has to be taken into account. As a result, investigation of ion size effects on EDL and EOF in nanochannels by experiments is recommended.

h. Experimental studies of EOF in nanochannels with various surface charge properties and overlapped EDLs in two dimensions should be carried out to fully understand EOF at the nanoscale.

i. The current slope method does not work very well when the ionic concentration of electrolyte media is too low or the channel size is too small; as a result, a new method is needed to characterize EOF in nanochannels with extremely low ionic concentration media (or extremely strong overlapping of EDLs).

j. Electric potential distribution in overlapped EDLs is complicated and there are no exact analytical solutions or simple solutions to this classical problem. Efforts would be made to improve.

k. EOF and EK motion under the condition of low electric fields have been proved to be linear; however, under the condition of high electric fields, nonlinear transport phenomena may happen, for example, over-limiting electrical current, EOF of the second kind etc. These behaviors at the nanoscale have not been fully understood yet. A series of experiments would be conducted on nanofluidic chips to investigate these phenomena.

l. In this thesis, only one nanoparticle was loaded in one nanochannel each time, interactions between nanoparticles inside a 1-D confined nanospace are unknown. These interactions could be further explored.

8.2.3 Applications of differential RPS nanofluidic chips

m. The resolution and sensitivity of the differential RPS detection chips developed in this thesis are good enough for nanoparticle detection and sizing, however, the throughput of the single-gate design is too low. As a result, efforts should be made to improve the design of the nanofluidic chips in order to characterize nanoparticles with high efficiency.

n. PDMS differential RPS chips could also be applied to detect bio-objects, such as virus, proteins, and bacteria, which are essential to the diagnosis of diseases.

o. The CNT-channel-based differential RPS chips can distinguish 15-nt ssDNA and 30-nt ssDNA; however, it is still far away from the destination, single base level, which is the key to DNA sequencing. Consequently, the length of the CNT channels would be minimized to one base pair level (sub-nanometer).

p. The CNT-channel-based differential RPS chips are capable of detecting single cations; as a result, the chips can also be applied in heavy metal ion detection, which is important for drinking water monitoring. New applications would be carried out.

q. The CNT-channel-based devices provide excellent platforms for experimental studies of mass transport in CNTs. It is reported that the superhydrophobic property of the CNT inner surface would give rise to a lot of new transport phenomena, such as frictionless motion of water molecules and gas molecules.

REFERENCES

(1) Guan, W.; Li, S. X.; Reed, M. a. *Nanotechnology* **2014**, *25*, 122001.

(2) Duan, C.; Wang, W.; Xie, Q. *Biomicrofluidics* **2013**, *7*, 26501.

(3) Li, D. *Electrokinetics in microfluidics*; Academic Press, 2004; Vol. 2.

(4) Movahed, S.; Li, D. *Electrophoresis* **2011**, *32*, 1259–1267.

(5) Sparreboom, W.; Van Den Berg, a.; Eijkel, J. C. T. *New J. Phys.* **2010**, *12*.

(6) Masliyah, J. H.; Bhattacharjee, S. *Electrokinetic and colloid transport phenomena*; John Wiley & Sons, 2006.

(7) Chen, T.; Amin, I.; Jordan, R. *Chem. Soc. Rev.* **2012**, *41*, 3280–3296.

(8) Han, M.; Lee, W.; Lee, S.-K.; Lee, S. S. *Sensors Actuators A Phys.* **2004**, *111*, 14–20.

(9) O'Sullivan, G.; Kilbane, D.; D'Arcy, R. *J. Mod. Opt.* **2012**, *59*, 855–872.

(10) Ito, T.; Okazaki, S. *Nature* **2000**, *406*, 1027–1031.

(11) Lin, B. J. *J. Vac. Sci. Technol.* **1975**, *12*, 1317.

(12) Wang, L.; Huang, J.; Tang, K.; Xia, Y. In *Lithography*; 2010; pp 227–240.

(13) Heuberger, A. *J. Vac. Sci. Technol. B* **1985**, *3*, 535–556.

(14) Tandon, U.; Pant, B.; Kumar, A. *Vacuum* **1991**, *42*, 1219–1228.

(15) Hector, S. *Microelectron. Eng.* **1998**, *42*, 25–30.

(16) Selzer, R.; Heaton, J. *Microelectron. Eng.* **2000**, *53*, 591–594.

(17) Leontowich, A. F. G.; Hitchcock, A. P.; Watts, B.; Raabe, J. *Microelectron. Eng.* **2013**, *108*, 5–7.

(18) Leontowich, A. F. G.; Hitchcock, A. P. *Microfluid. Nanofluidics* **2013**, *15*, 509–518.

(19) Sunday, D. F.; Hammond, M. R.; Wang, C.; Wu, W.; Kline, R. J.; Stein, G. E. *J. Micro/Nanolithography, MEMS, MOEMS* **2013**, *12*, 31103.

(20) Innocenzi, P.; Kidchob, T.; Costacurta, S.; Falcaro, P.; Marmiroli, B.; Cacho-Nerin, F.; Amenitsch, H. *Soft Matter* **2010**, *6*, 3172.

(21) Costacurta, S.; Malfatti, L.; Patelli, A.; Falcaro, P.; Amenitsch, H.; Marmiroli, B.; Grenci, G.; Piccinini, M.; Innocenzi, P. *Plasma Process. Polym.* **2010**, *7*, 459–465.

(22) Romanato, F. *Microelectron. Eng.* **2004**, *73–74*, 870–875.

(23) Miao, H.; Gomella, A. a; Chedid, N.; Chen, L.; Wen, H. *Nano Lett.* **2014**, *14*, 3453–3458.

(24) Kim, S.; Marelli, B.; Brenckle, M. a; Mitropoulos, A. N.; Gil, E.-S.; Tsioris, K.; Tao, H.; Kaplan, D. L.; Omenetto, F. G. *Nat. Nanotechnol.* **2014**, *9*, 306–310.

(25) Tseng, A.; Chen, K.,Chen, C. D.,Ma, K. J.; *IEEE Trans.* **2003**, *26*, 141–149.

(26) Chen, W.; Ahmed, H. *Appl. Phys. Lett.* **1993**, *62*, 1499.

(27) Fujita, J.; Ohnishi, Y.; Ochiai, Y.; Matsui, S. *Appl. Phys. Lett.* **1996**, *68*, 1297.

(28) Harnett, C. K.; Coates, G. W.; Craighead, H. G. *J. Vac. Sci. Technol. B Microelectron. Nanom. Struct.* **2001**, *19*, 2842.

(29) Devlin, N. R.; Brown, D. K.; Kohl, P. a. *J. Vac. Sci. Technol. B Microelectron. Nanom. Struct.* **2009**, *27*, 2508.

(30) Ma, S.; Con, C.; Yavuz, M.; Cui, B. *Nanoscale Res. Lett.* **2011**, *6*, 446.

(31) Danelon, C.; Santschi, C.; Brugger, J.; Vogel, H. *Langmuir* **2006**, *22*, 10711–10715.

(32) Perry, J. M.; Harms, Z. D.; Jacobson, S. C. *Small* **2012**, *8*, 1521–1526.

(33) Manfrinato, V. R.; Zhang, L.; Su, D.; Duan, H.; Hobbs, R. G.; Stach, E. a; Berggren, K. K. *Nano Lett.* **2013**, *13*, 1555–1558.

(34) Vieu, C.; Carcenac, F.; Pepin, A.; Chen, Y. *Appl. Surf. Sci.* **2000**, *164*, 111–117.

(35) Chang, T. H. P. *J. Vac. Sci. Technol.* **1975**, *12*, 1271.

(36) Pease, R. F. W. *Contemp. Phys.* **1981**, *22*, 265–290.

(37) Liu, C. Y.; Datta, a.; Wang, Y. L. *Appl. Phys. Lett.* **2001**, *78*, 120.

(38) Tseng, A. a.; Insua, I. a.; Park, J. S.; Li, B.; Vakanas, G. P. *J. Vac. Sci. Technol. B Microelectron. Nanom. Struct.* **2004**, *22*, 82.

(39) Li, H.; Kang, D.; Blamire, M.; Huck, W. *Nanotechnology* **2003**, *220*.

(40) Tong, H. D.; Jansen, H. V; Gadgil, V. J.; Bostan, C. G.; Berenschot, E.; Rijn, C. J. M. Van; Elwenspoek, M. *Nano Lett.* **2004**, *4*, 283–287.

(41) Cannon, D. M.; Flachsbart, B. R.; Shannon, M. a.; Sweedler, J. V.; Bohn, P. W. *Appl. Phys. Lett.* **2004**, *85*, 1241.

(42) Tseng, A. a. *Small* **2005**, *1*, 924–939.

(43) Sridhar, M.; Maurya, D. K.; Friend, J. R.; Yeo, L. Y. *Biomicrofluidics* **2012**, *6*, 12819–1281911.

(44) Tseng, A. a; Insua, I. a; Park, J.-S.; Chen, C. D. *J. Micromechanics Microengineering* **2005**, *15*, 20–28.

(45) Tseng, A. a. *J. Micromechanics Microengineering* **2004**, *14*, R15–R34.

(46) Menard, L. D.; Ramsey, J. M. *Nano Lett.* **2011**, *11*, 512–517.

(47) Geng, Y. Q.; Yan, Y. D.; Zhao, X. S.; Hu, Z. J.; Liang, Y. C.; Sun, T.; Dong, S. *Appl. Surf. Sci.* **2013**, *266*, 386–394.

(48) Kato, Z.; Sakairi, M.; Takahashi, H. *Surf. Coatings Technol.* **2003**, *170*, 195–198.

(49) Choi, C.-Y.; Moon, K.-S.; Koo, S.-M. *J. Nanosci. Nanotechnol.* **2011**, *11*, 1310–1313.

(50) Chen, J.-M.; Liao, S.-W.; Tsai, Y.-C. *Synth. Met.* **2005**, *155*, 11–17.

(51) Li, Y.; Maynor, B. W.; Liu, J. *J. Am. Chem. Soc.* **2001**, *123*, 2105–2106.

(52) Noy, A.; Miller, A. E.; Klare, J. E.; Weeks, B. L.; Woods, B. W.; DeYoreo, J. J. *Nano Lett.* **2002**, *2*, 109–112.

(53) Salaita, K.; Wang, Y.; Mirkin, C. A. *Nat. Nanotechnol.* **2007**, *2*, 145–155.

(54) Ginger, D. S.; Zhang, H.; Mirkin, C. A. *Angew. Chem. Int. Ed. Engl.* **2004**, *43*, 30–45.

(55) Gates, B. D.; Xu, Q.; Stewart, M.; Ryan, D.; Willson, C. G.; Whitesides, G. M. *Chem. Rev.* **2005**, *105*, 1171–1196.

(56) Xia, D.; Ku, Z.; Lee, S. C.; Brueck, S. R. J. *Adv. Mater.* **2011**, *23*, 147–179.

(57) Elman, N. M.; Daniel, K.; Jalali-Yazdi, F.; Cima, M. J. *Microfluid. Nanofluidics* **2009**, *8*, 557–563.

(58) Oh, Y.-J.; Bottenus, D.; Ivory, C. F.; Han, S. M. *Lab Chip* **2009**, *9*, 1609–1617.

(59) Oh, Y.-J.; Gamble, T. C.; Leonhardt, D.; Chung, C.-H.; Brueck, S. R. J.; Ivory, C. F.; Lopez, G. P.; Petsev, D. N.; Han, S. M. *Lab Chip* **2008**, *8*, 251–258.

(60) O'Brien, M. J.; Bisong, P.; Ista, L. K.; Rabinovich, E. M.; Garcia, a. L.; Sibbett, S. S.; Lopez, G. P.; Brueck, S. R. J. *J. Vac. Sci. Technol. B Microelectron. Nanom. Struct.* **2003**, *21*, 2941.

(61) Hoffnagle, J. A.; Hinsberg, W. D.; Houle, F. A.; Sanchez, M. I. *J. Photopolym. Sci. Technol.* **2003**, *16*, 373–

379.

(62) Chou, S. Y. *J. Vac. Sci. Technol. B Microelectron. Nanom. Struct.* **1997**, *15*, 2897.

(63) Chou, S. Y.; Krauss, P. R.; Renstrom, P. J. *Appl. Phys. Lett.* **1995**, *67*, 3114.

(64) Abgrall, P.; Low, L.-N.; Nguyen, N.-T. *Lab Chip* **2007**, *7*, 520–522.

(65) Mijatovic, D.; Eijkel, J. C. T.; van den Berg, A. *Lab Chip* **2005**, *5*, 492–500.

(66) Poulsen, R. G. *J. Vac. Sci. Technol.* **1977**, *14*, 266.

(67) Mijovic, J. S.; Koutsky, J. a. *Polym. Plast. Technol. Eng.* **1977**, *9*, 139–179.

(68) Oehrlein, G. *Mater. Sci. Eng. B* **1989**, *34*, 429–436.

(69) Gottlieb, S. *Mater. Sci. Eng. B* **1989**, *B4*, 441–450.

(70) Zhuang, D.; Edgar, J. H. *Mater. Sci. Eng. R Reports* **2005**, *48*, 1–46.

(71) Huang, Z.; Geyer, N.; Werner, P.; de Boor, J.; Gösele, U. *Adv. Mater.* **2011**, *23*, 285–308.

(72) Prakash, A. A. *IJCA Proc. …* **2013**, 26–31.

(73) Wu, B.; Kumar, A.; Pamarthy, S. *J. Appl. Phys.* **2010**, *108*, 51101.

(74) Martinu, L.; Poitras, D. *J. Vac. Sci. Technol. A Vacuum, Surfaces, Film.* **2000**, *18*, 2619.

(75) Helmersson, U.; Lattemann, M.; Bohlmark, J.; Ehiasarian, A. P.; Gudmundsson, J. T. *Thin Solid Films* **2006**, *513*, 1–24.

(76) Galloway, J.; Thornton, J. *Prog. Mater. science* **2007**, *52*, 1–61.

(77) Corni, I.; Ryan, M. P.; Boccaccini, A. R. *J. Eur. Ceram. Soc.* **2008**, *28*, 1353–1367.

(78) Kumar, M.; Ando, Y. *J. Nanosci. Nanotechnol.* **2010**, *10*, 3739–3758.

(79) Haneveld, J.; Jansen, H. *J. …* **2003**, *13*, S62–S66.

(80) Yeom, J.; Wu, Y.; Selby, J. C.; Shannon, M. a. *J. Vac. Sci. Technol. B Microelectron. Nanom. Struct.* **2005**, *23*, 2319.

(81) Hug, T. S.; de Rooij, N. F.; Staufer, U. *Microfluid. Nanofluidics* **2006**, *2*, 117–124.

(82) Peng, C.; Pang, S. W. *J. Vac. Sci. Technol. B Microelectron. Nanom. Struct.* **2006**, *24*, 1941.

(83) Sparreboom, W.; Eijkel, J.; Bomer, J.; Berg, A. Van Den. *Lab Chip* **2008**, No. 8, 402–407.

(84) Hsu, C.-M.; Connor, S. T.; Tang, M. X.; Cui, Y. *Appl. Phys. Lett.* **2008**, *93*, 133109.

(85) Hoang, H. T.; Segers-Nolten, I. M.; Tas, N. R.; van Honschoten, J. W.; Subramaniam, V.; Elwenspoek, M. C. *Nanotechnology* **2011**, *22*, 275201.

(86) Lee, S. J.; Kim, D. *Microfluid. Nanofluidics* **2011**, *12*, 897–906.

(87) Li, X.; Li, X.; Di, S.; Jin, J.; Wang, X. *Micro Nano Lett.* **2012**, *7*, 1320–1323.

(88) Love, J.; Paul, K.; Whitesides, G. *Adv. Mater.* **2001**, *13*, 604–607.

(89) Chen, L.; Chan-Park, M.; Yang, C.; Zhang, Q. *Nanotechnology* **2008**, *19*, 155301.

(90) Sordan, R.; Miranda, A.; Traversi, F.; Colombo, D.; Chrastina, D.; Isella, G.; Masserini, M.; Miglio, L.; Kern, K.; Balasubramanian, K. *Lab Chip* **2009**, *9*, 1556–1560.

(91) Xie, Q.; Zhou, Q.; Xie, F.; Sang, J.; Wang, W. *Biomicrofluidics* **2012**, *6*, 16502.

(92) Cheng, E.; Zou, H.; Yin, Z.; Jurčíček, P.; Zhang, X. *J. Micromechanics Microengineering* **2013**, *23*, 75022.

(93) Chu, K. S.; Kim, S.; Chung, H.; Oh, J.-H.; Seong, T.-Y.; An, B. H.; Kim, Y. K.; Park, J. H.; Do, Y. R.; Kim, W. *Nanotechnology* **2010**, *21*, 425302.

(94) Gong, W.; Xue, J.; Zhuang, Q.; Wu, X.; Xu, S. *Nanotechnology* **2010**, *21*, 195302.

(95) Zhang, L.; Gu, F.; Tong, L.; Yin, X. *Microfluid. Nanofluidics* **2008**, *5*, 727–732.

(96) Fan, R.; Wu, Y.; Li, D.; Yue, M.; Majumdar, A.; Yang, P. *J. Am. Chem. Soc.* **2003**, *125*, 5254–5255.

(97) Pang, P.; He, J.; Park, J. H.; Krstić, P. S.; Lindsay, S. *ACS Nano* **2011**, *5*, 7277–7283.

(98) Oh, J.; Kim, G.; Mattia, D.; Noh, H. (Moses). *Sensors Actuators B Chem.* **2011**, *154*, 67–72.

(99) Qin, X.; Yuan, Q.; Zhao, Y.; Xie, S.; Liu, Z. *Nano Lett.* **2011**, *11*, 2173–2177.

(100) Liu, H.; He, J.; Tang, J.; Pang, P.; Cao, D.; Krstic, P.; Joseph, S.; Lindsay, S.; Nuckolls, C. *Science* **2010**, *327*, 64–67.

(101) Scruggs, N.; Robertson, J. *Nano …* **2009**, *9*, 3853–3859.

(102) Holt, J. K.; Park, H. G.; Wang, Y.; Stadermann, M.; Artyukhin, A. B.; Grigoropoulos, C. P.; Noy, A.; Bakajin, O. *Science* **2006**, *312*, 1034–1037.

(103) Yu, S.; Lee, S. B.; Kang, M.; Martin, C. R.; Uni, V.; Gaines, V. *Nano Lett.* **2001**, *1*, 495–498.

(104) Kasianowicz, J. J.; Brandin, E.; Branton, D.; Deamer, D. W. *Proc. Natl. Acad. Sci. U. S. A.* **1996**, *93*, 13770–13773.

(105) Czaplewski, D. a.; Kameoka, J.; Mathers, R.; Coates, G. W.; Craighead, H. G. *Appl. Phys. Lett.* **2003**, *83*, 4836.

(106) Park, S. H.; Shin, H.-J.; Kim, Y.-H.; Yang, D.-Y.; Lee, J.-C.; Lee, S. *J. Micromechanics Microengineering* **2012**, *22*, 95019.

(107) Xu, S.; Zhao, Y. *Microfluid. Nanofluidics* **2011**, *11*, 359–365.

(108) Bellan, L. M.; Strychalski, E. a.; Craighead, H. G. *J. Vac. Sci. Technol. B Microelectron. Nanom. Struct.* **2008**, *26*, 1728.

(109) Butler, T. Z.; Pavlenok, M.; Derrington, I. M.; Niederweis, M.; Gundlach, J. H. *Proc. Natl. Acad. Sci. U. S. A.* **2008**, *105*, 20647–20652.

(110) Huang, Y.; Bu, N.; Duan, Y.; Pan, Y.; Liu, H.; Yin, Z.; Xiong, Y. *Nanoscale* **2013**, *5*, 12007–12017.

(111) Shin, M. K.; Kim, S.-K.; Lee, H.; Kim, S. I.; Kim, S. J. *Nanotechnology* **2008**, *19*, 195304.

(112) Noy, A.; Park, H.; Fornasiero, F. *Nano Today* **2007**, *2*, 22–29.

(113) Fan, R.; Karnik, R.; Yue, M.; Li, D.; Majumdar, A.; Yang, P. *Nano Lett.* **2005**, *5*, 1633–1637.

(114) Wu, C.; Jin, Z.; Wang, H.; Ma, H.; Wang, Y. *J. Micromechanics Microengineering* **2007**, *17*, 2393–2397.

(115) Xu, B.-Y.; Xu, J.-J.; Xia, X.-H.; Chen, H.-Y. *Lab Chip* **2010**, *10*, 2894–2901.

(116) Grimes, A.; Breslauer, D. N.; Long, M.; Pegan, J.; Lee, L. P.; Khine, M. *Lab Chip* **2008**, *8*, 170–172.

(117) Sivanesan, P.; Okamoto, K.; English, D. *Anal. Chem.* **2005**, *77*, 2252–2258.

(118) Choi, S.; Yan, M.; Adesida, I. *Appl. Phys. Lett.* **2008**, *93*, 163113.

(119) Huang, Y. Y.; Zhou, W.; Hsia, K. J.; Menard, E.; Park, J.-U.; Rogers, J. a; Alleyne, A. G. *Langmuir* **2005**, *21*, 8058–8068.

(120) Huh, D.; Mills, K. L.; Zhu, X.; Burns, M. A.; Thouless, M. D.; Takayama, S. *Nat. Mater.* **2007**, *6*, 424–428.

(121) Hui, C. Y.; Jagota, a.; Lin, Y. Y.; Kramer, E. J. *Langmuir* **2002**, *18*, 1394–1407.

(122) Lee, J.; Yoon, Y.; Kim, J.; Kim, Y.; Jo, K. *Bull. Korean Chem. Soc.* **2011**, *32*, 33–34.

(123) Park, S.; Huh, Y. *PNAS* **2009**, *106*, 15549–15554.

(124) Shih, W.; Hui, C.; Tien, N. *J. Appl. Phys.* **2004**, *95*, 2800–2808.

(125) Zhou, W.; Huang, Y.; Menard, E.; Aluru, N. R.; Rogers, J. a.; Alleyne, a. G. *Appl. Phys. Lett.* **2005**, *87*, 251925.

(126) Li, J.; Liu, C.; Ke, X.; Xu, Z.; Duan, Y.; Fan, Y.; Li, M. *Lab Chip* **2012**, No. 12, 4059–4062.

(127) Thamdrup, L. H.; Klukowska, A.; Kristensen, A. *Nanotechnology* **2008**, *19*, 125301.

(128) Kim, B.; Heo, J.; Kwon, H. J.; Cho, S. J.; Han, J.; Kim, S. J.; Lim, G. *ACS Nano* **2013**, *7*, 740–747.

(129) Mariazzi, S.; Bettotti, P.; Larcheri, S.; Toniutti, L.; Brusa, R. S. *Phys. Rev. B* **2010**, *81*, 235418.

(130) Mills, K. L.; Huh, D.; Takayama, S.; Thouless, M. D. *Lab Chip* **2010**, *10*, 1627–1630.

(131) Angeli, E.; Manneschi, C.; Repetto, L.; Firpo, G. In *9th IEEE conference on Nanotechnology*; 2009; Vol. 7, pp 626–629.

(132) Quist, J.; Trietsch, S. J.; Vulto, P.; Hankemeier, T. *Lab Chip* **2013**, *13*, 4810–4815.

(133) Douville, N.; Huh, D.; Mills, K. *US Pat. App. 12/ …* **2008**, *0*.

(134) Cheng, Y.; Liao, Y.; Sugioka, K. *Proc. SPIE* **2014**, *8967*, 896708.

(135) Liao, Y.; Cheng, Y.; Liu, C.; Song, J.; He, F.; Shen, Y.; Chen, D.; Xu, Z.; Fan, Z.; Wei, X.; Sugioka, K.; Midorikawa, K. *Lab Chip* **2013**, *13*, 1626–1631.

(136) Mei, Y.; Thurmer, D. J.; Cavallo, F.; Kiravittaya, S.; Schmidt, O. G. *Adv. Mater.* **2007**, *19*, 2124–2128.

(137) Chung, S.; Lee, J. H.; Moon, M.-W.; Han, J.; Kamm, R. D. *Adv. Mater.* **2008**, *20*, 3011–3016.

(138) Chung, J. Y.; Nolte, A. J.; Stafford, C. M. *Adv. Mater.* **2009**, *21*, 1358–1362.

(139) Mei, Y.; Kiravittaya, S.; Harazim, S.; Schmidt, O. G. *Mater. Sci. Eng. R Reports* **2010**, *70*, 209–224.

(140) Chung, J. Y.; Nolte, A. J.; Stafford, C. M. *Adv. Mater.* **2011**, *23*, 349–368.

(141) Alaca, B. E.; Sehitoglu, H.; Saif, T. *Appl. Phys. Lett.* **2004**, *84*, 4669.

(142) Raimundo, D. S.; Stelet, A. B.; Fernandez, F. J. R.; Salcedo, W. J. *Microelectronics J.* **2005**, *36*, 207–211.

(143) Chen, Y.-W.; Tang, Y.-H.; Pei, L.-Z.; Guo, C. *Adv. Mater.* **2005**, *17*, 564–567.

(144) Fan, H. J.; Werner, P.; Zacharias, M. *Small* **2006**, *2*, 700–717.

(145) Meng, Y.; Gu, D.; Zhang, F.; Shi, Y.; Cheng, L.; Feng, D.; Wu, Z.; Chen, Z.; Wan, Y.; Stein, A.; Zhao, D.; April, R. V; Re, V.; Recei, M.; July, V. *Chem. …* **2006**, No. 4, 4447–4464.

(146) Zeng, Y.; Harrison, D. J. *Anal. Chem.* **2007**, *79*, 2289–2295.

(147) Darling, S. B. *Prog. Polym. Sci.* **2007**, *32*, 1152–1204.

(148) Fang, J. *J. Mater. Chem.* **2007**, *17*, 3479.

(149) Xia, D.; Zhang, J.; He, X.; Brueck, S. R. J. *Appl. Phys. Lett.* **2008**, *93*, 71105.

(150) Li, D.; Jiang, C.; Jiang, J.; Lu, J. *Chem. Mater.* **2008**, No. 12, 253–258.

(151) Han, W.; Byun, M.; Zhao, L.; Rzayev, J.; Lin, Z. *J. Mater. Chem.* **2011**, *21*, 14248.

(152) Choi, E.; Kwon, K.; Lee, S. *Micro Electro Mech. …* **2012**, No. February, 1313–1315.

(153) Soberats, B.; Yoshio, M.; Ichikawa, T.; Taguchi, S.; Ohno, H.; Kato, T. *J. Am. Chem. Soc.* **2013**, *135*, 15286–15289.

(154) Yamaguchi, A.; Uejo, F.; Yoda, T.; Uchida, T.; Tanamura, Y.; Yamashita, T.; Teramae, N. *Nat. Mater.* **2004**, *3*, 337–341.

(155) Kim, J.; Anderson, W. a. *Nano Lett.* **2006**, *6*, 1356–1359.

(156) Cheng, J. Y.; Zhang, F.; Chuang, V. P.; Mayes, A. M.; Ross, C. a. *Nano Lett.* **2006**, *6*, 2099–2103.

(157) Shan, Y.; Fonash, S. *ACS Nano* **2008**, *2*, 429–434.

(158) Xia, Y.; Rogers, J. a.; Paul, K. E.; Whitesides, G. M. *Chem. Rev.* **1999**, *99*, 1823–1848.

(159) Kim, C.-B.; Chun, H.; Chung, J.; Song, K.-B.; Lee, S.-H. *2011 11th IEEE Int. Conf. Nanotechnol.* **2011**,

1723–1727.

(160) Bowden, N.; Huck, W. T. S.; Paul, K. E.; Whitesides, G. M. *Appl. Phys. Lett.* **1999**, *75*, 2557.

(161) Zhu, X.; Mills, K. L.; Peters, P. R.; Bahng, J. H.; Liu, E. H.; Shim, J.; Naruse, K.; Csete, M. E.; Thouless, M. D.; Takayama, S. *Nat. Mater.* **2005**, *4*, 403–406.

(162) Xu, Y.; Wang, C.; Dong, Y.; Li, L.; Jang, K.; Mawatari, K.; Suga, T.; Kitamori, T. *Anal. Bioanal. Chem.* **2012**, *402*, 1011–1018.

(163) Kim, S. H.; Cui, Y.; Lee, M. J.; Nam, S.-W.; Oh, D.; Kang, S. H.; Kim, Y. S.; Park, S. *Lab Chip* **2011**, *11*, 348–353.

(164) Gu, J.; Gupta, R.; Chou, C.-F.; Wei, Q.; Zenhausern, F. *Lab Chip* **2007**, *7*, 1198–1201.

(165) Hu, X.; He, Q.; Zhang, X.; Chen, H. *Microfluid. Nanofluidics* **2010**, *10*, 1223–1232.

(166) Mao, P.; Han, J. *Lab Chip* **2005**, *5*, 837–844.

(167) Garcia, A. L.; Ista, L. K.; Petsev, D. N.; O'Brien, M. J.; Bisong, P.; Mammoli, A. a; Brueck, S. R. J.; López, G. P. *Lab Chip* **2005**, *5*, 1271–1276.

(168) Schoch, R. B.; Han, J.; Renaud, P. *Rev. Mod. Phys.* **2008**, *80*, 839–883.

(169) Hibara, A.; Saito, T.; Kim, H. B.; Tokeshi, M.; Ooi, T.; Nakao, M.; Kitamori, T. *Anal. Chem.* **2002**, *74*, 6170–6176.

(170) Graczyk, M.; Balaz, M.; Kvennefors, A.; Linke, H.; Maximov, I. *J. Vac. Sci. Technol. B Microelectron. Nanom. Struct.* **2012**, *30*, 06FF09.

(171) Nam, S.-W.; Lee, M.-H.; Lee, S.-H.; Lee, D.-J.; Rossnagel, S. M.; Kim, K.-B. *Nano Lett.* **2010**, *10*, 3324–3329.

(172) Kim, S. J.; Han, J. *Anal. Chem.* **2008**, *80*, 3507–3511.

(173) Xia, Q.; Morton, K. J.; Austin, R. H.; Chou, S. Y. *Nano Lett.* **2008**, *8*, 3830–3833.

(174) Wong, C.; Agarwal, A. *Nanotechnology* **2007**, *18*, 135304 (6PP).

(175) van Helvoort, a. T. J.; Knowles, K. M.; Holmestad, R.; Fernie, J. a. *Philos. Mag.* **2004**, *84*, 505–519.

(176) Knowles, K. M.; van Helvoort, a. T. J. *Int. Mater. Rev.* **2006**, *51*, 273–311.

(177) Rayleigh, Lord. *Philos. Mag. Ser. 5* **1892**, *34*, 481–502.

(178) DeBlois, R. W.; Bean, C. P. *Rev. Sci. Instrum.* **1970**, *41*, 909.

(179) Saleh, O. A. A novel resistive pulse sensor for biological measurements, 2003, Vol. Ph.D.

(180) DeBlois, R. W.; Bean, C. P.; Wesley, R. K. A. *J. Colloid Interface Sci.* **1977**, *61*, 323–335.

(181) Smythe, W. R. *Phys. Fluids* **1961**, *4*, 756.

(182) Suh, Y. D.; Yeo, J.; Lee, H.; Hong, S.; Kwon, J.; Kim, K.; Ko, S. H. *Sci. Rep.* **2015**, *5*, 1–10.

(183) Nam, K. H.; Suh, Y. D.; Yeo, J.; Woo, D. *Sci. Rep.* **2016**, *6*, 2–9.

(184) Yin, Z.; Lu, B.; Zou, H. *Microsyst. Technol.* **2017**, *23*, 1–7.

(185) Kim, M.; Ha, D.; Kim, T. *2015 Transducers - 2015 18th Int. Conf. Solid-State Sensors, Actuators Microsystems, TRANSDUCERS 2015* **2015**, 1366–1369.

(186) Kim, M.; Kim, D.-J.; Ha, D.; Kim, T. *Nanoscale* **2016**, *8*, 9461–9479.

(187) Xu, Y. *Adv. Mater.* **2017**, *1702419*, 1702419.

(188) Kim, M.; Kim, T. *Anal. Chem.* **2015**, *87*, 11215–11223.

(189) Kim, M.; Ha, D.; Kim, T. *Nat. Commun.* **2015**, *6*, 1–8.

(190) Peng, R.; Li, D. *Biomicrofluidics* **2015**, *9*, 24117.

(191) Verschuuren, M. Substrate Conformal Imprint Lithography for Nanophotonics, Utrecht University, 2010.

(192) Schmid, H.; Michel, B. *Macromolecules* **2000**, *33*, 3042–3049.

(193) Brown, H. *Polymer (Guildf).* **1978**, *19*, 1186–1188.

(194) Jacques, C. H. M.; Wyzgoski, M. G. *J. Appl. Polym. Sci.* **1979**, *23*, 1153–1166.

(195) Hansen, C. M. *Polym. Degrad. Stab.* **2002**, *77*, 43–53.

(196) Earl, B.; Loneragan, R.; Crook, M. *J. Mater. Sci.* **1973**, *8*, 9–11.

(197) Kefalas, V.; Argon, A. *J. Mater. Sci.* **1988**, *23*, 253–258.

(198) Spurr, O.; Niegisch, W. *J. Appl. Polym. Sci.* **1962**, *VI*, 585–599.

(199) Sternstein, S.; Ongchin, L. *Polym. Prepr.* **1969**.

(200) Kambour, R. P.; Gruner, C. L.; Romagosa, E. E. *J. Polym. Sci. Polym. Phys. Ed.* **1973**, *11*, 1879–1890.

(201) Kambour, R. P. *J. Polym. Sci. Macromol. Rev.* **1973**, *7*, 1–154.

(202) Kambour, R. P.; Gruner, C. L.; Romagosal, E. E. *Macromolecules* **1973**, *7*, 248–253.

(203) Kambour, R.; Smith, S. *J. Polym. Sci. Polym. Phys. Ed.* **1982**, *20*, 2069–2082.

(204) Hoare, J.; Hull, D. *Philos. Mag.* **2006**, *26*, 443–455.

(205) Barton, A. *Chem. Rev.* **1975**, *75*, 731–751.

(206) Hansen, C. M.; Just, L. *Ind. Eng. Chem. Res.* **2001**, *40*, 21–25.

(207) Narisawa, I. *J. Polym. Sci. Part A-2* **1972**, *10*, 1789–1797.

(208) Iisaka, K. *J. Polym. Sci. Polym. Phys. Ed.* **1979**, *17*, 791–798.

(209) Riquet, a M.; Bose, V.; Feigenbaum, a. *Food Addit. Contam.* **2001**, *18*, 165–176.

(210) Hansen, C. M. *Hansen solubility parameters: a user's handbook*, Second edi.; CRC press, 2012.

(211) Seehra, M. S.; Yalamanchi, M.; Singh, V. *Polym. Test.* **2012**, *31*, 564–572.

(212) Corp., M. SU-8 2000 Data Sheet http://www.microchem.com/.

(213) Ai, Y.; Zhang, M.; Joo, S. W.; Cheney, M. a.; Qian, S. *J. Phys. Chem. C* **2010**, *114*, 3883–3890.

(214) Cheng, L. J.; Guo, L. J. *ACS Nano* **2009**, *3*, 575–584.

(215) Apel, P. Y.; Blonskaya, I. V; Orelovitch, O. L.; Ramirez, P.; Sartowska, B. a. *Nanotechnology* **2011**, *22*, 175302.

(216) White, H. S.; Bund, A. *Langmuir* **2008**, *24*, 2212–2218.

(217) Pu, Q.; Yun, J.; Temkin, H.; Liu, S. *Nano Lett.* **2004**, *4*, 1099–1103.

(218) Xuan, X.; Li, D. *Electrophoresis* **2007**, *28*, 627–634.

(219) Van Der Heyden, F. H. J.; Stein, D.; Dekker, C. *Phys. Rev. Lett.* **2005**, *95*, 9–12.

(220) Andersen, M. B.; Bruus, H.; Bardhan, J. P.; Pennathur, S. *J. Colloid Interface Sci.* **2011**, *360*, 262–271.

(221) Daiguji, H. *Chem. Soc. Rev.* **2010**, *39*, 901–911.

(222) Piruska, A.; Gong, M.; Sweedler, J. V; Bohn, P. W. *Chem. Soc. Rev.* **2010**, *39*, 1060–1072.

(223) Sparreboom, W.; van den Berg, a; Eijkel, J. C. T. *Nat. Nanotechnol.* **2009**, *4*, 713–720.

(224) Yuan, Z.; Garcia, A. L.; Lopez, G. P.; Petsev, D. N. *Electrophoresis* **2007**, *28*, 595–610.

(225) Qu, W.; Li, D. *J. Colloid Interface Sci.* **2000**, *224*, 397–407.

(226) Burgreen, D.; Nakache, F. R. *J. Phys. Chem.* **1964**, *68*, 1084–1091.

(227) Rice, C. L.; Whitehead, R. *J. Phys. Chem.* **1965**, *69*, 4017–4024.

(228) Hunter, R. J. *Zeta potential in colloid science: principles and applications*; Academic press, 1981.

(229) Bhattacharyya, S.; Zheng, Z.; Conlisk, a. T. *J. Fluid Mech.* **2005**, *540*, 247.

(230) Baldessari, F. *J. Colloid Interface Sci.* **2008**, *325*, 526–538.

(231) Melchionna, S.; Marini Bettolo Marconi, U. *EPL (Europhysics Lett.* **2011**, *95*, 44002.

(232) González-Tovar, E.; Lozada-Cassou, M.; Olivares, W. *J. Chem. Phys.* **1991**, *94*, 2219.

(233) Zheng, Z.; Hansford, D. J.; Conlisk, A. T. *Electrophoresis* **2003**, *24*, 3006–3017.

(234) Pennathur, S.; Santiago, J. *Anal. Chem.* **2005**, *77*, 6772–6781.

(235) Qiao, R.; Aluru, N. R. *Langmuir* **2005**, *21*, 8972–8977.

(236) Hildreth, D. *J. Phys. Chem.* **1970**, *74*, 2006–2015.

(237) Choi, Y. S.; Kim, S. J. *J. Colloid Interface Sci.* **2009**, *333*, 672–678.

(238) Ma, Y.; Yeh, L. H.; Lin, C. Y.; Mei, L.; Qian, S. *Anal. Chem.* **2015**, *87*, 4508–4514.

(239) Liu, J.; Wang, M.; Chen, S.; Robbins, M. O. *J. Comput. Phys.* **2010**, *229*, 7834–7847.

(240) Sofos, F.; Karakasidis, T. E.; Liakopoulos, A. *Int. J. Heat Mass Transf.* **2010**, *53*, 3839–3846.

(241) Levine, S.; Marriott, J. R.; Neale, G.; Epstein, N. *J. Colloid Interface Sci.* **1975**, *52*, 136–149.

(242) Chen, Y.; Ni, Z.; Wang, G.; Xu, D.; Li, D. *Nano Lett.* **2008**, *8*, 42–48.

(243) Yeh, L.-H.; Xue, S.; Joo, S. W.; Qian, S.; Hsu, J.-P. *J. Phys. Chem. C* **2012**, *116*, 4209–4216.

(244) Qiao, R.; Aluru, N. R. *J. Chem. Phys.* **2003**, *118*, 4692.

(245) Baldessari, F. *J. Colloid Interface Sci.* **2008**, *325*, 539–546.

(246) Pennathur, S.; Santiago, J. G. *Anal. Chem.* **2005**, *77*, 6782–6789.

(247) Chatterjee, A. N.; Cannon, D. M.; Gatimu, E. N.; Sweedler, J. V.; Aluru, N. R.; Bohn, P. W. *J. Nanoparticle Res.* **2005**, *7*, 507–516.

(248) Stein, D.; Kruithof, M.; Dekker, C. *Phys. Rev. Lett.* **2004**, *93*, 35901.

(249) Duan, C.; Majumdar, A. *Nat. Nanotechnol.* **2010**, *5*, 848–852.

(250) Jacobson, S. C.; Alarie, J. P.; Ramsey, J. M. *Micro Total Anal. Syst.* **2001**, 57–59.

(251) Haywood, D. G.; Harms, Z. D.; Jacobson, S. C. *Anal. Chem.* **2014**, *86*, 11174.

(252) Mela, P.; Tas, N. R.; Berenschot, E. J. W.; van Nieuwkasteele, J.; van den Berg, A. *Electrophoresis* **2004**, *25*, 3687–3693.

(253) Sadr, R.; Yoda, M.; Zheng, Z.; Conlisk, A. T. *J. Fluid Mech.* **2004**, *506*, 357–367.

(254) Ren, L.; Escobedo-Canseco, C.; Li, D. *J. Colloid Interface Sci.* **2002**, *250*, 238–242.

(255) Unlu, M.; Morgan, M. E.; Minden, J. S. *Electrophoresis* **1997**, *18*, 2071–2077.

(256) Xia, D.; Yan, J.; Hou, S. *Small* **2012**, *8*, 2787–2801.

(257) Mijatovic, D.; Eijkel, J. C. T.; van den Berg, A. *Lab Chip* **2005**, *5*, 492–500.

(258) Yasui, T.; Rahong, S.; Motoyama, K.; Yanagida, T.; Wu, Q.; Kaji, N. *ACS Nano* **2013**, *7*, 3029–3035.

(259) Sackmann, E. K.; Fulton, A. L.; Beebe, D. J. *Nature* **2014**, *507*, 181–189.

(260) Plesa, C.; Verschueren, D.; Pud, S.; van der Torre, J.; Ruitenberg, J. W.; Witteveen, M. J.; Jonsson, M. P.; Grosberg, A. Y.; Rabin, Y.; Dekker, C. *Nat. Nanotechnol.* **2016**, *11*, 1093–1097.

(261) Napoli, M.; Eijkel, J. C. T.; Pennathur, S. *Lab Chip* **2010**, *10*, 957–985.

(262) Jeffet, J.; Kobo, A.; Su, T.; Grunwald, A.; Green, O.; Nilsson, A. N.; Eisenberg, E.; Ambjörnsson, T.; Westerlund, F.; Weinhold, E.; Shabat, D.; Purohit, P. K.; Ebenstein, Y. *ACS Nano* **2016**, acsnano.6b05398.

(263) Menard, L. D.; Ramsey, J. M. *Anal. Chem.* **2013**, *85*, 1146–1153.

(264) Wang, Y. C.; Stevens, A. L.; Han, J. *Anal. Chem.* **2005**, *77*, 4293–4299.

(265) Fu, J.; Schoch, R. B.; Stevens, A. L.; Tannenbaum, S. R.; Han, J. *Nat. Nanotechnol.* **2007**, *2*, 121–128.

(266) Davenport, M.; Healy, K.; Pevarnik, M.; Teslich, N.; Cabrini, S.; Morrison, A. P.; Siwy, Z. S.; Létant, S. E. *ACS Nano* **2012**, *6*, 8366–8380.

(267) Harms, Z. D.; Haywood, D. G.; Kneller, A. R.; Selzer, L.; Zlotnick, A.; Jacobson, S. C. *Anal. Chem.* **2015**, *87*, 699–705.

(268) Zhou, K.; Perry, J. M.; Jacobson, S. C. *Annu. Rev. Anal. Chem.* **2011**, *4*, 321–341.

(269) Delgado, A. V.; González-Caballero, F.; Hunter, R. J.; Koopal, L. K.; Lyklema, J. *J. Colloid Interface Sci.* **2007**, *309*, 194–224.

(270) Dukhin, S. S. *Adv. Colloid Interface Sci.* **1993**, *44*, 1–134.

(271) Henry, D. C. In *Proceedings of the Royal Society of London A: Mathematical, Physical and Engineering Sciences*; The Royal Society, 1931; Vol. 133, pp 106–129.

(272) Ohshima, H. *Journal of Colloid and Interface Science*. 1994, pp 269–271.

(273) Ohshima, H. *J. Colloid Interface Sci.* **1996**, *180*, 299–301.

(274) Swan, J. W.; Furst, E. M. *J. Colloid Interface Sci.* **2012**, *388*, 92–94.

(275) Ohshima, H.; Healy, T. W.; White, L. R. *J. Chem. Soc. Faraday Trans. 2 Mol. Chem. Phys.* **1983**, *79*, 1613–1628.

(276) Chen, S. B.; Keh, H. J. *AIChE J.* **1988**, *34*, 1075–1085.

(277) Wiersema, P. .; Loeb, a. .; Overbeek, J. T. . *J. Colloid Interface Sci.* **1966**, *22*, 78–99.

(278) Keh, H.; Anderson, J. *J. Fluid Mech.* **1985**, *153*, 417–439.

(279) Keh, H.; Chen, S. *J. Fluid Mech.* **1988**, *194*, 377–390.

(280) Shugai, A.; Carnie, S. *J. Colloid Interface Sci.* **1999**, *213*, 298–315.

(281) Movahed, S.; Li, D. *J. Nanoparticle Res.* **2012**, *14*, 1–15.

(282) Liu, Y. W.; Pennathur, S.; Meinhart, C. D. *J. Colloid Interface Sci.* **2016**, *461*, 32–38.

(283) Keh, H. J.; Chiou, J. Y. *AIChE J.* **1996**, *42*, 1397–1406.

(284) Hsu, J.-P.; Chen, Z.-S. *Langmuir* **2007**, *23*, 6198–6204.

(285) Ennis, J.; Anderson, J. *J. Colloid Interface Sci.* **1997**, *185*, 497–514.

(286) Hsu, J. P.; Ku, M. H.; Kao, C. Y. *J. Colloid Interface Sci.* **2004**, *276*, 248–254.

(287) Miloh, T.; Boymelgreen, A. *Phys. Fluids* **2014**, *26*.

(288) Hsu, J. P.; Lo, H. M.; Yeh, L. H.; Tseng, S. *J. Phys. Chem. B* **2012**, *116*, 12626–12632.

(289) O'Brien, R. W.; Hunter, R. J. *Can. J. Chem.* **1981**, *59*, 1878–1887.

(290) Keh, H. J.; Hsieh, T. H. *Langmuir* **2008**, *24*, 390–398.

(291) Chen, W. J.; Keh, H. J. *J. Phys. Chem. B* **2013**, *117*, 9757–9767.

(292) Liu, Y. W.; Pennathur, S.; Meinhart, C. D. *Phys. Fluids* **2014**, *26*.

(293) Hsu, J. P.; Yee, C. P.; Yeh, L. H. *Langmuir* **2012**, *28*, 10942–10947.

(294) Wang, N.; Yee, C. P.; Chen, Y. Y.; Hsu, J. P.; Tseng, S. *Langmuir* **2013**, *29*, 7162–7169.

(295) Nedelcu, S.; Sommer, J. U. *Polymers (Basel).* **2014**, *6*, 2942–2960.

(296) O'Brien, R. W.; White, L. R. *J. Chem. Soc. Faraday Trans. 2 Mol. Chem. Phys.* **1978**, *74*, 1607–1626.

(297) Semenov, I.; Raafatnia, S.; Sega, M.; Lobaskin, V.; Holm, C.; Kremer, F. *Phys. Rev. E - Stat. Nonlinear, Soft Matter Phys.* **2013**, *87*, 1–7.

(298) Tseng, S.; Lin, C.; Hsu, J.; Yeh, L. *Langmuir* **2013**, *29*, 2446–2454.

(299) Zhang, X.; Hsu, W. L.; Hsu, J. P.; Tseng, S. *J. Phys. Chem. B* **2009**, *113*, 8646–8656.

(300) Lee, T. C.; Keh, H. J. *Microfluid. Nanofluidics* **2014**, *16*, 1107–1115.

(301) Qian, S.; Joo, S. W.; Hou, W.; Zhao, X. *Langmuir* **2008**, No. 24, 5332–5340.

(302) Wang, L. J.; Keh, H. J. *J. Phys. Chem. C* **2009**, *113*, 12790–12798.

(303) H., O. *Adv. Colloid Interface Sci.* **1995**, *62*, 189.

(304) Ohshima, H. *Colloids Surfaces A Physicochem. Eng. Asp.* **1995**, *103*, 249–255.

(305) Huang, C.-H.; Hsu, H.-P.; Lee, E. *Phys. Chem. Chem. Phys.* **2012**, *14*, 657–667.

(306) Li, W. C.; Keh, H. J. *Colloids Surfaces A Physicochem. Eng. Asp.* **2016**, *497*, 154–166.

(307) Schnitzer, O.; Frankel, I.; Yariv, E. *J. Fluid Mech.* **2014**, *753*, 49–79.

(308) Hsu, J. P.; Ku, M. H. *J. Colloid Interface Sci.* **2005**, *283*, 592–600.

(309) Li, D.; Daghighi, Y. *J. Colloid Interface Sci.* **2010**, *342*, 638–642.

(310) Yoon, B. J.; Kim, S. *J. Colloid Interface Sci.* **1989**, *128*, 275–288.

(311) Mangelsdorf, C. S.; White, L. R. *J. Chem. Soc., Faraday Trans.* **1992**, *88*, 3567–3581.

(312) Ohshima, H. *J. Colloid Interface Sci.* **2002**, *248*, 499–503.

(313) Ohshima, H. *J. Colloid Interface Sci.* **2003**, *262*, 294–297.

(314) Ohshima, H. *Colloids Surfaces A Physicochem. Eng. Asp.* **2005**, *267*, 50–55.

(315) Hsu, J. P.; Yeh, L. H.; Ku, M. H. *J. Colloid Interface Sci.* **2007**, *305*, 324–329.

(316) Khair, A. S.; Squires, T. M. *Phys. Fluids* **2009**, *21*.

(317) Lee, S. Y.; Yalcin, S. E.; Joo, S. W.; Sharma, A.; Baysal, O.; Qian, S. *Microgravity Sci. Technol.* **2010**, *22*, 329–338.

(318) Yeh, L. H.; Liu, K. L.; Hsu, J. P. *J. Phys. Chem. C* **2012**, *116*, 367–373.

(319) Liu, Y.-W. Analysis of Electromigration in Nanofluidics, 2015.

(320) Liu, H.; Qian, S.; Bau, H. H. *Biophys. J.* **2007**, *92*, 1164–1177.

(321) Xuan, X.; Raghibizadeh, S.; Li, D. *J. Colloid Interface Sci.* **2006**, *296*, 743–748.

(322) Xuan, X.; Ye, C.; Li, D. *J. Colloid Interface Sci.* **2005**, *289*, 286–290.

(323) Hulings, Z. K.; Melnikov, D. V.; Gracheva, M. E. *Phys. Rev. E - Stat. Nonlinear, Soft Matter Phys.* **2015**, *91*, 1–7.

(324) Han, R.; Wang, G.; Qi, S.; Ma, C.; Yeung, E. S. *J. Phys. Chem. C* **2012**, *116*, 18460–18468.

(325) Napoli, M.; Atzberger, P.; Pennathur, S. *Microfluid. Nanofluidics* **2011**, *10*, 69–80.

(326) Weerakoon-Ratnayake, K. M.; Uba, F. I.; Oliver-Calixte, N. J.; Soper, S. A. *Anal. Chem.* **2016**, *88*, 3569–3577.

(327) Loewenberg, M.; Davis, R. H. *J. Fluid Mech.* **1995**, *288*, 103.

(328) Shugai, A. A.; Carnie, S. L.; Chan, D. Y. C.; Anderson, J. L. *J. Colloid Interface Sci.* **1997**, *371*, 357–371.

(329) Keh, H. J.; Yang, F. R. *J. Colloid Interface Sci.* **1991**, *145*, 362–389.

(330) Ding, J. M.; Keh, H. J. *J. Colloid Interface Sci.* **2001**, *236*, 180–193.

(331) Keh, H. J.; Chen, J. B. *J. Colloid Interface Sci.* **1993**, *158*, 199–222.

(332) Peng, R.; Li, D. *Nanoscale* **2016**, *8*, 12237–12246.

(333) Ai, Y.; Liu, J.; Zhang, B.; Qian, S. *Anal. Chem.* **2010**, *82*, 8217–8225.

(334) Dongqing Li. *Encyclopedia of Microfluidics and Nanofluidics*; 2008; Vol. 1.

(335) Uba, F. I.; Pullagurla, S. R.; Sirasunthorn, N.; Wu, J.; Park, S.; Chantiwas, R.; Cho, Y.-K.; Shin, H.; Soper, S. A. *Analyst* **2015**, *140*, 113–126.

(336) German, S. R.; Hurd, T. S.; White, H. S.; Mega, T. L. *ACS Nano* **2015**, *9*, 7186–7194.

(337) Wang, Y.; Kececi, K.; Mirkin, M.; Mani, V. *Chem. Sci.* **2013**, *4*, 655–663.

(338) German, S. R.; Luo, L.; White, H. S.; Mega, T. L. *J. Phys. Chem. C* **2013**, *117*, 703–711.

(339) Song, Y.; Zhang, H.; Chon, C. H.; Pan, X.; Li, D. *Sensors Actuators, B Chem.* **2011**, *155*, 930–936.

(340) Terejánszky, P.; Makra, I.; Fürjes, P.; Gyurcsányi, R. E. *Anal. Chem.* **2014**, *86*, 4688–4697.

(341) Rudzevich, Y.; Lin, Y.; Wearne, A.; Ordonez, A.; Lupan, O.; Chow, L. *Colloids Surfaces A Physicochem. Eng. Asp.* **2014**, *448*, 9–15.

(342) Song, Y.; Peng, R.; Wang, J.; Pan, X.; Sun, Y.; Li, D. *Electrophoresis* **2013**, *34*, 684–690.

(343) Wei, R.; Gatterdam, V.; Wieneke, R.; Tampé, R.; Rant, U. *Nat. Nanotechnol.* **2012**, *7*, 257–263.

(344) Zhou, K.; Li, L.; Tan, Z.; Zlotnick, A.; Jacobson, S. C. *J. Am. Chem. Soc.* **2011**, *133*, 1618–1621.

(345) Harms, Z. D.; Mogensen, K. B.; Nunes, P. S.; Zhou, K.; Hildenbrand, B. W.; Mitra, I.; Tan, Z.; Zlotnick, A.; Kutter, J. P.; Jacobson, S. C. *Anal. Chem.* **2011**, *83*, 9573–9578.

(346) Song, Y.; Zhang, H.; Chon, C. H.; Chen, S.; Pan, X.; Li, D. *Anal. Chim. Acta* **2010**, *681*, 82–86.

(347) Song, W.; Pang, P.; He, J.; Lindsay, S. *ACS Nano* **2013**, *7*, 689–694.

(348) Somerville, J. A.; Willmott, G. R.; Eldridge, J.; Griffiths, M.; McGrath, K. M. *J. Colloid Interface Sci.* **2013**, *394*, 243–251.

(349) Darvish, A.; Goyal, G.; Aneja, R.; Kalyana Sundaram, R. V.; Lee, K.; Ahn, C. W.; Kim, K.-B.; Vlahovska, P.; Kim, M. J. *Nanoscale* **2016**, *8*, 14420–14431.

(350) Holden, D. A.; Watkins, J. J.; White, H. S. *Langmuir* **2012**, *28*, 7572–7577.

(351) Menard, L. D.; Mair, C. E.; Woodson, M. E.; Alarie, J. P.; Ramsey, J. M. *ACS Nano* **2012**, *6*, 9087–9094.

(352) Saleh, O. A.; Sohn, L. L. *Nano Lett.* **2003**, *3*, 37–38.

(353) Cherf, G. M.; Lieberman, K. R.; Rashid, H.; Lam, C. E.; Karplus, K.; Akeson, M. *Nat. Biotechnol.* **2012**, *30*, 344–348.

(354) Zhang, B.; Wood, M.; Lee, H. *Anal. Chem.* **2009**, *81*, 5541–5548.

(355) Kozak, D.; Anderson, W.; Vogel, R.; Chen, S.; Antaw, F.; Trau, M. *ACS Nano* **2012**, *6*, 6990–6997.

(356) Eldridge, J. A.; Willmott, G. R.; Anderson, W.; Vogel, R. *J. Colloid Interface Sci.* **2014**, *429*, 45–52.

(357) Arjmandi, N.; Van Roy, W.; Lagae, L.; Borghs, G. *Anal. Chem.* **2012**, *84*, 8490–8496.

(358) Sun, L.; Crooks, R. M. *J. Am. Chem. Soc.* **2000**, *122*, 12340–12345.

(359) Pevarnik, M.; Healy, K.; Toimil-Molares, M. E.; Morrison, A.; Létant, S. E.; Siwy, Z. S. *ACS Nano* **2012**, *6*, 7295–7302.

(360) Cai, H.; Wang, Y.; Yu, Y.; Mirkin, M. V.; Bhakta, S.; Bishop, G. W.; Joshi, A. a.; Rusling, J. F. *Anal. Chem.* **2015**, *87*, 6403–6410.

(361) Lan, W. J.; Holden, D. A.; Zhang, B.; White, H. S. *Anal. Chem.* **2011**, *83*, 3840–3847.

(362) Luo, L.; German, S. R.; Lan, W. J.; Holden, D. A.; Mega, T. L.; White, H. S. *Annu Rev Anal Chem* **2014**, *7*, 513–535.

(363) Gao, C.; Ding, S.; Tan, Q.; Gu, L. Q. *Anal. Chem.* **2009**, *81*, 80–86.

(364) Liang, X.; Chou, S. Y. *Nano Lett.* **2008**, *8*, 1472–1476.

(365) Kozak, D.; Anderson, W.; Vogel, R.; Trau, M. *Nano Today* **2011**, *6*, 531–545.

(366) Zhang, Y.; Edwards, M. A.; German, S. R.; White, H. S. *J. Phys. Chem. C* **2016**, *120*, 20781–20788.

(367) Blundell, E. L. C. J.; Mayne, L. J.; Billinge, E. R.; Platt, M. *Anal. Methods* **2015**, *0*, 1–12.

(368) Yang, L.; Yamamoto, T. *Front. Microbiol.* **2016**, *7*, 1–7.

(369) Ito, T.; Sun, L.; Crooks, R. M. *Anal. Chem.* **2003**, *75*, 2399–2406.

(370) Ito, T.; Sun, L.; Bevan, M. A.; Crooks, R. M. *Langmuir* **2004**, *20*, 6940–6945.

(371) Angeli, E.; Volpe, A.; Fanzio, P.; Repetto, L.; Firpo, G.; Guida, P.; Lo Savio, R.; Wanunu, M.; Valbusa, U. *Nano Lett.* **2015**, *15*, 5696–5701.

(372) Han, Y.; Wu, H.; Liu, F.; Cheng, G.; Zhe, J. *Anal. Chem.* **2014**, *86*, 9717–9722.

(373) Wu, X.; Chon, C. H.; Wang, Y.-N.; Kang, Y.; Li, D. *Lab Chip* **2008**, *8*, 1943–1949.

(374) Plesa, C.; Dekker, C. *Nanotechnology* **2015**, *26*, 84003.

(375) Liu, Q.; Wu, H.; Wu, L.; Xie, X.; Kong, J.; Ye, X.; Liu, L. *PLoS One* **2012**, *7*, 1–9.

(376) Blundell, E. L. C. J.; Vogel, R.; Platt, M. *Langmuir* **2016**, *32*, 1082–1090.

(377) Peng, R.; Li, D. *Microfluid. Nanofluidics* **2017**, *21*, 12.

(378) Weatherall, E. *Analyst* **2015**, *140*, 3318.

(379) Johnson, R. P.; Fleming, A. M.; Beuth, L. R.; Burrows, C. J.; White, H. S. *J. Am. Chem. Soc.* **2016**, *138*, 594–603.

(380) Gregg, E. C.; Steidley, K. D. *Biophys. J.* **1965**, *5*, 393–405.

(381) Green, Y.; Park, S.; Yossifon, G. *Phys. Rev. E - Stat. Nonlinear, Soft Matter Phys.* **2015**, *91*, 1–6.

(382) Prabhakaran, R. A.; Zhou, Y.; Zhao, C.; Hu, G.; Song, Y.; Wang, J.; Yang, C.; Xuan, X. *Phys. Fluids* **2017**, *29*, 62001.

(383) Cho, I.; Sung, G. Y.; Kim, S. J. *Nanoscale* **2014**, *6*, 4620.

(384) Yossifon, G.; Chang, H. C. *Phys. Rev. Lett.* **2008**, *101*, 1–4.

(385) Zaltzman, B.; Rubinstein, I. *J. Fluid Mech.* **2007**, *579*, 173–266.

(386) Dydek, E. V.; Zaltzman, B.; Rubinstein, I.; Deng, D. S.; Mani, A.; Bazant, M. Z. *Phys. Rev. Lett.* **2011**, *107*, 1–5.

(387) Blundell, E. L. C. J.; Vogel, R.; Platt, M. *Langmuir* **2016**, *32*, 1082–1090.

(388) Goudie, J. L.; Owen, M. J.; Corporation, D. C. *Electr. Insul. Dielectr. Phenomena, 1998. Annu. Report. Conf. , vol.1, no., pp.120,127 vol. 1*, **1998**, *1*, 120–127.

(389) Weatherall, E.; Hauer, P.; Vogel, R.; Willmott, G. R. *Anal. Chem.* **2016**, *88*, 8648–8656.

(390) Tsutsui, M.; He, Y.; Yokota, K.; Arima, A.; Hongo, S.; Taniguchi, M.; Washio, T.; Kawai, T. *ACS Nano* **2016**, *10*, 803–809.

(391) Qin, Z.; Zhe, J.; Wang, G. *Meas. Sci. Technol.* **2011**, *22*, 45804.

(392) Qiu, Y.; Siwy, Z. *Nanoscale* **2017**, 13527–13537.

(393) Hall, J. E. *J. Gen. Physiol.* **1975**, *66*, 531–532.

(394) Lee, C. Y.; Choi, W.; Han, J.-H. J.-H.; Strano, M. S. *Science (80-.).* **2010**, *329*, 1320–1324.

(395) Ellison, M. D.; Menges, S.; Nebel, L.; D'Arcangelo, G.; Kramer, A.; Drahushuk, L.; Benck, J.; Shimizu, S.; Strano, M. S. *J. Phys. Chem. C* **2017**, *121*, 2005–2013.

(396) Choi, W.; Ulissi, Z. W.; Shimizu, S. F. E.; Bellisario, D. O.; Ellison, M. D.; Strano, M. S. *Nat. Commun.* **2013**, *4*, 2397.

(397) Choi, W.; Lee, C. Y.; Ham, M. H.; Shimizu, S.; Strano, M. S. *J. Am. Chem. Soc.* **2011**, *133*, 203–205.

(398) Peng, R.; Li, D. *Nanoscale* **2017**, *9*, 5964–5974.

(399) Heng, J. B.; Ho, C.; Kim, T.; Timp, R.; Aksimentiev, A.; Grinkova, Y. V.; Sligar, S.; Schulten, K.; Timp, G. *Biophys. J.* **2004**, *87*, 2905–2911.

(400) Steinbock, L. J.; Otto, O.; Chimerel, C.; Gornall, J.; Keyser, U. F. *Nano Lett.* **2010**, *10*, 2493–2497.

(401) Raillon, C.; Granjon, P.; Graf, M.; Steinbock, L. J.; Radenovic, A. *Nanoscale* **2012**, *4*, 4916.

(402) Bell, N. A. W.; Keyser, U. F. *Nat. Nanotechnol.* **2016**, *11*, 645–651.

(403) Waduge, P.; Hu, R.; Bandarkar, P.; Yamazaki, H.; Cressiot, B.; Zhao, Q.; Whitford, P. C.; Wanunu, M. *ACS Nano* **2017**, *11*, 5706–5716.

(404) Blundell, E. L. C. J.; Mayne, L. J.; Lickorish, M.; Christie, S. D. R.; Platt, M. *Faraday Discuss.* **2016**, *193*, 487–505.

(405) Larkin, J.; Henley, R. Y.; Muthukumar, M.; Rosenstein, J. K.; Wanunu, M. *Biophys. J.* **2014**, *106*, 696–704.

(406) Li, W.; Bell, N. A. W.; Hernández-Ainsa, S.; Thacker, V. V.; Thackray, A. M.; Bujdoso, R.; Keyser, U. F. *ACS Nano* **2013**, *7*, 4129–4134.

(407) Platt, M.; Willmott, G. R.; Lee, G. U. *Small* **2012**, *8*, 2436–2444.

(408) Kozak, D.; Anderson, W.; Grevett, M.; Trau, M. *J. Phys. Chem. C* **2012**, *116*, 8554–8561.

(409) Traversi, F.; Raillon, C.; Benameur, S. M.; Liu, K.; Khlybov, S.; Tosun, M.; Krasnozhon, D.; Kis, A.; Radenovic, A. *Nat. Nanotechnol.* **2013**, *8*, 939–945.

(410) Geng, J.; Kim, K.; Zhang, J.; Escalada, A.; Tunuguntla, R.; Comolli, L. R.; Allen, F. I.; Shnyrova, A. V.; Cho, K. R.; Munoz, D.; Wang, Y. M.; Grigoropoulos, C. P.; Ajo-Franklin, C. M.; Frolov, V. A.; Noy, A. *Nature* **2014**, *514*, 612–615.

(411) Park, J. H.; He, J.; Gyarfas, B.; Lindsay, S.; Krstić, P. S. *Nanotechnology* **2012**, *23*, 455107.

(412) Liu, H. H.; He, J.; Tang, J.; Pang, P.; Cao, D.; Krstic, P.; Joseph, S.; Lindsay, S.; Nuckolls, C.; Liu, H. H.; Pang, P.; Cao, D.; Krstic, P.; Joseph, S.; Lindsay, S.; Nuckolls, C. *Science* **2010**, *327*, 64–67.

(413) He, J.; Liu, H.; Pang, P.; Cao, D.; Lindsay, S. *J. Phys. Condens. Matter* **2010**, *22*, 454112.

(414) Liu, L.; Yang, C.; Zhao, K.; Li, J.; Wu, H.-C. *Nat. Commun.* **2013**, *4*, 2989.

(415) Ito, T.; Sun, L.; Bevan, M.; Crooks, R. *Langmuir* **2004**, No. 4, 12340–12345.

(416) Qin, X.; Yuan, Q.; Zhao, Y.; Xie, S.; Liu, Z. *Nano Lett* **2011**, *11*, 2173–2177.

(417) Holt, J. K.; Park, H. G.; Wang, Y.; Stadermann, M.; Artyukhin, A. B.; Grigoropoulos, C. P.; Noy, A.; Bakajin, O. *Science (80-.).* **2006**, *312*, 1034–1037.

(418) Skoulidas, A. I.; Ackerman, D. M.; Johnson, J. K.; Sholl, D. S. *Phys. Rev. Lett.* **2002**, *89*, 185901.

(419) Kim, S.-H.; Shin, U. S. *Bull. Korean Chem. Soc.* **2016**, *37*, 1558–1566.

(420) Ulissi, Z. W.; Shimizu, S.; Lee, C. Y.; Strano, M. S. *J. Phys. Chem. Lett.* **2011**, *2*, 2892–2896.

(421) Wu, X.; Kang, Y.; Wang, Y. N.; Xu, D.; Li, D.; Li, D. *Electrophoresis* **2008**, *29*, 2754–2759.

(422) Shadmehr, S.; Coleman, M.; Liu, B.; Liu, J.; Tang, X. S. *RSC Adv.* **2017**, *7*, 611–616.

(423) Mazloumi, M.; Shadmehr, S.; Rangom, Y.; Nazar, L. F.; Tang, X. S. *ACS Nano* **2013**, *7*, 4281–4288.

(424) Geim, A. K.; Novoselov, K. S. *Nat. Mater.* **2007**, *6*, 183–191.

(425) Smeets, R. M. M.; Keyser, U. F.; Krapf, D.; Wu, M. Y.; Dekker, N. H.; Dekker, C. *Nano Lett.* **2006**, *6*, 89–95.

(426) Chang, H.; Kosari, F.; Andreadakis, G.; Alam, M. A.; Vasmatzis, G.; Bashir, R. *Nano Lett.* **2004**, *4*, 1551–1556.

(427) Li, Y.; Chen, S.; Kaneko, T.; Hatakeyama, R. *Chem. Commun.* **2011**, *47*, 2309–2311.

(428) Yang, C.; Kang, Y.; Huang, X. *Encyclopedia of Microfluidics and Nanofluidics*; 2008; pp 506–516.

(429) Ruggeri, F.; Zosel, F.; Mutter, N.; Różycka, M.; Wojtas, M.; Ożyhar, A.; Schuler, B.; Krishnan, M. *Nat. Nanotechnol.* **2017**, *12*.

(430) Yossifon, G.; Mushenheim, P.; Chang, Y.-C.; Chang, H.-C. *Phys. Rev. E* **2009**, *79*, 46305.

(431) Kim, S. J.; Wang, Y. C.; Lee, J. H.; Jang, H.; Han, J. *Phys. Rev. Lett.* **2007**, *99*, 1–4.

(432) Cho, I.; Sung, G. Y.; Kim, S. J. *Nanoscale* **2014**, *6*, 4620–4626.

Appendix A

Details of the homemade squeezing system

In the nanoimprint process, a pressure gauge is needed to monitor the force applied to the samples. Figure A-1 shows a homemade squeezing system for nanoimprint lithography with force monitored by KgF. The force adjusting bolt is used for pressure adjustment, and the sample is sandwiched by two PMMA stages. A force sensor disassembled from a balance is mounted beneath the lower part of the PMMA stage to detect the force applied. The force value is displayed on the monitor of the balance. This system was verified by using the pressure gauge (Mark-10) as mentioned in CHAPTER 3.

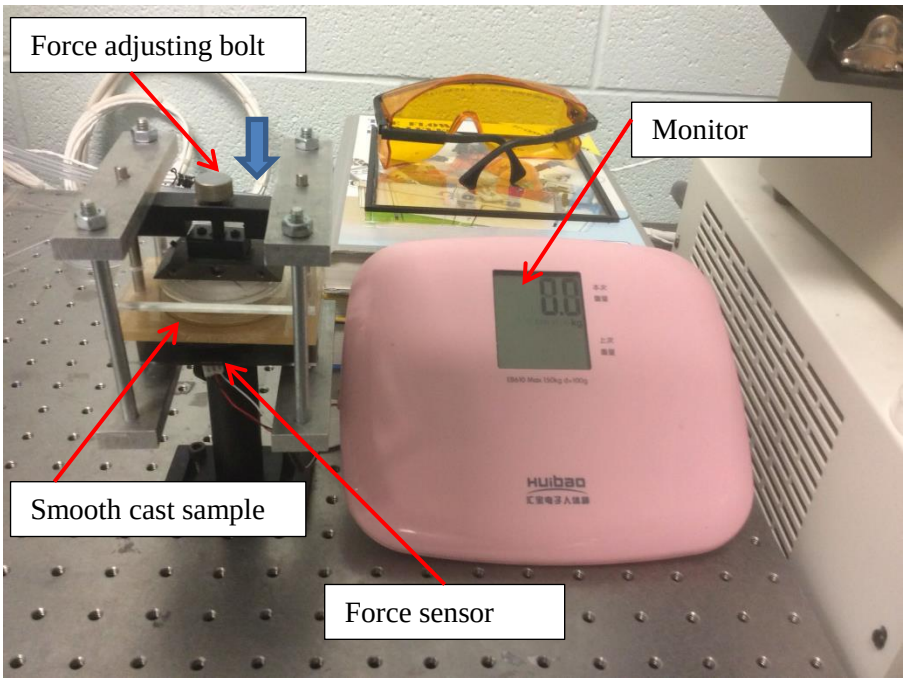

Figure A-1 Picture of a homemade squeezing system for nanoimprint lithography.

Appendix B

Experimental results of electrical current in a single nanochannel and over-limiting current behavior in a nanochannel

Single nanochannel devices and multiple nanochannel devices are powerful tools for nanofluidic studies, such as manipulation of individual nanoparticles or molecules, stretching of DNA, biomolecular preconcentration and electrokinetic transport phenomena in nanoscale. To prove the reliability of the PDMS nanochannel devices made by the methods developed in CHAPTER 3, a series of practical experiments have been conducted. For example, to study the electrical characteristics of the PDMS nanochannels, the conductivity of PDMS nanochannels filled with electrolyte solutions with different ionic concentrations has been measured by an electrometer (Keithley, 6517A). Figure A-2 (a) shows the concentration effects and the applied electric field effects on the electric current in a 254nm deep, 873 nm wide and 200 μm long nanochannel filled with KCl solutions. Obviously, the current increases with the concenration almost linearly when the concentration is higher than 10^{-2} M (the slope of the black dashed line depicts the conductance of the bulk solution), as the concentration decreases, the conductivity of the nanochannel is highly enhanced due to the surface-charge-governed ion transport properties in nanochannels [248]. Similar experimetal results can be found elsewhere [249]. Besides, ohmic-limiting-overlimiting behavior [430,431] in nanochannels has also been studied. Figure A-2 (b) shows an example of I-V curves in a 174nm deep, 509nm wide and 200 μm long nanochannel filled with KCl soltions measured by the electrometer. DC power was applied between the nanochannel with an increment of 0.1V step for 3s duration through Pt electrodes. Obviously, when the applied electric field is lower than 25V, the currents are almost linear with the aplied electric voltage, and as the electric field increases, a limiting region appears for the low concentration cases (0.04 mM and 0.4 mM), however, as the electric field inceases further, the I-V curves become linear again, which is called the “overlimiting” region [430–432].

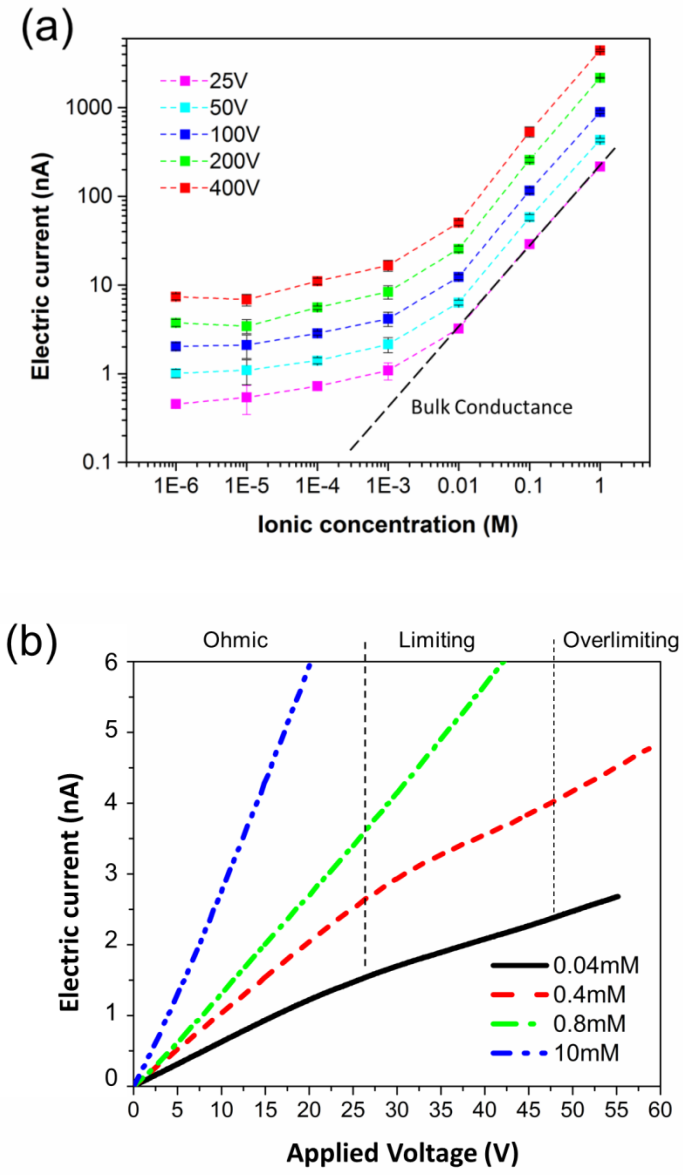

Figure A-2 Experimental results of electrical current in a single nanochannel and over-limiting current behavior in a nanochannel. (a) surface-charge-governed ion transport in a single nanochannel of 254 nm deep; (b) Ohmic-limiting-over-limiting current behavior in a single nanochannel of 174 nm deep.

Appendix C

An example of Matlab code for calculating EOF in a nanochannel

Find electric potential at the middle plane of nanochannel

```
clc
eps_r=80; %% dielectric constant
eps_0=8.854e-12; %% permittivity of vacuum
k_b=1.38e-23; %% Boltzmann constant
temp=298;   %% Temperature
zeta=-0.025; %% Zeta potential calculated from experiments
h_d=10e-9; %% Half height of the nanochannel
c_inf=0.1; %% Concentration of electrolyte solution
na=6.022e23;  %% Avogadro constant
mu=0.001;  %% Viscosity of electrolyte solution
e_u=1.602e-19; %% Unit charge
n_inf=c_inf*na;
lamda=(2*n_inf*e_u^2)/(eps_0*eps_r*k_b*temp);
k_d=sqrt(lamda);
a=k_d*h_d/2;
b=e_u/(2*k_b*temp);
syms x  %%x=ψ_u
eqn=cos(a*exp(b*x))-exp(b*(x-zeta))==0;
solx=solve(eqn,x)
```

Profile of EOF velocity

```
clc
eps_r=80; %% dielectric constant
eps_0=8.854e-12; %% permittivity of vacuum
k_b=1.38e-23; %% Boltzmann constant
temp=298;   %% Temperature
zeta=-0.025; %% Zeta potential calculated from the fitting curve
e_x=2500;   %% externally applied electric potenial
h_d=52e-9; %% Half height of the nanochannel
c_inf=1; %% Concentration of electrolyte solution
na=6.022e23;  %% Avogadro constant
mu=0.001;  %% Viscosity of electrolyte solution
e=1.602e-19; %% Unit charge
x=(-h_d:0.5e-9:h_d);
n_inf=c_inf*na;
lamda=(2*n_inf*e^2)/(eps_0*eps_r*k_b*temp);
k_d=sqrt(lamda);
a=(e*zeta)/(4*k_b*temp);
b=tanh(a).*exp(-k_d*(x+h_d));
c=tanh(a).*exp(-k_d*(h_d-x));
d=atanh(b);
f=atanh(c);
v_potential=(4*k_b*temp/e)*(d+f);
g=1-(v_potential/zeta);
v_eof=-eps_0*eps_r*zeta*e_x*g./mu;
plot (x,v_eof);
hold on
```

Appendix D

Joule heating effects in a nanochannel

(a) Calculated temperature increase in a single nanochannel

Figure A-3 shows a model in calculating Joule heating effect in a nanochannel. The cross area of the nanochannel is A, and an electric potential difference of U is applied along the nanochannel. The electrical current in the channel is I, and the EOF velocity is assumed to be V_{EOF}, which is measured by the current slop method. Here we assume that no heat transfer at the channel wall.

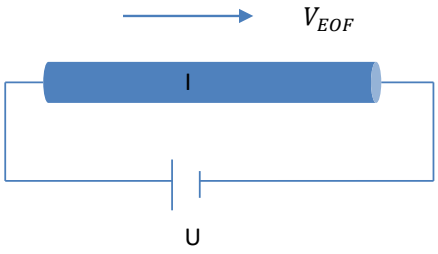

Figure A-3 Schematic of Joule heating in a nanochannel.

For the steady state, the temperature increment inside the nanochannel can be calculated by

$$\Delta T = \frac{UI}{\rho_w A c_p V_{EOF}}$$

The table shows the parameters in detail.

ΔT	Temperature increase
U	Voltage applied
I	Electrical current
ρ_w	Density of buffer solution
A	Cross section of nanochannel
V_{EOF}	EOF velocity
c_p	Specific heat

For a nanochannel of 600 nm wide and 90 nm deep, when the applied electric field is 250V/cm, the current is only 3.6e-11 A. As a result, the calculated temperature increment is about 76℃ if no heat transfer exits at the nanochannel surface. However, in reality, the temperature increment may much lower than this value due to the heat transfer at the boundary.

(b) Measured temperature increase in a single nanochannel

To evaluate the Joule heating effects in single nanochannels, a single-nanochannel was fabricated and the following experiments were conducted:

1. Coat the microchannel molds with a thin layer of x-PDMS (about $50\mu m$) and put the molds into the oven to solidify the x-PDMS layer at 70℃ for 30min;
2. Locate a thermocouple sensor at the microchannel gap;
3. Pour another layer of 2~3 mm thick regular PDMS onto the microchannel molds;
4. Put the microchannel molds into the oven to process another heating process at 70℃ for 2 hours;
5. Peel off the microchannel and bond it to a PDMS nanochannel;
6. Fill the channel with electrolyte solutions and apply electric fields and measure the temperature changes at the gap of the channel.

In the Experiments, the nanochannel size was 241nm deep and 867nm wide, and the ionic concentration of the electrolyte solution was 1M (KCl). The chip was placed on a large piece of aluminum plate to minimize the heating effects. For each electric field value, the temperature is recorded by an electrometer (Keithley 6517a) for at least 20 min until the temperature reached almost constant (steady state). The layout of the nanofluidic chip is shown in Figure A-4, a thermocouple is located at the channel gap. The nanochannel is just beneath the thermocouple. Figure A-5 is a schematic of the cross-section of the temperature measurement system.

It is clear that when the electric field is lower than 100V/cm, the temperature of the chip shows constant, equal to the room temperature about 22.1℃, and the Joule heating effect can be negligible; however, when the electric field is as high as 6000V/cm, the temperature increases to about 32℃ in few minutes and levels off at about 32.9℃, and the Joule heating effect is appreciable.

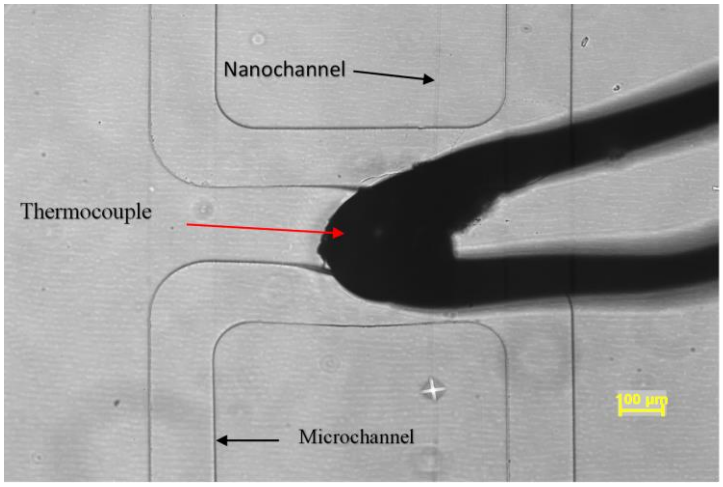

Figure A-4 Layout of the thermocouple and the micro-nanochannel system during the temperature measurement.

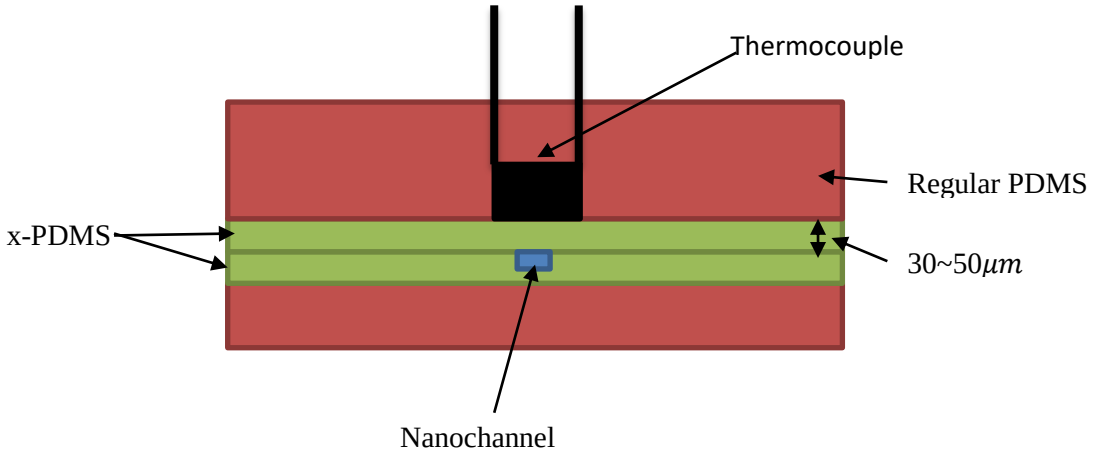

Figure A-5 Schematic of the temperature measurement system developed on a micro-nanofluidic chip.

Table A-1 Results of the temperature measured during the experiments.

E field (V/cm)	0	50	100	250	500	1000	2500	4000	5000	6000
Temperature (℃)	22.1(RT)	22.1	22.1	22.2	22.3	22.5	23.2	25.2	28.1	32.9

Appendix E

Choosing of DC power for nano-RPS chips

To minimize the noise during RPS detection, both hardware and software have to be considered. For the hardware, 4 kinds of DC power supplies have been tried to power the RPS nanofluidic chip. Figure A-7 and Table A-2 show the signals of these 4 power supplies and the frequency distributions of these output signals. From Table A-2 one can get that the battery is the best choice. For other three power supplies, strong noises (50~70Hz) dominate the output signals due to the AC-DC transformation; as a result, the signals of the events are easily immersed in the strong noises. For the battery, the low-level noises of 50~70Hz come from the environment which can be removed by a Faraday case. As a consequence, batteries are applied to power the RPS chips and shielding cable and a shielding box are used to minimize the noises from the environment. All the power supplies and the amplifier are integrated and shielded in the box. For the software part, low pass filters are also used.

Table A-2 Noise level of the power supplies.

Power supply	Noise amplitude	Frequency domain (Hz)
3645A	0.8V	50~70
6517A	0.06V	50~70
CS112001X	0.005V	50~70, 0~10
Battery	0.0025V	50~70, 0~10

(a) 3645A DC power

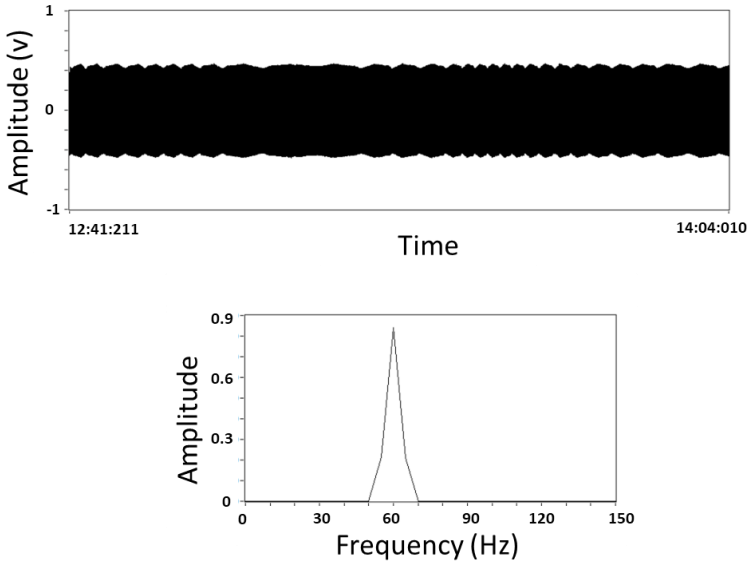

(b) Electrometer 6517A DC power

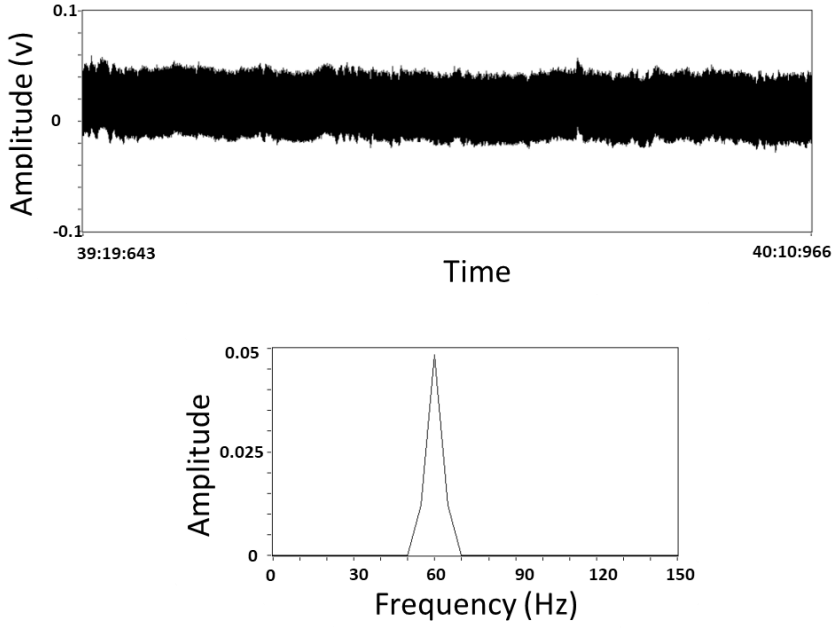

(c) CS112001X DC power supply

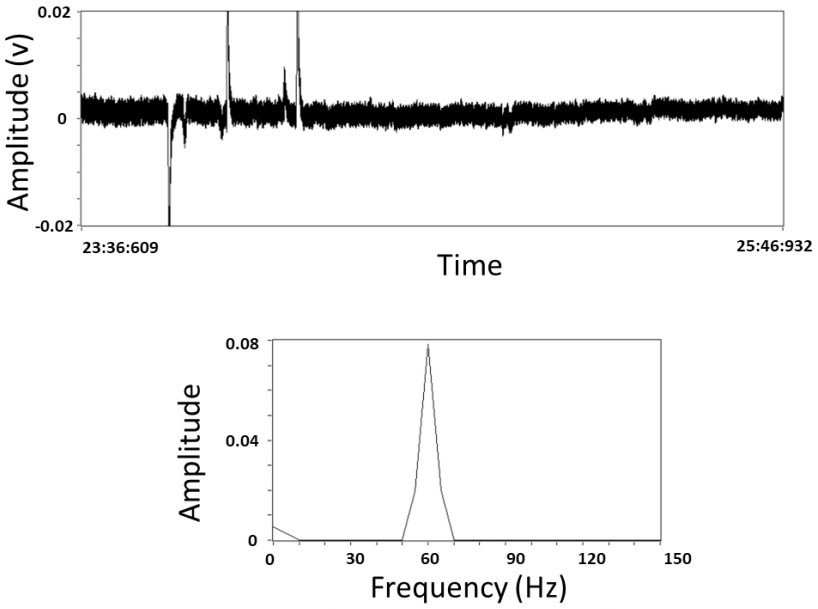

(d) Battery DC power

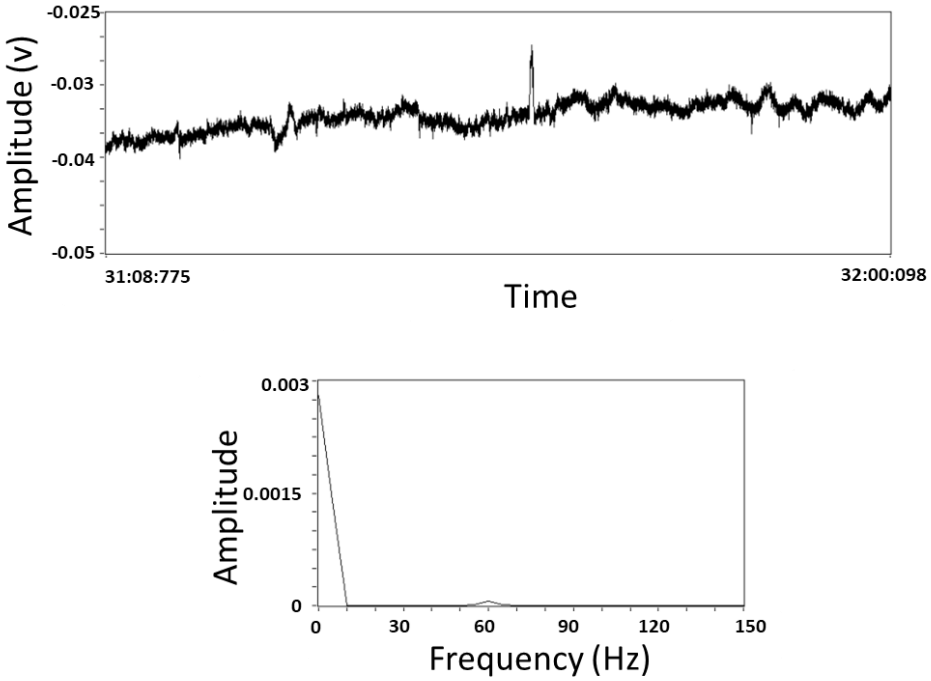

Figure A-7 Amplitudes and frequency domains of the DC powers.

Appendix F

X-PDMS replication tips

Regular PDMS is too soft to support small nanochannels or microchannels with very low aspect ratio. X-PDMS with high Young's modulus can be used to solve this problem. However, x-PDMS is brittle and is easy to break during the peeling off process, especially at the corners of the microchannels. Figure A-8 shows an example of broken channels on x-PDMS after peeling off.

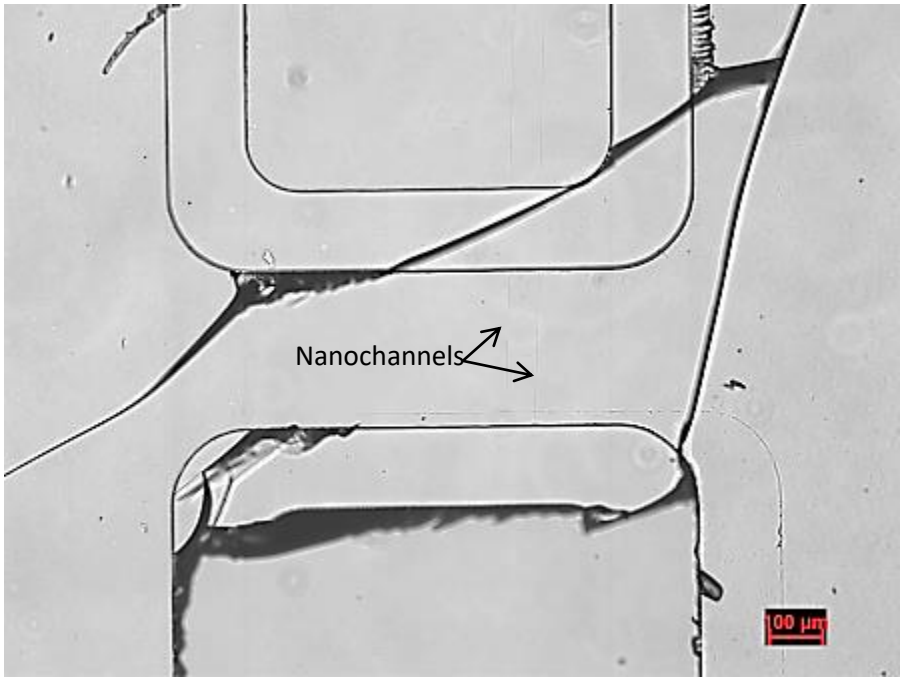

Figure 2 An example of broken channels on x-PDMS after peeling off.

To solve this problem, one can make the channel as smooth as possible and without any sharp corners; however, it is almost impossible for photolithography techniques, because the microchannel is always sharp at the corners. Another way to minimize cracking of the x-PDMS layer is to peel off the PDMS stamps while they are still soft. After extensive try and error, this problem has been solved as follows: firstly, a thin layer of x-PDMS is cast onto the channel molds followed by a 10-min heating process at 70℃ in the oven; secondly, another layer of regular PDMS is cast onto the x-PDMS followed by another heating process at 70℃ for about 1 hour; finally, the PDMS stamp is peeled off from the channel mold as it is still warm and soft but strong enough for peeling off. Then, the PDMS stamp is stored in the oven at 70℃ or higher to further solidify the material. As a result, both the x-PDMS and regular PDMS become harder. To be noted, nanochannels with smaller sizes need longer heating time, generally 1 day or more. Figure A-9 shows an example of PDMS

nanochannels of 54 nm deep after bonding with 1-hour heating time. Obviously, the nanochannel fabricated with 2-hour-heating time collapses in the middle part after bonding.

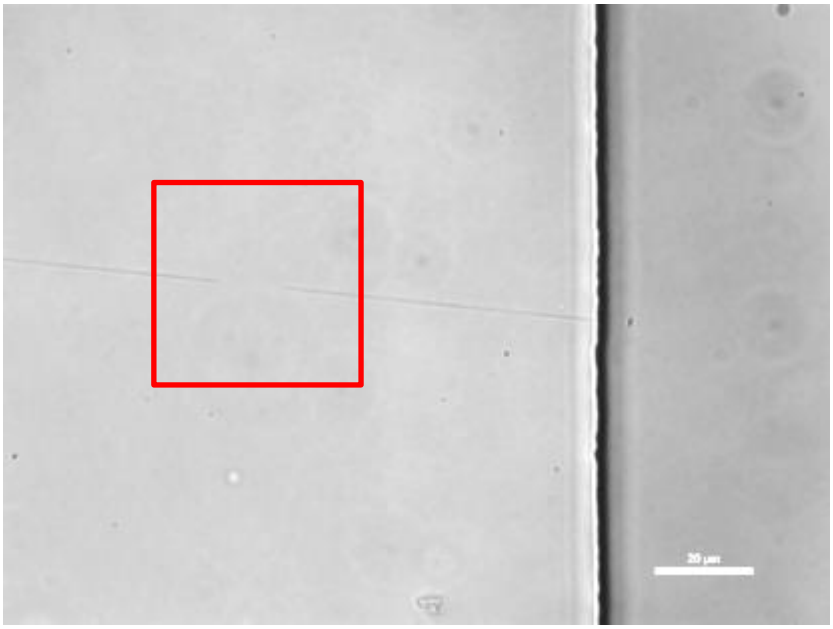

Figure A-9 Collapse of a nanochannel of 54 nm deep after bonding due to insufficient heating time.

Appendix G

Efforts to integrate microchannel and nanochannel on one mold

To integrate microchannels and nanochannels onto the same plate, microchannel system on a PDMS stamp is filled with the liquid form smooth cast; thereafter, the solidifying smooth cast microchannel is attached to a solidified smooth cast nanochannel mold to connect the nanochannel, forming the final micro-nanochannel system. To enhance the adhesion force between the solidified smooth cast nanochannel mold and the solidifying microchannel system, the nanochannel mold is treated with plasma for a certain period of time. As a consequence, the surface energy of the plasma-treated nanochannel mold is high, and it is hard to remove or peel off solidified PDMS from the channel mold surface. To solve this problem, one has to wait for a certain period of time before conducting the PDMS duplication to make sure the surface energy of the channel mold is low enough. Generally, 12 hours are enough.

Effects of plasma treatment on the size of the nanochannel mold

As mentioned above, to enhance the adhesion force between the solidifying smooth cast and the solidified smooth cast nanochannel mold, plasma treatment is needed. However, the plasma may change the size of the positive nanochannels, triggering errors in the channel characterization and the following applications. To study the plasma effects on the channel size, a solidified smooth cast nanochannel mold is treated with plasma for 20 s, 40 s and 60 s and scanned by AFM for at least 3 times. Figure A-10 shows 3D-view images and cross sections of these nanochannels before plasma treatment and after plasma treatment. The original nanochannel is about 651 nm wide and 140 nm high, and after 20 s, 40 s, and 60 s plasma treatment, and the channel sizes are 642 nm wide and 141 nm high, 646 nm wide and 137 nm high, 643 nm wide and 133 nm high, respectively. As a result, one can conclude that plasma treatment has little effect on the channel size. However, one has to handle the adhesion force problem during the PDMS replication.

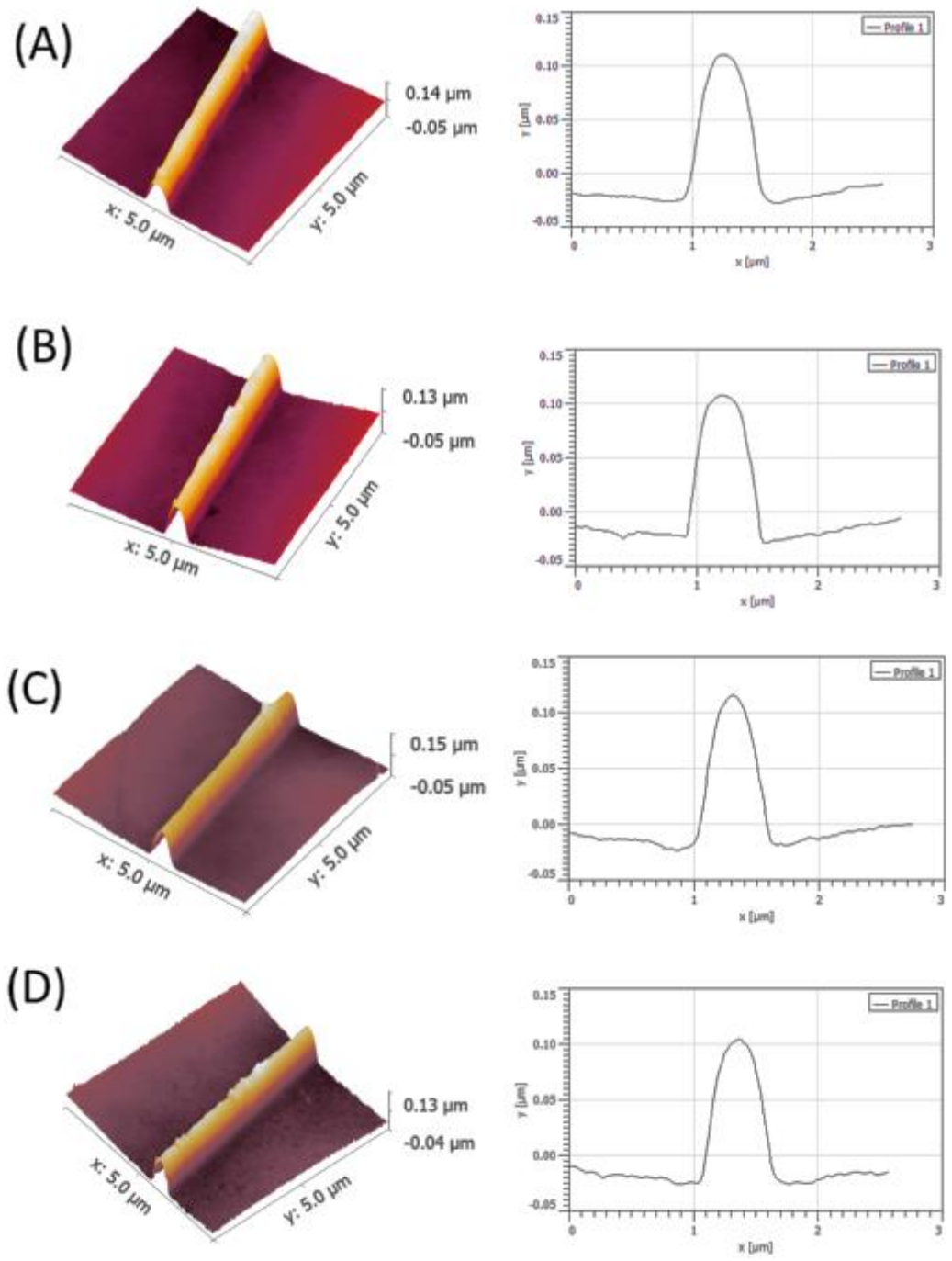

Figure A-11 Plasma treatment time effect on the nanochannel size. (A) Original nanochannel on smooth cast surface, (B) 20s plasma treatment, (C) 40s plasma treatment, (D) 60s plasma treatment.

Figure A-11 (a) is a PDMS micro-nanochannel before bonding, and the zoomed-in view of the two ends of this nanochannel after bonding are also shown in the corners of the figure. It is clear that the straight nanochannel is still open and smooth after bonding. Figure A-11 (b) shows a 3D view image and a cross-section of this nanochannel of about 590 nm wide and 84 nm deep.

A smaller size nanochannel of 616 nm wide and 65 nm deep is shown in Figure A-12. All the nanochannels after bonding are verified by buffer loading. The results show that the nanochannels are open, which means that the micro-nanochannel connection technique we used is reliable.

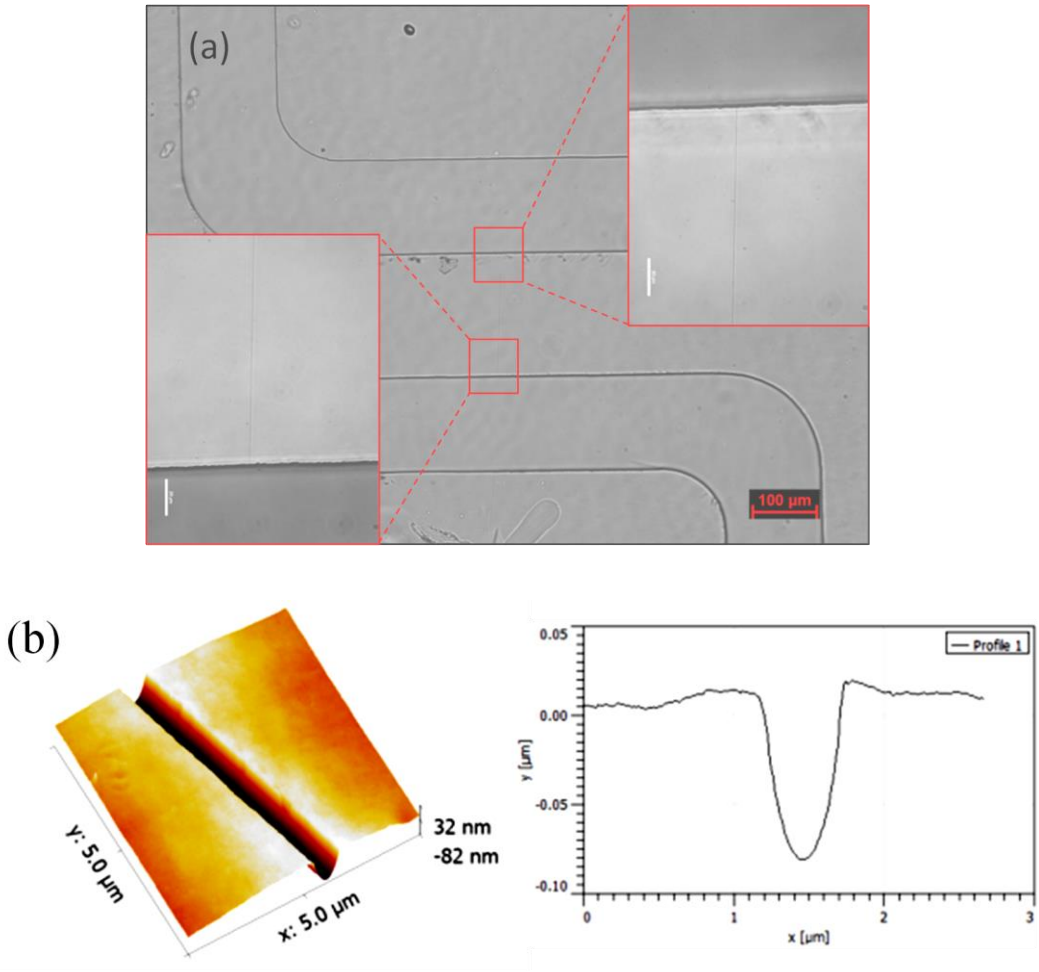

Figure A-11 (a) optical image of a micro-nanochannel system and the entrances of the nanochannel. (b) A 3D image of the nanochannel and a cross-section of this nanochannel.

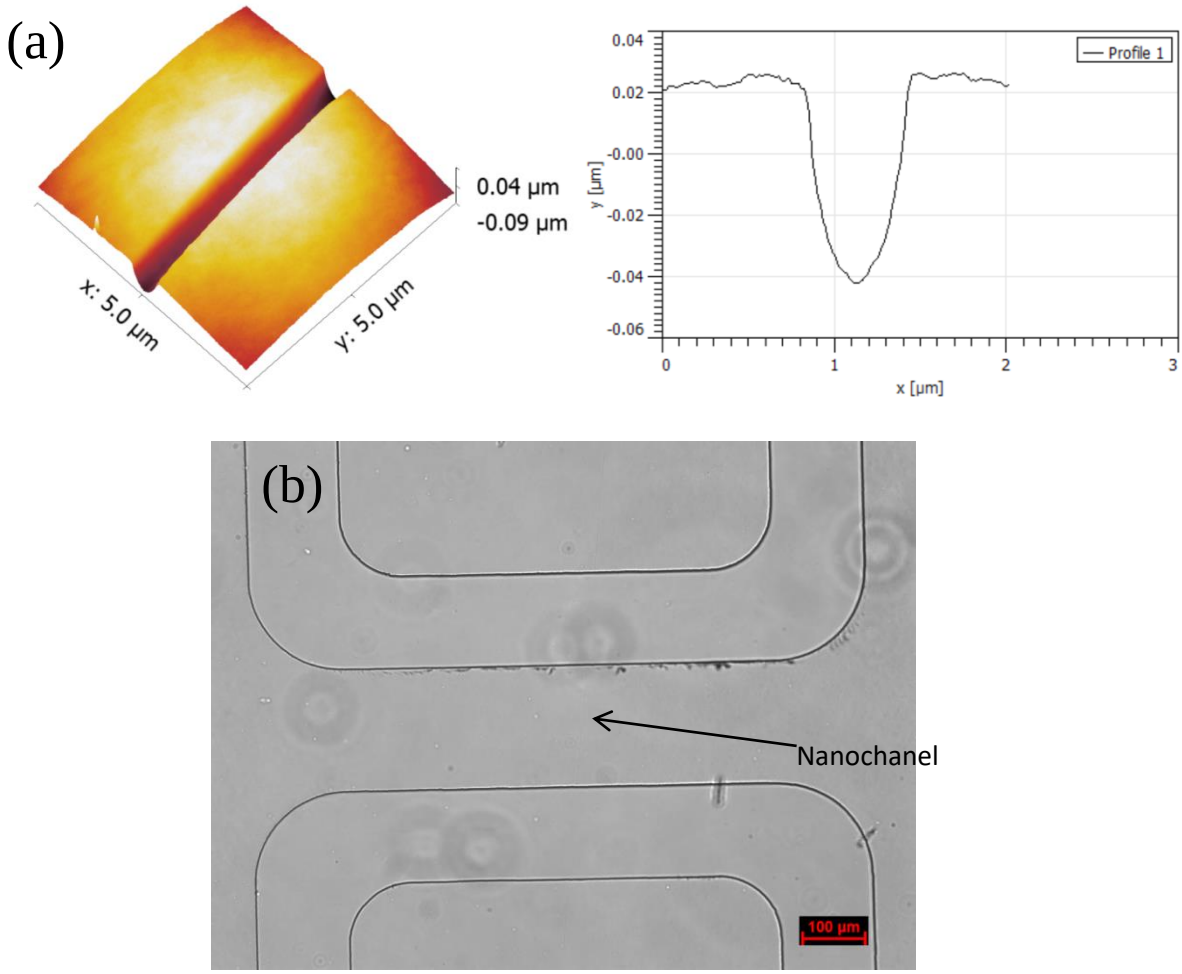

Figure A-12 Smaller nanochannel of 616 nm wide and 65 nm deep is integrated with microchannels. (a) 3D view and a cross section this nanochannel, (b) optical image of the PDMS micro-nanochannel system.

Appendix H

Ran Peng, Xiaowu (Shirley) Tang and Dongqing Li*, "Detecting of Individual Molecules and Ions by Carbon Nanotube-based Differential Resistive Pulse Sensor," ***Small,*** (Accepted)

Ran Peng and Dongqing Li*, "Detecting and Sizing of Nanoparticles and DNAs on PDMS Nanofluidic Chips Based on Differential Resistive Pulse Sensing," ***Nanoscale***, 9, 5964-5974 (2017).

Ran Peng and Dongqing Li*, "Electrokinetic Motion of Single Nanoparticles in Single PDMS Nanochannels," ***Microfluidics. Nanofluidics***, *21*, 12 (2017).

Ran Peng and Dongqing Li*, "Fabrication of Polydimethylsiloxane (PDMS) Nanofluidic Chips with Controllable Channel Size and Spacing," ***Lab Chip***, *16*, 3767 -3776 (2016).

Ran Peng and Dongqing Li*, "Electroosmotic Flow in Single PDMS Nanochannels," ***Nanoscale***, 8, 12237 -12246 (2016).

Ran Peng and Dongqing Li*,"Fabrication of Nanochannels on Polystyrene Surface," ***Biomicrofluidics***, 9, 2, 024117 (2015).